

Atomistic Simulation of Dislocation Motion and Interaction with Crack Tips and Voids

Von der Fakultät Maschinenbau der Universität Karlsruhe (TH)
zur Erlangung des akademischen Grades eines
Doktors der Ingenieurwissenschaften
genehmigte Dissertation

von

DIPL.-PHYS. ERIK BITZEK

aus Ludwigsburg

Hauptreferent: Prof. Dr. rer. nat. P. Gumbsch
Korreferent: Prof. Dr. rer. nat. A. Wanner
Tag der mündlichen Prüfung: 31. 10. 2006

INSTITUT FÜR ZUVERLÄSSIGKEIT VON BAUTEILEN UND SYSTEMEN
UNIVERSITÄT KARLSRUHE (TH)

Parts of this work are already published:

- E. Bitzek, D. Weygand, and P. Gumbsch, “Atomistic study of edge dislocations in fcc metals: drag and inertial effects”, In *IUTAM Symposium on Mesoscopic Dynamics of Fracture Process and Material Strength*, H. Kitagawa and Y. Shibutani, eds., pp. 45 – 57 (Kluwer Academic Publishers , Dordrecht, 2004).
- E. Bitzek and P. Gumbsch, “Atomistic study of drag, surface and inertial effects on edge dislocations in face-centered cubic metals,” *Mater. Sci. Eng. A* **387-389**, 11–15 (2004).
- E. Bitzek and P. Gumbsch, “Dynamics aspects of dislocation motion: atomistic simulations”, *Mater. Sci. Eng. A* **400-401**, 40–44 (2005).
- E. Bitzek and P. Gumbsch, “Atomistic simulations of dislocation - crack interaction”, In *High Performance Computing in Science and Engineering*, (Springer, Heidelberg, 2006), accepted for publication.
- E. Bitzek, P. Koskinen, F. Gähler, M. Moseler and P. Gumbsch, “Structural relaxation made simple”, *Phys. Rev. Lett.* **97**, 170201 (2006)
- M. Moseler, P. Gumbsch, E. Bitzek, P. Koskinen, “Method for calculating a local extremum of a multidimensional function“, pending US patent application.

Erik Bitzek

Atomistische Simulationen zur Versetzungsbewegung und zur Wechselwirkung von Versetzungen mit Risspitzen und Poren

Zusammenfassung

Die Untersuchung des Versagensverhalten von Materialien stellt eine der Hauptaufgaben der Werkstoffwissenschaft dar. Neben der experimentellen Materialforschung und der theoretischen Materialphysik hat sich in letzter Zeit die Werkstoffmodellierung und -simulation als weitere Disziplin herausgebildet. Dabei spielen atomistische Simulationsmethoden besonders bei der Aufklärung der grundlegenden Eigenschaften von Kristalldefekten eine wesentliche Rolle.

Die vorliegende Arbeit beschäftigt sich mit den für das Materialversagen elementaren Kristalldefekten: der Versetzung und dem Riss. Dementsprechend besteht die Arbeit aus zwei Teilen.

In Teil I wird dem Zusammenhang zwischen der Struktur und den Eigenschaften von Versetzungen auf der atomaren Skala und deren Auswirkung auf die Versetzungsbewegung nachgegangen. Im Vordergrund steht dabei die Frage, wie die Dynamik der Versetzungsbewegung deren Wechselwirkung mit kurzreichweitigen Hindernissen beeinflusst. Hierzu wurden zunächst Molekulardynamiksimulationen an Stufen- und Schraubenversetzungen in Aluminium, Nickel und Kupfer durchgeführt, und die grundlegenden Parameter der Versetzungsbewegung bestimmt. Die Simulation der Wechselwirkung einer Stufenversetzung mit Poren unterschiedlicher Größe dient als Modellsystem zur Untersuchung dynamischer Effekte in der Versetzungs-Hindernis-Wechselwirkung. Dabei zeigten sich selbst bei Raumtemperatur ausgeprägte Trägheitseffekte die zu einer Erniedrigung der zur Hindernisüberwindung benötigten kritischen Spannung führen. Diese Trägheitseffekte konnten mit den aus den atomistischen Simulationen bestimmten Parametern der Versetzungsbewegung sowohl in einem dynamischen Linienspannungsmodell als auch in Versetzungsdynamiksimulationen quantitativ abgebildet werden. Solche Modelle ermöglichen somit das Studium dynamischer Versetzungseffekte auf Längen- und Zeitskalen, die der atomistischen Simulation nicht zugänglich sind.

In Teil II steht die Untersuchung der Entstehung von Versetzungen an Rissfronten im Vordergrund. Hierzu wurden dreidimensionale atomistische Simulationen an atomar scharfen und abgestumpften Rissen in der γ -Orientierung in Ni durchgeführt. Dabei zeigten sich fundamentale Unterschiede zwischen der Versetzungsemission von propagierenden und statischen Rissen. Eine lokale Änderung der Rissfrontorientierung kann bei dynamischen Risse zur Emission von abstumpfenden Versetzungen führen. Für statische Risse ist dieser Mechanismus nicht ohne weiteres möglich. Dies kann die im Experiment beobachteten Unterschiede in den aktiven Gleitsystemen erklären. Insbesondere erklärt dieser Mechanismus die Entstehung von "V"-förmigen Versetzungsquellen in dynamischen Bruchversuchen in Si [1]. Weiterhin wurde erstmals die Wechselwirkung bereits bestehender Versetzungen mit einer Rissfront simuliert. Dabei konnten grundlegende, teilweise bisher unbekannte, Mechanismen der Versetzungs-Riss-Wechselwirkung identifiziert werden. Insbesondere konnte der auch experimentell beobachtete Mechanismus der "stimulierten Versetzungsemission" [2] näher untersucht werden.

Erik Bitzek

Atomistic Simulation of Dislocation Motion and Interaction with Crack Tips and Voids

Abstract

The study of materials failure and its relationship to the microstructure of the material lies at the heart of materials science. In this context, computational modeling has become a reliable tool to investigate the behavior of materials and complements the traditional theoretical and experimental approaches in materials science. In particular atomistic simulation methods can provide valuable information on fundamental properties of crystal defects.

This work addresses the fundamental defects responsible for the failure of crystalline materials: dislocations and cracks. Accordingly this thesis consists of two parts.

In part I, the structure and properties of dislocations are studied on the atomic scale, and their relationship with the dynamic properties of dislocations is investigated. A major question in this context is how the dynamics of dislocation motion affects its interaction with short-ranged obstacles. For this purpose the motion of edge and screw dislocations in aluminum, nickel and copper was studied by molecular dynamics simulations. From the dislocation trajectory at different loads and temperatures the parameters governing the dislocation motion were determined. Simulations of the interaction of edge dislocations with voids of different sizes were then used as model system to study dynamic effects in dislocation - obstacle interaction. It could be shown that effects due to the inertia of dislocations can significantly lower the critical stress required to pass an obstacle. With the parameters determined from the atomistic simulations of dislocation motion, the inertial effects can be quantitatively modeled by dynamic line tension or dislocation dynamics models. These methods allow to study dynamic dislocation effects on length and time scales not accessible to atomistic simulations.

Part II is dedicated to the study of the generation of dislocations at crack fronts. Dislocation nucleation processes from crack tips were studied by large scale, three dimensional atomistic simulations of a γ -oriented mode I crack in nickel. The simulation of static, subcritical ($K < K_{Ic}$) and dynamically propagating cracks revealed fundamentally different mechanisms of dislocation nucleation. For propagating cracks a local reorientation of the crack front can lead to the emission of blunting dislocation half loops. This mechanism is specific to propagating cracks, which can explain the differences in the activated slip systems between experiments on static and on propagating cracks. In particular, this mechanism offers an explanation for the "V"-shaped dislocation sources observed in dynamic fracture experiments in Si [1]. Furthermore the interaction of preexisting lattice dislocations with crack fronts was studied for the first time on the atomic scale. These simulations allowed to identify – to a large part hitherto unknown – fundamental interaction mechanisms. In particular, the experimentally observed stimulated emission of dislocations [2] is studied in detail.

Erik Bitzek

Simulations à l'échelle atomistique du mouvement de dislocations et de leur interaction avec fronts de fissures et cavités

Résumé

L'étude de la défaillance des matériaux et du rapport entre microstructure et défaillance se trouve au coeur de la science des matériaux. Dans ce contexte, la modélisation et simulation du comportement des matériaux sur ordinateur est devenue un outil fiable qui complète les approches théoriques et expérimentales traditionnelles dans la science des matériaux. Dans ce domaine, en particulier les méthodes de simulation à l'échelle atomique peuvent fournir des informations utiles sur les propriétés fondamentales des défauts du réseau cristallin.

Ce travail traite les défauts fondamentaux responsables de la défaillance de matériaux cristallins: les dislocations et les fissures. En conséquence cette thèse se compose de deux parties.

Dans la première partie, la structure et les propriétés de dislocations statiques sont étudiées à l'échelle atomique, et leur rapport avec les propriétés dynamiques des dislocations est examiné. Une question importante dans ce contexte est comment la dynamique du mouvement de dislocation affecte l'interaction entre dislocation et obstacles de courte portée. A cette fin, le mouvement des dislocations coin et vis a été étudié par simulations de dynamique moléculaires utilisant différents potentiels d'aluminium, de nickel et de cuivre. A partir de la trajectoire de dislocations soumit à différentes charges et températures, il a été possible d'établir les paramètres qui régissent le mouvement des dislocations. Des simulations de l'interaction d'une dislocation coin avec des cavités de tailles différentes ont servi de système modèle pour étudier les effets dynamiques dans l'interaction entre dislocation et obstacle. Ces simulations ont pu montrer que les effets dus à l'inertie des dislocations peuvent réduire de manière significative la contrainte critique nécessaire pour surmonter un obstacle. Avec les paramètres déterminés à partir des simulations atomistiques du mouvement de dislocation, les effets d'inertie peuvent être reproduits quantitativement par un modèle de tension de ligne dynamique ou par des modèles de dynamique de dislocation. Ces méthodes permettent ainsi d'étudier les effets dynamiques de dislocation sur des échelles de temps, de longueur non accessibles aux simulations atomistiques.

La partie II est consacrée à l'étude de l'origine des dislocations aux fronts de fissures. Les processus de nucléation de dislocation ont été étudiés par des simulations atomistiques en 3D de fissures dans un cristal de nickel en orientation γ soumis à un chargement en mode I. Les simulations de fissures statiques soumis à une charge sous-critiques ($K < K_{Ic}$) et de fissures dynamiques montrent des différences fondamentales des mécanismes de nucléation de dislocation aux fissures statiques et dynamiques. Une modification locale de l'orientation du front de fissure peut en cas de fractures dynamiques conduire à l'émission de dislocations qui réduisent l'acuité du front de fissure. Ce mécanisme est spécifique à la rupture dynamique, ce qui peut expliquer les différences dans les systèmes de glissement actifs entre les expériences sous charge statique et de rupture dynamique. En particulier, ce mécanisme offre une explication pour les sources en forme de "V" observées dans des expériences d'arrêt de rupture dynamiques dans le silicium [1]. De plus, l'interaction du front de fissure avec des dislocations existantes a pu être étudiée pour la première fois à l'échelle atomique. Ceci a permis d'identifier des mécanismes d'interaction entre dislocation et fissure qui étaient jusqu'à présent en grande partie inconnues. En particulier, l'émission stimulée de dislocations, qui était observée expérimentalement [2] a pu être étudiée en détail.

Contents

List of symbols	3
1 Introduction	6
2 Theoretical background and literature overview	9
2.1 Dislocations	9
2.1.1 Continuum theory of dislocations	9
2.1.2 Effects of crystal structure on dislocations	12
2.1.3 Dislocation dynamics	15
2.1.4 Atomistic simulations of dislocations	27
2.2 Fracture	29
2.2.1 Intrinsically brittle versus intrinsically ductile solids	29
2.2.2 Brittle-to-ductile transition	29
2.2.3 Atomistic fracture simulations	39
3 Simulation methods	41
3.1 Molecular dynamics	41
3.1.1 Interatomic potentials	41
3.1.2 Temperature control	42
3.1.3 Boundary conditions	43
3.2 Simulation set-up	43
3.2.1 Simulation set-up for dislocations	43
3.2.2 Simulation set-up for cracks	45
3.3 Visualisation and characterization of defects	49
I Dislocation Motion and Interaction with Obstacles	51
4 Properties of straight static dislocations	52
4.1 Dislocation core structure	52
4.2 Dislocation strain energy	57
4.3 Peierls stress	60
5 Properties of straight moving dislocations	62
5.1 General results and simulation aspects	62
5.1.1 Details of dislocation motion	63
5.1.2 Temperature control and dislocation motion	64

5.1.3	Influence of hydrostatic pressure	64
5.1.4	Size effects in dislocation motion	66
5.2	Dislocation velocity	69
6	Dislocation - obstacle interaction	79
6.1	Void properties	79
6.2	Dislocation pinning by voids	80
6.3	Dynamics of dislocation - void interaction	82
7	Discussion	91
7.1	Static dislocation properties	91
7.1.1	Dislocation dissociation	91
7.1.2	Peierls stress	95
7.1.3	Line energy	96
7.2	Moving dislocations	98
7.2.1	Dislocation inertia	98
7.2.2	Dislocation drag	101
7.2.3	High velocity dislocations	105
7.3	Static and dynamic dislocation - obstacle interactions	108
7.3.1	Static dislocation depinning	108
7.3.2	Dynamics of dislocation - void interactions	112
8	Conclusion I: Dislocation Motion and Interaction with Obstacles	123
9	Outlook I	126
II	Dislocation Nucleation and Multiplication at Crack Tips	129
10	Properties of straight cracks	131
10.1	Griffith load	131
10.2	Stress field of the cracks	133
10.3	Stability of imperfect crack fronts	135
10.4	Dynamic fracture and dislocation emission	135
10.5	Dynamic crack interacting with a void	139
11	Dislocations interacting with cracks	141
11.1	Simulation set-up and symmetry considerations	141
11.2	Blunted cracks	143
11.2.1	Incoming dislocations on the (<i>a</i>)-Plane	143
11.2.2	Incoming dislocations on the (<i>c</i>)-plane	167
11.3	Sharp cracks	168
11.3.1	Large sample, plane stress	168
11.3.2	Large sample, plane strain	170
11.4	Dynamic cracks and dislocations	172

12 Discussion	174
12.1 Simulation specific aspects	174
12.2 Interaction mechanisms between dislocations and cracks	175
12.2.1 Dislocation emission from static cracks	176
12.2.2 Dislocation emission from propagating cracks	176
12.2.3 Dislocation generation during crack-obstacle interactions	177
12.2.4 Interactions between preexisting dislocations and cracks	177
12.3 Dislocations in the stress field of cracks	179
12.4 Atomistic aspects	186
12.5 Relation to experiments	187
12.5.1 Nickel versus silicon	189
12.5.2 Comparison of observed dislocations	189
12.5.3 Sources of dislocations	191
13 Conclusions II:	
Dislocation Nucleation and Multiplication at Crack Tips	194
14 Outlook II	196
A Properties of the atomic interaction potentials	198
B Relaxation methods	201
C Influence of boundary conditions	205
Literature	207

List of symbols

Roman letters

A	anisotropy constant
a_0	lattice constant
B	drag coefficient
\mathbf{b}	Burgers vector
b	magnitude of Burgers vector
c_{ij}	elastic constants
c_l	velocity of longitudinal sound waves
c_R	velocity of Rayleigh waves
$c_t, c_{t,1,2}$	velocity of longitudinal sound waves
D	void diameter
d	dislocation dissociation distance
E_{el}	elastic strain energy of a dislocation
E_{core}	core energy of a dislocation
E_{dis}	dissipated energy
E_{kin}	kinetic energy
E_{pot}	potential energy
\mathbf{F}	force vector
K	energy coefficient
K_I, K_{Ic}	stress intensity factor, critical value of (fracture toughness)
K_{Ia}	crack arrest toughness
L	dislocation line length
L	obstacle spacing
l	free flight distance between obstacles
m	mass of a dislocation per unit length
N	number of particles
P	hydrostatic pressure
R	radius of curvature
R_{void}	void radius
R, r_0	outer and inner cutoff radius for the calculation of the dislocation energy
r_0^m	dislocation core radius determined from the dislocation mass
$S_{pr,se}$	primary, secondary dislocation source
T	temperature
T_m	melting point
t	time
t_r	relaxation time

V	volume
v	velocity
v_c	crossover velocity
v_{ss}	steady state velocity
v_i	impinging velocity
W	work
w	obstacle width
w	width of partial dislocation
z	number of atoms per unit cell

Greek letters

α	Nye tensor
Γ	dislocation line tension
γ	normalized damping coefficient in the Labusch model
γ	crack orientation
γ_{sf}	stacking fault energy
γ_{usf}	unstable stacking fault energy
γ_{utf}	unstable twin fault energy
$\gamma_{(ijk)}$	surface energy
ϵ	strain
ϵ_G	strain corresponding to the Griffith criterion
η_0	normalized obstacle range in the Schwarz-Labusch model
ζ	width of a dislocation
Θ_D	Debye temperature
θ	angle between Burgers vector and dislocation line direction
λ	Lamé constant
$\mu(\mu')$	shear modulus (in the according coordinate system)
$\nu(\nu')$	Poisson's ratio (in the according coordinate system)
ν_A	effective anisotropic Poisson's ratio
ν	phonon frequency
ξ	dislocation line direction
ρ	mass density
ρ	linear Burgers vector density
σ_0	scattering cross section
σ_{ij}	components of the stress tensor
τ, τ_c	resolved shear stress, critical value of
$\tau_{c,F}$	Friedel stress
τ_d	critical stress for dynamic obstacle passing
$\tau_{d,l}, \tau_{d,c}$	lower, upper critical shear stress in the Schwarz-Labusch model
τ_P	Peierls stress
τ_r	radiation friction
τ_η^{-1}	thermostat coupling constant
Φ, Φ_c	half the cusp angle between tangents to dislocation at an obstacle, critical value of
Φ_d	dynamic angle
ω	angular frequency
ω_0	ground frequency

Chapter 1

Introduction

The study of the failure of materials and its relationship to the microstructure of the material lies at the heart of materials science. Materials failure can be divided into two generic types: brittle and ductile. Materials characterized as ductile under certain conditions show extensive plastic deformation before they break, whereas brittle materials only show limited plasticity and break shortly after the elastic regime. Both types of macroscopic failures are ultimately determined on the atomic scale. This is particularly evident in the case of brittle fracture where individual atomic bonds are broken by an atomically sharp crack [3]. However, also the ability of the material to generate dislocations, which are the carriers of plasticity, and the mobility of dislocations is ultimately determined by the nature of the atomic bond. It is therefore obvious that a detailed understanding of brittle fracture and plasticity requires an understanding of the elementary processes on the atomic scale. Experimental information on this length scale is difficult to obtain, therefore atomistic modeling is in many cases the only way to study such processes in detail.

Materials failure generally involves processes on several length and time scales. The macroscopic continuum mechanics for example dictates the stress state around a crack. At the scale where the polycrystalline nature of the material becomes apparent, elasticity and plasticity are however inherently inhomogeneous and anisotropic. Within a grain, the zone around the crack-tip is controlled by the long-range elastic interactions of dislocations with the crack, with each other and with other obstacles like precipitates or grain boundaries. The according length scale is often of the order 10^{-6} m and is usually referred to as a mesoscale [4] between the atomistic and the macroscopic scales. These length scales are connected with each other and processes in all of them may contribute to the total fracture energy. Fracture is therefore inherently a *multiscale* phenomenon of considerable complexity. Similarly, crystal plasticity presents a multiscale problem in time and space, which involves e.g. the formation of entangled dislocation structures. Typically materials are neither fully ductile nor absolutely brittle. The combination of plasticity and fracture can lead to complex phenomena like fatigue or the brittle-to-ductile transition (BDT).

Computational modeling has become a reliable tool for investigating the behavior of materials and complements the traditional theoretical and experimental approaches in materials science. Within the multiscale materials modeling (MMM) approach [5, 6] dislocation dynamics (DD) simulations [7] have a key role: they bridge the gap between the continuum and the atomistic scale where continuum approaches begin to break down and atomistic methods reach their time and length-scale limitations. However, DD simulations require input from the

atomic scale. One important point for example is the determination of the obstacle strength of localized obstacles. Of similar importance for the modeling of dislocation-obstacle interactions on the mesoscale are the parameters governing the actual dynamics of the dislocation motion. So far most dislocation simulations are based on viscous laws of motion which neglect the inertia of dislocations. This approximation is adequate for the simulation of overdamped dislocations under quasistatic loading conditions. However, such a simplified equation of motion is likely to be insufficient for high speed or high strain rate deformation of materials, including cutting processes or shock loading, and for situations with abruptly varying driving forces, like low temperature dislocation-obstacle interaction processes or dislocations in the vicinity of cracks [8].

A fundamental aspect of all types of mesoscale simulations is the inclusion of information from atomistic simulations on processes which can not be simulated on the mesoscale but have to be included by constitutive rules. Short range dislocation-dislocation interaction, cross-slip and dislocation nucleation are typical examples. Currently, dislocations in DD simulations can only be generated by initially specified pre-existing dislocation sources. However, dislocation nucleation and multiplication at crack tips obviously are important processes for which no reliable models exist. Experimental studies on the interaction of single dislocations with loaded cracks in silicon single crystals using in situ X-ray topography showed for example massive and rapid dislocation multiplication when the dislocation impinges on the crack front [2]. Atomistic simulations are currently the only possibility to investigate such fundamental – but largely unexplained – processes in full detail.

The purpose of this work is twofold. One aim is to provide *quantitative* information on the parameters governing the dynamics of dislocations in fcc metals. The focus thereby is on *dynamic dislocation effects*, i.e. effects which are caused by the inertia of dislocation and by the dislocation drag forces [9]. The second objective is to gain a *qualitative* understanding of the atomistic processes during the interaction of dislocations with cracks.

This thesis is accordingly divided into two parts. Part I reports on a comprehensive atomistic study on the static and dynamic properties of dislocations in Al, Ni and Cu. The static dislocation properties include the dislocation line energy, core structure and the Peierls stress of the dislocation. From simulations of moving dislocations subjected to various temperatures and stresses the dislocation drag coefficient, the rest mass and behavior at high velocities are determined. In addition static and dynamic simulations of dislocations interacting with voids are performed to study dynamic dislocation effects in dislocation-obstacle interactions.

Part II addresses the interaction of single dislocations of different orientations and Burgers vectors with atomically sharp and blunted crack tips. Experimentally this has been studied in dislocation free silicon single crystals [2], which represents a special case. However, the interaction of dislocations with cracks, and the generation and multiplication of dislocations at or near crack fronts are of fundamental importance in all materials showing a BDT. The dislocation-crack interaction is studied by molecular dynamics (MD) simulation using a potential for nickel. Ni shares the basic aspects of the glide systems of Si and has a high mobility of dislocations, in agreement with the mobility of dislocations in Si at temperatures near the brittle-to-ductile transition temperature. Although Ni usually is a ductile material, brittle fracture takes place in atomistic simulations when the crack is oriented on certain cleavage planes corresponding to the experimental fracture planes in Si. The use of EAM potentials in combination with high-performance computing furthermore allows the simulations of large systems needed to account for the long range stress fields of cracks.

In the following chapter, a brief introduction to the physics of dislocations and cracks is

given, together with an overview of the current literature on the dynamics on dislocations and crack tip plasticity. It is however assumed that the reader is already familiar with the basic aspects of dislocation theory and fracture mechanics. Chapter 3 introduces the methods and the set-ups used in the present studies, as well as some methods for the analysis of the results. The results of the studies on dislocation dynamics and dislocation-crack interaction are presented, discussed and summarized separately in part I and part II respectively.

Chapter 2

Theoretical background and literature overview

2.1 Dislocations

The properties of dislocations, their creation, motion, multiplication, annihilation and their interaction with each other and with other crystal defects lies at the heart of the discussion of plastic deformation of crystalline materials. The theory of dislocations is presented in depth in several basic reference works [10–13]. The presentation of this theory is therefore limited to the aspects necessary for the understanding of the following chapters, with a focus on the dynamics of dislocations. For an introduction to dislocations and their geometrical properties the reader is referred to above literature. Throughout this work the naming conventions according to Hirth and Lothe [12] are used.

2.1.1 Continuum theory of dislocations

2.1.1.1 Energy of a dislocation

The energy of a dislocation can be divided into the linear elastic part E_{el} of the strain energy outside the dislocation core (radius r_0) and the core energy E_{core} :

$$E_{\text{total}} = E_{\text{el}} + E_{\text{core}} . \quad (2.1)$$

The energy per length L stored in the elastic strain field of a infinite straight dislocation in a region bounded by cylinders with radius r_0 and R can be calculated by integration of the stress field [12]. In an isotropic elastic continuum (characterized by the shear modulus μ and Poisson's ratio ν) the energy per unit length of a screw (s) or edge (\perp) dislocation of Burgers vector b is

$$\frac{E_{\text{el}}^s}{L} = \frac{\mu b^2}{4\pi} \ln \frac{R}{r_0} \quad (2.2)$$

$$\frac{E_{\text{el}}^\perp}{L} = \frac{\mu b^2}{4\pi(1-\nu)} \ln \frac{R}{r_0} . \quad (2.3)$$

By introducing the energy coefficient K the above expressions can be generalized to the anisotropic case [12]:

$$\frac{E_{\text{el}}}{L} = \frac{Kb^2}{4\pi} \ln \frac{R}{r_0}. \quad (2.4)$$

For a perfect screw dislocation oriented along the $\langle 110 \rangle$ axis of a fcc crystal the energy coefficient can be expressed via the stiffness tensor c_{ij} (in abbreviated subscript notation, the apostrophe denotes the elastic constant in the appropriate coordinate system) as [12]

$$K_s = (c'_{44}c'_{55} - c'^2_{16})^{1/2}. \quad (2.5)$$

For edge and mixed dislocations the determination of the energy factor is rather tedious. Teutonico [14] and Duncan [15] show methods how to derive these energy factors. In the case of isotropic elasticity, the energy of mixed dislocations where the Burgers vector forms an angle θ with the line direction, the energy of a mixed dislocation is

$$\frac{E_{\text{el}}^{\text{mixed}}}{L} = \frac{\mu b^2 (1 - \nu \cos^2 \theta)}{4\pi(1 - \nu)} \ln \frac{R}{r_0}. \quad (2.6)$$

The above equations implicate that the dislocation energy depends logarithmically on r_0 and the crystal size R . For crystals containing many dislocations the dislocations tend to form low energy configurations in which the long range stress fields are canceled. An appropriate value for R in the case of randomly arranged dislocations is approximately half the average dislocation spacing [13].

The radius r_0 is usually considered to delimit the region in which the linear elastic theory breaks down. However, the choice of the inner cutoff radius r_0 in Eq. 2.2 is arbitrary, as long as the total energy, Eq. 2.1, is not affected. Therefore r_0 is frequently chosen such that $E_{\text{core}} = 0$. Alternative choices include $r_0 = b$ and $r_0 = r_0^{\text{phys}}$, where r_0^{phys} defines a physical core in which the local atomic order (e.g. coordination number or inversion symmetry) differs from that of an unfaulted crystal by some measure.

An increase of dislocation line length results in an increase in energy. Therefore a line tension Γ with units of energy per unit length can be attributed to a dislocation. In a first approximation the line tension of a dislocation Γ can be set equal to its energy per unit length, Eq. 2.2. However, the character of the dislocation changes as it bows out. This is neglected in the isotropic line tension approximation, i.e. edge, screw and mixed segments are assumed to have the same energy per unit length. This would only be the case for $\nu = 0$. In all other cases, the dislocation line will experience additional forces tending to rotate the dislocation towards screw orientation. The line tension is therefore defined as [13]

$$\Gamma = E_{\text{el}}(\theta) + \frac{d^2 E_{\text{el}}}{d\theta^2}. \quad (2.7)$$

For a more thorough discussion of the concept of line tension the reader is referred to [16] and [17].

2.1.1.2 Dislocations and obstacles

Apart from diffusion effects at high temperatures, plastic deformation in crystalline materials occurs by the glide of dislocations. Hence the critical shear stress for the onset of plastic

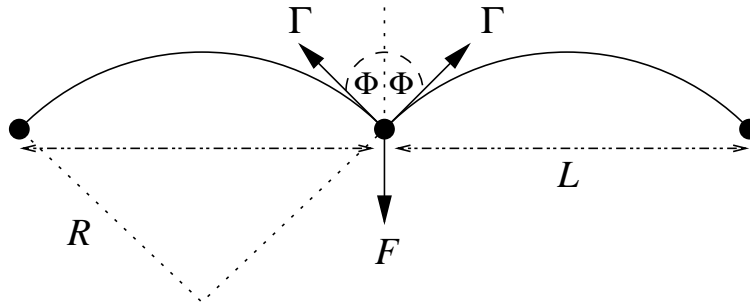


Figure 2.1: Interaction of a dislocation with localized obstacles which exert a glide resistance force F which in equilibrium is balanced by line tension forces Γ .

deformation is the stress required to move dislocations. Creation of obstacles to the dislocation motion therefore leads to an increase of the flow stress. The understanding of the strengthening mechanisms due to interaction of dislocations with various types of obstacles has been one of the successes of dislocation theory. The foundations of dislocation - obstacle interaction are given in various text books, e.g. [13,18,19]. A detailed discussion of individual strengthening mechanisms like work hardening, solid solution and particle strengthening can be found in [20].

Therefore the treatment of dislocation - obstacle interactions is limited here to the special case of equally spaced, localized obstacles. This case corresponds to the configuration which is later modeled in the MD study of dislocation-obstacle interaction. In this situation, the resistance to dislocation motion due to obstacles is represented by a force $F_{\text{obst.}}$ acting on a point of the dislocation line. Under an applied shear stress τ the dislocation will bow out between two obstacles. The radius of curvature R is then related to τ and the line tension Γ by [13]:

$$\tau b = \frac{\Gamma}{R}. \quad (2.8)$$

The bowing of the dislocation is shown in Fig. 2.1. The equilibrium of the line tension and the obstacle force at the pinning point leads to the following relationship for the cusp angle 2Φ :

$$F_{\text{obst.}} = 2\Gamma \cos \Phi. \quad (2.9)$$

The dislocation will break away from obstacles separated by a distance L if the maximum resisting force $F_{\text{obst.}}^{\text{max}}$ at the obstacle is reached by the driving force $\tau b L$ which is acting on the entire dislocation line between the obstacles. With Eq. 2.9 the obstacle strength can be characterized by a critical angle Φ_c given by the critical stress τ_c for dislocation break-away:

$$\Phi_c = \cos^{-1} \left(\frac{\tau_c b L}{2\Gamma} \right). \quad (2.10)$$

The flow stress for a regular square array of localized obstacles can thus be expressed as

$$\tau_c = \frac{2\Gamma}{bL} \cos \Phi_c. \quad (2.11)$$

The different theories to derive the critical resolved shear stress for an *random* array of obstacles are presented in detail in [9].

2.1.2 Effects of crystal structure on dislocations

In the previous section dislocations were treated in an ideal linear elastic continuum. This approach however can not be used to describe the dislocation core where the linear elastic solution diverges. In reality dislocations exist in a crystalline lattice, and the effect of lattice periodicity needs to be taken into account in the description of dislocations. The probably most successful model of a dislocation which takes into account the discreteness of the lattice structure is the so-called Peierls-Nabarro (PN) model [21, 22] which is introduced in the next section. Specific features of dislocations in face-centered cubic (fcc) metals are briefly introduced in section 2.1.2.2. Sec. 2.1.2.3 gives a brief introduction to cross-slip in fcc crystals, which is relevant for the study of dislocations near cracks.

2.1.2.1 The Peierls-Nabarro model of dislocations

A dislocation in a crystalline lattice introduces a *disregistry* of atomic coordination across the slip plane. The disregistry is usually defined as the displacement difference (or slip distribution) $\delta(x)$ between two atoms on adjacent sites above (∇) and below (Δ) the slip plane [13]:

$$\delta(x) = u_{\Delta}(x) - u_{\nabla}(x). \quad (2.12)$$

The *width of a dislocation* ζ is then defined as the distance over which the disregistry is greater than one-half of its maximum value [13]. The width of the dislocation core is determined by the nature of interatomic bonding. An other useful representation of the core structure is given by the *distribution of Burgers vector* $\rho(x)$ which is the derivative of the disregistry curve.

The disregistry in the dislocation core leads to a core energy and to a resistance against motion of the dislocation which are both a function of the interatomic forces. The continuous distribution of Burgers vectors leads to an additional elastic energy. In the first estimate of the lattice resistance [21,22] in a simple cubic model lattice it was assumed that the atoms on the planes Δ and ∇ interact with a simple sinusoidal force relation. A balance of this forces with the elastic stresses from the two half-crystals gives the well-known analytical function solution [22, 23]

$$\delta_{\text{PN}}(x) = \frac{b}{\pi} \tan^{-1} \left(\frac{x}{\zeta} \right) + \frac{b}{2} \quad (2.13)$$

$$\zeta = \frac{Kb}{4\pi\tau_{\text{max}}}, \quad (2.14)$$

where K is an appropriate elastic constant and τ_{max} is the maximum restoring stress [23]. In this framework the Peierls stress τ_P necessary to surmount the periodic Peierls barriers is [12, 23]

$$\tau_P = 4\pi K \exp \left(-\frac{4\pi\zeta}{b} \right). \quad (2.15)$$

It is interesting to note that the Peierls-Nabarro model is one of the first "hybrid" models of multi-scale simulations in so far that it combines continuum theory with a discrete description of the dislocation. There is extensive literature concerning the Peierls-Nabarro model and its extensions and generalizations. Schoeck for example has used a variational principle [24–27]

with parameterized functions for the disregistry function, the Peierls-Nabarro solution ansatz and the generalized stacking-fault energy, to carry out 2-dimensional studies which can take into account anisotropic effects and the relaxation of the dislocation structure. An other approach to extend the original PN model is the semidiscrete variational PN model [23, 28] which can be extended to non-planar dislocation cores.

2.1.2.2 Dislocations in face-centered cubic metals

In face-centered cubic (fcc) metals with lattice constant a_0 the shortest lattice vectors, and therefore the most likely Burgers vectors, are of the type $\mathbf{b} = \frac{a_0}{2}\langle 110 \rangle$. These perfect dislocations are however usually dissociated into two Shockley partial dislocations according to the reaction [12, 13]:

$$\frac{a_0}{2}\langle 110 \rangle \rightarrow \frac{a_0}{6}\langle 211 \rangle + SF + \frac{a_0}{6}\langle 12\bar{1} \rangle, \quad (2.16)$$

including an intrinsic stacking fault (SF) between the two partial dislocations. Within the framework of isotropic linear elasticity the calculation of the separation distance d between the two partial dislocations \mathbf{b}_1 and \mathbf{b}_2 with line direction $\boldsymbol{\xi}$ is straight forward by equating the repulsive force caused by the stress fields of the dislocations with the attractive action of the stacking fault energy γ_{sf} (see e.g. [12]):

$$\gamma_{sf} = \frac{\mu}{2\pi d} \left[(\mathbf{b}_1 \cdot \boldsymbol{\xi})(\mathbf{b}_2 \cdot \boldsymbol{\xi}) + \frac{(\mathbf{b}_1 \times \boldsymbol{\xi}) \cdot (\mathbf{b}_2 \times \boldsymbol{\xi})}{1 - \nu} \right]. \quad (2.17)$$

Using the energy coefficient of the anisotropic elasticity theory for the edge (\perp) and screw (s) components of the partial dislocation, the anisotropic elastic separation of the partial dislocations is given by [12, 29]

$$d = \frac{2}{\gamma_{sf}} (K_s b_s^2 - K_{\perp} b_{\perp}^2). \quad (2.18)$$

The intrinsic stacking fault energy γ_{sf} can thus be determined e.g. from transmission electron microscopy (TEM) of dissociated dislocations. The concept of stacking fault energy was generalized to the generalized stacking fault energy (GSF), or γ -surface, by Vitek [30]. It is defined as the energy density obtained when a crystal is divided along a glide plane in two halves which are rigidly shifted against each other and the atoms are allowed to relax only perpendicular to the glide plane. The γ surface has proven extremely useful for the description of dislocation core structures in connection with the PN model, and the modeling of dislocation nucleation from grain boundaries [31] or cracks [32].

Throughout this work extensive use of the *Thompson notation* is made to describe dislocations in fcc crystals and their reactions. The Thompson tetrahedron is shown in Fig. 2.2, and an example of its use is given in the figure caption.

The sequential arrangement of the partial dislocations is not arbitrary as they have to enclose the intrinsic stacking fault. A way of ensuring this is to use the following axiom together with the naming convention of [12]: When a dislocation (e.g. CD) is viewed from the *outside* of the Thompson tetrahedron along its positive line direction, the stacking fault is limited on the left by the "Greek-Roman" partial βD and to the right by the "Roman-Greek" partial $C\beta$. Viewed along the same positive line direction from *inside* the tetrahedron the sequence of the partial dislocations has to be $C\beta$ on the left and βD on the right [12].

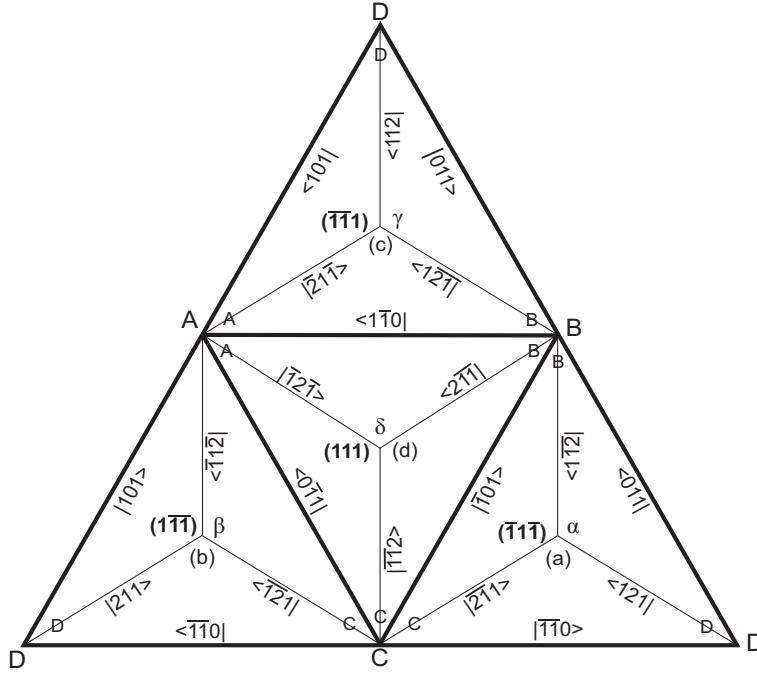


Figure 2.2: Opened up Thompson tetrahedron presenting both the Thompson notation and the usual crystallographic notation. The notation $\langle \bar{1}\bar{1}0 \rangle$ is used instead of the usual notation $[\bar{1}\bar{1}0]$ to indicate the sense of the direction. For example, the perfect dislocation with Burgers vector $a_0/2[\bar{1}\bar{1}0]$ on the $(1\bar{1}\bar{1})$ plane is denoted in the Thompson notation by $CD(b)$. This dislocation can dissociate into $C\beta + \beta D$.

2.1.2.3 Cross-slip in face-centered cubic metals

The dissociation of dislocations into Shockley partials has direct influences on the motion of screw dislocations. In fcc metals, screw dislocations are constraint to a glide in the plane containing their stacking fault, and cross-slip to an other plane is more difficult than for undissociated screw dislocations [13]. It is widely accepted that cross-slip in fcc metals usually takes place by the so-called Friedel-Escaig (FE) mechanism [12]. In the FE cross-slip mechanism the dislocation has to form a constriction in the primary plane, which is then followed by a re-dissociation in the cross-slip plane, see Fig. 2.3a.

An alternative cross-slip mechanism has been suggested by Fleischer [33]: the leading partial dislocation could change glide planes by dissociating into two partial dislocations, one of them on the new glide plane, the other being sessile. The trailing partial dislocation then combines with the sessile partial dislocation to form the trailing partial dislocation in the cross-slip plane. Contrary to the FE mechanism, the Fleischer (FL) mechanism is sensitive to the angle through which the cross-slip takes place. For an obtuse angle cross-slip by the Fleischer mechanism can be described for $CD(b) \rightarrow CD(a)$ by

$$C\beta \rightarrow \alpha D + CD/\beta\alpha \quad \text{and} \quad (2.19)$$

$$\beta D + CD/\beta\alpha \rightarrow C\alpha . \quad (2.20)$$

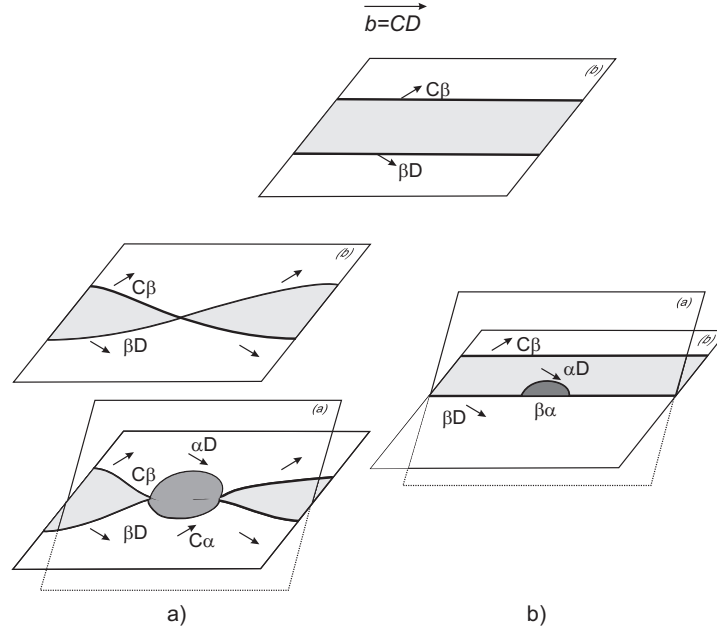


Figure 2.3: Cross-slip mechanisms for a screw dislocation in an fcc crystal (top): a) Friedel-Escaig (FE); b) Fleischer mechanism (FL) to a cross-slip plane making an acute angle with the primary plane. Please note that the (*b*)-plane is viewed from inside the Thompson tetrahedron, whereas the (*a*)-plane is viewed from the outside.

The cross-slip of the same dislocation by an acute angle is realized by

$$\beta D \rightarrow \alpha D + \beta \alpha \quad \text{and} \quad (2.21)$$

$$C\beta + \beta \alpha \rightarrow C\alpha \quad , \quad (2.22)$$

See Fig. 2.3b.

The Fleischer mechanism has recently been observed in MD simulations at high stresses and low temperatures [34, 35]. The FE mechanism on the other hand was also studied with atomistic simulations [36], however it has been argued that the simulation set-up in [36] favors the FE mechanism over the FL by symmetry [34, 37]. There exist therefore currently an uncertainty whether the Fleischer mechanism of cross-slip maybe a viable alternative to the Friedel-Escaig mechanism, especially at high stresses [34, 37].

2.1.3 Dislocation dynamics

2.1.3.1 Equation of motion of a dislocation

The force F_a that an applied shear stress τ exerts on a dislocation segment of unit length with Burgers vector b leads to an acceleration of the dislocation if the resolved shear stress is larger than the Peierls stress, which can be regarded as an internal force F_i . The rate of acceleration is determined by the inertia (or effective mass) m of the dislocation. A deceleration comes from damping or drag effects which dissipate energy. They are characterized by the viscous drag coefficient B . For non-straight dislocations the dislocation self-interaction which can be regarded as a line tension Γ acts in the way to minimize the line energy. In the string model of

a dislocation [38–40], the following equation of motion for a dislocation of unit length aligned along the x -direction and moving with speed $v = \frac{\partial y}{\partial t}$ in the y -direction can be formulated [16]:

$$\frac{\partial}{\partial t} \left(m \frac{\partial y}{\partial t} \right) + B \frac{\partial y}{\partial t} - \Gamma \frac{\partial^2 y}{\partial x^2} = F_a(t) + F_i + F_t(t) + F_r(x, y) . \quad (2.23)$$

Here, an additional interaction of the dislocation with obstacles is included by an obstacle resistance $F_r(x, y)$, which determines the boundary conditions for y and dy/dx at the obstacle. In addition to external forces, random thermal forces can also excite oscillations of the dislocation [41]. They are represented in Eq. 2.23 by a randomly fluctuating Langevin thermal force $F_t(t)$ [16, 40, 41].

For many practical purposes, the internal forces as well as the thermal forces can be neglected, and Eq. 2.23 can be further reduced to describe the motion of a straight dislocation segment under the influence of the Peach-Koehler force τb :

$$\frac{\partial}{\partial t} \left(m \frac{\partial y}{\partial t} \right) + B \frac{\partial y}{\partial t} = \tau b . \quad (2.24)$$

However, the applicability of Eq. 2.23 and Eq. 2.24 to the dynamics of dislocations has several limitations. First of all the radiation of elastic waves by accelerating dislocation segments is not directly taken into account, but incorporated in B . Granato and Lücke [39] solved this by coupling the string model to the equation of elastic waves in an isotropic linear elastic continuum. For subsonic dislocations, the accelerating dislocation is moving through its own radiated field which in principle requires special treatment since the force on the dislocation then is an integral function of its history [42]. Continuum elasticity theory furthermore does not take into account the discrete nature of the crystal in which the dislocation moves. Effects of the crystal lattice are discussed further in sections 2.1.3.3 and 2.1.3.4.

Experiments and simulations (see section 2.1.4) have however shown that in many cases Eq. 2.23 gives an adequate description of the motion of dislocations upto a sizable fraction of the sound velocity [43]. Determining the range in which Eq. 2.23 can be applied is together with the determination of the parameters which govern the motion of dislocation a goal of this thesis.

2.1.3.2 The effective mass of a dislocation

As discussed in [44, 45] the effective mass of a uniformly moving dislocation is closely related to its energy. The energy of a dislocation segment of unit length moving at a velocity v can be calculated by integrating the strain energy and the kinetic energy [46, 47]:

$$E^s = \frac{E_0^s}{\gamma} \quad (2.25)$$

$$E^l = E_0^s \frac{c_t^2}{2v^2} (16\gamma_l + 8\gamma_l^{-1} - 14\gamma - 12\gamma^{-1} + 2\gamma^{-3}) \quad (2.26)$$

where $\gamma = \sqrt{1 - v^2/c_t^2}$, $\gamma_l = \sqrt{1 - v^2/c_l^2}$, c_t is the transverse sound velocity, and c_l is the longitudinal sound velocity. E_0^s is the energy of a screw dislocation at rest, see Eq. 2.2. Weertman [47] derived the expression for the effective mass of uniformly moving screw dislocations in analogy to classical mechanics as one half of the coefficient of v^2 in the Taylor expansion of

the total energy $E^s = E_0^s/\gamma$. The mass per unit length of a screw dislocation at low velocities is then given by

$$m_0^s = \frac{E_0^s}{c_t^2}. \quad (2.27)$$

At high velocities the total energy can be written as

$$E^s = \frac{m_0^s v^2}{\sqrt{1 - v^2/c_t^2}} = m^s v^2 \quad (2.28)$$

giving the relativistic expression for the inertia $m^s = m_0^s/\gamma$.

In contrast to the screw dislocation, the Taylor expansion of the total energy of a moving edge dislocation contains no terms in v^2 . Therefore the above approach to derive the mass of a dislocation can not be applied to edge dislocations. For slow moving dislocations, however, the following expression was derived by Weertman [47]:

$$m_0^\perp = \left(1 + \frac{c_t^4}{c_l^4}\right) m_0^s. \quad (2.29)$$

The rest masses of edge and screw dislocations are very similar, since the longitudinal wave speed $c_l = \sqrt{\frac{\lambda+2\mu}{\rho}}$ is usually about twice the transverse wave velocity $c_t = \sqrt{\mu/\rho}$ (with Lamé constant λ , shear modulus μ and mass density ρ). With the above, one can estimate the rest mass of a length b of dislocation to be about $m_0 b \approx \frac{1}{2}\rho b^3$, i.e. roughly one half atom per Burgers vector. Equations 2.2, 2.27 and 2.29 lead to following relation between rest mass of and edge dislocation and its line energy at rest:

$$E_0^\perp = \frac{m_0^\perp c_t^2}{1 - \nu} \left(1 + \frac{c_t^4}{c_l^4}\right)^{-1}. \quad (2.30)$$

The effective mass of a fast moving edge dislocation can be derived by considering the change in the energy E^\perp of the dislocation caused by a force F [43, 48]:

$$dE^\perp = F dx = F v dt. \quad (2.31)$$

Using the chain rule

$$dE^\perp = \frac{dE^\perp}{dv} \frac{dv}{dt} dt \quad (2.32)$$

the force can be written as

$$F = \frac{1}{v} \frac{dE^\perp}{dv} \frac{dv}{dt} = m_1^\perp \frac{dv}{dt}. \quad (2.33)$$

Hirth *et al.* [43] and Sakamoto [48] independently derived different expressions for the dynamic mass of a moving edge dislocation. However, in the following it is shown that the two expressions are equivalent to each other by taking into account the appropriate definition of the force in Eq. 2.23. Hirth *et al.* [43] identified in Eq. 2.33 the factor multiplying the acceleration as mass m_1^\perp .

Sakamoto [48], however, defined the mass m_2^\perp by the change of momentum with time

$$F = \frac{dp}{dt} = \frac{d}{dt} m_2^\perp v \quad (2.34)$$

$$= \left(\frac{dm_2^\perp}{dv} \cdot v + m_2^\perp \right) \frac{dv}{dt} = m_1^\perp \frac{dv}{dt} , \quad (2.35)$$

thereby obtaining the following integral expression for the mass:

$$m_2^\perp = \frac{1}{v} \int_0^v \frac{1}{v} \frac{dE}{dv} dv = \frac{1}{v} \int_0^v m_1^\perp dv . \quad (2.36)$$

The kinetic energy of a moving edge dislocation is then simply given by

$$E_{\text{kin}}^\perp = \frac{1}{2} m_2^\perp v^2 . \quad (2.37)$$

Both expressions for the effective mass can be calculated using the total energy of the moving edge dislocation (Eq. 2.25) [43, 48]:

$$m_1^\perp = \frac{E_0^s c_t^2}{v^4} (-8\gamma_l - 20/\gamma_l + 4/\gamma_l^3 + 7\gamma + 25/\gamma - 11/\gamma^3 + 3/\gamma^5) \quad (2.38)$$

$$m_2^\perp = E_0^s (-2/c_t^2 \gamma + 4c_t^2/c_l^4 \gamma_l - 16c_t^4 \gamma/5v^6 + 8c_t \gamma^3/5v^6 + 8c_t^4 \gamma^5/5v^6 - 64c_t^2 \gamma/15v^4 + 16c_t^2 \gamma^3/15v^4 + 8c_t^2 \gamma_l/v^4 - 68\gamma/15v^2 + 4c_t^2 \gamma_l/c_l^2 v^2 + v^2/ct^4 \gamma^3) . \quad (2.39)$$

In the limit of small velocities both equations reduce to Eq. 2.29 [43, 48]. The assumptions leading to the derivation of the expression for the dislocation mass, Eqs. 2.31 - 2.33, are generally applicable, and the so derived expressions for the mass can be used in Eq. 2.24 to describe the uniform or non-uniform motion of a dislocation [43].

The mass of an edge dislocation approaches infinity as γ^{-3} while it approaches infinity as γ^{-1} for screw dislocations. In figure (2.4) the effective mass of edge (Eq. 2.39) and screw (Eq. 2.28) dislocations are plotted as function of their velocity. It can be seen that the effective mass of an edge dislocation differs from the rest mass by 20% at a velocity about $v \approx c_t/3$, whereas the mass of a screw dislocation is increased by 20% at $v \approx c_t/2$.

The effective mass m of a mixed dislocation (θ : angle between Burgers vector and line direction) moving with uniform velocity v is given by [48]:

$$m(\theta) = m^s \cos^2(\theta) + m_2^\perp \sin^2(\theta) . \quad (2.40)$$

2.1.3.3 Special velocities

The continuum theory of high velocity dislocations and of special velocities which put a limit to the maximal dislocation velocity is reviewed in [44, 47] and in [12]. Therefore this section provides only a brief summary on the continuum theory of high velocity dislocation motion. Models which include the discreteness of the crystalline lattice are discussed in [49] and are covered here in some more detail. These theories will be later compared to the results of the atomistic simulations.

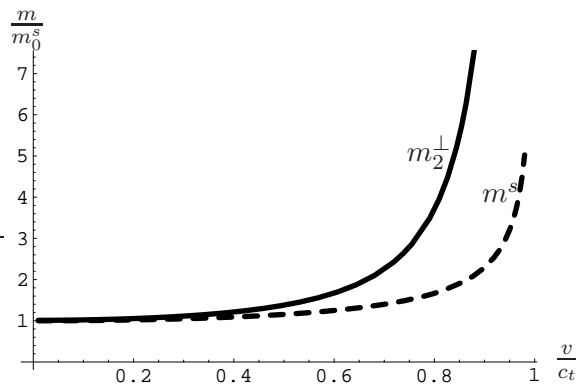


Figure 2.4: The mass of an edge and a screw dislocation as function of their velocity (compare Eq. 2.39 and Eq. 2.27) calculated with the values of c_t, c_l of Cu.

The dislocation motion is typically classified as either subsonic, transonic or supersonic. Subsonic dislocations are slower than the shear wave velocity $v < c_t$. Screw dislocations are called supersonic for $c_t < v$, whereas supersonic edge dislocations are faster than the velocity of longitudinal waves: $c_l < v$. Transonic velocities are $v = c_t$ for screw dislocations and $c_t < v < c_l$ for edge dislocations. Within the continuum theory a uniformly moving subsonic dislocation has a stress and displacement field which is constant in the coordinate system moving with the dislocation. In this case no sound waves are radiated from the dislocation. The energy of the dislocation is constant and in the absence of drag forces no external stresses are required to keep the dislocation in motion [44].

At the transverse shear wave velocity c_t the effective mass and the energy of the moving dislocation are both diverging. Therefore it is not possible to accelerate a dislocation above this speed. In anisotropic crystals two transversal waves of different polarization exist. The velocities $c_{t_{1,2}}$ of the two shear waves in the $\langle 111 \rangle$ direction are [50]:

$$c_{t_1} = \sqrt{(c'_{44} + \sqrt{2}c'_{14})/\rho} \quad (2.41)$$

$$c_{t_2} = \sqrt{(c'_{44} - c'_{14}/\sqrt{2})/\rho}, \quad (2.42)$$

where the c'_{ij} denote the elastic constants in the appropriate coordinate system of the dislocation. The slower of the two shear wave velocities is the limiting velocity for dislocation motion. Depending on the elastic anisotropy of the material, the limiting velocity can be significantly smaller than the usual expression for the shear wave velocity $c_t = \sqrt{c'_{44}/\rho}$ (e.g. in Cu $c_{t_2} = 0.756c_t$). With these appropriate sound velocities the velocity dependence of the mass of edge and screw dislocations can be compared as plotted in Fig. 2.4.

At the Rayleigh wave velocity c_R the width of edge dislocations goes to zero [12]. This fact is not by itself limiting the dislocation velocity, but it causes edge dislocations of like sign that move faster than c_R to attract each other, which can in principle lead to a spontaneous multiplication of dislocations. For dislocations in a crystal with free surfaces c_R would appear as the limiting velocity, because at this velocity resonance with the surface waves occurs and the energy of the solid would approach infinity as v is accelerated towards c_R [12]. The appropriate Rayleigh wave velocity c_R in an anisotropic crystal can be calculated by solving

following equation [51]:

$$\frac{c_R^2}{c_l^2} \sqrt{\frac{c_{22}'}{c_{33}'} \left(1 - \frac{c_R^2}{c_l^2}\right)} = \left(1 - \frac{c_{23}^2}{c_{22}'c_{33}'} - \frac{c_R^2}{c_l^2}\right) \sqrt{1 - \frac{c_R^2}{c_{t_2}^2}}. \quad (2.43)$$

For the metals considered here the differences between c_{t_2} and c_R are less than 5%.

Continuum elasticity does not take into account the discrete nature of the underlying crystal. The discreteness of the lattice has important consequences on the propagation of sound waves. According to the dispersion relation low frequency sound wave propagate at wave speeds according to the continuum theory. High frequency waves travel at lower speeds. Fast moving dislocations can thus be supersonic with respect to some high frequency plane waves and subsonic with respect to other waves. Such partially supersonic dislocations can therefore be expected to radiate high frequency phonons. This was first analyzed by Eshelby [52] for the case of a screw dislocation in a Peierls-Nabarro model within an isotropic medium. According to Eshelby the dislocation begins to radiate when its velocity exceeds the phase velocity $c_p = \frac{\omega}{k}$ of the slowest phonon mode (characterized by its wave vector k and frequency ω) in the first Brillouin zone. According to [52] the radiative damping depends exponentially on the dislocation width ζ and is for velocities slightly larger than c_p proportional to $(v - c_p)^{3/2}$. It has however been argued that due to Umklapp processes (i.e. phonon-phonon interactions which change the total crystal momentum by a reciprocal lattice vector) there is no slowest mode at which the dislocation can radiate, and that radiative damping should be also important at lower dislocation velocities, see [12, 53].

Celli and Flytzanis [54, 55] have derived a relation between the applied strain and the dislocation velocity for a screw dislocation in a two-dimensional lattice using lattice dynamics and nearest neighbors interactions. Like the Eshelby model, the dislocation will radiate only when its velocity equals the phase velocity of some lattice waves. However, their model brakes down when there are elastic waves with phase velocity and group velocity both equal to the dislocation velocity. The energy fed from the dislocation core to these lattice waves propagates in the medium with the group velocity of the waves and therefore never escapes from the core of the dislocation [54]. Bhate [56] has suggested that this might be the physical reason for stress independent velocity plateaus at $v_p < c_R$ observed in MD simulations of edge dislocations subjected to high stresses [53, 56–60], see also sec. 2.1.4.

One of the most recent attempts to model high velocity dislocation motion close to critical velocities is the augmented Peierls-Nabarro model by Rosakis [61]. Rosakis modified the Peierls model to include drag and gradient effects and thus to provide a kinetic relation between shear stress and velocity of uniformly moving dislocations. The model can explain the transonic results obtained by Gumbsch and Gao [57, 62] and predicts unstable motion for $c_R < v < c_t$. However, the model, though nonlocal in nature, is still based on continuum elasticity and thus fails to capture the reported special subsonic velocities v_p [53].

2.1.3.4 Dislocation drag

Any dislocation moving in a crystal experiences drag forces due to its interaction with various elementary excitations. The drag force \mathbf{F}_{drag} per unit length is characterized by the drag coefficient B , which is usually taken to be velocity independent (Newtonian viscous material):

$$\mathbf{F}_{\text{drag}} = -B\mathbf{v} \quad (2.44)$$

The drag coefficient of pure metals comprises contributions from dislocation interaction with phonons (B_{ph}), electrons (B_{e}) and, in magnetic materials, magnons (B_{m}) [16]. At temperatures T smaller than 20% of the Debye temperature Θ_{D} (see App. A for the values of the Debye temperature), the constant electron viscosity is the dominating term, but it can be safely neglected for higher temperatures where the phonon viscosity outweighs B_{e} .

Detailed discussions of dislocation drag processes and compilations of experimentally determined drag coefficients can be found in the reviews by Nadgorny [16] and Alshits [49,63,64]. Therefore only a brief overview of the most important drag mechanisms is provided in the following.

Phonon wind One of the most important drag mechanisms is the *phonon wind*. Phonons are scattered by anharmonicities of the strain field of the moving dislocation. Using Born's theory of scattering and the thermal energy density $E_V = 3kTz/a_0^3$ (k : Boltzmann constant, z : number of atoms per unit cell, a_0 : lattice constant) Leibfried [65] estimated the magnitude of this effect to be

$$B_{\text{ph}}^{\text{w}} = \frac{\sigma_0}{10c_t} \frac{3kTz}{a_0^3}. \quad (2.45)$$

The scattering cross section σ_0 is in the original treatment taken to $\sigma_0 = a_0$ [65], however, it is frequently set to $\sigma_0 = b$, see e.g. [16,49]. As discussed by Nadgorny [16] the reliability of equation (2.45) and the numerical factor 1/10 is limited by approximations and due to the implicit linear temperature dependence of B_{ph}^{w} . According to Lothe [66] the numerical factor may vary between 1/60 and 1/5. More elaborate treatments of the drag by phonon wind lead to a temperature dependence of $B_{\text{ph}}^{\text{w}} \sim T^5$ for $T \ll \Theta_{\text{D}}$ and $B_{\text{ph}}^{\text{w}} \sim T$ for $T \gtrsim \Theta_{\text{D}}$ [16].

Slow phonon viscosity The *slow-phonon viscosity* is caused by the interaction of dislocation with phonons with relatively small group velocities $d\omega/dk$. The phonon viscosity is related to the density of phonon modes per unit frequency range $D(\omega)$, which is inversely proportional to the group velocity. The density of slow phonons is only appreciable for high temperatures $T \approx \Theta_{\text{D}}$, where their contribution to the phonon drag is constant with T and becomes comparable to B_{ph}^{w} .

Flutter effect Energy dissipation by the *flutter effect* is due to the excitation of vibrations of the dislocation line by phonons, which then re-radiate energy. When the dislocation is moving this gives rise to a net force opposing the motion. The flutter effect can be ignored at high temperatures $T \approx \Theta_{\text{D}}$ ($\frac{B_{\text{ph}}^{\text{fl}}}{B_{\text{ph}}^{\text{w}}} \lesssim 0.1$), but it makes an essential contribution at low temperatures $T \ll \Theta_{\text{D}}$ ($\frac{B_{\text{ph}}^{\text{fl}}}{B_{\text{ph}}^{\text{w}}} \approx 1$ for $T \approx 0.2\Theta_{\text{D}}$). For intermediate temperatures the magnitude of the flutter effect is proportional to the temperature [16].

Radiation friction When a dislocation moves in a crystalline lattice its atomic configuration and elastic energy experiences periodic changes due to the Peierls relief. The periodic changes of the configuration of the dislocation core and its nonuniform motion over the relief should lead to radiation of elastic waves by the dislocation, i.e. to radiation friction [63]. In general the radiation friction is not proportional to v , and is thus best described by the radiation friction stress τ_r . It is defined by the constant external force necessary to compensate

for radiation losses $\tau_r = F_{\text{ext,rad}}/b$. At high velocities, where the dislocation kinetic energy is much higher than the Peierls level, perturbations of the uniformity of the dislocation motion can be regarded as negligible. In this regime only the oscillations of the strain field contribute to the radiation friction. It appears that this contribution to the radiation friction can be noticeable against the background of phonon dragging only for near-sonic dislocations at low temperatures [63]. With decreasing dislocation velocity the degree of nonuniformity of its motion increases, and accordingly the radiation losses due to the dynamic oscillations due to the variations of the velocity increases, and the radiation at higher harmonics becomes more and more effective [49]. The viscous dissipation stabilizes the motion of the dislocation. Depending on the drag coefficient an effect of the "dry friction" type should occur [16, 49]. There τ_r approaches the static Peierls stress τ_P with decreasing v .

In the most recent studies of lattice wave emission on dislocations moving in square or triangular lattices, Koizumi *et al.* [67, 68] postulated however, that the energy loss due to radiation is about one order of magnitude larger than the theoretical estimates of phonon-scattering mechanisms - even at room temperature. The statement by Nadgornyi [16] that the problem of radiation friction is still too inadequately studied to allow consistent or quantitative conclusions therefore seems to still hold true.

Electron drag The interaction of moving dislocations with conduction electrons is attributed to the interaction of the electrons with the propagating elastic waves [16]. It is independent of temperature since it involves only the energy of the electrons at the Fermi surface and the thermal energy is small compared to the Fermi energy. A typical value is $B_e = 1 \mu\text{Pa s}$ [16], electron drag is therefore only noticeable at low temperatures.

The knowledge of "typical" drag coefficients is crucial for assessing various effects linked to the dynamics of dislocations – some of which will be discussed in this thesis. Compilations of experimental values for drag coefficients can be found in [16, 49, 63, 64]. However, the experimental values scatter widely – even when the same method is used^a. A generally used value for the drag coefficient at room temperature in aluminum is $B(\text{Al,RT})=26 \mu\text{Pa s}$, other published values range from $B(\text{Al,RT})=8-60 \mu\text{Pa s}$ [16]. For copper, usually $B(\text{Cu,RT})=17 \mu\text{Pa s}$ is assumed (experimental range: 10-85 $\mu\text{Pa s}$), see also table 5.1 on page 229 of [16].

2.1.3.5 Effects of dislocation inertia

The motion of dislocations is usually described by assuming that at each moment in time the velocity of a dislocation is only determined by the momentarily acting Peach-Koehler force [7, 16]^b: $v(t) = \frac{\tau b}{B}$. The assumption of over-damped dislocation motion fails however for rapidly changing forces (e.g. in high strain rate deformation, shock loading, interaction with localized obstacles or high frequency agitation) and for high velocity dislocations at low temperatures or high stresses (e.g. near crack tips). In these cases the inertia of the dislocation can not be neglected and dynamic effects have to be taken into account.

^aCommonly used methods include the measurement of the velocity of individual dislocations, amplitude independent internal friction, high-speed deformation of crystals and slip-band mobility [16].

^bThis over-damped dislocation motion has to be distinguished from the quasi-static (or strain rate independent) regime. In the latter a dislocation configuration is assumed to be always in mechanical equilibrium with externally applied loads, thus not following a dynamic evolution of the dislocation configuration.

Accelerated motion of dislocations As can be seen in Fig. 2.4 the dislocation mass stays nearly constant for velocities $v < c_t/3$. Thus for small velocities Eq. 2.23 can be rewritten for a dislocation of unit length subjected to a force due to an applied shear stress τ as

$$m_0 \frac{\partial}{\partial t} v + Bv = \tau b , \quad (2.46)$$

which can be integrated to

$$v(t) = \frac{\tau b}{B} \left(1 - e^{-\frac{tB}{m_0}} \right) . \quad (2.47)$$

After the relaxation time $t_r = m_0/B$ the velocity of a dislocation accelerating from zero velocity differs from the uniform steady state velocity

$$v_{ss} = \frac{\tau b}{B} \quad (2.48)$$

by less than $1/e$. For typical values of B at room temperature (see pervious section), this time is in the range of few tens of ps. For this reason acceleration is usually neglected in DD simulations, which have typical timesteps in the μs range [7]. However, for resolved shear stresses which would lead to steady state velocities larger than about $c_t/3$ (for edge dislocations) or $c_t/2$ (for screw dislocations) the velocity dependence of the mass can not be neglected anymore. At room temperature this is typically the case for stresses in the range between $\tau = 1/3c_t B/b \geq 50$ MPa (edge dislocation in Cu) to $\tau \geq 100$ MPa (screw dislocation in Al). In these cases Eq. 2.24 has to be solved numerically.

Overdamped versus underdamped dislocation motion The transverse sound velocity puts an upper limit to the attainable steady state velocity. Thus, the dislocations in metals subjected to resolved shear stresses which would lead to $v_{ss} = \frac{\tau b}{B} > c_t$ are clearly not in the steady state and their motion is dominated by inertia rather than dissipation – their motion is underdamped. From this point of view, dislocation motion in material systems with high yield strength and low lattice resistance (e.g. nanocrystalline copper [69]) is very likely to be underdamped.

A more general way to determine whether the motion of a dislocation segment is over- or underdamped is to use the model of a harmonic oscillator [16]. The ground frequency $\omega_0 = \sqrt{k/m}$ is then determined by the stiffness k and the mass m of the system, and the damping is defined as $\beta = B/2m$ with drag coefficient B . If the ratio β/ω_0 is smaller than 1, oscillatory motion is possible (underdamped case), for $\beta/\omega_0 > 1$ no oscillations are possible, the system is overdamped. In the constant line tension model of a dislocation, the stiffness is equivalent to the line tension Γ , B and m are the dislocation drag coefficient and the dislocation rest mass per unit length [16]^c The ground frequency of a dislocation segment of length L can be taken as $\omega_0 = \pi c_t/L$, thus the critical drag coefficient B_c is

$$B_c = \frac{2\pi m_0 c_t}{L} , \quad (2.49)$$

^cEquating the stiffness k of a harmonic oscillator with the line tension Γ as proposed by Nadgornyi [16] is questionable as the restoring force in a line tension model is not of the form $-ky$ but $-\Gamma \frac{d^2 y}{dx^2} = -\Gamma/R(y)$ (see Eq. 2.23). In the constant line tension approximation for small bow-outs the radius of curvature is given by $R(y) = \frac{L^2 + 4y^2}{8y}$, thus for small y the restoring force can be linearized to $-\frac{8}{L^2}\Gamma$. This would lead in Eq. 2.49 to a factor of $4\sqrt{2}$ instead of 2π . In the following this small difference is neglected.

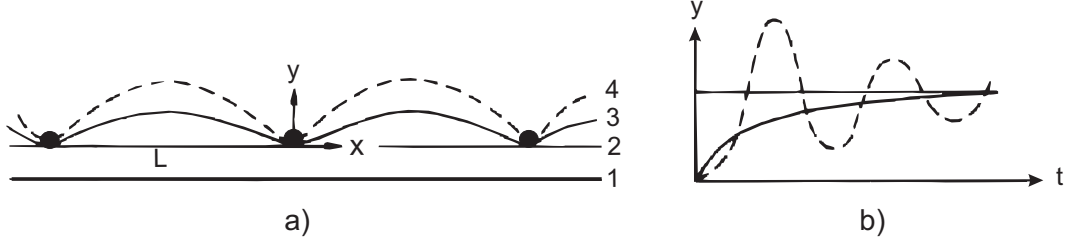


Figure 2.5: Sketch of the process of inertial overshooting according to [71]. a) schematic of the motion of the dislocation line. The solid line at position 3 represents the static equilibrium position of the dislocation line subjected to shear stress τ . The dashed line represents the overshoot position of the underdamped dislocation at the same stress. b) shows the assumed displacement $y(t, x = 0)$ as function of time for a underdamped (dashed line) and a overdamped dislocation (solid line).

or with equations 2.30 and 2.27

$$B_c^s = \frac{2\pi\Gamma^s}{Lc_t} \quad (2.50)$$

$$B_c^\perp = \frac{2\pi\Gamma^s}{Lc_t} \left(1 + \frac{c_t^4}{c_l^4} \right) . \quad (2.51)$$

For estimating whether dislocations are under- or overdamped the segment length L is usually set to the effective obstacle spacing, e.g. the Friedel length [16]. For typical values of B and $E_0 = \mu' b^2/2$ as suggested by Nadgorny^d [16], underdamped dislocation motion at room should take place below an effective obstacle spacing of about $L \approx 300$ nm (Cu) or $L \approx 80$ nm (Al). From this estimation one can expect that even at room temperature a significant fraction of dislocation segments in heavily cold worked [70] or irradiated [5] fcc metals, as well as in some particle strengthened alloys [9] are in the underdamped regime.

Dynamic effects in dislocation - obstacle interactions An important consequence of underdamped dislocation motion is the possibility for a moving dislocation which is running up against obstacles to pass over its static equilibrium position by virtue of its inertia. The notion of *inertial overshooting* of dislocations was first proposed independently by Suenaga and Gallingan [72] and by Granato [71] to explain the enhanced plasticity of superconductors in the superconducting state compared to the normal state. The process of inertial overshooting is visualized in Fig. 2.5. After depinning from an obstacle a dislocation segment accelerates and moves towards the next obstacles (pos. 1 in Fig. 2.5a) and meets the obstacles with the impinging velocity v_i (pos. 2). Its static equilibrium position under the applied shear stress would correspond to pos. 3. An overdamped dislocation would approach this configuration as indicated by the solid curve in Fig. 2.5b. Underdamped dislocations, however, can overshoot the equilibrium position and oscillate about the static configuration. Like in the static case (see sec. 2.1.1.2) the dynamic configurations can be characterized by the angle formed by the dislocation near the obstacles. For dynamic release of the dislocation from the obstacle the minimum *dynamic* angle Φ_d then has to be smaller than the critical angle Φ_c determined from the static equilibrium of forces. Dynamical obstacle passing by inertial overshooting is

^dIn section 7.3.2 it will be shown that this frequently used expression can in many cases lead to a significant overestimation of B_c .

sometimes also referred to as *weak dynamic effect* [9,73]. A different mechanism is postulated to be at work for very small drag coefficients and high dislocation velocities. For *strong dynamic effects* the dislocation segment which is directly interacting with the obstacle has to have accumulated enough kinetic energy to directly break through the obstacle upon contact [9,73].

The effect of inertia on the motion of a dislocation through a random array of obstacles was included in some mesoscopic models [73–80], see e.g. the review by Nadgornyi [16]. In the following we briefly resume the educative results of Schwarz and Labusch [73,74] who were the first to develop such a model.

In addition to inertial effects Schwarz and Labusch [73] also allowed for a finite width w of the randomly arranged obstacles, which were modeled by one dimensional force-distance profiles. Their model, however, is limited to weak obstacles with a not too high volume fraction $f \lesssim 0.2$. The constant line tension approximation is used and interactions between the dislocation segments are neglected (quasi-straight line approximation). Furthermore thermal activation is disregarded. Schwarz and Labusch reduced the usual parameters $m_0, B, \Gamma, \Phi_c, L, w$ by introducing normalized parameters and coordinates to only two characteristic parameters: the normalized obstacle range

$$\eta_0 = \frac{w}{L \cos \Phi_c^{1/2}} \quad (2.52)$$

and the normalized drag coefficient

$$\gamma = \frac{BL}{\sqrt{4\Gamma m_0 \cos \Phi_c}}. \quad (2.53)$$

The stress is normalized by the Friedel stress

$$\tau_{c,F} = \frac{2\Gamma \cos \Phi_c^{3/2}}{bL}. \quad (2.54)$$

With the reduced parameters and coordinates the equation of motion of a dislocation through a planar array of random obstacles was solved numerically [73].

One fundamental finding of their calculations is that in case the normalized drag is small enough ($\gamma \lesssim 3$), one has to distinguish two different (normalized) critical resolved shear stresses (CRSS) [73]. The upper CRSS $\tau_{d,c}$ is the highest stress which still leads to a stable configuration when the dislocation has no starting velocity and the stress is applied quasistatically. The lower CRSS $\tau_{d,l}$ is the lowest stress (starting from $\tau_{d,c}$) at which a moving dislocation would move indefinitely. Under standard experimental conditions $\tau_{d,c}$ is measured [9]. It has to be stressed that $\tau_{d,c}$ is only equal to the (appropriately normalized) static critical stress τ_c for high damping $\gamma > 3$. Below $\gamma \approx 3$ dynamic effects come into play as the first breakaway event in the random array of obstacles is seen to dynamically trigger the depinning from other obstacles [73]. The possibility of such dynamic unzipping processes was also pointed out by Indenbom and Chernov [81]. These processes are caused by the local acceleration due to the dislocation obstacle interaction, which generates waves that can travel along the dislocation and assist the unpinning of the dislocation from other obstacles.

The calculated normalized critical dynamic stresses $\tau_{d,c}$ and $\tau_{d,l}$ are shown in Fig. 2.6 for different normalized drag coefficients and obstacle sizes. Three different regimes can be identified. For very low damping $\tau_{d,c}$ is larger than $\tau_{d,l}$ and independent of γ , whereas

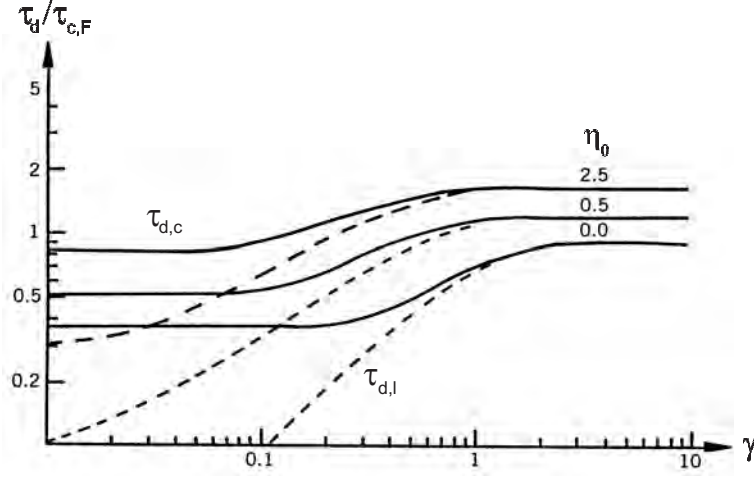


Figure 2.6: Critical normalized upper and lower dynamic stress $\tau_{d,c}$ and $\tau_{d,l}$ as function of normalized damping γ for different normalized obstacle widths η_0 as calculated by Schwarz and Labusch [73]. For clarity only smoothed curves are shown.

$\tau_{d,l}$ is increasing with γ . For point-obstacles ($\eta_0 = 0$) the lower critical dynamic stress is proportional to the normalized drag: $\tau_{d,l} \sim \gamma$. For medium damping $0.1 \lesssim \gamma \lesssim 3$ the upper CRSS $\tau_{d,c}$ and $\tau_{d,l}$ increase with γ . Above $\gamma \approx 1$ both CRSS are approximately the same. For strong damping $\gamma > 3$ the dislocation motion is overdamped and there are no dynamic effects [73]. This empirical finding can be used to derive a critical drag factor which includes information of the obstacle strength. With the definition of γ and using $\Gamma = m_0 c_t^2$ the critical drag coefficient for point-like obstacles is

$$B_c^{\text{Schwarz}} = \frac{3 \cdot 2m_0 c_t}{L} \sqrt{\cos \Phi_c}, \quad (2.55)$$

which for weak obstacles $\Phi_c \approx \pi/2$ is comparable to Eq. 2.49. For larger obstacles the critical drag γ_c at which $\tau_{d,c}$ and $\tau_{d,l}$ deviate from their high- γ -value is reduced. Schwarz and Labusch [73] described the variation of γ_c with η_0 by

$$\frac{\gamma_c(\eta_0)}{\gamma_c(\eta_0 = 0)} = \frac{1}{(1 + 3\eta_0)^{1/2}}. \quad (2.56)$$

Due to the statistical nature of the model no functional form for $\tau_{d,c}$ and $\tau_{d,l}$ can be given.

The direct observation of inertial effects in dislocation - obstacle interactions is only possible with atomistic simulations. However, to the authors knowledge no detailed simulations targeting these effects have been reported yet. Indirect experimental evidence for inertial effects have been frequently reported for pure superconductors [71, 72, 82] and solid solutions [83–86], as well as for some precipitation hardened materials [87, 88]. In these experiments the low temperature anomalies of the CRSS are usually attributed to inertial effects. However, also the bimodal stress relaxation during creep experiments at low temperatures (10 K) has been interpreted as a consequence of inertial effects [86].

2.1.4 Atomistic simulations of dislocations

Since the first atomistic calculations of dislocation core structures and energies about half a century ago [89–91] atomistic calculations have increasingly been used to study dislocation properties. Instead of providing a broad review, only selected recent works on fcc metals in the following areas relevant to this thesis are presented: dislocation core structures and -energies, Peierls stress, dynamic properties of dislocations, dislocations at high velocities, static and dynamic dislocation-obstacle interactions.

The dissociation of perfect dislocations in fcc metals into Shockley partial dislocations was the subject of several atomistic studies [29,36,92–98]. These studies characterized the internal structure of the dissociated dislocation through the disregistry function [93,95,97], as well as through the separation distance and core width. In most of these studies the values are compared with the theoretical estimates based on elasticity theory and the Peierls-Nabarro model [93,95–97]. The deviations of the elastic stress field derived from atomistic simulations of dislocations from the stress field of Volterra dislocations have been analyzed recently in more detail in terms of dislocation core fields [98].

The Peierls stress τ_P was also calculated in many of the above studies [29,92–97,99], showing however large differences, see sec. 7.1.2. The Peierls stress is very sensitive to the boundary conditions. The effect of boundary forces on the Peierls stress of edge, screw and mixed dislocations in Al were computed and subsequently subtracted in a careful study by Olmsted *et al.* [94]. This work will be used as reference for the calculations of τ_P .

Much less work has been reported on the actual atomistic dynamics of dislocation motion. Amongst the first simulations of dislocation motion is the work by Daw *et al.* [100,101] on edge dislocations in nickel with and without hydrogen interstitial impurities. For pure nickel at room temperature they observed dislocation motion with a steady velocity which is in good agreement with Leibfried’s estimate of phonon damping [65]. At high stresses a saturation velocity was observed at about $0.6c_t$. Later simulations of the dynamics of edge dislocations in nickel and aluminum by Rodney [58,102] and Bhate [56] showed basically the same characteristics: a nearly linear increase of the dislocation drag coefficient with temperature and a saturation of the dislocation velocity significantly below c_t . The dynamics of screw dislocation dipoles in Cu was studied by Mordehai *et al.* [103] who observed a deviation from the linear increase of dislocation velocity with stress at velocities larger than about half the transverse sound velocity. An extensive study on the dislocation mobility of edge and screw dislocations in Al and Ni was recently published Olmsted *et al.* [53]. They report two regimes of dislocation motion, one in which the dislocation velocity is linear in τ/T (applied shear stress over temperature), and a nonlinear regime which differs for edge and screw dislocations. The nonlinear regime for screw dislocation is believed to be caused by radiative damping [53]. However, no relationship between the subsonic velocity plateau exhibited by edge dislocations and any special or ”forbidden” velocities could be determined. A convincing physical interpretation of the plateau velocity has not yet been offered.

Atomistic simulations of the interaction of dislocations with obstacles have been performed for various types of obstacles, like other dislocations [104,105], grain boundaries [106,107], solute atoms [108,109] or precipitates [110,111]. Recently, however, especially the interaction processes of moving dislocations with defect clusters created by irradiation has attracted much interest [5,112–118]. Elasticity theory can be used for a simple treatment of hardening due to these defects, however knowledge of the individual short-range interactions, which are atomic-scale in nature, can be obtained only from atomistic simulations. An example of

the importance of atomic scale processes is the interaction of dislocations with stacking fault tetrahedra (SFTs). Depending on the geometry different reactions can take place [117, 118], involving partial absorption, shearing or restoration of the SFTs. These mechanisms can explain the formation of the experimentally observed defect-free channels cleared by gliding dislocations. The atomic scale structure of the dislocation is also influencing the interaction of dislocations with voids, leading to deviations from the continuum treatment [114, 116].

Although the above studies also include dynamic (in contrast to quasistatic) simulations, there are currently no systematic studies addressing dynamical effects in dislocation-obstacle interactions (see sec. 2.1.3.5).

2.2 Fracture

Fracture, the separation of a material body under load into two, or more, pieces can proceed by different mechanisms [119], e.g.:

- the rupture of atomic bonds by tensile stresses (*cleavage fracture*)
- complete plastic necking
- void growth and coalescence
- cavity growth and coalescence by stress-directed diffusion (*creep fracture*)
- strain-rate assisted localized chemical attack at the crack tip (*stress corrosion cracking*)

In the following we will look more closely at cleavage fracture in crystals in combination with plasticity at the crack tip. In contrast to the quantitative study of dislocation motion, the study of dislocation processes at crack tips in part II of this thesis is of more qualitative nature. Therefore only basic knowledge of linear elastic fracture mechanics (LEFM) is required and no separate introduction in LEFM is given here. For a comprehensive introduction to fracture mechanics the reader is referred to [120–123]. Textbooks, however, usually do not cover the brittle-to-ductile transition in much detail. The difference between brittle and ductile fracture and the brittle-to-ductile transition are therefore addressed in the sections 2.2.1 and 2.2.2. The origin of the dislocations near the crack tip in an otherwise dislocation free crystal is one of the underlying questions in the study of the brittle-to-ductile transition and the main topic of the second part of this thesis. Therefore sec. 2.2.2 gives special attention to the review of the experimental and theoretical literature on nucleation and multiplication of dislocations at crack tips. The theoretical background and literature overview is closed with an overview of atomistic simulations of fracture processes.

2.2.1 Intrinsically brittle versus intrinsically ductile solids

In linear elastic fracture mechanics it is assumed that once the applied stress intensity factor K_A exceeds the material's toughness K_C fracture propagates by cleavage. Conversely to such intrinsically brittle materials, intrinsically ductile materials develop a plastic zone (PZ) at the crack tip. Within this plastic zone the singularity of the stress field proportional to $r^{-1/2}$ vanishes. In the first approximation the stress within the PZ is equal to the yield stress of the material [124].

The first theoretical attempt to determine whether a material will fail by brittle fracture or show plastic relaxation at the crack tip was based on the comparison of the theoretical strength of a crystal under tension versus the theoretical shear strength. From atomistic pair potential calculations Kelly *et al.* [125] concluded that cleavage fracture should take place in diamond or rock salt, whereas the fcc metals should deform plastically. The application of their model to materials showing intermediate behavior, however, is less straight forward.

2.2.2 Brittle-to-ductile transition

Most materials do not fall in the categories of ideally ductile or ideally brittle, but show an intermediate behavior which depends on the temperature and loading rate. Many crystalline materials like steels, refractory metals, intermetallic phases, semiconductor crystals, ceramics

and some ionic crystals exhibit two distinct failure regimes: at low temperatures or high loading rates they fail by brittle fracture, whereas at high temperatures or low loading rates they deform plastically. Between these two stages the so called brittle-to-ductile transition (BDT) takes place [126–130].^e The brittle-to-ductile transition temperature (BDTT) as well as the fracture toughness of semi-brittle materials are determined by the competition between the breaking of chemical bonds at the crack tip and the mechanism which lead to plastic deformation at the crack tip [3, 132]. Materials which show a BDT are frequently called semi-brittle, relating to the fact that they are intrinsically brittle, but this feature can be masked if a plastic zone can develop sufficiently fast to stop the crack [133].

The importance of the brittle-to-ductile transition for engineering applications has been highlighted by several accidents involving the brittle fracture of steel structures, like the large scale fracture of the Liberty ships during and after World War II [18, 134]. Therefore significant theoretical and experimental efforts were made to uncover the limiting and therefore controlling processes during the development of plastic zones. Two processes are required to form a plastic zone: the *nucleation* of dislocations and their *motion* away from the crack tip. As detailed below, the question whether the brittle to ductile transition is controlled by the ability of the material to generate dislocations or whether the BDT is dominated by the dislocation mobility has been subject of intense discussion [2, 133–135]. Still today’s understanding of the BDT does not allow to transfer results between different loading situations and between different material classes [133]. Furthermore, the microstructural complexities of real world materials including grain boundaries or precipitates are generally not taken into account in the models describing the BDT.

Most BDT models are based on *static* cracks subjected to a constant loading rate \dot{K}_I . The technically more relevant issue of *propagating cracks* is less frequently addressed with BDT models. The processes at the crack tip which lead to an arrest of a propagating crack by the evolution of a PZ below the crack arrest toughness K_{Ia} (or above the BDTT) have not yet been studied in detail.

2.2.2.1 Experiments

Semibrittle materials lose most of their fracture resistance and ductility when the temperature is lowered below the BDTT. This temperature is often the lowest temperature at which such a material can be used for engineering purposes. There exists a large body of experimental studies on the fracture behavior of different materials under various testing conditions such as temperature, loading rate, specimen geometry, environment, composition, microstructure, crystallographic orientations, etc. For the study of the underlying mechanisms of the BDT, well defined experiments – ideally with constant stress intensity rate and on single crystals – are necessary. Such studies have been performed by Riedle and Gumbsch [136–138] on the brittle-to-ductile transition in tungsten single crystals. From these experiments it is concluded that the nucleation of dislocation is the dominant factor controlling the fracture toughness at low temperatures. However, if the number of active sources is sufficiently high – either by pre-deformation or due to thermal activation – the fracture toughness is rate dependent, which indicates that the dislocation mobility becomes the controlling factor [136–138]. An overview about how the BDT in W can be modeled by dislocation dynamics simulations is given in [139, 140]. The most thoroughly studied model material however is single crystalline

^eBrittle-to-ductile transitions are not limited to crystalline materials, but the underlying mechanisms of the BDT e.g. in polymers [18] or quasicrystals [131] differ from crystalline materials and are not discussed here.

silicon. The simulations in part II of this thesis were mainly motivated by careful experiments on single crystalline Si. The according experimental data is therefore reviewed in more detail.

Since single crystalline silicon exhibits a sharp brittle-to-ductile transition [126] and since high purity, dislocation free single crystals are commercially available, the BDT in silicon has been studied extensively by many groups [2, 126–128, 135]. In these studies a static crack is subjected to a driving force which increases at a constant rate \dot{K}_I until cleavage fracture or large scale plastic deformation occurs at a given temperature. Although due to different experimental set-up, specimen geometry and dopant content the measured BDTT vary amongst the different groups, the following results can be generalized as follows [128]:

- Si shows an abrupt BDT in which the fracture toughness rises suddenly in a narrow temperature range (less than 5K).
- The fracture toughness at temperatures below the BDTT, where silicon fractures by cleavage, is nearly independent of temperature.
- The BDTT is correlated with the loading rate \dot{K}_I by an Arrhenius-type law. The activation energy (2.2 eV) equals that for dislocation motion in Si; it is influenced by the content of dopants, just like the dislocation mobility.
- For temperatures above the BDTT and constant K , dislocation nucleation occurs nearly independent of temperature at about $0.25K_{Ic}$.

From these experiments the common view has emerged that dislocation mobility is the rate controlling parameter which determines the BDT and the BDTT at a given loading rate [126, 127, 141]. However, it was observed that pre-deformation of the silicon specimens causes a semi-brittle regime to occur in which the fracture toughness rises slowly from the low temperature value [142]. It was furthermore shown [2, 135, 143], that the BDTT can be shifted to higher temperatures by increasing the perfection of the crack front, e.g. reducing the number of cleavage steps. This indicates that dislocation nucleation at the crack front is *inhomogeneous*. From these and other observations it was concluded that although the mechanism of the BDT is governed by the mobility of dislocations, the brittle-to-ductile transition temperature is strongly dependent on the activity and density of dislocation sources [144–148]. Detailed studies on dislocation loop nucleation at crack fronts and of the early stages of plastic zone formation in Si show that the dislocation nucleation is indeed a highly inhomogeneous process [2, 135, 143, 147, 149]. Hirsch, Roberts and Samuels [145] and later Michot and coworkers [150] identified the distance between the dislocation sources along the crack tip as a sensitive parameter for the BDT.

Argon and Gally [1, 151] developed an experimental technique in which a cleavage crack propagate up a temperature gradient with different externally controlled velocities. These experiments yield complementary information to the above mentioned fracture experiments at constant \dot{K} and constant temperatures. In their experiments the crack tip advances in a series of jerky steps between which the crack tip stress field samples different material 'elements' for a certain time at increasingly higher temperatures until the residence time of the crack tip becomes of the order of the time required to fully develop a crack tip shielding zone where the crack is arrested [1]. Under these conditions cleavage crack arrest occurs at increasing temperatures with increasing average crack velocity.

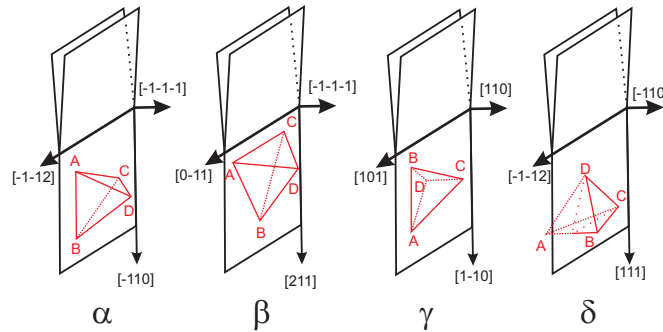


Figure 2.7: The four crystallographic specimen orientations used in the study of mode I fracture in Si. The Thompson tetrahedron shows the orientation of the slip systems with respect to the crack front (after [147]).

Sources of dislocations at crack tips The early stages of plastic zone formation in initially dislocation free Si were subject of detailed studies to clarify the origin and the nature of the first dislocations which nucleated at the crack front [1, 2, 134, 147, 152–154]. The four types of crystallographic specimen orientations used to study mode I cracks in Si are shown in Fig. 2.7. The orientations with $\{110\}$ cleavage planes, in particular the so called γ -orientation, thereby generally lead to cleavage surfaces of better quality compared to fracture along $\{111\}$ -planes [147]. In the following, the experimental results relevant to the study of dislocation sources at crack tips are summarized.

One of the first comprehensive studies of dislocation emission in all four specimen orientations of Fig. 2.7 was performed by George and Michot [147]. Their *in-situ* observations using synchrotron X-ray topography and subsequent analysis by chemical etching of the fracture surfaces revealed that in each orientation only a limited number of the possible slip systems are activated. The observed Burgers vectors are often active only in one of the two possible glide planes. In many cases the observed predominant slip systems do not correspond to the ones subjected to the largest driving forces. George and Michot therefore concluded, that the choice of the slip system is not only influenced by the stress state, but is also dictated by the nature of the dislocation source [147].

Sources were frequently detected at the intersection of the crack front with the free surfaces [147, 149]. Dislocation nucleation in the early stages also takes place at a limited number of special sites along the crack front [147]. Only in some cases these sites correspond to observable crack front ledges [149]. Crack tip ledges can therefore act as dislocation sources, but not all visible ledges lead to dislocation emission, and not all emissions can be traced to ledges [147].

The detailed study of dislocation source configurations in the α -orientation (see Fig. 2.7) revealed that a few sources emit only dislocations with one Burgers vector, sometimes involving cross-slip. In some cases these one-Burgers-vector sources are linked to crack tip ledges. One case was observed were cross-slip from a dislocation from a one-Burgers-vector source produced a source at the crack tip in the cross-slip plane [147]. Most sources however emit several Burgers vectors on several slip systems [147], forming at least two main rows of dislocations. These sources could not be traced back to defects on the crack front. The etch pits on both cleavage surfaces coincide ahead of the crack front. Behind the crack front only one row is visible on each half-sample [147]. The same experimental set-up was later used by

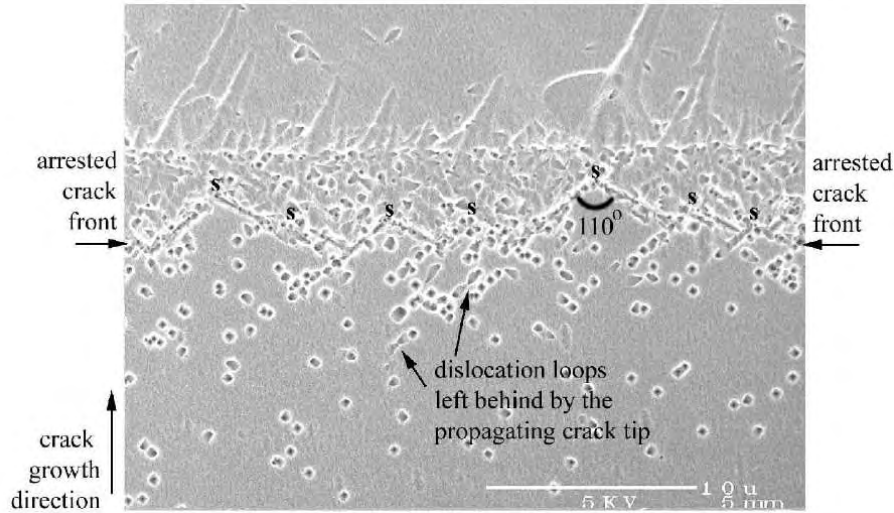


Figure 2.8: Etch pit pattern of dislocations emitted on the (a) and (b) planes as observed in the crack arrest experiments of Gally and Argon [1]. The sources (S) are supposed to be cleavage ledges from which screw dislocations DC are emitted towards the flank regions of the crack.

Author	Slip plane			
	(a)	(b)	(c)	(d)
George and Michot [147]	BC, DB	AD, CA	$DB, (AD)$	$(BC), (CA)$
Loyola de Oliveira <i>et al.</i> [152]	-	AD, CA	AD	CA
Gally and Argon [1]	?	?	-	-

Tab. 2.1: Observed slip systems activated at crack tips in the γ orientation. Burgers vectors in brackets denote slip systems which were inactive in a few samples, but still frequently observed.

Loyola de Oliveira [152] to study dislocation nucleation at γ -oriented cracks. It was found that in the early stages of plastic zone development at least two Burgers vectors are activated which are generally distributed over four slip systems. In the later stages usually four Burgers vectors are present, each corresponding to loops formed in both of the glide planes available to the Burgers vector [152].

A distinction between "primary" and "secondary" sources was subsequently introduced by Michot and coworkers [148]. Primary sources are often connected to crack front ledges. Typically relatively few primary sources are observed in the experiments by Michot *et al.* [149]. With a minimum distance of about $50 \mu\text{m}$ between these sources they can only provide limited crack front shielding which is insufficient to avoid brittle fracture. Therefore the existence of other dislocation sources is required to explain the BDT [149]. These sources which are supposed to be activated during growth of the plastic zone are called secondary sources [148]. Analysis by atomic force microscopy (AFM) confirmed that secondary sources are not associated with preexisting defects like ledges [135]. These secondary sources emit only few dislocations per slip plane, but are much closer spaced than the primary sources [135]. Michot *et al.* postulate that plastic relaxation at a crack tip starts by the activation of few primary sources which emit tens of dislocations, followed by the triggering of many secondary sources, each of them emitting only few dislocations on other glide planes [135, 148, 149]. A mechanism

of dislocation source multiplication has been proposed in which the intersection of a dislocation with the crack front triggers a secondary source through the process of "stimulated emission" [135, 148, 149]. This mechanism is presented in some more detail in the next two sections.

A qualitatively different source configuration was found by Gally and Argon in their experiments on crack arrest in a temperature gradient [1, 134, 151]. Their experiments on cracks in the γ -orientation indicate that the plasticity of the entire crack arrest process is accomplished by the slip activity on the symmetric (a) and (b) planes. This leads to the " \wedge "-shaped source configuration indicated by an 's' in Fig. 2.8. The distance between the sources is about $5 \mu\text{m}$, while the average spacing of observable ledges was 2-3 times larger [151]. The etch pits forming the \wedge do not match across the fracture surface. Ahead of the well delineated zone of sources is a region with high density of etch pits which is sharply terminated about $5 \mu\text{m}$ in front of the sources. Contrary to the experiments by Michot *et al.* which showed long rows of etch pits in front of the crack, nearly no etch pits are found further in front of the arrested crack [1]. The Burgers vector of the dislocations could not be determined.

Gally and Argon assume that the dislocation sources in Fig. 2.8 correspond to cleavage ledges from which screw dislocations with Burgers vector CD are nucleated [1, 134, 151]. It is argued that the nucleation of these dislocations from cleavage ledges is kinetically favored. The screw dislocations CD should experience a very low energy barrier, as it does not require the creation of a free surface. In contrast, the nucleation of dislocations on the (c) and (d)-planes should be connected to a very large energy barrier [134]. The nature of the resolved shear stress on the (a) and (b) plane allow dislocations with $\mathbf{b} = CD$ only to expand slightly ahead of the crack and favor their *backwards* expansion [1].

Besides the different source configurations, one of the main differences between the observations in the experiments of Michot and coworkers [2, 135, 147, 152] at constant \dot{K} and the crack arrest experiments by Gally and Argon [1, 134, 151] is the absence of dislocations on the (c) and (d) planes in the latter. Gally and Argon argue in favor of the emission of screw dislocations CD , whereas George and Michot observed 60° dislocations on the (a) and (b) planes [147], see also Tab. 2.1. These differences are attributed by Gally and Argon to the predominance of plane stress conditions in the thin samples used in [2, 135, 147, 152] (0.6 mm compared to 3 mm in [1]) which significantly changes the resolved shear stress acting on the various slip systems [1]. The observed slip systems in fracture experiments on initially dislocation free single crystalline Si specimens in the γ -orientation are summarized in Tab. 2.1.

Stimulated dislocation emission Rapid dislocation multiplication immediately after intersection of the crack front by an attracted dislocation generated from a remote source was first reported by Michot in fracture experiments on GaAs [150]. The process of such "stimulated emission" of dislocations at a crack tip was studied in detail by Scandian [2, 153]. The schematic geometry used by Scandian [153] in his study on γ -oriented cracks in 300-600 μm thick Si single crystals is shown in Fig. 2.9. In this case the incoming dislocations were created by placing an indent at a certain distance from the crack tip. The experiments were performed *in-situ* at high temperatures and subcritical loading. The evolution of the plastic zone was followed by *in-situ* X-ray topography using synchrotron radiation. In general it was found that one incoming dislocation can produce tens of dislocation lines. The generated dislocations have different Burgers vectors [2] and usually glide on different planes. Stimulated dislocation emission corresponds therefore not to pure multiplication of the incoming dislocation.

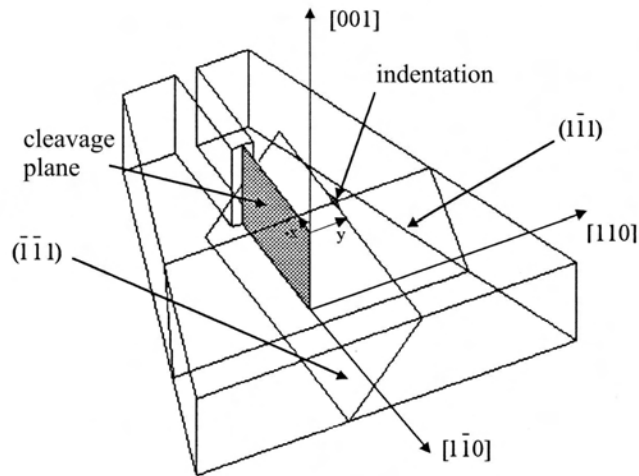


Figure 2.9: Experimental geometry used by Scandian to study the stimulated dislocation emission on a γ -oriented crack in silicon [153].

A sequence of topographs showing stimulated dislocation emission in the γ -orientation is shown in Fig. 2.10. The dislocations created by the indentation in Fig. 2.10a are of type $CA(b)$. In Fig. 2.10b some of these half loops have traversed the crystal (arrow). In Fig. 2.10c a $DB(a)$ loop appears (arrow). In Fig. 2.10d this loop has developed and traversed the crystal. Its screw segments are found on the two sides of the crack (arrows). A significant decrease of the crack tip stress field can be noted in this figure which is related to a massive development of a plastic zone. The results of Scandian's study on stimulated emission are summarized in Tab. 2.2 in which the stimulating dislocation and the stimulated glide systems are characterized. Similar results by Scandian *et al.* on stimulated dislocation emission at cracks in the β -orientation are reported in [2].

The mechanism behind the stimulated emission remains unclear. Nucleation by stimulated emission is assumed to be an easy process, since it is operative already at small applied loads ($0.3 K_{Ic}$) [135,150]. It thus can by-pass the high energy processes required in the homogeneous nucleation processes. Stimulated emission is not necessarily linked to the creation of an atomic crack ledge by the incident dislocation. Also dislocations with Burgers vectors parallel to the cleavage plane can lead to stimulated emission [2]. It is argued that the stress amplitude attained locally at the intersection point between the dislocation core and the crack front is of the order of the theoretical shear strength. This could lead to a local mechanical instability of the lattice [150]. An alternative hypothesis is that the relative atomic displacements induced by the dislocation on nearby slip planes could lead to the formation of a dislocation nucleus which can then grow due to the applied stress field [153]. Stimulated emission is believed to be a general mechanism which should work in any material containing bulk sources [150].

2.2.2.2 Models of dislocation emission from crack tips

The emission of a dislocation from an atomistically sharp crack tip was first studied in depth by Rice and Thomson [132]. They studied the evolution of a dislocation half loop in front of a

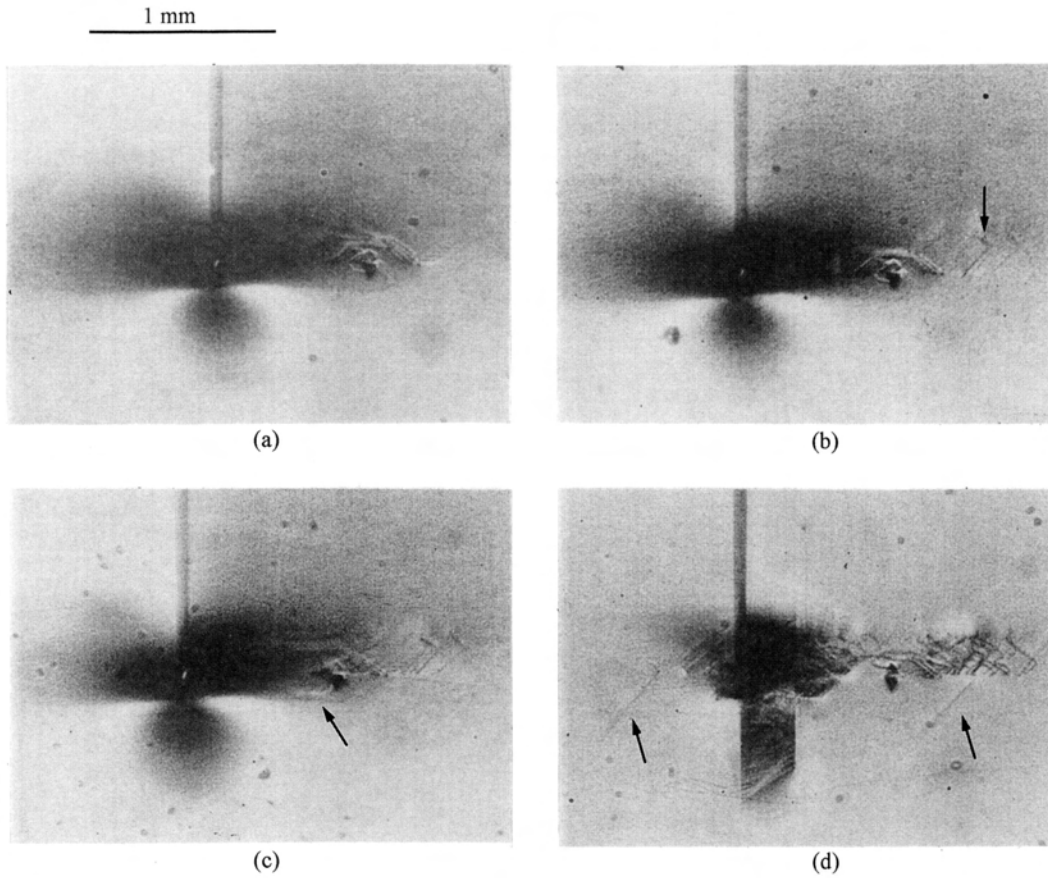


Figure 2.10: Emission of dislocations stimulated by one dislocation coming from an indentation (γ -orientation, $T = 1023$ K, loading: $0.5 K_{IC}$, diffraction vector $\mathbf{g} = [2\bar{2}0]$). *in-situ* X-ray topographs by Scandian [153]. (a) to (d) *in-situ* X-ray topography observations. (a): $t = 36$ min, (b): $t = 52$ min, (c): $t = 65$ min, (d): $t = 105$ min.

crack tip under the combined action of the (repulsive) stress field of the crack, the (attractive) image forces due to the free crack surfaces and the surface tension force from the creation of surface ledges by the dislocation nucleation (attractive). The configuration in which the mechanical stability of the dislocation loop is evaluated is depicted in Fig. 2.11a. If the dislocation loop reaches a critical radius $r_c \approx (\mu b / K_I)^2$ it will spontaneously grow. Rice and Thomson assumed that for a critical radius of the order of the dislocation core radius r_0 there should be no barrier to dislocation nucleation. Comparing the critical value of K_I for spontaneous dislocation emission with the critical value K_{Ic} for cleavage, they predicted brittle fracture for materials with $\mu b^2 / r_0 \gamma_s > 10$. As in the model by Kelly *et al.* [125] all fcc metals are predicted to be ductile, whereas all bcc metals should fail by cleavage. Rice and Thomson also considered thermal activation of the dislocation nucleation process as one way of explaining the BDT. The calculated energy barriers are however prohibitive for most semibrittle materials.

The original Rice and Thomson model [132] of dislocation emission from a crack tip has

Stimulating dislocation	predominant dislocations	other dislocations
$DB(a)$	$CB(a)$ & $CB(d)$	-
$DA(b)$	$CA(d)$	$DB(c)$ & ?
$DB(a)$	$CA(d)$	$DA(b)$
$CB(a)$	$CB(a)$ & $DB(a)$ & $CB(d)$	$CA(b)$ & ?

Tab. 2.2: Observed slip systems during stimulated emission in the study of Scandian [153]. The configuration shown in Fig. 2.10 corresponds to the third sample.

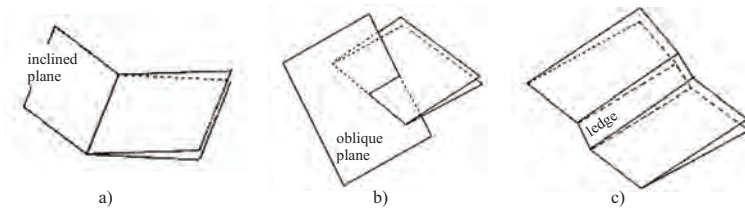


Figure 2.11: Different possible configurations for the emission of dislocations from a crack tip: (a) inclined slip plane intersecting the crack front along its whole length, (b) oblique plane intersecting the crack front, (c) cleavage surface ledge in at the crack front (adapted from [134]).

been refined by many authors, especially by taking into account atomistic considerations in the nucleation of dislocations by the introduction of a Peierls-Nabarro potential along the slip plane [32, 155–160]. The treatment of Rice and coworkers [32, 158, 161] of the dislocation generation is based on stress arguments, whereas the treatment of Schoeck [156, 157, 159, 160] is based on the total Gibbs free energy. In principle these two approaches should lead to the same results, but it was argued that the energy based approach should lead to a more realistic comparison with atomic simulations [160]. Including the Peierls-Nabarro potential in the Rice and Thomson model overcomes the problem of using an ill defined dislocation core radius r_0 . With the so-called unstable stacking fault energy γ_{usf} Rice [32] introduced a material specific parameter which measures the materials resistance to dislocation nucleation at the crack tip^f. The stress intensity factor required for dislocation nucleation is then proportional to $\sqrt{\gamma_{\text{usf}}}$. In these models the calculated energy barrier to dislocation emission is lowered compared to the original Rice and Thomson model, but still too high for thermal activation. Further refinements of Rice’s Peierls model include corrections for the creation of surface ledges, crack tip blunting, effects of crystal anisotropy, tension-shear coupling and surface stresses, see the discussions in [163–165].

All these models have in common that they describe the dislocation nucleation at the crack tip as a homogenous process – even when the problem is treated in three dimensions (dislocation half loop on an inclined plane intersecting the crack front) [155]. Zhou and Thomson [166] were the first to consider *inhomogeneous* dislocation nucleation at defects of the crack tip. They discussed in detail the emission of dislocations from ledges on cracks. Their basic idea is that a ledge on a crack loaded in mode I has locally a stress intensity factor

^fThe unstable stacking fault energy is defined as the excess energy of an interplanar shear configuration in which two atomic layers are displaced by half a periodicity displacement parallel to each other. It can be accurately calculated using first-principle total energy methods [162].

with a large mode III component. A crack with a ledge is described in terms of dislocations as composed of fictive edge dislocations with \mathbf{b} normal to the crack plane which have at the ledge jogs of pure screw character. These screw dislocations can then be emitted ahead of the crack tip. Although Zhou and Thomson's treatment shows that ledges on cracks can be efficient sources for dislocations, it can not account for the complicated slip geometries observed in experiments [147].

Xu *et al.* [167, 168] used their variational boundary integral (VBI) technique to study the emission of dislocations from tips of cleavage cracks for the three geometries shown in Fig. 2.11. The VBI method has the advantage to be able to deal with the expected three-dimensional configurations of the critical dislocation nucleus. Their results for α -iron indicate that thermally activated dislocation nucleation on inclined slip planes which contain the crack front (Fig. 2.11a) is very unlikely (the activation energy $\Delta U_{\text{act.}}$ at K_{Ic} is about 22 eV). Also, the nucleation on oblique planes cutting the crack front (Fig. 2.11b) in the interior of a solid can be excluded ($\Delta U_{\text{act.}} \approx 55$ eV). According to Xu [168] the only possible mechanism of dislocation nucleation in α -Fe is the one from cleavage ledges ($\Delta U_{\text{act.}} \approx 1$ eV for a ledge height of 50 nm), which with realistic values for the crack velocity also leads to reasonable estimates for the BDTT. The existence of ledge-like defects along the crack front therefore is proposed to have a significant influence on the brittle-to-ductile transition. The above mentioned models of dislocation nucleation at the crack front are discussed in detail in the recent review by Xu [164].

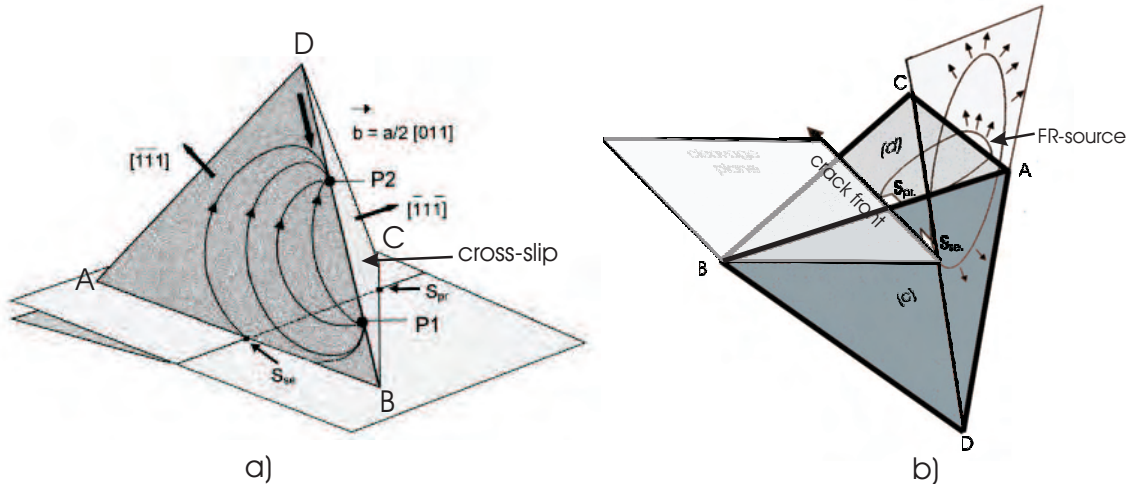


Figure 2.12: Suggested dislocation source multiplication mechanisms based on stimulated emission: a) as suggested by Michot [148] for the α -orientation; b) suggested by Scandian [153] for the γ -orientation.

Based on their observation that a dislocation source can be easily activated at the intersection point between the crack front and an attracted dislocation [2, 150, 153] (see the preceding section), Michot and coworkers developed a model of dislocation source multiplication based on the process of stimulated emission [135, 148]. To explain the observed step increase of dislocation density around the crack tip in Si [2, 150], Michot and coworkers proposed the following "avalanche multiplication" mechanism [135, 148]: a dislocation emitted by the primary source (S_{pr} in Fig. 2.12 a)) on the plane with maximum resolved shear stress

cross-slips to a plane where it is attracted by the crack; the intersection leads to a secondary source S_{se} which emits dislocations which can then cross-slip again. This leads to a repetitive process. The required cross-slip in this avalanche mechanism is enabled by the back-stress of the dislocations previously emitted by S_{pr} . The shielding effect by these dislocations is smaller than their loop radius [169], therefore the shielding at the secondary source is very low and it can emit a new bundle of dislocations [148]. The cross-slip process suggested by Michot (Fig. 2.12a) which leads to a direct intersection of the crack front by the cross-slipped dislocation is however not universal, but depends on the crystallographic orientation of the crack system and the available slip systems. For other crystallographic orientations in Si other mechanisms have to be considered. A more general mechanism suggested by Scandian [153], Fig. 2.12b, involves the creation of a Frank-Read (FR) source by the cross-slip of the screw part of a dislocation loop emitted by the primary source. The dislocations emitted by the FR source then stimulate the creation of a secondary source at the crack front.

2.2.3 Atomistic fracture simulations

Two dimensional atomistic studies have provided valuable information on many aspects of fracture like lattice trapping [170–172], cleavage anisotropy [173], forbidden velocities and dynamic instabilities like crack branching and dislocation emission in dynamic brittle fracture [174–176], and the role of non-linear elasticity on dynamic fracture [177, 178]. An overview about atomistic theory and simulation of fracture is given e.g. in [179–181].

Fully three dimensional atomistic simulations of fracture processes in single crystals are however relatively scarce [35, 182–188]. Perhaps best known is the work of Abraham *et al.* on large scale simulations of ductile failure with up to one billion atoms [35, 182–184]. The three-dimensional simulations on notched fcc crystals under constant tension revealed that using a Lennard-Jones potential, brittle crack propagation in the γ -orientation planes is possible upto about one third of the Rayleigh wave speed [182]. At this velocity the crack tip roughens on the atomic scale. This instability results in the massive emission of dislocations and crack propagation stops by crack tip blunting [182]. Their largest simulations of a Lennard-Jones crystal with two opposing sharp cracks showed complex interactions of thousands of dislocations leading to work-hardening [183]. The analysis of these simulations by Buehler *et al.* [35, 184] revealed as main mechanisms of work hardening dislocation cutting processes (including jog formation and point defect creation), activation of secondary slip system by cross-slip and Frank-Read sources, and formation of sessile dislocations like Lomer-Cottrell locks.

Zhou and coworkers [185, 186] have studied ductile failure at constant strain rate in fcc crystals in the (010)[101] crack system using an EAM and a Morse potential. They observed the emission of joggling dislocations at the intersection of the crack with the free surface, and of blunting or joggling dislocations along the crack front. The type of the emitted dislocation depends thereby on the potential [186]. Different potentials were also used in the study of Kimizuka *et al.* [187] on γ -oriented cracks subjected to a constant strain rate. Using an aluminum EAM potential they observed the emission of $\langle 100 \rangle$ dislocations on $\{010\}$ -planes which break up into $1/2\langle 110 \rangle$ dislocation loops. In Cu only the usual $1/2\langle 110 \rangle$ dislocations are observed. The characteristics of the dislocation emission is however found to be different for 0 K and temperatures above 50 K. At 0 K the crack starts to propagate by brittle cleavage and with increasing strain starts to emit dislocations. In contrast at 50 K no brittle fracture takes place and dislocation emission occurs early and less abruptly than at 0K, leading to a

less concentrated dislocation 'cloud' [187].

The above simulations provide interesting insights into the general aspects of ductile failure. Direct connections to experimental observations were however not intended. Quantitative calculations of the activation energy for dislocation loop emission in copper were performed by Zhu *et al.* [188]. Their 3D calculation of the saddle-point configuration led to a significantly higher activation energy than the continuum estimate. Homogenous dislocation nucleation on inclined slip planes is therefore considered highly unlikely [188]. It is now widely accepted that the presence of any heterogeneity along the crack front should significantly reduce the activation energy for dislocation emission [134,148,168,188]. However, to the authors knowledge no corresponding detailed three dimensional atomistic simulations of defective crack fronts have been published so far. In particular, the atomistic mechanisms during the interaction of cracks with preexisting lattice defects have not yet been the topic of thorough investigations.

Chapter 3

Simulation methods

3.1 Molecular dynamics

Molecular dynamics (MD), the numerical solution of Newton's equation of motion for a system of interacting particles using discrete time steps, is a well established simulation method in physics, biochemistry and materials science [189–191]. The method is described in detail in several books, e.g. [189, 192, 193]. The current state of the art of molecular dynamics simulations for atomistic modeling in materials science is summarized in chapter 2 of the "Handbook of Materials Modeling" [194]. The MD software package used for all the simulations in this thesis, IMD (ITAP Molecular Dynamics), is described in [195–197] and is documented in [198]. Therefore this section concentrates on the characteristics determining the simulations, namely the interaction potential and the initial and boundary conditions. For an introduction to the MD method the reader is referred to the above cited literature.

The determination of equilibrium structures and of the stability of atomic configurations under mechanical loads requires different methods, which are sometimes referred to as *molecular statics*. Several such methods for structural optimization of atomic configurations by energy minimization exist, see [190, 199]. For our purposes, however, the standard methods showed relatively poor performance or had severe limitations^a. Therefore a new method (Fast Inertial Relaxation Engine, FIRE) for fast structural relaxation was developed. It is described in [200] and in the appendix B.

3.1.1 Interatomic potentials

To model the atomic interactions, potentials which follow the Embedded Atom Method (EAM) [201–204] representation of the interaction energy are used. The ability to capture the most essential features of metallic bonding together with their computational efficiency lead to a widespread use of these semi-empirical potentials. For information about the theory behind the embedded-atom potential the reader is referred to the recent review by Mishin [205]. The details of the implementation of EAM potentials in IMD are described in [197].

To study the sensitivity of dislocation properties on the interatomic potential, different potentials were used for the same material. The properties of the potentials relevant for the present study are listed in appendix A.

^aEnergy minimization by the current state of the art Broyden-Fletcher-Goldfarb-Shanno (BFGS) method for example fails to determine the stability of configurations under load, see [200].

For aluminum the widely used potential by Ercolessi and Adams [206], in the following denoted by Al_I , is applied. It is one of the few potentials which are fitted to material properties extrapolated to 0 K. I.e. simulations at 300 K yield the lattice constant and elastic properties corresponding to those of Al at room temperature – contrary to the other potentials in this study. Subsequently, the melting point of the potentials is very close to the experimental one. Al_{II} is a more recent potential by Mishin *et al.* [207]. The development of this potential, like the other potentials by Mishin, included the fitting to a large set of energies of alternative crystal structures generated by *ab initio* calculations. The potential is therefore expected to be very well suited to model the different local environments encountered in atomistic simulations of lattice defects. The phonon-dispersion curve calculated with Al_{II} furthermore agrees very well with the experimental curve. This aspect can be important for the realistic modeling of the dislocation - phonon interaction. Whereas the elastic properties of the two Al potentials differ by less than 10%, the stacking fault energy γ_{sf} is about 30% lower in Al_I than in Al_{II} . From this different dissociation widths can be expected for dislocations modeled by the two potentials. The generalized stacking fault curves of the two potentials were discussed and compared to *ab initio* calculations by Zimmerman *et al.* [208].

Nickel was modeled by a potential of Angelo *et al.* [209, 210] (Ni_I)^b and a potential recently developed by Mishin [213] (Ni_{II}). The difference in elastic constants between the two potentials are smaller than 5%. The potential by Angelo *et al.* however has an unrealistically low stacking fault energy, leading to a difference of 50% between the γ_{sf} of the two potentials. This difference is expected to be reflected in the dislocation core structure of dislocations in the two potentials.

Additionally dislocations were also studied in Cu, modeled by the potential of Mishin *et al.* [214]. The fracture simulations were only performed with Ni_{II} .

3.1.2 Temperature control

The control of temperature is of special importance for the study of dislocation - phonon interaction. The canonical ensemble with constant number of particles N , constant volume V and constant temperature T (NVT ensemble) was applied. To control the temperature of a system after an equilibration phase a Nosé-Hoover thermostat [215, 216] is used (see also [192] for a discussion and comments on the implementation). Special care was taken to optimize the thermostat coupling to produce canonical temperature fluctuations about the desired thermostat temperature.

Holian *et al.* [217] suggested to choose a coupling rate of the Nosé-Hoover thermostat which is identical to the characteristic vibrational frequency of the system under study. For this purpose the Einstein frequency is frequently used [198]. However, the coupling can be further optimized by analyzing the frequency spectrum of NVT simulations using different coupling constants. A bad choice of the coupling rate produces an extra peak outside the native frequency spectrum. With a good choice of the coupling, the frequency spectrum is only slightly distorted, see also [198]. In the present study the dynamics of dislocations subjected to a shear stress is studied. I.e. the temperature of a *driven* system has to be

^bDuring the course of this study the original tabulated potential [211] however showed serious flaws. The first derivative of the tabulated potential is discontinuous, leading to jumps in the forces. The potential was therefore independently refitted by the author and by Dupuy [212]. This refitting was complicated by the fact that the published mathematical form of the potential [209, 210] does not correspond to the original tabulated potential.

controlled. Therefore the above optimization of the coupling parameter is performed under boundary conditions that perform work on the system (see next section). A good coupling does not significantly disturb the original frequency spectrum of the system, while still keeping the temperature fluctuating about the desired temperature (for details see [198]). The used coupling constants are listed in Tab. A.1.

As alternative thermostating method, a local thermostat suggested by Finnis [218] was used with the published parameters for nickel. The time step in all simulations was set to 2 fs.

3.1.3 Boundary conditions

In the present study four types of different boundary conditions were used. Atoms in *fixed boundaries* were not allowed to move at all, whereas atoms with restricted motion were allowed to move only in some directions. This way for example *2D dynamic* boundary conditions [219] can be realized in which atoms were free to move in one plane. The boundary layers should be large enough that the atoms inside the volume limited by the boundaries interact only with atoms which have bulk properties. In the present study, 2D dynamic boundary conditions were frequently used together with *force boundary conditions*. Under these conditions atoms belonging to outer planes were subjected to extra, external forces. Of course care has to be taken that the system is not subject to a net impulse or torque.

Periodic boundary conditions (PBC) are used to mimic the presence of an infinite bulk surrounding the simulation box. The simulation box is in this case used as a primitive cell from which a lattice of identical cells is constructed which surrounds the original simulation box. The particles in the simulation box are then interacting with all other particles within the simulation box and all the other cells – including its own periodic images, see also [189, 192]. The studied configurations have to be compatible to periodic extension. For edge dislocations this means that because of the additional half-plane periodic boundary conditions can only be applied parallel to the glide plane of the dislocation. It should furthermore be noted, that under periodic boundary conditions all defects interact with their own periodic copies.

3.2 Simulation set-up

3.2.1 Simulation set-up for dislocations

Two types of simulation set-ups were used for the study of dislocations. To study static properties like dislocation core structures and the strain energy of dislocations, a cylindrical set-up was used. All the atoms in the cylinder were displaced according to the anisotropic elastic solution of the displacement field [12] of the dislocation in the center of the cylinder using the program DISLOELAST [220]. The outermost atoms were fixed in these positions and periodic boundary conditions were applied along the direction of the dislocation line.

To study the Peierls stress and the properties of moving dislocations as well as their interaction with obstacles a rectangular simulation box was used. A sketch of the simulation box together with its crystallographic orientation and the Burgers vectors of the dissociated dislocation in Thompson's notation is shown in Fig. 3.1. By applying periodic boundary conditions along the dislocation line and in glide direction an infinite array of equally spaced infinite dislocation lines is modeled. Atoms belonging to the four outer $(1\bar{1}\bar{1})$ -layers were free to move in the x - and y -direction but were fixed in z -direction. With these 2D-dynamic

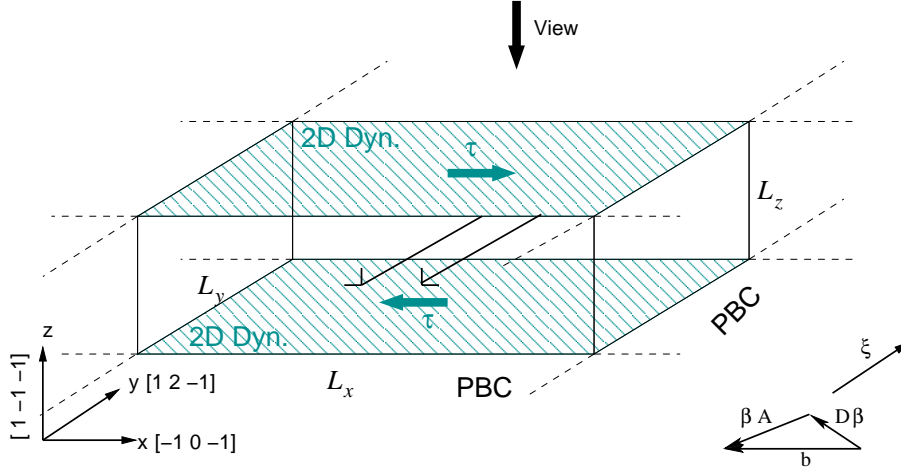


Figure 3.1: Sketch of the used simulation box and its crystallographic orientation for the simulation of an edge dislocation. Periodic boundary conditions (PBC) are used in the line- and glide-direction, whereas 2D-dynamic boundary conditions are applied in z -direction. Upon relaxation the dislocation splits into two Shockley partial dislocations (here the edge dislocation $DA \rightarrow D\beta + \beta A$).

boundary conditions the curving of the slab is suppressed, thus modeling conditions in bulk material. Contrary to fixed boundary conditions the 2D-dynamic BC do not significantly alter the temperature distribution within the slab.

To introduce the dislocation the approach of Rodney [58,102] was followed and generalized to screw and mixed dislocations. The atoms in the slab are displaced in x and y -direction according to an approximation of the isotropic elastic solution for the displacement field of the dislocation [12]. Thereafter, the ledge at the surface, caused by the edge component of the dislocation, is removed. The introduction of an additional half plane by edge dislocation is accounted by adding $b_x/2$ to the periodicity length in x direction L_x . In this way a dislocation is created in a simulation box which is periodically extendable in the x and y -directions while maintaining flat z surfaces. Upon relaxation the dislocation dissociates into the two Shockley partial dislocations.

The combination of PBC and 2D-dynamic boundary conditions corresponds to the application of forces on the sample which balance the lattice rotation normally associated with dislocations having an edge dislocation component. These forces influence the dislocation properties. However, by using large enough box sizes these effects could be minimized. The box sizes were chosen such that comparison to the dislocation core structures obtained in the cylindrical set-up yielded no significant differences. Typical box sizes were between $48 \times 4 \times 25 \text{ nm}^3$ and $86 \times 4 \times 41 \text{ nm}^3$, see sec. 5.1.4 for details. The alternative use of free surfaces in z direction would lead to a buckling of the slab which induces unrealistically short dissociation distances and unrealistic surface waves for moving dislocations [221].

The Peierls stress and dislocation motion were studied by applying extra forces on the atoms of the outermost $(1\bar{1}\bar{1})$ -layers (force boundary conditions) leading to the desired shear stress τ . The starting conditions were equilibrated structures which were sheared according to the anisotropic elastic solution corresponding to τ . The Peierls stress was determined using an iterative procedure in which τ is increased in steps by consecutively applying additional shear to the last relaxed configuration.

3.2.2 Simulation set-up for cracks

3.2.2.1 Geometry and boundary conditions

The simulation set-up for the study of cracks and their interaction with dislocations is shown in Fig. 3.2. The simulated systems correspond to cubic crystals with side lengths of 25 nm (small system, 1.4 million atoms) and 75 nm (large system, 38.4 million atoms). On the side surfaces along the crack front direction 2D dynamic boundary conditions were used. These allow for crack propagation or closure. On all other side surfaces fixed boundary conditions were used. The boundary regions consisted of five atomic layers and are indicated in Fig. 3.2. In this crystal a crack, and additionally a dislocation, can be introduced (see sec. 3.2.2.3 below). The crack tip is positioned at about $2/5L_x$ of the system size L_x in x -direction.

This simulation set-up provides enough space for dislocation processes at the crack tip. It furthermore allows for crack propagation under conditions of nearly constant energy release rate G [175]. This would not be the case if the atoms at the top and bottom of the cube were not clamped by flat 'grips' in y -direction but displaced according to the linear elastic solution of a semi-infinite stable crack.

Along the x - and y -direction different boundary conditions than in Fig. 3.2 could be used. However, due to the later introduction of dislocations, periodic boundary conditions along the crack front direction (z) are not possible. To simulate free boundary conditions on the z -surface, the Poisson contraction would have to be taken into account when straining the system. However, even then preliminary simulations showed a strong tendency towards dislocation nucleation at the boundaries of the free surface and at the crack tip (see also the simulations by Zhou [186]). Similarly, 2D-dynamic or fixed boundary conditions have to be used along the x -direction to avoid nucleation at the edges between the x and y surfaces.

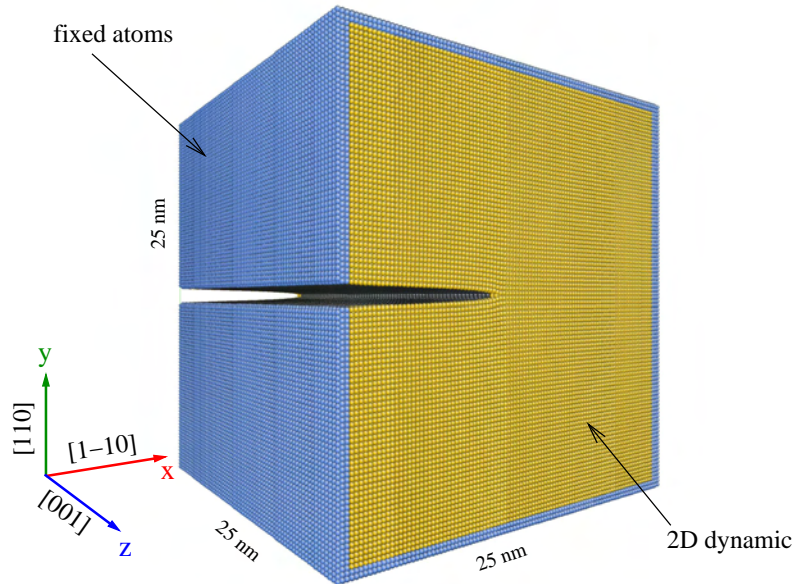


Figure 3.2: Simulation set-up used for the study of the interaction between cracks and dislocations in the γ -orientation. The small sample (1.4 million atoms) shown here contains a relaxed crack which is blunted by the removal of one atomic layer.

All the crack simulations used either standard molecular dynamics simulations at 0 K or static relaxation methods, see appendix B. By using a nickel potential [213], this study can build on prior 2D fracture simulations in Ni [175]. The large number of atoms involved in these simulations required the use of high-performance computing platforms. Details on the computational issues involved in the massively parallel MD simulations are given in [222].

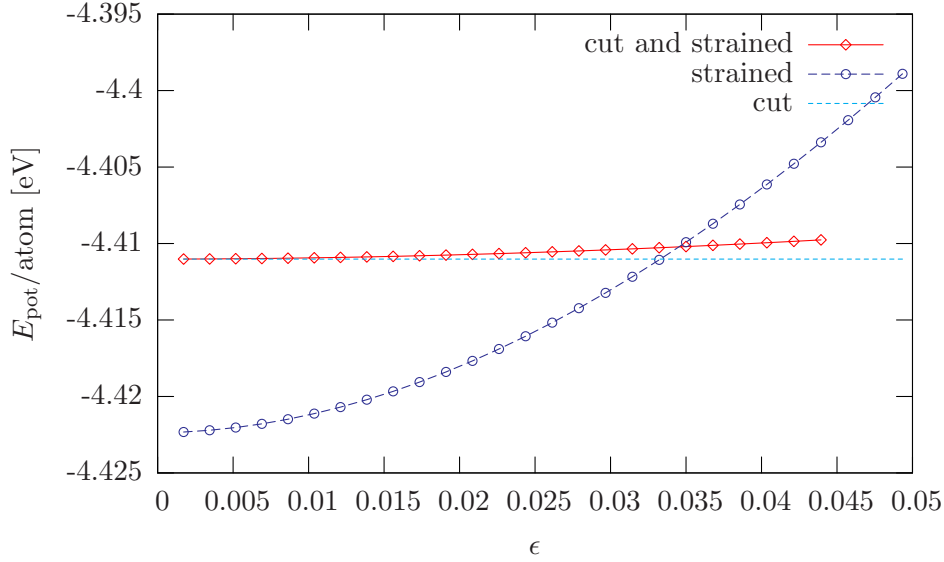


Figure 3.3: Plot of the potential energy per atom as function of strain ϵ to determine the Griffith strain ϵ_G in the small sample. Because of the additional energy due to the straining of the grips ('cut and strained'), the Griffith strain can not be calculated from the strained sample ('strained') and the energy of the cut sample ('cut').

3.2.2.2 Determination of the Griffith strain

According to the Griffith concept of energy balance (see e.g. [121, 122]), a crack is thermodynamically stable when the reduction of strain energy by crack advance equals the energy of the newly created surface. The critical strain ϵ_G at which a sharp crack is stable is therefore related to the box size (volume $V = L_x \times L_y \times L_z$, area $A = L_x \times L_z$) by:

$$\epsilon_G = \sqrt{\frac{4\gamma^{(110)}A}{E^*V}} \sim L_y^{-\frac{1}{2}} \quad (3.1)$$

(E^* : Young's modulus for plane strain or plane stress loading in the appropriate orientation, $\gamma^{(110)}$: (110) surface energy). The simulation box therefore has to be sufficiently large to reach sensible strain values.

The critical strain can in principle be directly calculated using Eq. 3.1 and the theoretical values of E^* and $\gamma^{(110)}$ (see App. A). However, to avoid effects caused by the boundary conditions, ϵ_G was determined by applying the concept of energy balance directly on the potential energy of the simulation box. Fig. 3.3 shows as example the potential energy of the (free atoms) within the simulation box as function of homogeneous strain along y . Also shown is the potential energy of the sample with two free surfaces produced by a cut according to an

imaginary cleavage by the crack. However, due to the fixed boundary conditions, the creation of the free surfaces can not relieve all the strain. By the different lattice parameter, the fixed atoms in the strained grips influence the energy of the free atoms within the sample. This is shown in Fig. 3.3 where the energy of the strained sample with free surfaces is plotted. This small effect has to be taken into account to accurately determine the Griffith strain, which is in given by the intersection in Fig. 3.3 of the 'cut and strained' curve with the 'strained' curve.^c The Griffith strain was calculated for plane strain loading and for boundary conditions modeling plane-stress like loading, see the next section.

3.2.2.3 Initial conditions and loading of the crack

Sharp cracks were introduced by applying an approximate displacement field followed by relaxation. For the creation of blunted cracks one or three (110) half planes were additionally removed. The initial approximation of the crack displacement field was chosen following [223]. For this purpose the box was initially strained along the y -axis according to the Griffith load. Then the atoms were displaced along the y -direction so that the resulting crack is of elliptical shape. The center of the ellipse corresponds to the intersection of the cleavage plane with the left boundary (see Fig. 3.2). The short axis of the ellipse corresponds to $d = \epsilon_G L_y / 2$. The boundary atoms on the left of the center were not strained but displaced upwards and downwards by d . This way the boundary at the left is fully relaxed, whereas the region in front of the crack tip is strained according to the Griffith load. The fixed boundary conditions provide additional stability against crack closing. Upon relaxation, the atoms assume positions according to the strain field of the loaded crack under the given boundary conditions. The stress field of this crack of course does not correspond to the stress field of a semi-infinite crack in an infinite medium. However, the main characteristics of the stress field near the crack tip are maintained.

Two loading conditions were simulated: plane strain loading and plane stress like conditions. The mathematical idealization of the plane stress case is of course only valid for infinitely thin samples. However, by including the Poisson contraction along the z -direction, conditions more akin to plane stress can be modeled. Similar conditions closer to plane stress than to plane strain are assumed to prevail in the experiments on thin Si samples by George [147] and Scandian [2, 153], see also the discussion in [1]. The stress field in thin samples is expected to change significantly the resolved shear stresses on the various slip systems from the pure plane strain case [1]. The consideration of the Poisson contraction during straining is an attempt to model such effects of plane stress like loading conditions.

The displacement field of the stable crack was obtained after relaxation by determining the atomic displacements relative to the positions in the reference system without crack. This allowed to smoothly load or unload the crack without severely disturbing the crack field by scaling all atomic displacements. Such scaling of the displacement field does not change the overall shape of the simulation box or of the elastic strain field.

^cAn alternative is to *not* strain the grips. Therefore 2D dynamic boundary conditions in x - and z -direction and 1D dynamic boundary conditions along the edges would have to be used. As the Griffith strain is a very sensitive parameter, it is in any case advisable to determine ϵ_G under exactly the same conditions under which the crack will be simulated.

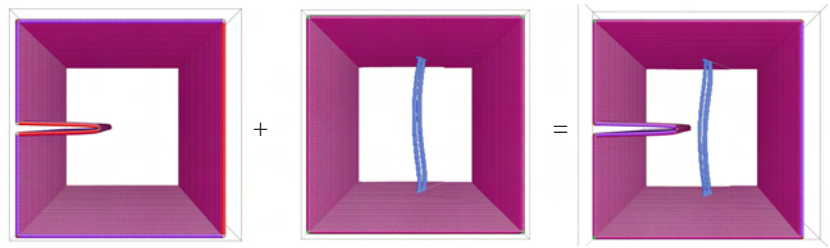


Figure 3.4: Sketch of the process used to create the initial configuration for the simulations of dislocation-crack interaction. The displacement field of a relaxed crack is added to the configuration of a dislocation relaxed under the same boundary conditions.

3.2.2.4 Combining crack and dislocation

Linear elasticity theory allows the superposition of strain fields. The initial configuration to study the interaction of dislocations with cracks was thus realized by adding the displacement field of the crack to the configuration of a relaxed dislocation, see Fig. 3.4. The dislocation therefore was created in the same crystal and with the same boundary conditions which were used to create the crack configuration (see sec. 3.2.1 for the creation of the dislocation). The influence of the boundary conditions on the dislocation can be seen in Fig. 3.4 where the dislocation is slightly bowed out due to image forces.

This superposition method can be also applied to other types of defects, e.g. to create a void in front of a crack or to study dislocation - dislocation interactions. Of course the combined configuration can only consist of atoms present in both original configurations.

3.3 Visualization and characterization of crystallographic defects

Changes in the regular structure of the crystalline lattice caused by crystallographic defects like vacancies, surfaces, interfaces or dislocations lead to an increase of the potential energy of the atoms surrounding the defect. A straightforward approach to visualize defects in a crystal is therefore to display only atoms with increased potential energy (typically $E_{\text{pot}} \gtrsim 0.98E_{\text{coh}}$). This *energy visualization*, however, fails when thermal energy comes into play. Methods which analyze the changes in geometry of the crystal lattice induced by a defect are less affected by thermal noise. The determination of atoms with a *coordination number* deviating from the given crystal structure is the simplest of these methods. However, it is not able to detect stacking faults. A more advanced geometrical method able to identify stacking faults is the *centrosymmetry parameter* introduced by Kelchner *et al.* [224]. In a centrosymmetric crystal structure like fcc, each atom has pairs of equal and opposite bonds to its nearest neighbors. The centrosymmetry parameter P_i of an atom i measures the local departure from the centrosymmetry. In an fcc structure with 12 nearest neighbors j it is defined as [224]

$$P_i = \sum_{j=1}^6 |\mathbf{R}_j + \mathbf{R}_{j+6}|^2, \quad (3.2)$$

where \mathbf{R}_j and \mathbf{R}_{j+6} are the vectors to the six pairs of opposite nearest neighbors [224]. A surface atom is thus characterized by a $P_i > a_0^2$, atoms in a stacking fault position have a $0.2a_0^2 \leq P_i < a_0^2$, and atoms in the core of a partial dislocations are characterized by $0.01a_0^2 \leq P_i < 0.2a_0^2$. An other geometrical method is to classify pairs of atoms according to their local environment. In the *common-neighbor analysis* (CNA) [225, 226] each pair of atoms having common nearest neighbors is characterized by a set of four indices $ijkl$. They describe whether the atom pair consists of nearest neighbor atoms (i), the number of common nearest neighbor atoms (j), the number of bonds between the common nearest neighbor atoms where bonded atoms are nearest neighbor atoms (k), and the number of bonds in the longest continuous chain formed by the k bonds between common nearest neighbors (l). The indices allow a robust discrimination between atoms in fcc or hcp stacking and dislocation core atoms. Centrosymmetry parameter as well as the CNA can be used to locate dislocations in crystals having temperatures upto half the melting temperature.

The above mentioned methods do not give any information on the Burgers vector of a dislocation. The simplest method to determine the Burgers vector of a dislocation is by analyzing the displacements of atoms on adjacent atomic planes caused by the glide of the dislocation between these planes. Zimmerman and coworkers formalized this approach by introducing the atomic *slip vector* [227]:

$$\mathbf{s}_i = -\frac{1}{n_s} \sum_{i \neq j}^n (\mathbf{x}^{ij} - \mathbf{X}^{ij}). \quad (3.3)$$

In this expression, n is the number of nearest neighbors of atom i , n_s is the number of slipped neighbors, \mathbf{x}^{ij} is the vector between atom i and j in the current configuration, whereas \mathbf{X}^{ij} is the corresponding vector in a reference configuration at zero stress and no mechanical deformation. Any inhomogeneous deformation near an atom will lead to a large magnitude of the slip vector. This method can provide quantitative information about lattice deformation and also about the Burgers vector of dislocations which have produced a certain amount of

slip. However, the determination of the Burgers vectors in configurations involving many dislocations on the same or adjacent slip plane, or complicated reactions (eventually leading to sessile dislocations) can become impossible.

Hartley and Mishin [228] have recently developed a method to describe the misfit in the vicinity of dislocation cores based on the *Nye tensor*. The Nye tensor α describes the distribution of infinitesimal dislocations and is related to the Eulerian deformation gradient \mathbf{G} by [228]

$$\alpha = -(\nabla \times \mathbf{G}) . \quad (3.4)$$

The numerical integration over the spatial distribution of components of the Nye tensor permits an accurate calculation of the Burgers vector^d.

An other way to gain more quantitative information about the structure of (partial) dislocation cores is to calculate the disregistry function Δu (Eq. 2.12) from the atomic displacements above and below the glide plane relative to a reference structure. The atomic misfit function ρ which represents the linear Burgers vector density can then be obtained by numerical differentiation of Δu . The edge and screw components of ρ from the two partial dislocations $b_{1,2}$ can be fitted by the derivatives of the analytical solution of the original Peierls-Nabarro model (Eq. 2.13) :

$$\rho_{\text{PN}}(x) = \frac{b_1}{\pi\zeta_2 \left(1 + \frac{(x-x_{c,1})^2}{\zeta_2^2}\right)} + \frac{b_2}{\pi\zeta_2 \left(1 + \frac{(x-x_{c,2})^2}{\zeta_2^2}\right)} , \quad (3.5)$$

which corresponds to two Lorentzians. An alternative method to determine the position and the width of partial dislocations is to plot energy of the atoms above and below the glide plane. Also in this case, Lorentz functions can be fitted to the data.

Further information on defects can be obtained by visualizing the associated stress and strain fields. The components of the atomistic stress tensor are calculated from the virial stress [189] using Voronoi tessellation to calculate the atomistic volume, see also [198]. The visualizations of atomistic configurations were realized with the free software AtomEye by Ju Li [229], which also allows for simple analysis (coordination number, centrosymmetry parameter).

Once the atoms constituting the dislocation core are found the dislocation line information can in principle be extracted from atomistic simulations. While this is a simple task for single, straight dislocations, the general 3D case with complicated dislocation arrangements requires methods from computational geometry. For this purpose parts of Mark Duchaineaus free software library LibGen [230] have been used.

Combining the CNA method for identifying dislocation core atoms with the LibGen tools for extracting the dislocation line information and the Nye tensor method for calculating Burgers vectors allows to generate directly from atomistic simulations dislocation configurations for dislocation dynamics simulations^e.

^dAlthough visualizing the spatial distribution of components of the Nye tensor provides an instructive way of representing dislocation core structures, accurate values of the splitting distance can not be determined by this method. This is due to the fact that for numerical reasons bond-angle distortions larger than a chosen angle have to be ignored. The location of the maximum of the Nye tensor distribution, however, depends on the choice of this angle.

^eA fully automatized computer tool for this purpose is currently under development in collaboration with M. Duchaineau, A. Hartmaier and C. Brandl.

Part I

Dislocation Motion and Interaction with Obstacles

Chapter 4

Properties of straight static dislocations

The core structure and the properties of straight periodic dislocation lines were obtained by relaxing the starting configurations created by the operations described in sec. 3.2.1. Two set-ups were used: a periodic dislocation line in a cylinder with fixed surfaces deformed according to the anisotropic displacement field and a rectangular simulation box with periodic boundary conditions along the line and glide directions and 2D dynamic boundary conditions in z -direction. The latter set-up will also be used for the dynamic simulations of dislocation motion. The radius of the cylinder was about 50 nm (containing about 0.7 million atoms), typical box sizes were $48 \times 4 \times 25 \text{ nm}^3$ (about 0.3 million atoms) and $96 \times 4 \times 46 \text{ nm}^3$ (about 1.2 million atoms), the maximal box size was $223 \times 4 \times 107 \text{ nm}^3$ (about 8 million atoms). The exact dimensions depend on the crystallographic orientation, the lattice constant and the thermal expansion of the potentials.

4.1 Dislocation core structure

Several methods to analyze crystallographic defects were introduced in sec. 3.3. These are now used to analyze the structure of the dissociated dislocations. Fig. 4.1 shows the different core structures of an edge dislocation in the two nickel potentials as example for the use of the methods of analysis. For comparison, the core structure of a screw dislocation in Ni_I is shown in Fig. 4.2a.

The determination of the splitting distance d between the partial dislocations by identifying the dislocation cores by the coordination number of their atoms^a (Fig. 4.1a) proved the easiest method. However, the exact location of the center of wide partial dislocation cores was sometimes difficult to obtain. Furthermore, the method fails when partial dislocations have pure screw character, like in the case of 30° dislocations. Fig. 4.1b shows the disregistry function Δu (Eq. 2.12) from which the linear Burgers vector density, Fig.4.1c was calculated. The fit of Lorentzians to the energy of the atoms is demonstrated in Fig. 4.1d. The full width at half maximum (FWHM) w provides a measure for the width of the partial dislocations. The measure of atomic energy can also be used to quickly estimate core energies of different potentials or dislocation types. Additional information can be obtained by plotting the stress

^aDefined here as the number of nearest neighbor atoms within a radius of $0.9a_0$.

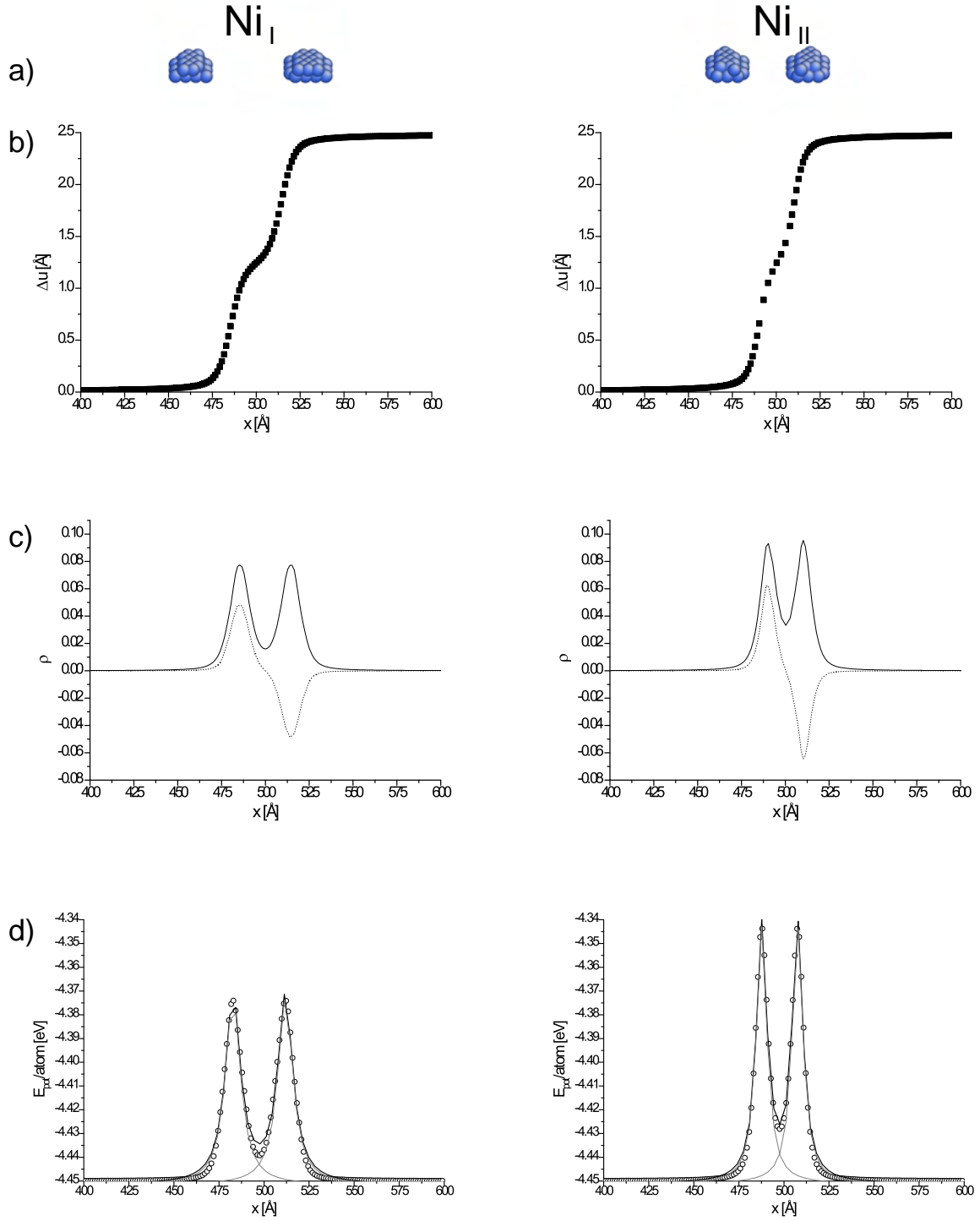


Figure 4.1: Comparison of the core structure of edge dislocations calculated with two Ni potentials: a) atoms with coordination number 13. b) disregistry Δu . c) Burgers vector distribution ρ . The edge (screw) component is represented by a continuous (\cdots) line. d) potential energy per atom along a line above the glide plane with fitted Lorentz functions.

field around the dislocation, see Fig. 4.3. The plots show a qualitative difference of the stress field depending on the splitting distance. For closely spaced partial dislocation the stress field of the screw dislocation component of the partial dislocations cancel each other. This is the case although the the Burgers vector components in screw orientation have fully formed (compare the relative intensities of the Nye tensor distribution in Fig. 4.4). Widely separated partial dislocations show clearly the characteristic stress field of the partial dislocations .

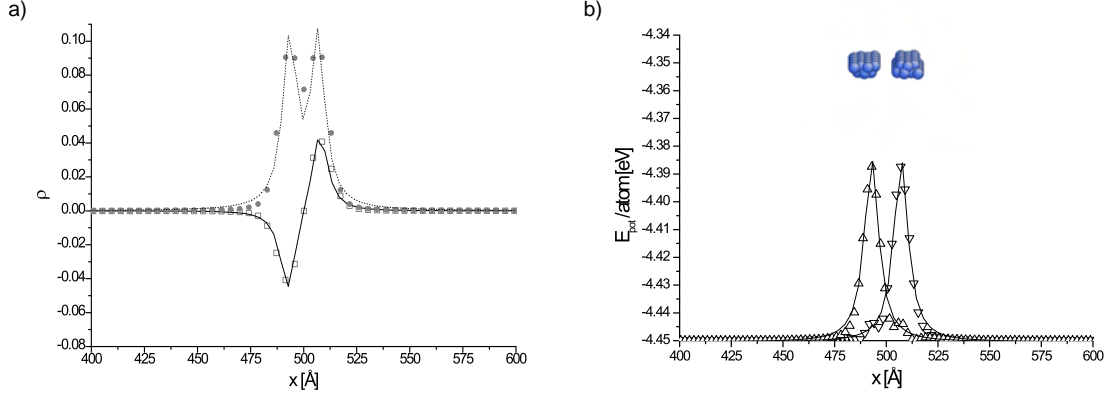


Figure 4.2: Core structure of a screw dislocation in NiI : a) Burgers vector density fitted by a Peierls-Nabarro mode. The edge edge (screw) component is represented by a continuous (\cdots) line. b) Potential energy of atoms above (∇) and below (Δ) the glide plane, fitted by Lorentz functions. The inset shows the core atoms as determined by their coordination number.

The values for d determined by identifying the partial dislocation cores by the coordination number of their atoms agreed in most cases well with the d determined by fitting the peaks of the potential energy of the atoms or the Burgers vector distribution. Peak fitting, however, can lead to peak position which fall between atomic positions. The two method can thus lead to d differing by up to $1b$. The error margin of d is therefore set to $\pm b$.

The boundary conditions in the cylindrical set-up represent the displacement field of a perfect dislocation. This configuration thus favors a small splitting distance. The introduction of a half plane leads to a curvature of the planes parallel to the glide plane of an edge dislocation. This curvature is prevented by the 2D dynamic boundary conditions in the thin film set-up. This set-up therefore favors a larger splitting distance. For the used box sizes, however, the splitting distance between the partial dislocations was independent of the box size (see also Tab. 4.3) and identical to d determined using the boundary conditions from anisotropic elasticity^b. Calculations of the Nye tensor distribution also revealed no significant differences between the dislocation core configurations from the large simulations of the dislocation within the cylindrical setup and the dislocations relaxed in the setup for dynamic simulations, see Fig. 4.4.

The splitting distances d and the two measures for the dislocation widths ζ and w for edge and screw dislocations are shown in Tab. 4.1. The width ζ of the partial dislocation Burgers vector distribution was taken from the fits to the widest distribution (i.e. to the edge Burgers vector distribution for an edge dislocation). The partial dislocation width is larger when it

^bSimulations on smaller boxes revealed significant differences in d for $L_x < 31$ nm and $L_y < 7.5$ nm.

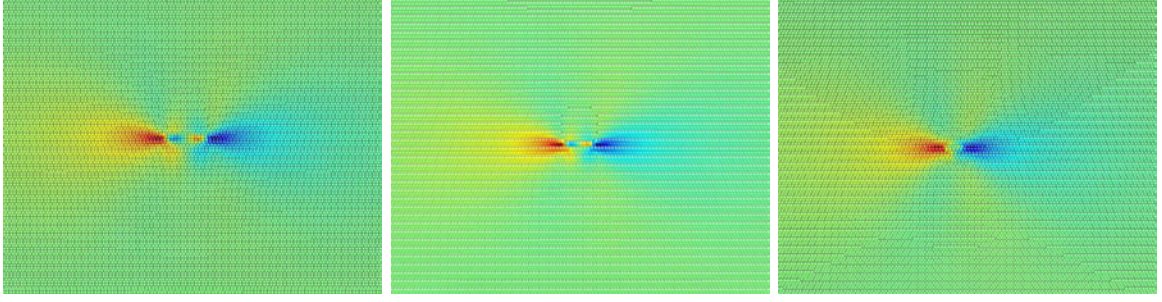


Figure 4.3: The local distribution of the shear stress σ_{zx} around an edge dislocation in Nickel (left, Angelo potential), Nickel (middle, Mishin potential) and Aluminum (right, Ercolessi potential) shows qualitative difference depending on the dissociation width d .

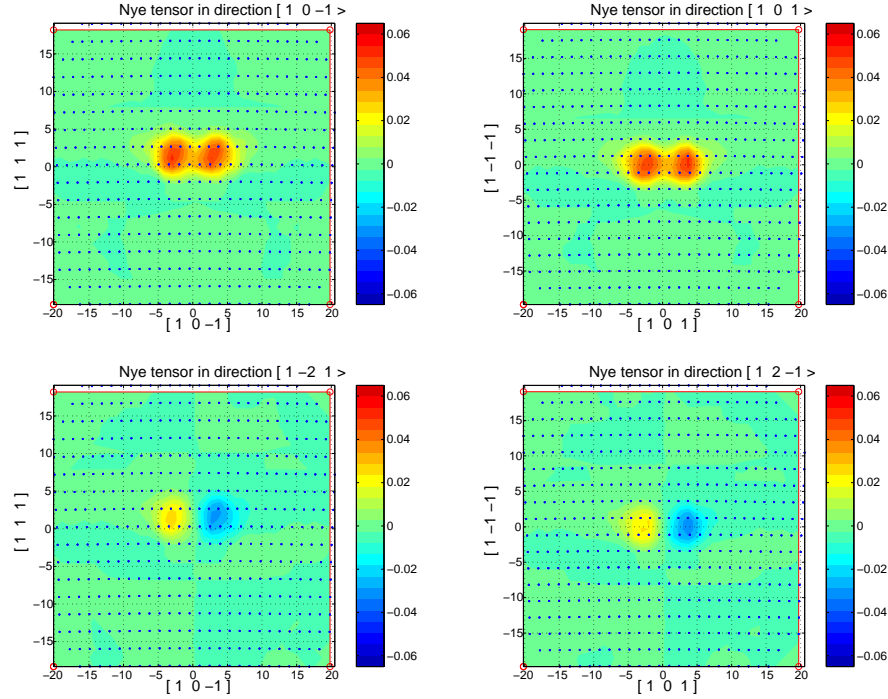


Figure 4.4: Calculated Nye tensor distributions for an edge dislocation in Al_I . Left: dislocation relaxed within a cylinder using and using atomistic displacement from anisotropic elastic theory. Right: dislocation relaxed in the setup for dynamic simulations, $L_x = 48$ nm, $L_z = 25$ nm. All units are in Å.

is determined from fits to the atomic energies than when it is determined from fits to the Burgers vector distribution. This can have several reasons. One reason is that the location of the maximum of the edge and of the screw components of the Burgers vector distribution are not identical. The energy of the core atoms is caused by both the edge and screw component of the displacement, the width w can therefore be larger than ζ . Furthermore the "energy of an atom"^c is not only caused by the strain directly at the position of the atom, but also by

^cThe energy of an individual atom can be defined in the EAM-framework. It has however no direct physical

the configuration in its surrounding. The spread out of the potential energy can therefore be different from the distribution of the Burgers vector.

As additional information the height of the energy peak of the partial dislocation is given in the form $(E_{\text{peak}} - E_{\text{coh}})/E_{\text{coh}}$, which provides a rough measure for the relative dislocation core energy.

The splitting distance d decreases with increasing stacking fault energy (see Appendix A) and is smaller for screw dislocations than for edge dislocations (see Tab. 4.1 and Figs. 4.1 and 4.2), in accordance with Eq. 2.18. Similarly, the width of the partial dislocations is larger for partial dislocations with strong edge component compared to more screw like partial dislocations. A small splitting distance can lead to core overlap, even though the partial dislocation cores identified by the coordination number are clearly separated, see Fig. 4.1. In the case of Al_{II} the strong core overlap can prevent the fitting of two discernable peaks in the Burgers vector distribution. With the exception of Ni_{II} the relative increase in potential energy of the atoms constituting the dislocation core shows no larger variations for the different potentials.

Potential	d [b]	ζ_1 [b]	w_1 [b]	ζ_2 [b]	w_2 [b]	$\Delta E/E_{\text{coh}}$
edge dislocation						
Al_I	5.2	1.9	3.5	1.9	3.5	0.015
Al_{II}	4.2	1.6	2.8	1.6	2.8	0.018
Ni_I	11.7	2	4.1	2	4.1	0.017
Ni_{II}	8	1.8	2.9	1.8	2.9	0.024
Cu	14.2	1.8	3.3	1.8	3.3	0.019
screw dislocation						
Al_I	3	1.3	2.7	1.3	2.7	0.014
Al_{II}	2.2	-	-	-	-	0.013
Ni_I	5.7	1.6	3.4	1.6	3.4	0.014
Ni_{II}	4	1.2	2.6	1.2	2.6	0.022
Cu	5.2	1.3	2.9	1.3	2.9	0.016
30° dislocation						
Al_I	3.5	1.7	2.1	1.3	3.4	
Al_{II}	2.5	-	-	-	-	
Ni_I	7.2	1.4	2	2.7	4.2	
Ni_{II}	5.2	1	1.6	1.8	2.9	
Cu	8	1.2	1.8	2.2	3.3	
60° dislocation						
Al_I	5	2	1.4	3.5	2.4	

Tab. 4.1: Partial dislocation splitting distance d , partial dislocation width ζ (from Burgers vector distribution) and w (FWHM of potential energy) as measured from peak fitting. The relative difference of the potential energy of the dislocation core atoms to the cohesive energy is used as indicator for the relative core energy.

relevance as the distribution of the energy between different atoms can be changed without changing the total energy.

4.2 Dislocation strain energy

The strain energy of a dislocation can be calculated by starting from the dislocation center and summing up the excess energy $E_{\text{pot}} - E_{\text{coh}}$ of all atoms within a cylinder of radius R [91]. Figs. 4.5 - 4.6 show plots of the so calculated strain energy per unit length versus $\ln R$ for the different simulation set-ups. The results for the cylindrical set-up with boundary conditions according to the anisotropic elastic solution for the respective dislocation follow a straight line for sufficiently large R . The results for the simulation boxes for the dynamic simulations follow the same line upto R_{dev} where the strain energy becomes larger than for the cylindrical set-up. The strain energy usually started to deviate from the cylindrical set-up by more than 2% for $R_{\text{dev}} \approx L_z/4$. The difference in total strain energy at $R \lesssim L_z/2$, however, was always less than 10%.

The deviation from the linear fit for large R were caused by the 2D dimensional boundary conditions. These boundary conditions led to a combination of positive (for the z -components of the stress field) and negative image dislocations, which alter the stress field of the dislocation. Such boundary effects are immanent to simulation set-ups for moving dislocations and have to be accounted for in the discussion.

Potential	prelog. fact. [eV/Å]	r_0 [b]	r_{dev} [b]	$E_{\text{core}}^{\text{dev}}$ [eV/Å]
edge dislocation				
Al _I	0.195	0.78	5	0.36
Al _{II}	0.1798	0.52	5	0.4
Ni _I	0.3797	1.02	11	0.9
Ni _{II}	0.3751	0.76	7	0.85
Cu	0.2398	0.97	14	0.65
screw dislocation				
Al _I	0.1294	0.54	6	0.32
Al _{II}	0.1174	0.35	6	0.33
Ni _I	0.2425	0.63	11	0.69
Ni _{II}	0.2346	0.47	7	0.65
Cu	0.131	0.45	7	0.48
60° dislocation				
Al _I	0.1794	0.74	6	0.36

Tab. 4.2: Results of the fits to the strain energy of cylinders containing a dislocation as function of the logarithm of its radius, see Figs. 4.5 - 4.6. The mathematical core radius r_0 is determined from the intercept of the straight line with the r axis, whereas r_{dev} is an estimate of the radius where the strain energy not longer follows the logarithmic relationship. The energy at this point is frequently taken as core energy $E_{\text{core}}^{\text{dev}}$.

The strain energy departed also from the linear fit for small values of R , see e.g. Fig. 4.6. This departure at r_{dev} is usually attributed to the brake-down of linear elasticity close to the dislocation core, and the Energy at r_{dev} is often taken as core energy $E_{\text{core}}^{\text{dev}}$ [13, 91]. The deviation is independent of the set-up ^d. Due to the lattice discreteness r_{dev} can be only determined with an error of at least $\pm b$. The slope of the line drawn tangent to the linear portion of the E_{strain} over $\ln R$ plots yields the anisotropic energy factor K of Eq. 2.4, while

^dThe different energies for the first point at $R = 5 \text{ \AA}$ in Fig. 4.5 are most probably due to an uncertainty of $b/2$ in the determination of the center of the cylinder.

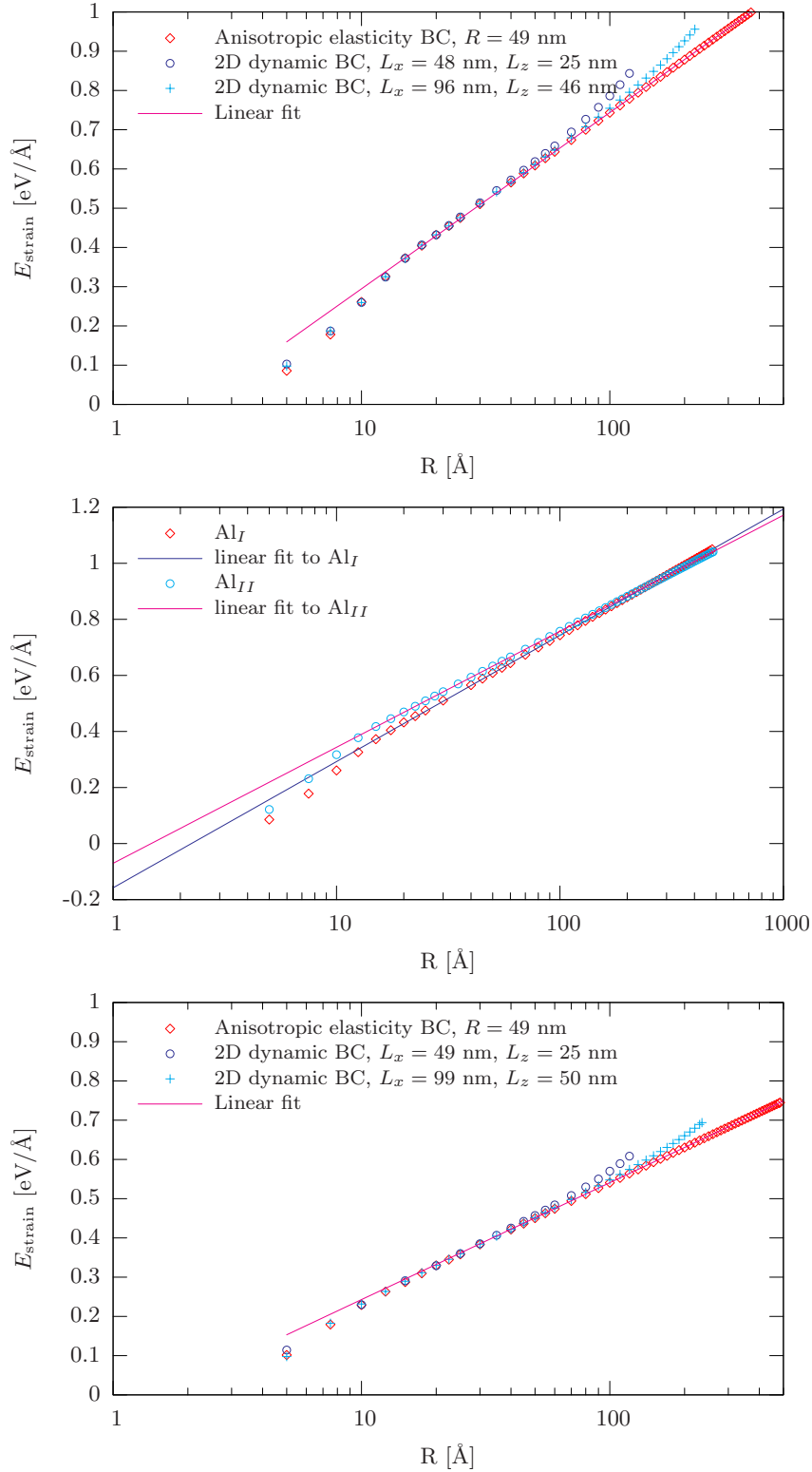


Figure 4.5: Plot of the strain energy per unit length contained within cylinders of radius R from the center of a dislocation. The strain energy was obtained using displacements from anisotropic elasticity as boundary conditions (BC) and two different box sizes for dynamic simulations. A straight line has been fitted to the strain energy using the logarithm of R . Top: edge dislocation in Al_I , middle: edge dislocation in Al_I compared to Al_{II} , bottom: screw dislocation in Al_I .

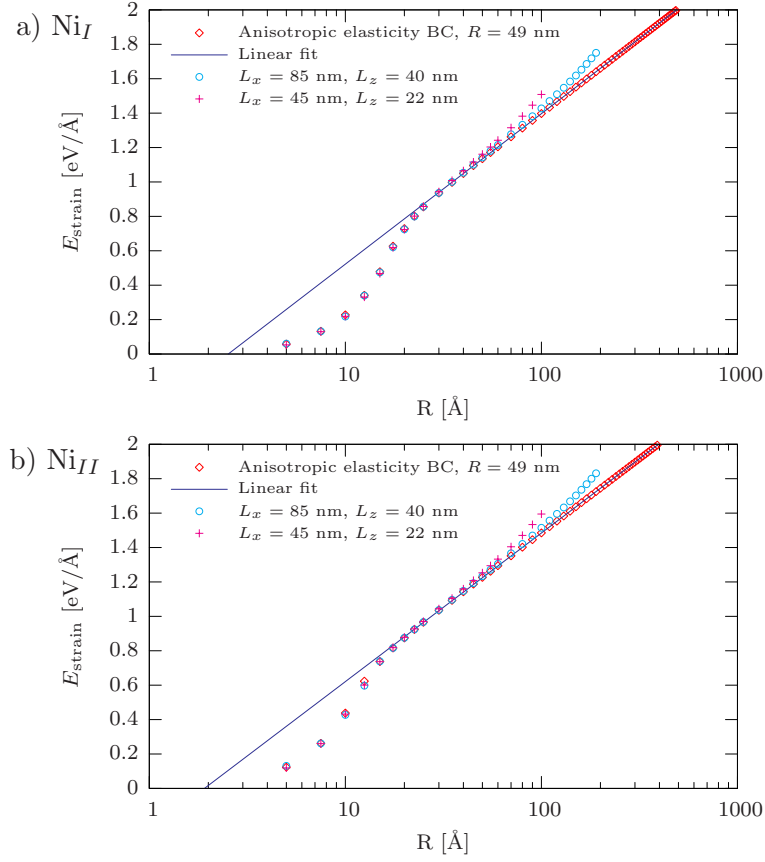


Figure 4.6: Plot of the strain energy contained in cylinders of Radius R around edge dislocations in two different nickel potentials.

the intercept with the x -axis yields the mathematical core radius r_0 . All these values are summarized for the different dislocations and potentials in Tab. 4.2.

The dissociation of the dislocation into partial dislocation clearly affected the strain energy as the deviation from the linear fit at r_{dev} is clearly linked to the splitting distance d , see e.g. Fig. 4.6. The energy at that point $E_{\text{core}}^{\text{dev}}$ is therefore not only the core energy but also contains the energy due to the strain field between the partial dislocations. Therefore $E_{\text{core}}^{\text{dev}}$ is higher for Ni_I than for Ni_{II} although the potential energy of the atoms within the partial dislocation cores is higher for Ni_{II} , see Tab. 4.1.

For roughly equally spaced partial dislocations the energy of the dislocation cores (see Tab. 4.1) can make a measurable difference in the total energy, see Fig. 4.5, middle. Upto a radius of about 30 nm the edge dislocation in Al_{II} has a higher potential energy than the edge dislocation in Al_I although Al_I is the elastically stiffer potential, see Tab. 4.2.

4.3 Peierls stress

The Peierls stress of dislocations is very sensitive to boundary effects and to the details of the interatomic forces. The Peierls stress in fcc metals has been subject of detailed atomistic studies, both by molecular dynamic and static methods [94–97] and in the Peierls-Nabarro model [23, 27]. The calculation of *exact* values for the Peierls stress τ_P is not intended here and would require special treatment of the boundary conditions [94]. The estimation of τ_P in the set-up for dynamic simulations can however serve to further characterize the dislocation core and its mobility in the various interatomic potentials and to estimate finite size effects.

Lower and upper boundaries for the Peierls barrier were calculated by iteratively shearing the sample and relaxing it under applied force boundary conditions. At the lower limit of τ_P the system relaxed into a local minimum, whereas at the upper limit no relaxation was possible. Tab. 4.3 shows the effect of the simulation box size on the splitting distance and the stress values bracketing τ_P for an edge dislocation in Al_I .

The values of the Peierls stress in Tab. 4.4 range from $10^{-7}\mu'$ (edge dislocation in Cu) to $10^{-4}\mu'$ (screw dislocation in Al), in agreement with the generally low Peierls stress for face centered cubic metals ($\tau_P \lesssim 10^{-6}\mu'$ to $10^{-5}\mu'$ [13]). The values of τ_P for Al_I in the large box furthermore agree exactly with the values determined by Olmsted *et al.* [94] which were corrected for image force effects. The applied method therefore is able to determine the Peierls stress, and at the used system sizes boundary effects should have only a relatively small impact on the most sensitive property of dislocations. However, at very low stresses ($\tau \lesssim 10^{-7}\mu'$) the gradients in the sample become very small which can lead to convergence problems in the relaxation method (GLOC, see appendix B). The determination of low Peierls barriers might therefore be problematic. The determination of the (larger) Peierls stress of screw dislocations is not affected by this problem. There the large difference of the Peierls stress in Ni_I and Ni_{II} shows that different potentials for the same material can lead to extremely different Peierls stresses.

boxsize (L_x, L_y, L_z [nm])	d [Å]	lower limit for τ_P [MPa]	upper limit for τ_P [MPa]
(48,1,11)	15	3.0	3.2
(48,19,11)	15	3.0	3.2
(48,4,25)	15	2.5	2.7
(48,4,46)	15	2.5	2.7
(96,4,25)	15	2.7	2.9
(96,4,46)	15	2.0	2.2

Tab. 4.3: Influence of the box size on the splitting distances d and on the Peierls stress τ_P determined from static simulations in Al_I .

Potential	lower limit for τ_P [MPa]	upper limit for τ_P [MPa]
edge dislocation		
Al_I	2.0	2.2
Al_{II}	1.3	1.5
Ni_I	0.24	0.26
Ni_{II}	0.02	0.04
Cu	-	0.02
screw dislocation		
Al_I	13	14
Ni_I	20	22
Ni_{II}	4	5
Cu	2.25	2.5
60° dislocation		
Al_I	17.5	20

Tab. 4.4: Upper and lower limits for the Peierls stress τ_P for edge and screw dislocations determined by energy minimization with force boundary conditions.

Chapter 5

Properties of straight moving dislocations

The motion of dislocations in aluminum, nickel and copper was studied under an applied shear stress at different temperatures. Most simulations were performed on edge dislocations, but also screw dislocations and in some cases 60° dislocations were simulated. The simulations were performed using a broad range of simulation box sizes. Exemplarily simulations were performed using different hydrostatic pressures.

Molecular dynamics simulations can only be run over small time spans, typically in the order of nanoseconds. In order to enable the study of dislocation motion at different temperatures, stresses, system-sizes and using various potentials, the typical simulated time ranged from 150 - 400 ps. Thus dislocation velocities below approx. $1/20c_t$ were not accessible within this study. The focus of this study is on dislocation motion in the linear stress - velocity regime. Most of the simulations were therefore performed with stresses leading to velocities of approx. $1/5c_t$, where relativistic effects can be neglected. Simulations were also performed in the high velocity regime ($v > c_t/2$), which is usually not reached during normal experimental deformation of bulk materials.

The general outcome of the simulations and the important question how they are influenced by the simulation set-up will be addressed in the next section. In sec. 5.2 the dislocation velocity is studied as a function of stress and temperature.

5.1 General results and simulation aspects

The outcome of the dynamic simulations under temperature control and applied stress were snapshots at different times of the atomistic configuration containing the dislocation. From these configurations the position of the dislocation line had to be extracted. Depending on the temperature induced noise, the dislocation cores were identified either by the stacking sequence or the more complicated common neighbor analysis (see sec. 3.3). The dislocation line position was subsequently determined by a 2D line tracking algorithm, see Fig. 5.1 for an example of the method. In the following, the dislocation position on the x -axis will be displayed as function of time – giving the trajectory of the dislocation. Thereby the position of the whole dislocation is represented by the center of mass of the leading partial along the x -direction. Depending on the dislocation line length and partial dislocation spacing, the method works well up to relatively high temperatures ($\sim 1/3 - 1/2T_m$). An example of

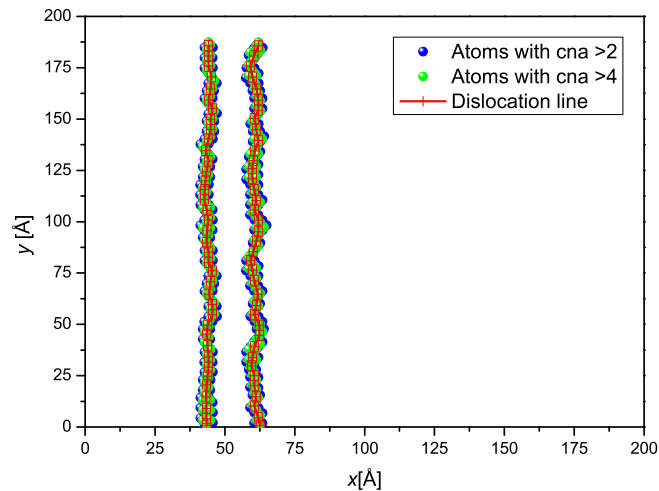


Figure 5.1: Example for the determination of the position of a moving edge dislocation line by the common neighbor analysis (CNA) and 2D line tracking. Only a part of simulation box is shown (Al_T , 30 K, 4 MPa, $48 \times 19 \times 11 \text{ nm}^3$).

typical trajectories $x(t)$ determined by the above method is shown in Fig. 5.2.

As can be seen in the example of Fig. 5.2 the dislocations reached nearly constant velocities v after a certain an acceleration period. For the same applied shear stress this steady state velocity and the acceleration period depend on temperature. the steady state velocity v_{ss} was estimated from such trajectories by measuring the (constant) slope of $x(t)$. Of course not all trajectories were so smooth as the ones shown in Fig. 5.2. Especially for low velocities the dislocation motion can become unsteady, leading to a rougher trajectory due to higher temperatures or lower stresses. However, also for low velocities the mean velocity showed the same proportionality to the stress as at higher velocities. Therefore the stress was chosen to produce smooth trajectories for all temperatures.

5.1.1 Details of dislocation motion

In the one dimensional representation of the moving dislocation line like in Fig. 5.2 the internal degrees of freedom of the dislocation are neglected. The dislocation line as whole as well as each of its partial dislocations can oscillate along its mean line direction. An example for such excitations of the dislocation lines is shown in Fig. 5.3b. The modulation of the splitting distance d can be used for a simplified study of the internal vibrations. Its behavior over time shows usually a mixture of characteristic frequencies (see Fig. 5.3a). As expected from Fig. 5.3b the characteristics and amplitude of the oscillation of d depend on the simulated line length. The splitting distance and the amplitude of the vibrations increases with increasing temperature, see Fig. 5.4. The slight increase of d (Typically by approx. $1b$ over 300 K) is most probably caused by a decrease of the stacking fault energy with the temperature.

Vibrations of partial dislocations can lead to drag forces on the entire dislocation, see sec. 2.1.3.4. In the following, however, the microscopic details are neglected and the net

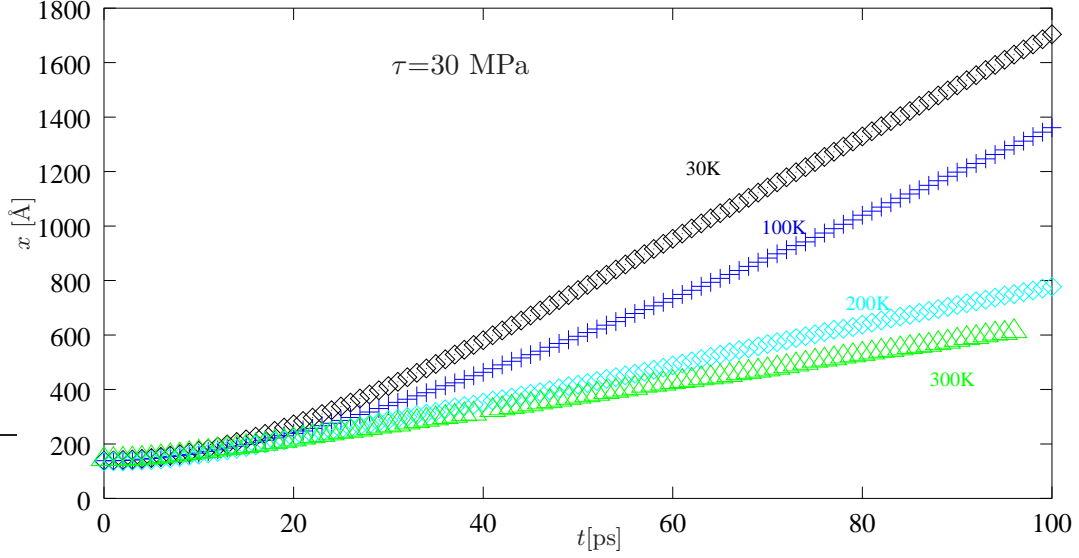


Figure 5.2: Example of dislocation trajectories: the motion of an edge dislocation in Ni_I under identical applied shear stress $\tau=30$ MPa but at different temperatures.

motion of the entire dislocation is studied.

5.1.2 Temperature control and dislocation motion

An important aspect in modeling the dynamic behavior of dislocations is the control of the temperature of the simulated system. The method to derive an appropriate coupling constant for the Nosé-Hoover thermostat was outlined in section 3.1.2. Different values for τ_η^{-1} were used to assess whether the choice of the thermostat parameter influenced the dislocation motion. Although the non-optimized values for τ_η^{-1} produced visible oscillations of the total temperature during the simulation runs, it can be seen from Fig. 5.5 that the dislocation trajectory and steady state velocity were not affected.

As further test, a local thermostat developed by Finnis [218] was used with the published parameters for nickel [218]. Although this thermostat uses a completely different method to control the temperature compared to the global temperature control by the Nosé-Hoover thermostat, the dynamics of the dislocation remained unchanged, see Fig. 5.5.

The restricted mobility of the atoms in the 2D dynamic boundary layers imposes a kinetic energy equal to 0 in the z -direction within the boundary. The effect of these boundary conditions on the temperature of the atoms within the box was assessed by calculating the velocity distribution in atomic planes normal to z and fitting them to a Maxwell distribution. The influence of the boundary layers on the kinetic temperature was very small even for layers next to the boundary. The velocity distribution was only slightly affected for the layers close to the boundary.

5.1.3 Influence of hydrostatic pressure

Most potentials use the room temperature lattice constant as equilibrium lattice parameter: $a_0^{\text{exp.}}(RT) = a_0^{\text{sim.}}(0 \text{ K})$. The potential parameters at 0 K then also represent other material

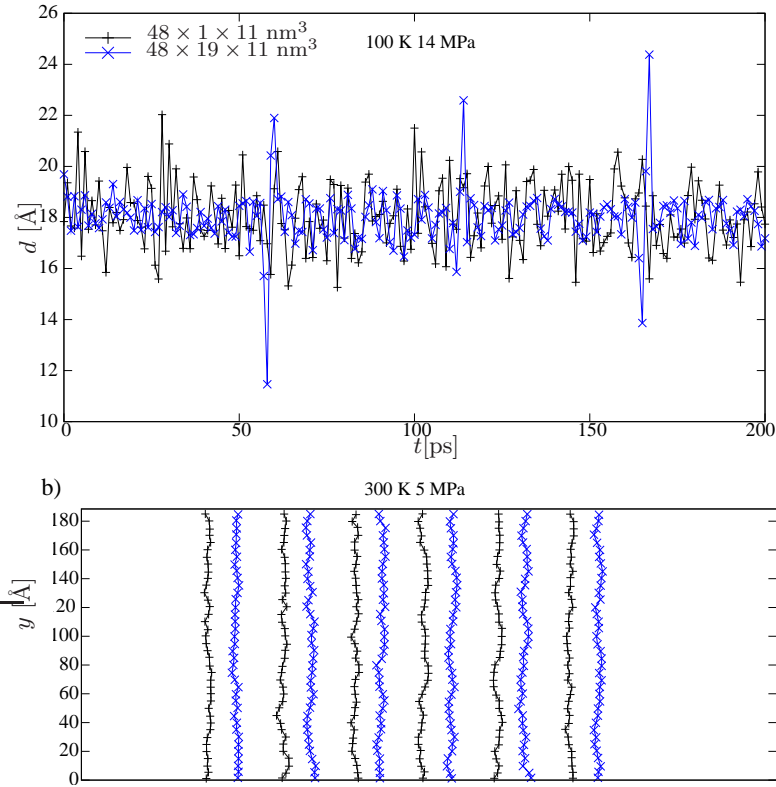


Figure 5.3: Details of the dislocation motion: a) splitting distance d as function of time for the longest and the shortest dislocation of Fig. 5.8, the 2 outlying peaks are artefacts from the periodic boundary conditions along x ; b) from left to right: subsequent configurations of partial dislocation lines. The time between the configurations in b) is 1 ps. At the stress of 5 MPa the motion of the dislocation is unsteady. During the displayed time period of 6 ps the center of mass of the dislocation moved by 1 Å, therefore the position of the subsequent dislocation configurations were shifted against each other.

properties at room temperature. This causes deviations from the experimentally accessible material properties at a certain temperature from the calculated material properties at the same temperature. The aluminum potential of Ercolessi [206] is in this case an exception as it uses the 0K lattice constant.

The effect of the use of the room temperature lattice constant as equilibrium lattice parameter on the dislocation motion can be assessed by performing simulations at 300 K with different lattice parameters. This corresponds to determining the influence of hydrostatic pressure P on the dislocation motion. Fig. 5.6 shows the trajectory of an edge dislocation in Al_I at 300 K using the lattice constants of the potential for different temperatures. For pressures below 1 GPa the trajectory and steady state velocity remained nearly unchanged.^a Slight hydrostatic pressure therefore seems to have no large effect on the dislocation motion.

Preliminary simulations of dislocation motion in Cu under shock loading conditions [231] at $P \approx 30$ GPa, however showed significant differences in the dislocation motion. At these

^aThe unsteady motion of the dislocation with $a_0(0\text{ K})$ is probably due to the fact that the starting configuration was deformed according to the elastic constants at $P = 0$.

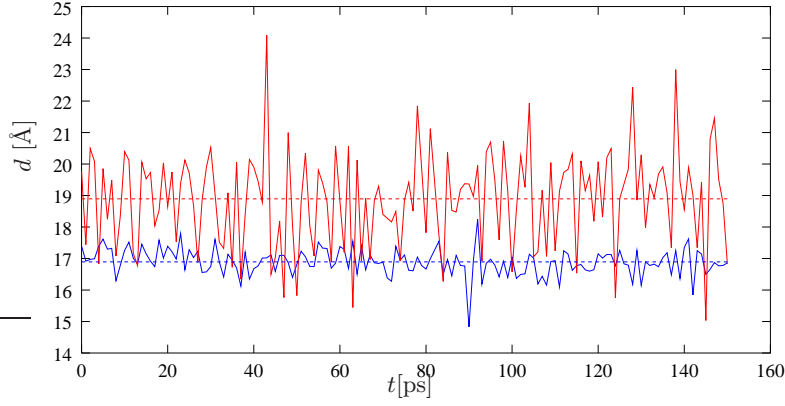


Figure 5.4: Dislocation dissociation distance d in Al_I as function of time for 30 K, 4.5 MPa (blue) and 300 K 30 MPa (red).

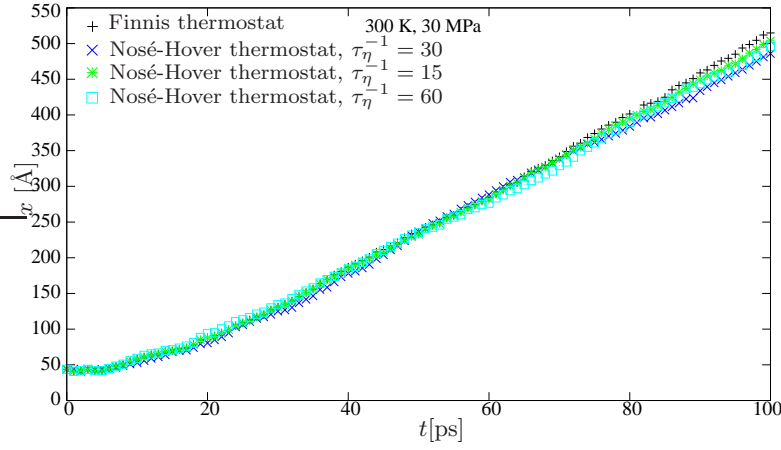


Figure 5.5: Effect of temperature control by different thermostats and thermostating parameters τ_η^{-1} on the dislocation trajectory (edge dislocation in Ni_{II} , $42 \times 4 \times 22 \text{ nm}^3$, 300K , 30MPa)

high pressures the elastic constants and the stacking fault energy differ strongly from their values at $P = 0$. The high resolved shear stresses under shock loading should however lead to highly relativistic dislocation motion. Dislocation motion under shock loading condition is outside the scope of this thesis.

5.1.4 Size effects in dislocation motion

Like in all simulations of defects that have a long range stress field, the size and the shape of the simulation box have an influence on the dynamics of the dislocation. This influence must be qualitatively understood and – where possible – minimized.

By applying periodic boundary conditions in x direction an array of linear dislocations spaced by L_x is simulated. The dislocation thus interacts with its own periodic images and with their emitted phonons. Fig. 5.7 shows two trajectories of edge dislocations in Al_I at $T = 300 \text{ K}$ and $\tau = 30 \text{ MPa}$ with $L_x = 48$ and $L_x = 96 \text{ nm}$. The steady state velocity was for both dislocations $v_{ss} = 6.7 \pm 0.1 \text{ Å/ps}$. The trajectories show slight deviations from the linear

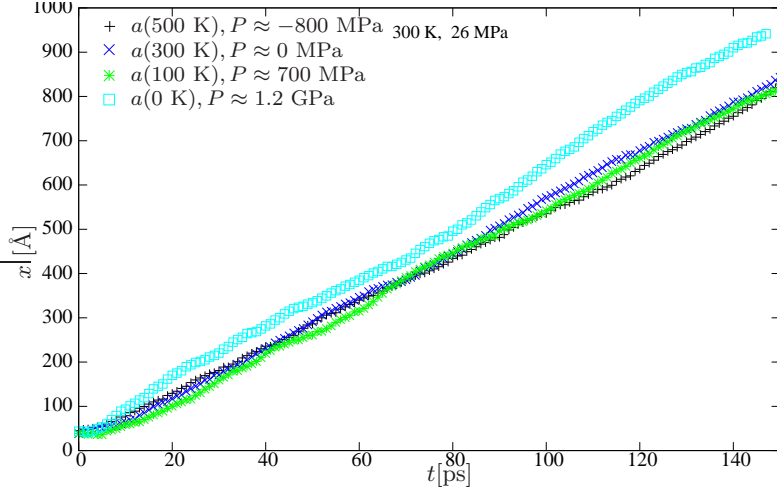


Figure 5.6: Effect of hydrostatic pressure on the motion of an edge dislocation in Al_I .

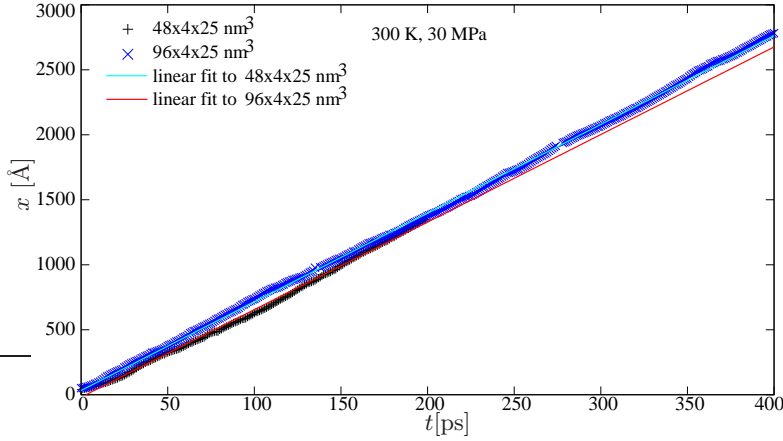


Figure 5.7: Effect of different box lengths L_x in x -direction on the motion of an edge dislocation in Al_I .

fits. These deviations could however not be directly correlated with the box dimensions and sound velocities.

The length of the dislocation line is related to its possible vibration modes. Phonon induced vibrations of the dislocation line cause a drag force by the flutter effect, see sec. 2.1.3.4. This effect is mainly important at low temperatures. Fig. 5.8 shows the influence of the periodic box width on the trajectory of an edge dislocation at 100 K. Linear fits to the dislocation trajectories yield approximately the same steady state velocities. However, the trajectory of the dislocation with the shortest periodic line length shows variations in the velocity where the other dislocations have reached steady state. These variations are most probably linked to the limitation of vibrational modes of the short dislocation. Stress fluctuations can locally retard the motion of a long dislocation and thereby excite vibrations on the whole line. Dislocations with a short periodicity length are stiffer, stress fluctuations therefore are more likely to influence the motion of the whole line.

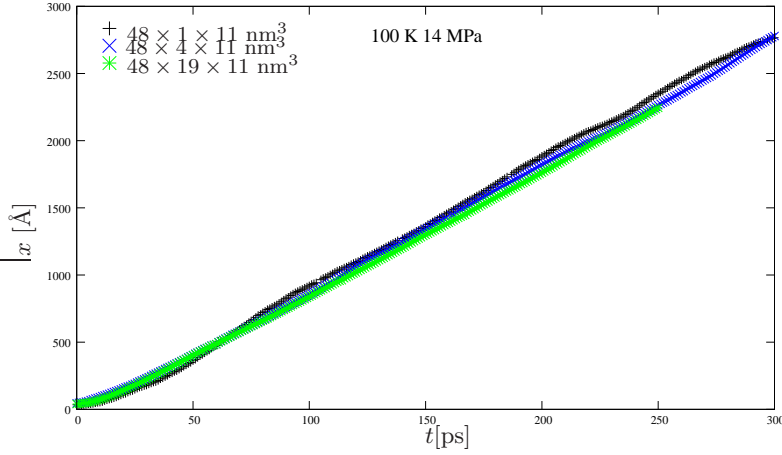


Figure 5.8: Effect of the dislocation line length L_y on the motion of an edge dislocation in AlI.

The influence of the box height on the dislocation motion can be clearly seen in Fig. 5.9. The increase of L_z was correlated with the acceleration period, whereas the steady state velocity was not influenced. The acceleration of a dislocation is determined by its mass (see sec. 2.1.3), which depends on the radius available to the strain field of the dislocation. Within the simulation box the shortest radius corresponds to $L_z/2$, which explains the observed change in the acceleration phase of the dislocation. The inertia of dislocations will be discussed in detail in sec. 7.2.1.

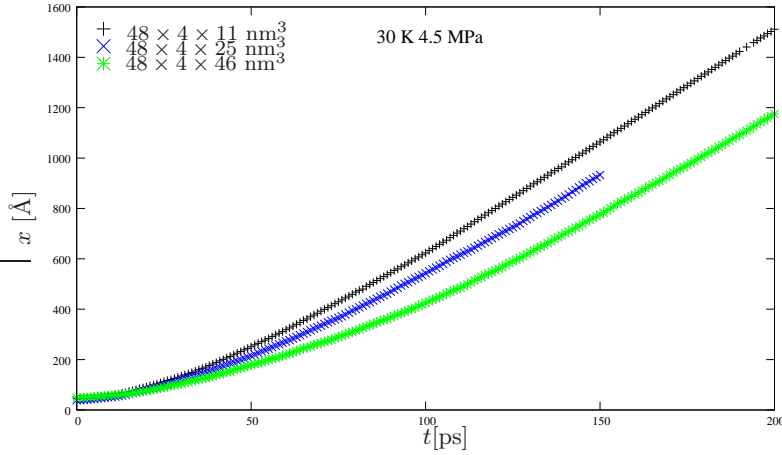


Figure 5.9: Effect of different box heights L_z on the motion of an edge dislocation in AlI.

The following results were obtained using typically box sizes of $48 \times 4 \times 25 \text{ nm}^3$ to $86 \times 4 \times 41 \text{ nm}^3$, which are significantly larger than the simulation boxes used in recent studies on dislocation motion [53, 58, 96, 103].

The determination of the steady state velocity is subjected to certain errors. The most important source of error is the possibility that the dislocation has not reached its steady state velocity. This effect was assessed and minimized by fitting on different subsets of the trajectory. By comparing the drag coefficient (see next section) determined by using different

stresses and box sizes the error in determining v_{ss} is estimated to about 5 to at maximum 10%.

5.2 Dislocation velocity as a function of stress and temperature

The measured steady state velocity of the dislocations in Al, Ni and Cu is shown in figures 5.10 to 5.12 as function of the applied shear stress τ and temperature T . Two regimes with different stress and temperature dependencies of the velocity can easily be distinguished. In the low velocity regime the dislocation velocity for edge and screw dislocations depends linearly on τ , and is approximately proportional to $1/T$. Whereas the behavior of edge and screw dislocations is similar at low velocities, it differs in the high velocity regime.

At high stresses the velocity of the edge dislocations increases only marginally with τ and depends only weakly on the temperature. Olmsted *et al.* [53] recently observed the existence of a temperature and stress independent "plateau velocity" for edge dislocations (at about 26 Å/ps for Al and 21 Å/ps for Ni). The present simulations however show that depending on the potential, the velocity of the edge dislocation can still significantly increase in the high velocity regime. The term plateau velocity is therefore somewhat misleading. A convincing physical interpretation of the high velocity has not been offered yet (see also the discussion in [53]). In particular, factors determining the onset of the high velocity regime have not been identified. It should be noted that the onset of the high velocity regime, as well as the "plateau velocity" are independent of the box size and its aspect ratio.

For screw dislocations the high velocity regime sets in at lower velocities compared to edge dislocations. Similar to the edge dislocation temperature dependence of the velocity is less pronounced for the high velocity dislocations than in the low velocity regime. The increase of the velocity of screw dislocations with τ is generally stronger than for edge dislocations, see Figs. 5.10 - 5.12. As the crossover to the high velocity regime occurs at lower velocities compared to the edge dislocations, the velocity of screw dislocations is for the same stress generally lower than that of edge dislocations. The behavior of the 60° dislocation in Al₁ (Fig. 5.10) is somewhere in between that of an edge and a screw dislocation.

The high velocity regimes in the different potentials are compared in Tab. 5.1. For this purpose a "crossover" velocity v_c is introduced to provide a measure of the velocity range within which the transition between the two velocity regime occurs. Furthermore the stress dependence of the dislocation velocity at low temperature is indicated. Relative to the velocity of transverse sound waves the crossover velocity v_c is the largest in Cu and smallest in Al. Relative to c_t the crossover velocity v_c does not show pronounced differences between the different potentials for the same material. However, there are differences between the potentials in the rate of velocity increase with τ .

The edge dislocation in copper seems to be a special case. Dislocation motion takes place in the low velocity regime upto about $0.9c_t$. The highest measured subsonic edge dislocation velocity $v_p = 15.99\text{Å/ps}$ at 900 MPa is just about $0.99c_R$. The velocity of the edge dislocation in this case seems to be limited either by c_t or c_R , which are nearly identical: $c_R = 0.99c_t$. It is therefore not clear if the same mechanism leads to the high velocity regime as in the other cases, or whether relativistic effects are at work.

Based on theoretical considerations, Roos *et al.* [232] proposed a velocity dependent flutter mechanism. To study the flutter effect of dislocation drag (see sec. 2.1.3.4), simulations with the dislocation length equal to the minimum repeat distance were performed on edge

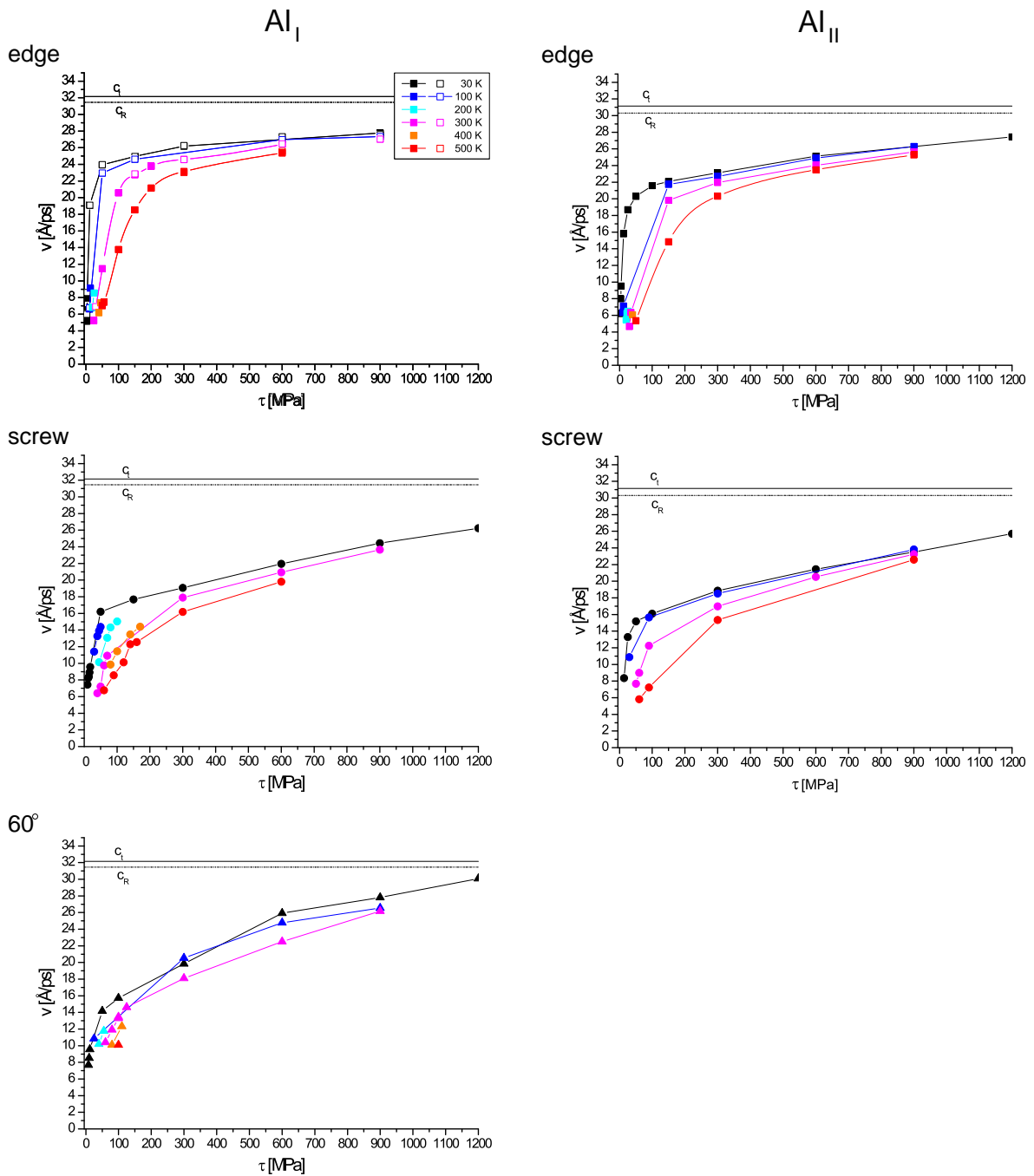


Figure 5.10: Dislocation velocity as function of stress and temperature for dislocations in Al. The open symbols denote simulations which were performed with dislocation length equal to the minimum repeat distance along the dislocation line.

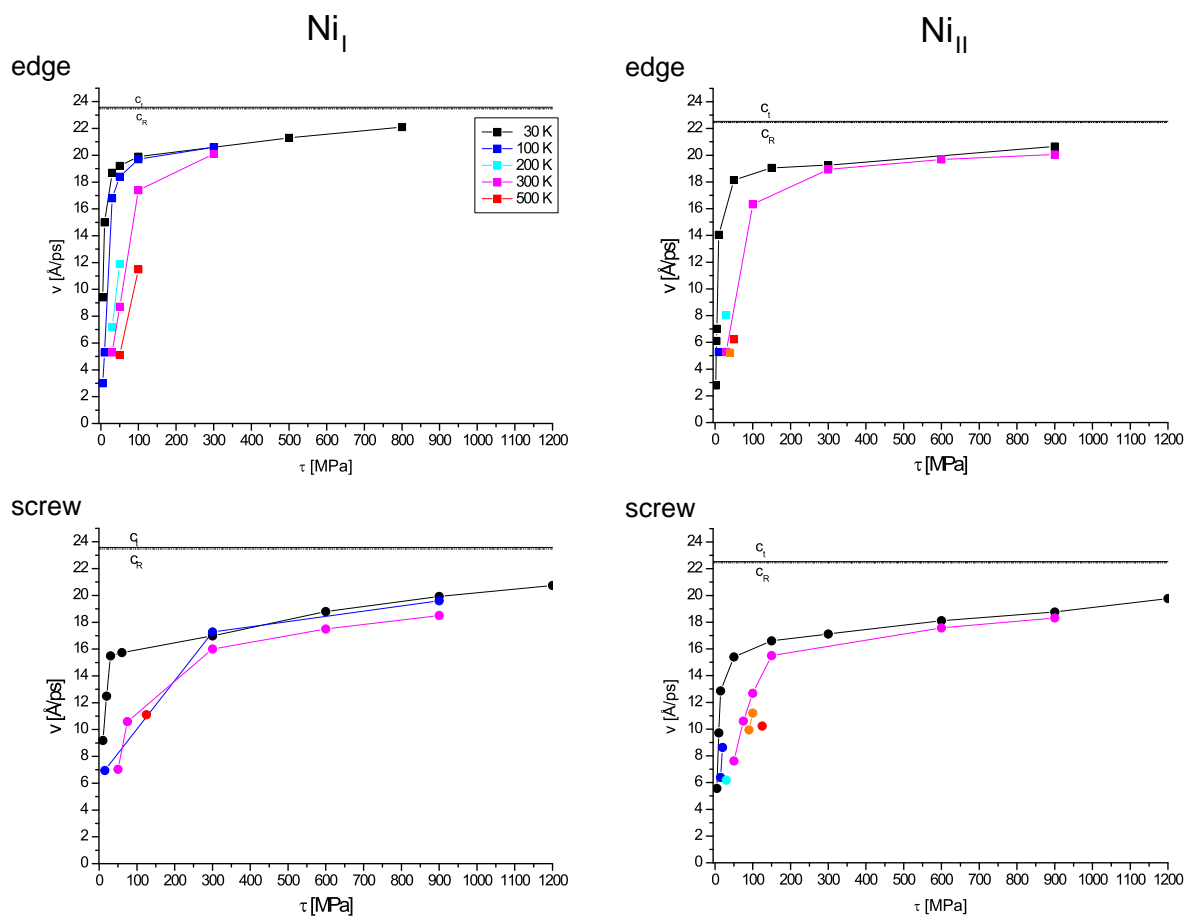


Figure 5.11: Dislocation velocity as function of stress and temperature for dislocations in nickel.

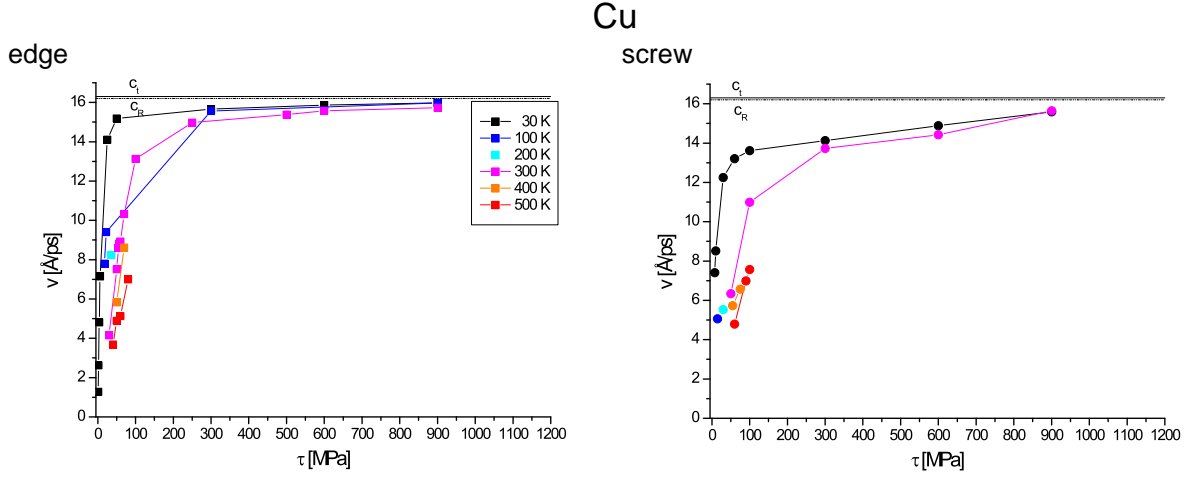


Figure 5.12: Dislocation velocity as function of stress and temperature for dislocations in Cu.

Potential	edge dislocation			screw dislocation		
	v_c [Å/ps]	v_c [c_t]	$\frac{dv}{d\tau}$ [Å/(ps MPa)]	v_c [Å/ps]	v_c [c_t]	$\frac{dv}{d\tau}$ [Å/(ps MPa)]
Al _I	20 - 22	0.65	0.002	14 - 15	0.44	0.008
Al _{II}	18 - 20	0.6	0.005	14 - 15	0.47	0.008
Ni _I	17 - 19	0.76	0.003	15 - 16	0.66	0.005
Ni _{II}	15 - 17	0.71	0.002	13 - 15	0.62	0.003
Cu	14 - 15	0.89	0.001	13 - 14	0.83	0.002

Tab. 5.1: Characteristics of the high-velocity regime in the different potentials. The crossover velocity v_c approximately determines the onset of the high-velocity regime. The stress dependence of the dislocation velocity at 30 K, $\frac{dv}{d\tau}$, is approximated by the slope of a linear fit.

dislocations in Al_I (open symbols in Fig. 5.10). Significant differences can only be seen in the low velocity regime at 30 K where the "short" dislocation is about $\Delta v = 0.7\text{Å}/\text{ps}$ faster than the dislocations with $L_y \geq 4$ nm. At 100 K the difference in velocity for the low velocity dislocations is only $\Delta v = 0.15\text{Å}/\text{ps}$. Simulations in the high velocity regime or at higher temperatures showed no differences between the dislocations of different lengths.

In some cases transonic dislocation velocities or the disintegration of the dislocation at very high stresses was observed. For example, the edge dislocation in Al_I at 30 K became transonic at $\tau = 1.2$ GPa and moved for about 150 ps with $v = 53\text{Å}/\text{ps} = 1.65c_t$ (see also Fig. 5.16). Transonic dislocation motion was also seen at 300 K in Cu (edge dislocation with $v = 1.51c_t$ at $\tau = 1$ GPa). Dislocation instability and multiplication was for example observed for the screw dislocation in Al_I at 30 K and $\tau = 1.5$ GPa. These special cases will not be addressed further, since the simulation set-up is not fully adequate for a detailed study of dislocations under extreme loading conditions.^b

^bOne problem is that the energy input by the work done by the force boundary conditions can lead to a melting of the boundary layers. Other problems can arise by the reflection of sound waves emitted by trans- or supersonic dislocations and due to too weak thermostat coupling. Displacement boundary conditions together with damping layers would be better suited for these simulations.

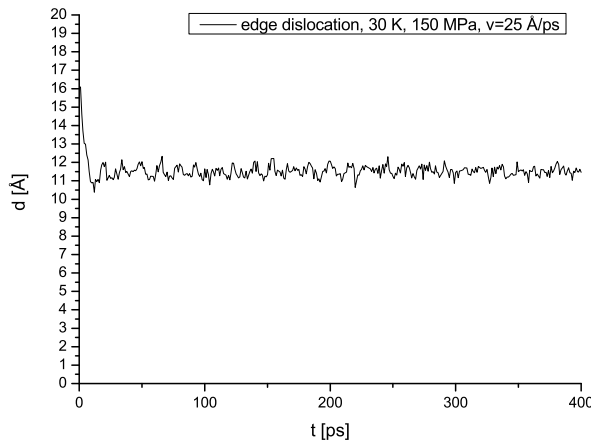


Figure 5.13: Dissociation distance d of an edge dislocation in Al_I as function of time.

The low velocity regime will be analyzed in more detail in section 7.2.2. Here the focus is on the high velocity regime where further information on the moving dislocation can be obtained by inspection of the dislocation core. For the sake of clarity and space only exemplary figures are presented. The qualitative behavior of the dislocations is similar for all cases.

Figure 5.13 shows the typical course of the distance d between the partial dislocation for a dislocation moving at high velocity. After a short time during which the dissociation distance continuously decreases, d fluctuates around a new, velocity and temperature dependent, dynamic equilibrium distance $d(v)$. This dynamic dissociation distance is shown as function of the dislocation velocity in Fig. 5.14. It can be seen that the temperature dependence of d is mainly due to the difference in the equilibrium distance at $v = 0$. For low dislocation velocities $v \lesssim c_t/2$ the partial dislocation distance is nearly velocity independent. At higher dislocation velocities a significant decrease of d with increasing v can be seen. Edge dislocations show typically a stronger decrease of d with v over a smaller velocity range than screw dislocations. A leveling off of d to nearly constant values can be seen in some cases at velocities close to c_t .^c The edge dislocation in Cu showed however nearly no decrease of d . A comparison of Fig. 5.14 with Tab. 5.1 furthermore shows that the velocity at which the partial dislocation cores would start to overlap, $d \approx w$ (see Tab. 4.1) is approximately correlated with the crossover velocity v_c of screw dislocations. For edge dislocations, this velocity gives a good indication of the velocity range in which the velocity changes only marginally with τ ("plateau velocity"). The velocity dependence of d will be discussed in detail in sec. 7.2.3.

Further analysis of the core structure showed in some cases changes of the dislocation core for very fast and close partial dislocations. As an example the edge dislocation at 30 K in Ni_{II} is shown in Fig. 5.15. The structure in the coordination number representation in Fig. 5.15a can be directly compared to that of the same dislocation at rest, Fig. 4.1a. In general, the potential energy of the atoms in the partial dislocation cores increases at

^cFor very small $d \lesssim 3b$ an accurate automatic determination of d is however not always possible, the error margin in is therefore larger for small d . A further problem for the determination of d arises by the change of the core structure.

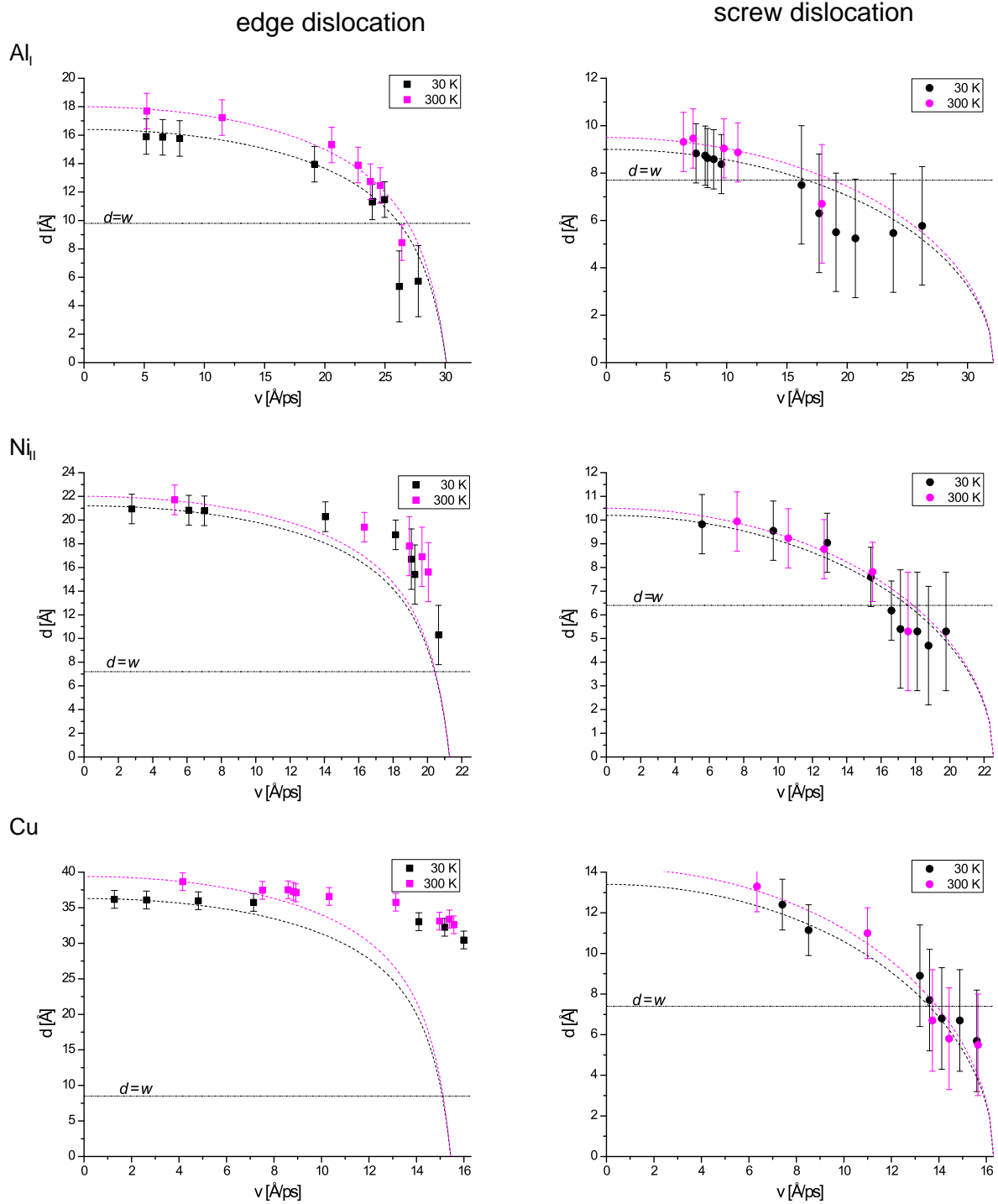


Figure 5.14: Dissociation distance d versus dislocation velocity for edge and screw dislocations. The dashed curves correspond to a isotropic model for the relativistic contraction of d . The horizontal line indicates the width w at $v = 0$ of a partial dislocation. See text and sec. 7.2.3 for details.

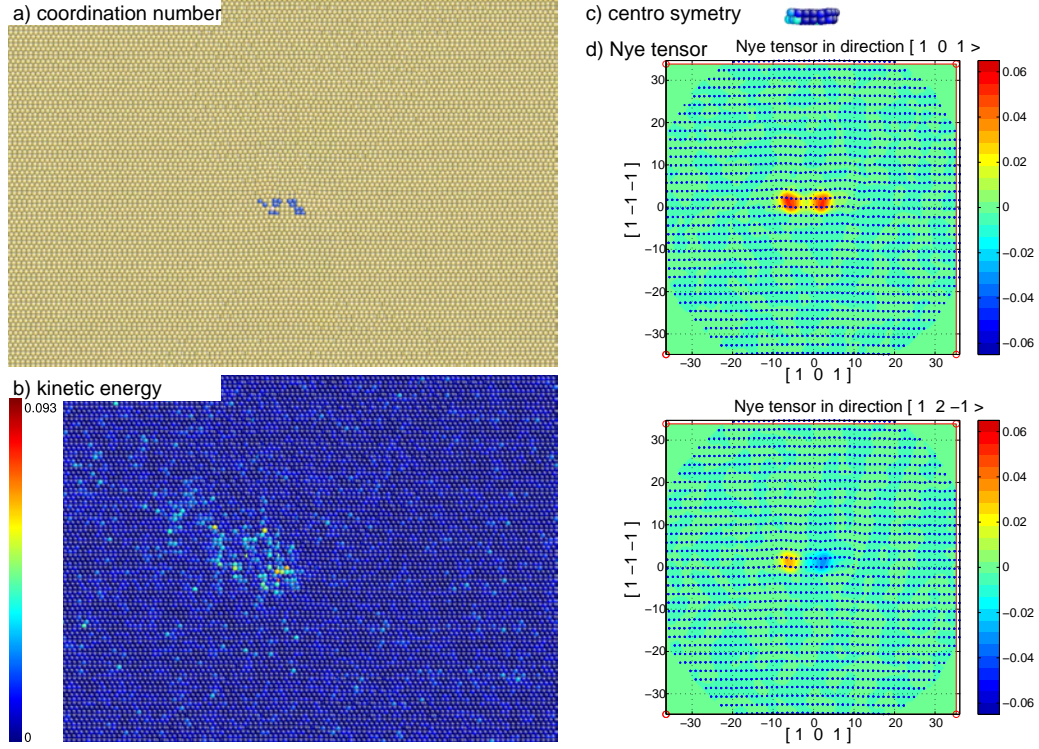


Figure 5.15: Kinetic energy (b) and core structure of a edge dislocation in NiII moving with $v = 20.65$ Å/ps from left to right ($\tau = 900$ MPa, 30 K).

lower separations. The potential energy of the atoms surrounding the dislocation cores is also increased compared to the dislocation at rest or at low velocities. In the coordination number representation of high velocity dislocations the configuration can show features which suggest an out of the plane spreading of the dislocation core, see Fig. 5.15a. However, careful analysis of the stacking fault (e.g. Fig. 5.15c) and the Nye tensor distribution (Fig. 5.15d) revealed no out of plane components of the Burgers vector distribution.

In addition to the core structure the kinetic energy around the region of fast moving dislocations is shown in the Figures 5.15 to 5.17. The special case of a transonic dislocation ($c_{t1} < v < c_{t2}$) is shown in Fig. 5.16a. Two Mach cones formed by transverse acoustic waves are clearly visible. The apex angle 2α of the Mach cone is related to the dislocation velocity v and the appropriate sound velocity c by [233]

$$\sin \alpha = \frac{c}{v} . \quad (5.1)$$

With $v = 5.3$ Å/ps, the measured angles $\alpha_1 \approx 36^\circ$ and $\alpha_2 \approx 42^\circ$ allow to determine the velocity of the two transverse acoustic waves in Fig. 5.16a to $c_{t1} \approx 35.5$ Å/ps and $c_{t2} \approx 31.2$ Å/ps, which compares well with the values according to the potential $c_{t1} = 36.78$ Å/ps and $c_{t2} = 32.15$ Å/ps (see Eq. 2.41 and Tab. A.1). This case illustrates how kinetic energy is radiated away from the moving dislocation. The propagation of kinetic energy away from the moving dislocation core can however also be seen for a fast moving *subsonic* edge and screw dislocations, Fig. 5.16b,c. The radiation is however not symmetric, and at approximately the

Dislocation	c_{w_1} [Å/ps]	c_{w_2} [Å/ps]	c_{p_1} [Å/ps]	c_{p_2} [Å/ps]
edge dislocation, Al _I	26	23	23.4	19.6
screw dislocation, Al _I	26	23	23.4	19.6
edge dislocation, Al _{II}	24	21	24.2	20.1
screw dislocation, Al _{II}	20	13	24.2	20.1
edge dislocation, Ni _{II}	14		23.9	17.4
screw dislocation, Ni _{II}	11		23.9	17.4

Tab. 5.2: Velocities c_w according to Eq. 5.1 of the waves exited by the fastest subsonic dislocations in different potentials. In addition the slowest phase velocities c_p of transverse phonons are given.

same velocity the screw dislocations shows less radiation than the edge dislocation. From the measured angles and the dislocation velocities, the velocity c_w of the emitted waves can be determined with Eq. 5.1. These velocities are summarized for the different dislocations in Tab. 5.2. They were determined from the fastest subsonic dislocations at 30 K, see Figs. 5.10 and 5.11. The determination of the angle α is not very accurate, therefore the values in Tab. 5.2 are only approximative. Indications of radiation of acoustic waves, however much weaker, were also found at lower velocities.

The edge dislocation in Cu, however, seems to be a special case. Although the dislocation in Fig. 5.17 moves at $v = 0.99c_R$, no indication of radiation could be detected. The atoms around the dislocation cores have high velocities. However, this excitation seems not to propagate as a wave away from the moving dislocation, but to move with the dislocation.

To analyze how the motion of the dislocation is connected to the generation of acoustic waves, the velocities of the atoms around the dislocations are shown in Fig. 5.18a-c. It can be clearly seen that the kinetic energy shown in Fig. 5.16b is mainly due to the motion of atoms in the y and z -directions. Fig. 5.18d shows the x and y -position of an atom directly above the glide plane during the passage of the edge dislocation. At $v = 27.8 \text{ \AA/ps}$ the entire dislocation, which has a width of about 12 \AA , passes the atom within about 0.4 ps. Whereas the x -position of the atom increases continuously according to the Burgers vector of the full dislocation, the atom is rapidly deflected in the y -direction according to the Burgers vector of the partial dislocations (the same holds true for the atoms below the glide plane). The period corresponds to a vibration frequency $\nu \approx 2.5 \text{ THz}$.

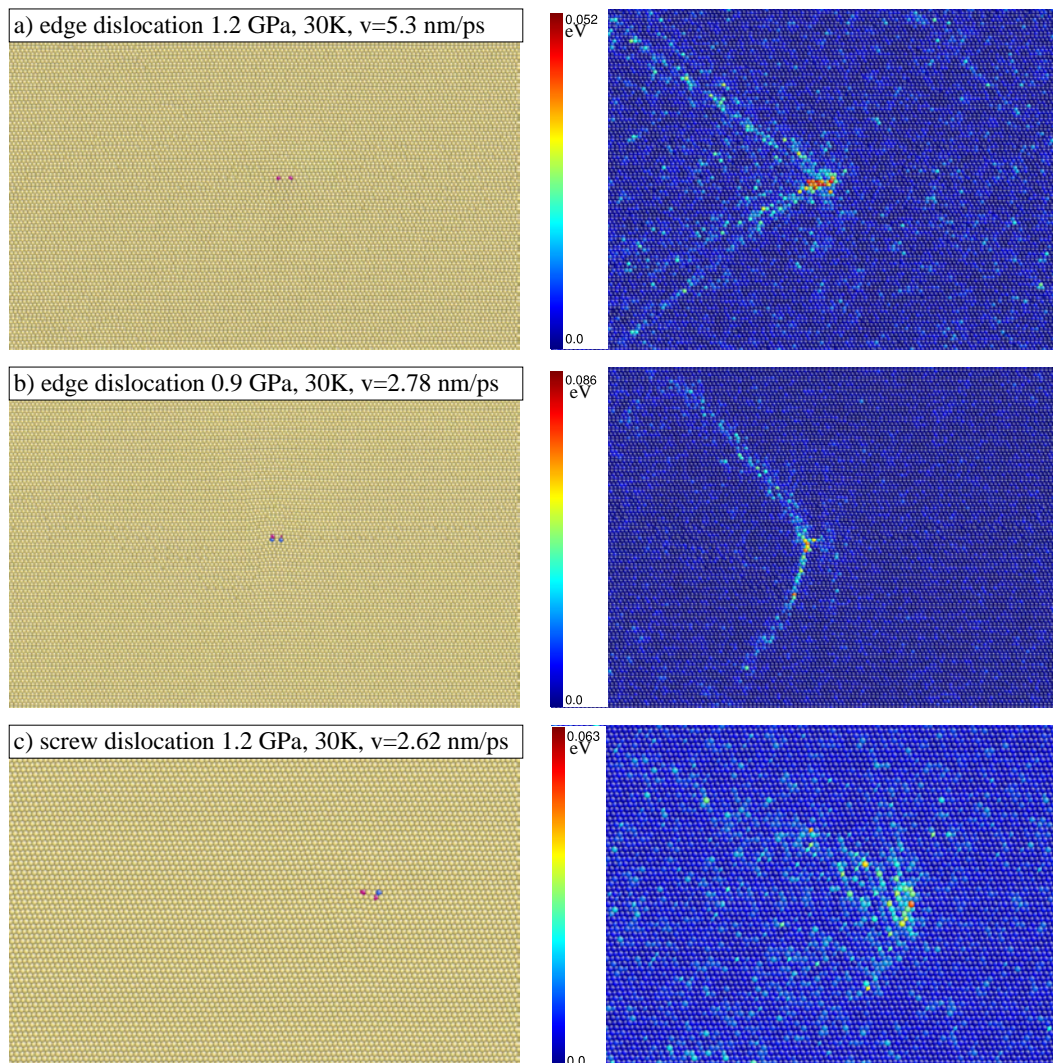


Figure 5.16: Structure (colored by coordination number, left) and kinetic energy (right) of fast transonic (a) and subsonic (b,c) dislocations in Al_I .

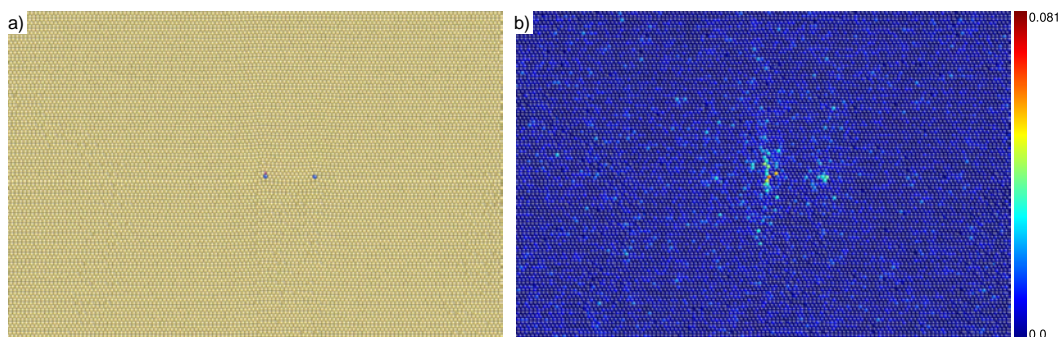


Figure 5.17: Core structure (a) and kinetic energy of a a edge dislocation in Cu moving with $v = 15.99$ $\text{\AA}/\text{ps}$ at $\tau = 900$ MPa and 30 K.

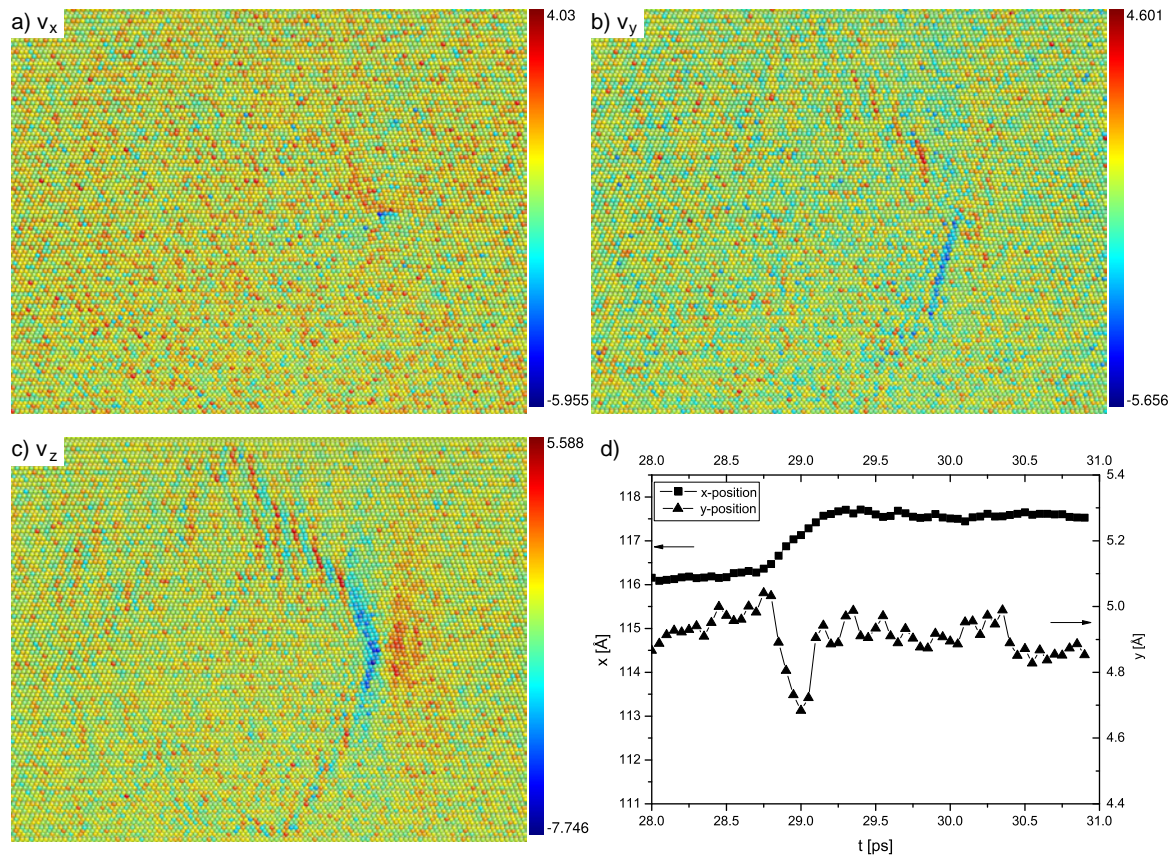


Figure 5.18: Velocity field around the fast moving edge dislocation in AlI (1.2 GPa, 30K, $v = 27.8$ Å/ps). a-c: atomic velocity in x, y and z -direction in units of Å/ps. d) shows the position of an atom above the glide plane during the passage of the edge dislocation: left axis: x -position, right axis: y -position.

Chapter 6

Dislocation - obstacle interaction

The interaction between dislocations and short range, localized obstacles was studied using nanovoids as model obstacles. Spherical voids are well defined and easily created in atomistic simulations. Compared to other typical localized obstacles like precipitates or stacking fault tetrahedra atomistic mechanisms are less important for the dislocation - void interaction. Elasticity theory of dislocations can thus be used to describe the dislocation - void interaction on the continuum scale [234]. Within the multi-scale modeling approach atomistic simulations of the interaction between dislocations and voids can be used to calibrate and validate higher scale models [5, 114]. Voids are furthermore ubiquitous in irradiated materials^a and therefore play an important role in irradiation hardening.

The interaction of edge dislocations with voids of different sizes was studied using the same set-up as for the study of the dynamics of dislocations in the previous chapter. The static depinning as well as the dynamic dislocation - void interaction at different temperatures was studied using two different Ni potentials and a regular array of voids with radii $R_{\text{void}} = 1b, 2b, 4b, 6b$ spaced by $L \approx 13$ and $L \approx 27$ nm. The box height was $L_z = 22$ nm. Additional simulations were performed on edge dislocations in Al_I and on screw dislocations in Ni_{II} . The present study is one of the most extensive surveys on dislocation - void interaction in fcc metals. It complements the recent detailed studies of Osetsky and Bacon [114, 115, 236] who applied loading at a constant strain rate. The use of constant stresses – necessary to study dynamic effects in dislocation - obstacle interaction – requires, however, to perform many simulations to bracket the critical depinning stresses. With typically about 2.4 million atoms per simulation this procedure requires significant computing resources.

The main emphasis of this study is on the exploration of general dynamic effects in the interaction of dislocations with obstacles. The void is thereby used as a model obstacle. Obstacle aspects specific to voids, like void degeneration by multiple shearing or the influence of the glide plane distance from the center of the void [116], were therefore not studied.

6.1 Void properties

The center of the voids was placed in the middle between two nearest neighbor atoms above and below the glide plane. The atomic configurations which were removed from the sample to form the void are shown in Fig. 6.1a. In this figure the energy of the voids defined by the energy

^aThe type of defects created upon irradiation depend on the material and irradiation conditions. Strong void formation is reported e.g. for copper under neutron irradiation at temperatures above 500 K [235].

difference between the perfect (relaxed) slab and the energy of the relaxed box containing the void, corrected for the different number of atoms, is shown for the two potentials. As a reference the surface energy of the void is calculated using the (111) surface energy $\gamma_{(111)}$ times the surface area of the void. Fig. 6.1b shows the increase in potential energy when the upper and lower halves of the voids are displaced relative to each other according to the passage of a dislocation.

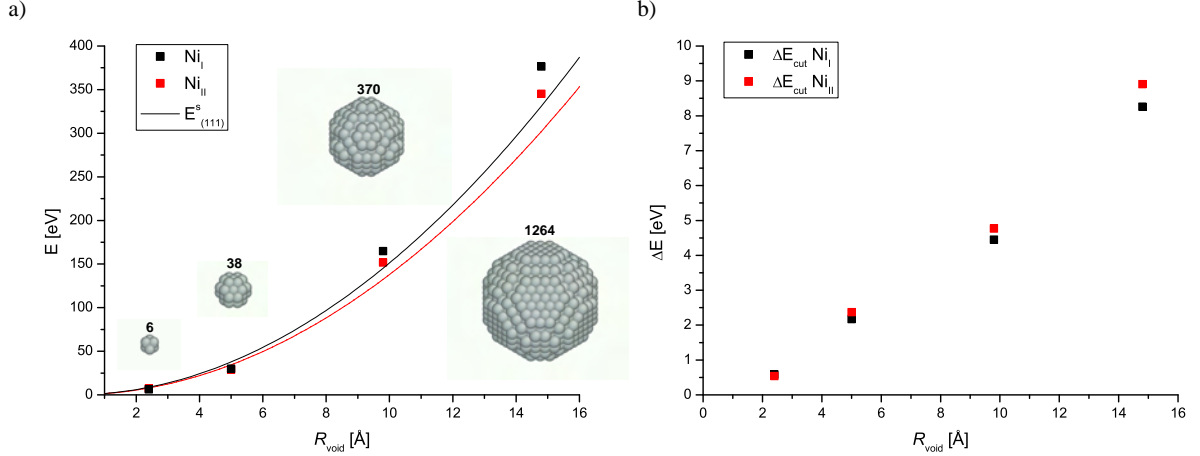


Figure 6.1: (a) The energy of voids as function of their radius R_{void} as determined by static relaxation using two nickel potentials. In addition the surface energy calculated by $E_{(111)}^s = 4\pi R_{\text{void}}^2 \gamma_{(111)}$ is plotted. (b) Excess energy of the surface step created by the passage of a dislocation through the center of the void.

6.2 Dislocation pinning by voids

The starting configurations for the determination of the static depinning stress of a dislocation from an array of voids were created by placing a dislocation close to the void array and minimizing the energy without applied stress. During the relaxation process the dislocation finds its minimum energy configuration where line energy is reduced by the annihilation of a part of the dislocation line at the void. The so obtained configuration was then deformed according to some initial stress and relaxed under constant force boundary conditions. The process is identical to the one used to determine the Peierls stress, see sec. 3.2.1.

The bracketing values for the critical stress for dislocation depinning are shown in Fig. 6.2 and are also summarized in the tables 6.1 and 6.2. The relaxed configurations at sub-critical stress $\tau < \tau_c$ are shown in Figs. 6.3 and 6.4. Fig. 6.2 shows the increase of the critical stress with increasing void size. For the two simulated void separations L , τ_c shows a decrease which is approximately proportional to $1/L$. The two Ni potentials show, however, significantly different critical stresses to depin from the voids. With the exception of the smallest void, the critical stress is larger in the Ni_{II} than in the Ni_I potential, the difference range from about 20% ($R_{\text{void}} = 6b$) to about 60% ($R_{\text{void}} = 4b$). The Ni_I potential has furthermore the same τ_c for voids of radius $R_{\text{void}} = 1b$ and $R_{\text{void}} = 2b$.

The dislocations at sub-critical load show three different configurations: for the smallest

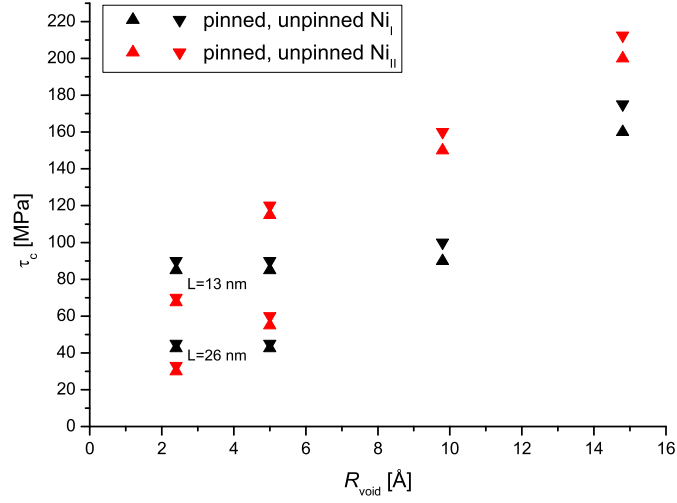


Figure 6.2: Depinning stress as determined from static simulations with edge dislocations using two potentials for nickel as function of void radius. The small voids interacted with dislocations of length $L \approx 14$ nm (higher τ_c) and $L \approx 28$ nm, the larger voids were only simulated with $L \approx 28$ nm.

void the dislocation was pinned with its leading partial dislocation (Fig. 6.3a), whereas the dislocation was pinned by its trailing partial dislocation at the next larger void (Fig. 6.3b). For voids larger than $R_{\text{void}} \geq 4b$ both partial dislocations were simultaneously pinned (Fig. 6.4) and depinned together from the voids. For the dislocation in the Ni_{II} potential the void diameter of $8b$ is equal to the partial dislocation separation (see Tab. 4.1). The dislocation in the Ni_I potential has a larger splitting distance, however the presence of the void lead to a constriction of the dislocation.

The sub-critical configurations in Figs. 6.3 and 6.4 show also other interesting details. The shape of the partial dislocation is not symmetric at the void. As consequence the angle Φ (see Fig. 2.1) is not identical on both sides of the void. The reason for this asymmetry is seen in the orientation dependence of the dislocation line energy. Partial dislocations with local screw orientations have locally a lower line energy. Reorientation of these segments is therefore energetically unfavorable. Local reorientation of segments can also lead to $\Phi \approx 0^\circ$ directly at the void, see Fig. 6.4b). Due to these effects, the geometrical determination of Φ_c is to a certain degree arbitrary (i.e. the choice of the tangent line determining Φ is not unique).

With respect to the smallest void it has to be recalled that it consist just of 6 vacancies. It therefore is better described as a small vacancy cluster. Both the energy in the perfect and in the sheared case in this cluster are higher in Ni_{II} than in Ni_I – in contrast to all other voids. The pinning of the leading partial dislocation instead of the partial dislocation in this case is probably due to a significant reduction of obstacle strength after the shearing of the cluster by one partial Burgers vector. The second partial dislocation thus is subjected to a lower pinning force which is overcome by the acting stress.

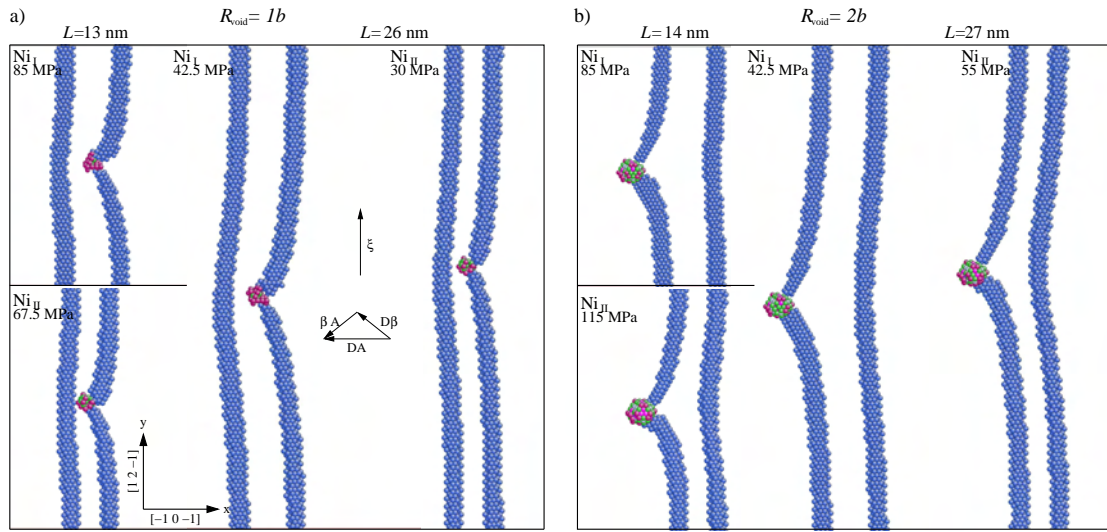


Figure 6.3: Relaxed configurations at sub-critical load for small voids in the two Ni potentials. The line direction of the dislocation and the orientation of the two partial dislocation of the dislocation $\mathbf{b} = DA$ is also indicated.

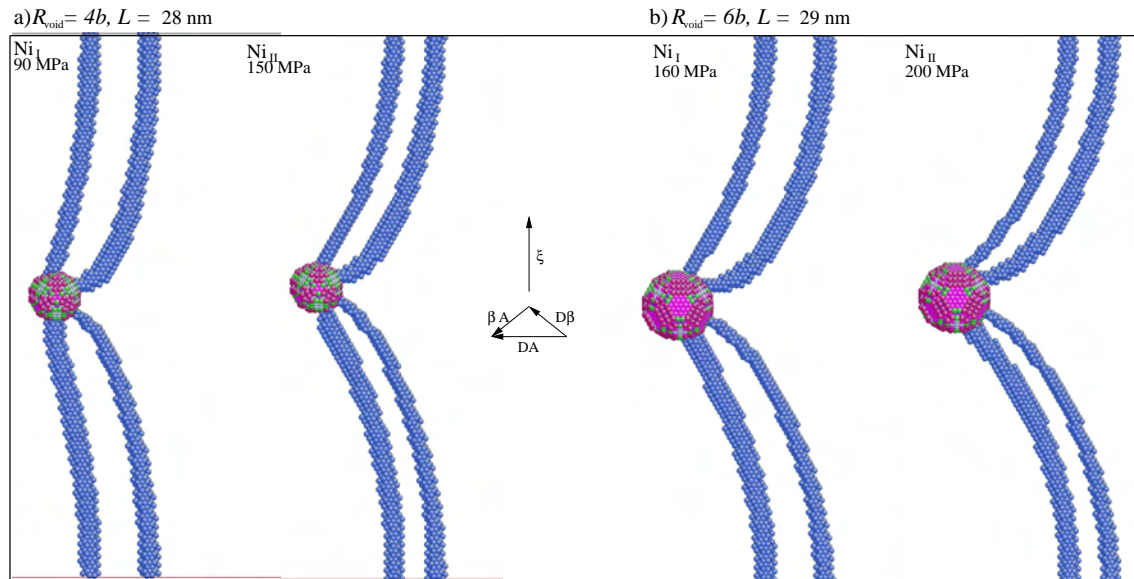


Figure 6.4: Same as Fig. 6.3 for large voids in the two Ni potentials.

6.3 Dynamics of dislocation - void interaction

To study the dynamics of the interaction of a moving dislocation with a void the dislocation is initially positioned $l \approx 30 \text{ nm}$ in front of the array of voids and relaxed. The entire system is then expanded according to the thermal expansion of the potential and equilibrated at the chosen temperature. The sample is then homogeneously deformed according to the applied shear stress. Force boundary conditions are used to keep this stress. The procedure is identical

to the one for the study of the accelerating dislocations, see section 3.2.1 and chapter 5. To determine the critical stress τ_d at which the dislocation passes the void, several simulations had to be performed to bracket τ_d .

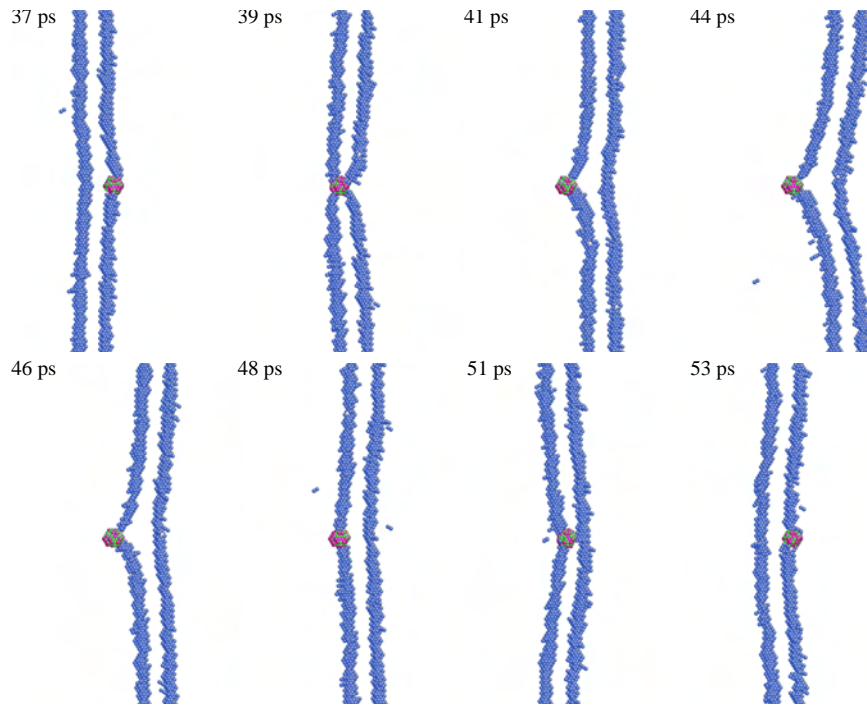
The simulation at constant stress mimics the situation in which a dislocation breaks free from an obstacle, accelerates and encounters an other obstacle. It can thus be compared to the situation for the determination of the lower critical resolved shear stress (CRSS) $\tau_{d,l}$ of the model of Schwarz and Labusch [73], but here for a regular array of obstacles (see sec. 2.1.3.5). Usually simulations of dislocation - defect interactions are performed at constant loading rates $\dot{\epsilon}$ (typically $\dot{\epsilon} \approx 10^7 \text{ s}^{-1}$) [113–117]. In these simulations the dislocation starts in the vicinity of the void and is therefore trapped already at low stresses. The critical stress in this situation corresponds therefore to the stress necessary to depin a pinned dislocation. It can not be compared with the upper CRSS $\tau_{d,c}$ of Schwarz and Labusch. Their definition $\tau_{d,c}$ accounts for dynamic effects after the first depinning event from a random array of obstacles [9, 73]. In a regular array such dynamic effects like dynamical unzipping which lower the the CRSS compared to overdamped simulations can not be detected. Contrary to the present simulations, MD simulations at constant $\dot{\epsilon}$ are not suited to study dynamical effects in dislocation-obstacle interactions.

Figures 6.5 to 6.7 show typical sequences of the interaction between moving dislocations and an array of voids. At sub-critical stresses $\tau < \tau_d$ the dislocation moves towards the voids, is attracted to the voids and gets pinned, see Figs. 6.5a, 6.6a, and 6.7. The part of the dislocation which is not directly interacting with the void, however, keeps moving. It is interesting to note that these parts of the dislocation propagate for a certain time as a nearly straight line (see e.g. Fig. 6.6a at 40 ps, or Fig. 6.7 from 32 to 36 ps). The arms of the dislocation then bow out to a maximum amplitude, swing back and oscillate.

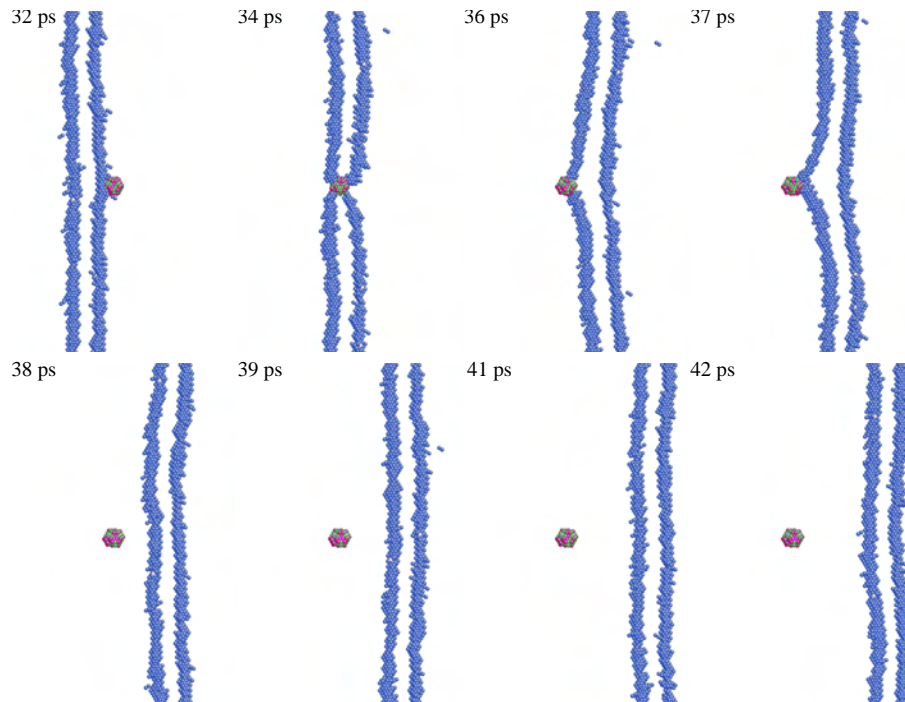
At low applied stress, the small voids are cut by the leading partial dislocation but the trailing partial dislocation remains pinned. During the swing back of the dislocation the trailing partial dislocation can unpin and the leading partial gets pinned again, see Fig. 6.5a. During the simulation of large voids the leading partial dislocation also frequently unpins during the bow-out, but subsequently gets pinned again after the maximum bow-out, see Fig. 6.6a. At stresses close to the dynamical depinning stress $\tau \lesssim \tau_d$, temporary depinning of the entire dislocation from large voids was sometimes observed, see Fig. 6.7. These processes at $\tau < \tau_d$ show the importance of the (permanent) detachment of the trailing partial dislocation as the critical step during the depinning of dislocations from voids.

At stresses $\tau > \tau_d$ the dislocation meets the void, bows-out, overshoots the critical configuration (see Fig. 6.3 and Fig. 6.4) and detaches from the void, see Fig. 6.5b and Fig. 6.6b. The velocity of the dislocations is in this cases still large enough to escape from the image forces and the attractive stress field of the void. The dynamic depinning from the void array leads to waves on the dislocation line, see e.g. Fig. 6.6b. Note that the stress for dynamical obstacle passing τ_d is much lower than the stress τ_c for unpinning in the static simulations (Tabs. 6.1 and 6.2).

The above findings point at the importance of the dislocation inertia in dynamical dislocation-obstacle interaction. A different situation was observed during the depinning process of a (initially moving) dislocation from the small vacancy cluster at 500K, see Fig. 6.8. At this high temperature (1/3 of the melting temperature T_m of the potential, see Tab. A.1) thermally activated processes at weak obstacles close to the critical stress can not be neglected



(a) $T = 100$ K, $\tau = 12.5$ MPa, $R_{\text{void}} = 2b$, $L = 27$ nm



(b) $T = 100$ K, $\tau = 15$ MPa, $R_{\text{void}} = 2b$, $L = 27$ nm

Figure 6.5: Snapshots from a dynamic simulation of a moving edge dislocation in Ni_{111} interacting with a void: (a) sub-critical stress $\tau < \tau_d$, the dislocation bows out and swings back; (b) at $\tau > \tau_d$ the dislocation overshoots and dips from the void. Only atoms with coordination number $\neq 12$ are shown.

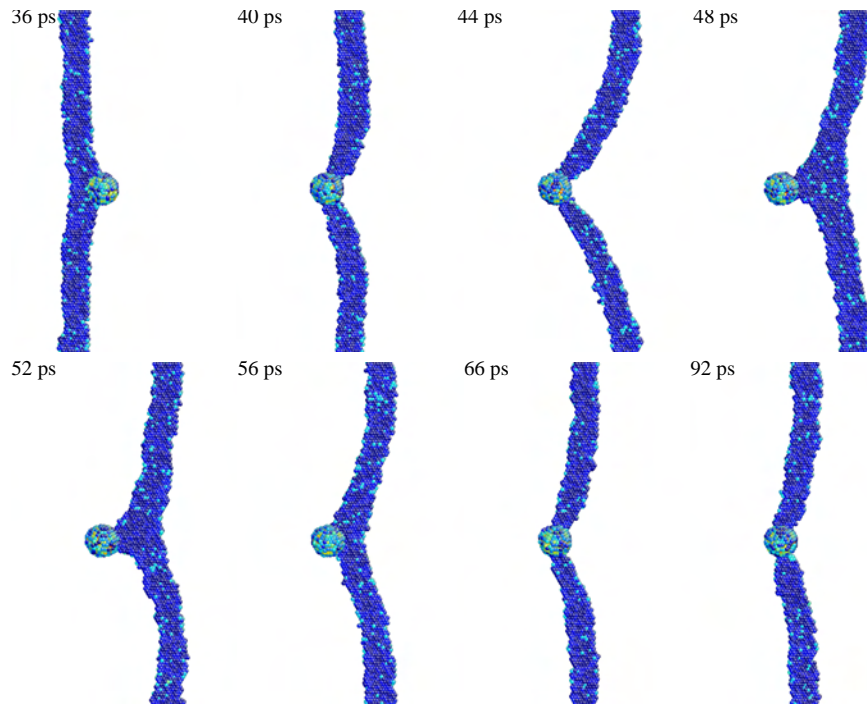
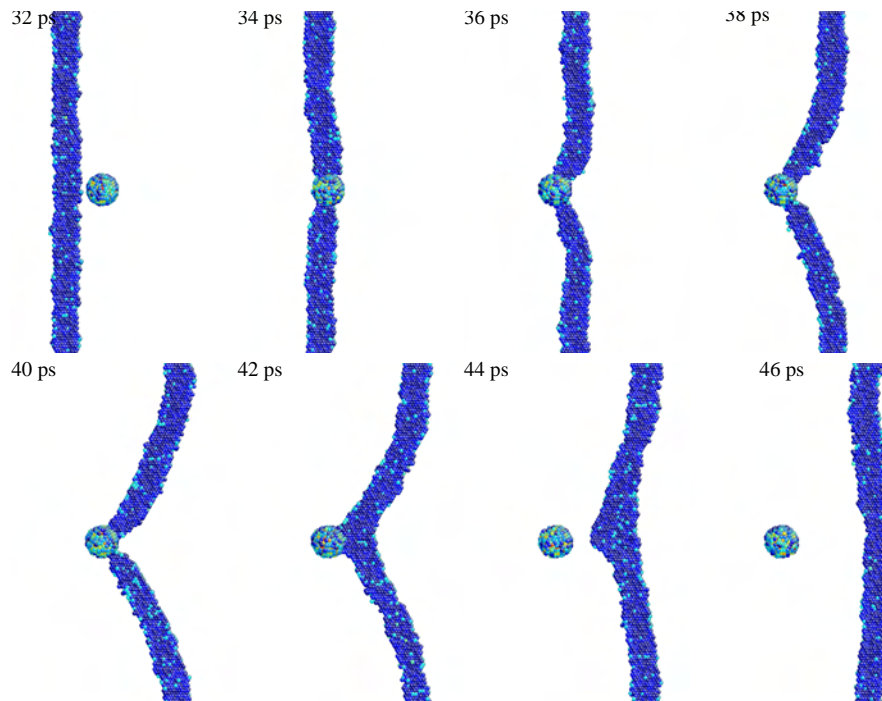
(a) $T = 300$ K, $\tau = 60$ MPa, $R_{\text{void}} = 4b$, $L = 28$ nm(b) $T = 300$ K, $\tau = 67.5$ MPa, $R_{\text{void}} = 4b$, $L = 28$ nm

Figure 6.6: Snapshots from a dynamic simulation of a moving edge dislocation interacting with a void in Ni_{II} at sub-critical (a) and over-critical (b) shear stress. The stacking fault ribbon of the dislocation and the void are identified by the centro-symmetry parameter.

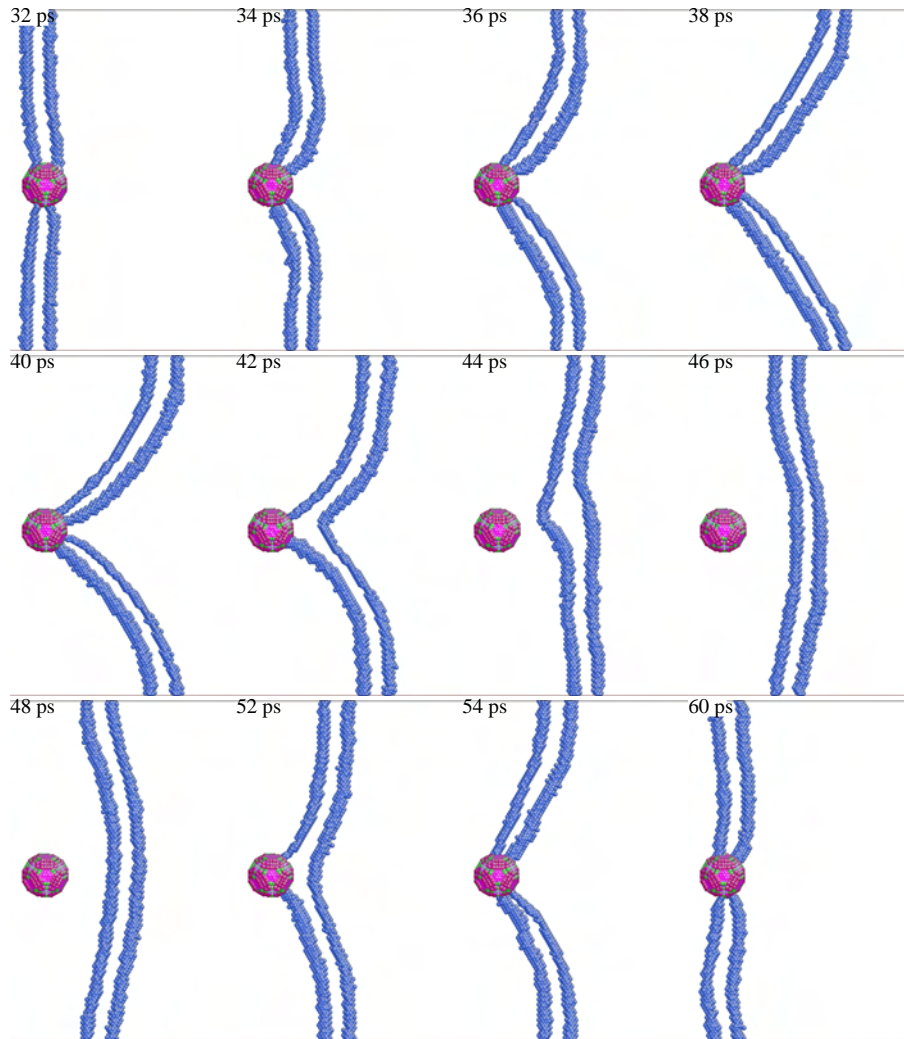


Figure 6.7: Snapshots from a dynamic simulation at 30 K of a moving edge dislocation interacting with a void of radius $R_{\text{void}} = 6b$ at an applied shear stress of $\tau = 40$ MPa. Only atoms with coordination number $\neq 12$ are shown. The dislocation dynamically reaches the critical angle and depins from the void. However, it can not sufficiently accelerate to escape the $1/r$ stress field of the void and the image forces.

any more. The time scale of these mechanisms is however much longer than for dynamical obstacle passing. Due to the well known time scale limitations of MD simulations and their stochastic nature, thermally activated processes are difficult to study quantitatively with the used simulation method. The focus of this study is on dynamical effects during dislocation-obstacle interactions. Therefore simulation runs which showed signs of thermally assisted depinning events were excluded from the study.

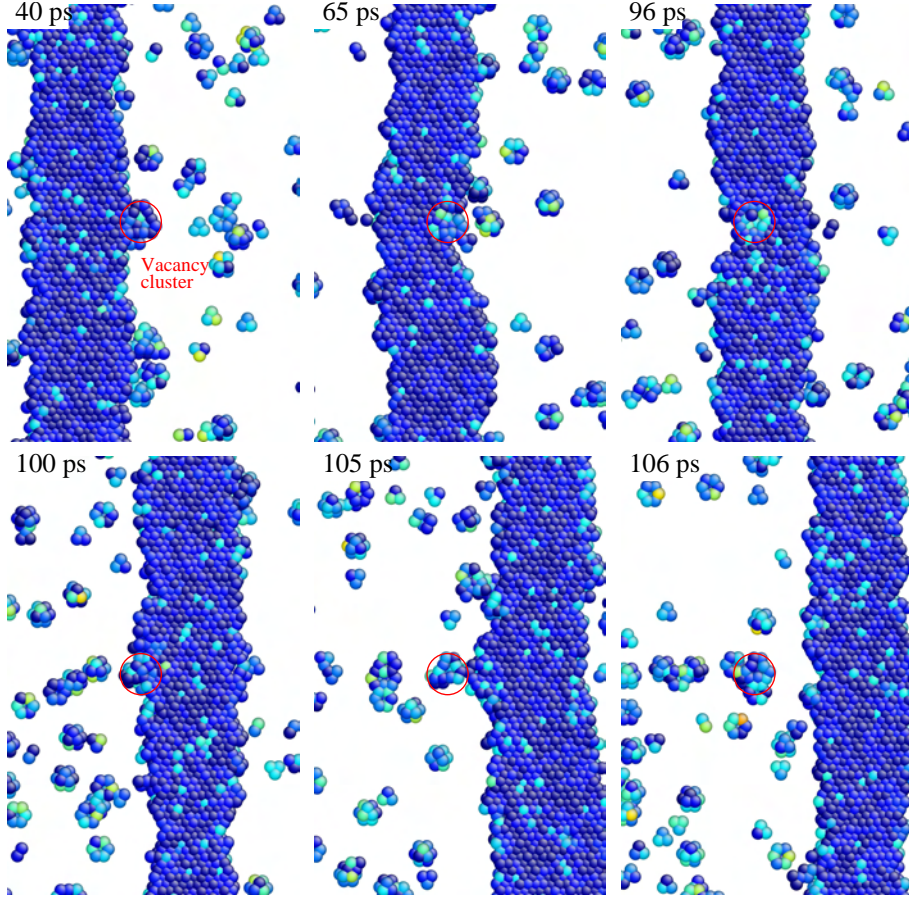


Figure 6.8: Example of thermally assisted dislocation unpinning in the case of a vacancy cluster in Ni_I at 500K and 45 MPa. Please note the timescale involved. The dislocation is identified by the centro-symmetry parameter. Due to thermal fluctuations also atoms not belonging to the dislocation or the void are shown.

The values of the dynamical depinning stress τ_d for the different obstacles, spacings and temperatures are summarized together with the critical stress τ_c determined from the static simulations (see previous section) in Tab. 6.1 for Ni_I and Tab. 6.2 for Ni_{II} .

The ratio τ_d/τ_c of dynamical depinning stress to the critical stress from the static simulations is plotted as function of temperature in figures 6.9 and 6.10. It can be seen that τ_d follows an approximately linear relationship with Temperature. The general slope of for all R_{void} and L is approximately 0.001 K^{-1} . Linear fits (Tab. 6.3) show a dependence of the slope of τ_d/τ_c on void spacing and on the void size. For the systems under study, the critical stress for dynamical obstacle passing at 30 K could be reduced by nearly one order of magnitude compared to the static case. Even at room temperature, dynamic effects lead to a reduction of the critical stress by about 30-50%. The increase of τ_d with temperature clearly shows that thermal effects (like thermally activated events or the decrease of the elastic constants with temperature) are not responsible for the reduction of the depinning stress. Furthermore, dynamic simulations which started with a pinned dislocation (relaxed and equilibrated at $\tau = 0$) showed a much higher depinning stress at the same temperature (values in brackets

R_{void} [b]	L_y [Å]	τ_c [MPa]	T [K]	τ_d [MPa]
1 ^b	150	75 - 80	100	15 - 16
		-	300	30 - 33
1	129	85 - 90		-
1	259	42.5 - 45		-
2	138	85 - 90	30	7.5 - 10
		-	100	15 - 17.5
		-	200	27.5 - 30
		-	300	40 - 45
2	267	42.5 - 45	30	6 - 7.5
		-	100	13 - 14
		-	200	17.5 - 20
		-	300	27.5 - 30
4	276	90 - 100	30	15 - 17.5
		-	100	25 - 30
		-	200	35 - 40
6	289	160 - 175	30	30 - 32.5
		-	100	45 - 50
		-	200	60 - 65
		-	300	80 - 90

Tab. 6.1: Critical stress for a edge dislocation in Ni_I to pass a row of voids with radius R_{void} spaced by L_y : τ_c - static calculation, τ_d - dynamic simulations. See also the plot of τ_c in Fig. 6.2. (^b This first set of simulations was performed with $L_z = 10$ nm and an initial distance from the void of $l = 15$ nm.)

in Tab. 6.2).

Several trends can be derived from Fig. 6.9 and Fig. 6.10: τ_d decreases with increasing L and – except at low temperatures $T \lesssim 100$ K – with increasing R_{void} . The dynamical depinning stress is furthermore generally lower in Ni_{II} than in Ni_I . These trends can be summarized by noting that obstacle configurations with a high static depinning stress τ_c exhibit a low ratio τ_d/τ_c and thus show pronounced dynamic effects.

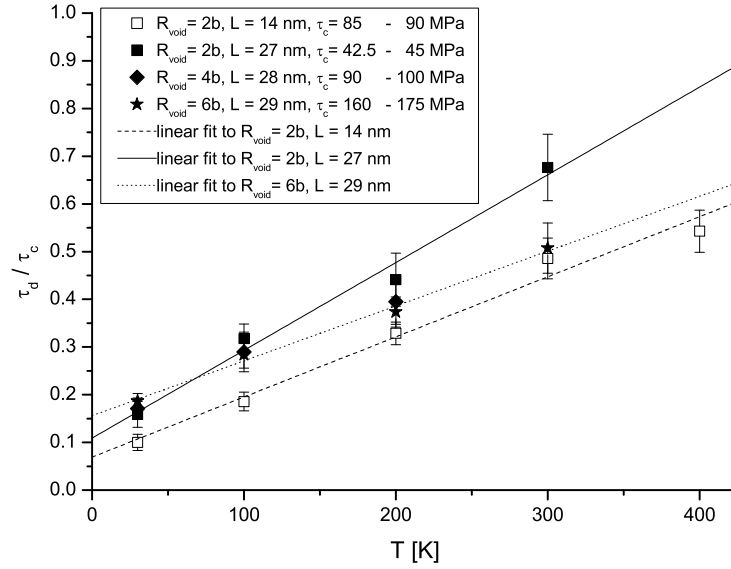


Figure 6.9: The ratio of the dynamic depinning stress τ_d over the static critical stress τ_c as function of temperature for different void arrays as determined from the simulations using the Ni_{II} potential. The slope of the linear fits are summarized in Tab. 6.3.

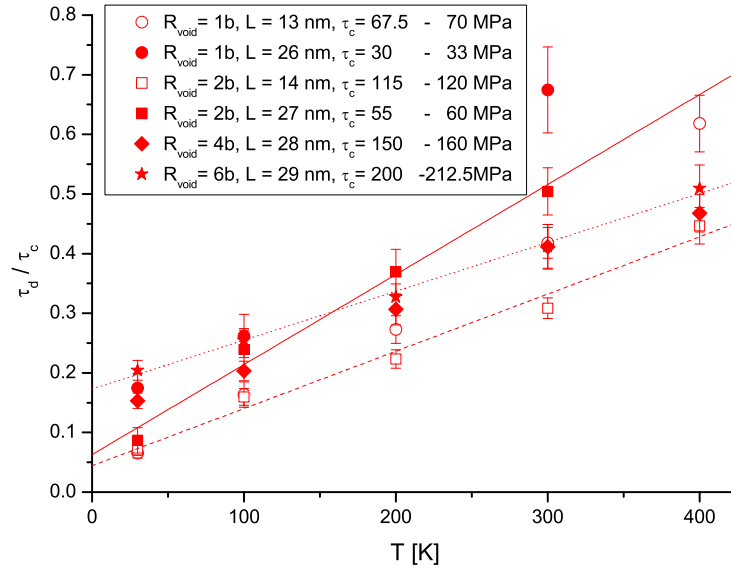


Figure 6.10: Same as Fig. 6.9 for Ni_{II} .

$R_{\text{void}} [b]$	$L_y [\text{Å}]$	$\tau_c [\text{MPa}]$	$T [\text{K}]$	$\tau_d [\text{MPa}]$
1	129	67.5 - 70	30	4 - 5
		-	100	10 - 12.5
		-	200	17.5 - 20
		-	300	27.5 - 30
		-	400	40 - 45
1	259	30 - 33	30	5 - 6
		-	100	7.5 - 9
		-	200	17.5 - 20
		-	300	20 - 22.5
2	138	115 - 120	30	7.5 - 9
		-	100	17.5 - 20
		-	200	25 - 27.5
		-	300	35 - 37.5
		-	400	50 - 55
2	267	55 - 60	30	4 (30) - 6 (30.25)
		-	100	12.5 (32.25) - 15 (35)
		-	200	20 (37.5) - 22.5 (40)
		-	300	28 (40) - 30 (45)
4	276	150 - 160	30	22.5 - 25
		-	100	30 - 33
		-	200	45 - 50
		-	300	60 - 67.5
		-	400	70 - 75
6	289	200 - 212.5	30	40 - 44.25
		-	100	50 - 55
		-	200	65 - 70
		-	300	80 - 90
		-	400	100 - 110

Tab. 6.2: Same as Tab. 6.1 for an edge dislocation in Ni_{II} , compare also to Fig. 6.2. The values in brackets denote the depinning stress from dynamic simulations of a pinned dislocation in subjected to *instantaneous* loading.

Potential	$R_{\text{void}} [b]$	$L_y [\text{Å}]$	$\tau_d/\tau_c/T [K^{-1}]$
Ni_I	2	138	0.0013
Ni_I	2	267	0.0018
Ni_I	4	276	0.0013
Ni_I	6	289	0.0012
Ni_{II}	1	129	0.0015
Ni_{II}	1	259	0.002
Ni_{II}	2	138	0.001
Ni_{II}	2	267	0.0015
Ni_{II}	4	276	0.0009
Ni_{II}	6	289	0.0008

Tab. 6.3: . Slope of τ_d/τ_c as determined from linear fits in Fig. 6.9 and 6.9. The error of the fits is about 5-10%.

Chapter 7

Discussion

7.1 Static dislocation properties

In chapter 4 static calculations with different atomic interaction potentials were used to determine the characteristics of the dislocation core configuration, the line energy and the Peierls stress of edge, screw and mixed dislocations. These properties of static dislocations can be compared to models from dislocation theory and to a wide range of experimental literature.

7.1.1 Dislocation dissociation

The dissociation width of dislocations in fcc metals plays an important role for the Peierls stress and the mobility of dislocations [237,238]. The elastic separation d of partial dislocations is given for the isotropic case by Eq. 2.17 in section 2.1.2.2. In this equation the effect of elastic anisotropy can be approximated by substituting the shear modulus μ with the shear modulus $\mu' = (c_{11} - c_{12} + c_{44})/3$ determined from the transformation of the tensor of elastic constants c_{ij} to the coordinate system of the dislocation.

To treat the elastic properties of dislocation in a fully anisotropic framework the Stroh formalism [239] can be used. Figs. 7.1 - 7.3 show the anisotropic solution for d calculated for different line orientations Θ using the program DISDI [240] which is based on the ANACALC routine designed by Head *et al.* [241]. This solution is compared with the results from the static calculations (see sec. 4.1) and with the solution of Eq. 2.17 for edge and screw dislocations (see appendix A for the material parameters).

In general the partial dislocation separations determined from the atomistic calculations are in good agreement with the selected experimental values.^a But it can not be argued and should not implicate that the agreement with experiment is any better than that of continuum theory. The partial dislocation separation determined from the atomistic simulations d_{sim} is in all cases larger than the analytical solution d_{aniso} , see Figs. 7.1 - 7.3. The deviation $\Delta d = d_{\text{sim}} - d_{\text{aniso}}$ is typically in the range of $1/2 - 2b$, not proportional to d , and larger for screw dislocations than for edge dislocations. For closely spaced partial dislocations like in the case of screw dislocations in Al this deviation can make a difference of up to 100%.

^aAn overview about experimentally determined stacking fault energies and measurements of d can be found in [243].

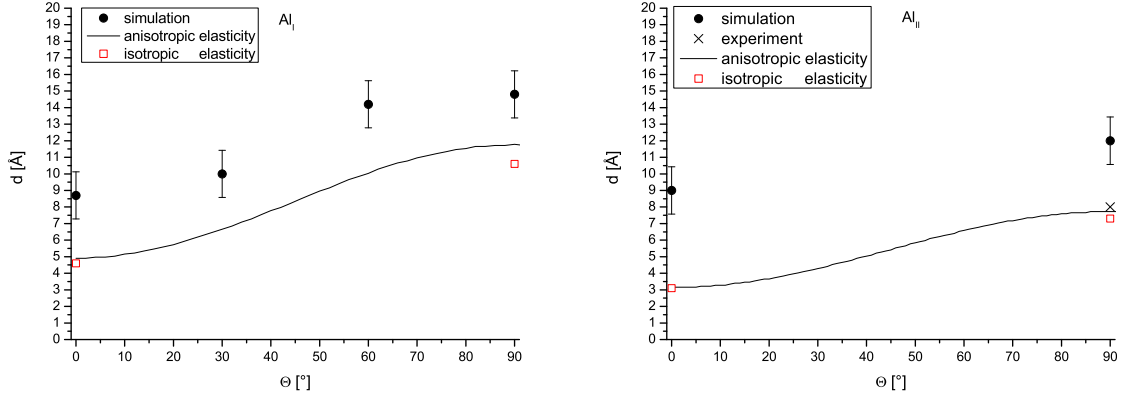


Figure 7.1: Splitting distance d for dislocations with different character as determined from the relaxation using two Al potentials compared to the theoretical predictions using linear elasticity theory. Screw dislocations are characterized by an angle of $\Theta = 0^\circ$ between line direction ξ and Burgers vector \mathbf{b} , edge dislocations have $\Theta = 90^\circ$. See also table 4.1. Experimental data according to [26]

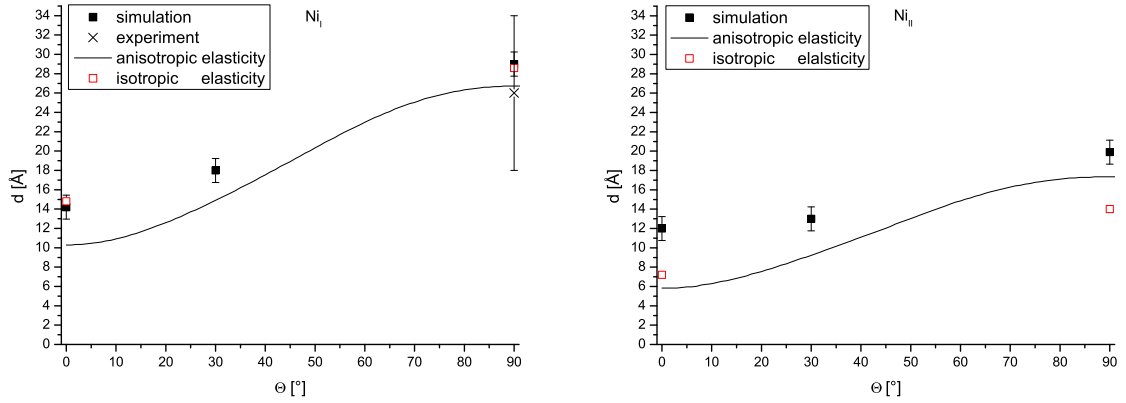


Figure 7.2: Same as Fig. 7.1 for two nickel potentials. Experimental data from [242].

Similar discrepancies between the results from atomistic simulations and analytical calculations using the stacking fault (SF) energy and elastic constants of the potentials were reported in the literature [29, 36, 94, 95, 97, 244] for different simulation set-ups and potentials. In the present study d was independent of the simulation set-up. Furthermore, the value for the edge dislocation in Al_I agrees with the result of Olmsted *et al.* [94], and the splitting distance for screw dislocations in Ni_I is identical to the one recently reported in [97]. In these studies, d was obtained by using boundary conditions and methods for measuring the dislocation position which were different from the present study. Together with the reports in the literature the findings indicate that the differences between anisotropic calculations and simulations might reflect a general aspect of partial dislocation splitting.

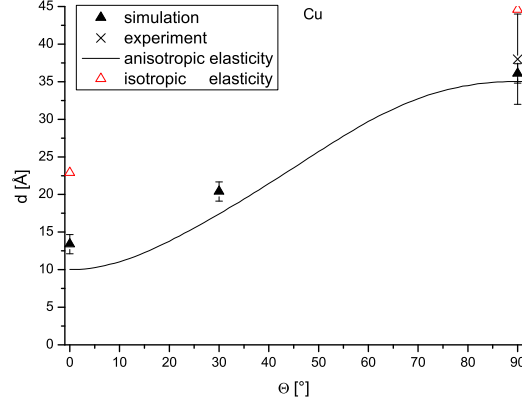


Figure 7.3: Same as Fig. 7.1 for copper. Experimental data according to [36].

According to Eq. 2.17 an increase in d is related to an effective decrease of the stacking fault energy γ_{sf} or to an effective increase of the repulsive stress between the two partial dislocations. At least for the larger splitting distances effects due to nonlinear elasticity should be negligible. Rasmussen *et al.* [36] argued that the in plane-smearing of the partial dislocations effectively reduces the stacking fault width. However, the force on the dislocations due to the stacking fault is independent of its extend, and it is not clear how the spreading of the partial dislocation core into the stacking fault should *decrease* its energy. Duesbery [29] put forward that if the two partial dislocations are close to each other the attractive Burgers vector component (e.g. in case of a edge dislocation the screw components) of the partial dislocations might not fully form, thus leading to a stronger repulsion. However, the Nye tensor analysis in Fig. 4.4 shows that at a splitting distance of $d \approx 5b$ the screw components have already fully formed. This effect should therefore be negligible for wider spaced partial dislocations.

The dissociation of extended dislocations in fcc metals has been extensively studied by Schoeck in the framework of the generalized *two* dimensional Peierls model [24–27, 245]. In this model the atomic misfit energy in the glide plane is calculated using the γ -surface [30], which is approximated by a two dimensional Fourier series. Schoeck’s generic γ -surface is for fcc metals fully characterized by γ_{sf} and the maximum fault energy γ_m . For the atomic displacements across the glide plane a two dimensional ansatz according to the original Peierls-model is chosen. The total (elastic and atomic misfit) energy is then minimized with respect to the dislocation separation d and width ζ .

Using this model it has been shown by Schoeck [25] that the splitting distance not only depends on the SF energy at the local minimum in the ‘stacking fault position’ but also on the structure of the γ -surface. For higher γ_m the generalized two dimensional Peierls model predicts a higher deviation Δd from the anisotropic solution [25], and a larger Δd for screw dislocations than for edge dislocations. These predictions are in qualitative agreement with the results shown in Figs. 7.1 - 7.3: all types of dislocations have a deviation Δd from the anisotropic solution which is larger for Al_{II} ($\gamma_m = 575 \text{ mJ/m}^2$) than for Al_I ($\gamma_m = 555 \text{ mJ/m}^2$). Similarly $\Delta d(\text{Ni}_{II}) > \Delta d(\text{Ni}_I)$ with $\gamma_m(\text{Ni}_{II}) = 1.613 \text{ J/m}^2 > \gamma_m(\text{Ni}_I) = 1 \text{ J/m}^2$.

A direct comparison of the dislocation splitting distance in atomistic simulations with the results of the generalized Peierls model is currently under way [245]. By using an approximation of the γ -surface corresponding to the Ni_I potential, Schoeck calculated the splitting distance for a screw dislocation [245], which is exactly identical to the one observed in the simulations (Tab. 4.1).

This clearly shows that the dislocation dissociation distance is not determined by the elastic constants and γ_{sf} alone. This has important consequences, e.g. for the determination of SF energies from TEM observations of d [25], and for the determination of cross-slip energies.

Assuming that the γ -surface of an EAM potential would perfectly represent the real material, the atomistically determined d would be identical to the splitting distance determined by a 'perfect' experiment. As seen above, this value will however be larger than the splitting distance of Volterra partial dislocations in a continuum d_{aniso} , Eq. 2.18. By using the experimental d in Eq. 2.18 to calculate the stacking fault energy γ_{sf} , the so determined γ_{sf} , are smaller than the real value. Judging e.g. from Fig. 7.1, the differences could be as large as approx. 30%. Experimental scatter can also account for errors of similar magnitude (see e.g. Fig. 7.2), but following the above conclusions, the values for γ_{sf} in the literature (see e.g. [243]) should *generally be too low*. A correction of these values would require accurate information on the 'real' γ -surface.

First-principles stacking fault energies are available for a number of fcc metals, see e.g. [208]. And as expected from the above arguments they tend to overestimate the experimental values [246,247]. It should be noted, however, that all defect energies are usually overestimated by first-principles calculations [247]. Due to the scatter in first-principles data for γ_{sf} and the availability of experimental data for many metals, EAM potentials are traditionally fit to experimental SF energies [247]. The above finding therefore has direct consequences for quantitative comparisons between atomistic simulations and experiment.

In section 4.1 the Peierls-Nabarro model was used to fit the width ζ of the edge and screw components of the two partial dislocations. In the *one* dimensional PN model, the width of one dislocation can be expressed as $\zeta = Kb/4\pi\tau_{\text{max}}$ (Eq. 2.13). The maximum restoring stress τ_{max} is in this case given by the maximal gradient of the γ -surface [248]. For dissociated dislocations in fcc crystals, τ_{max} is the maximal slope of the stacking fault curve in $\langle 112 \rangle$ direction, see Fig. A.1 in Appendix A. Eq. 2.13 has been applied to calculate ζ for partial dislocations. It yielded the same order of magnitude as the partial dislocation width determined from computer simulations [95]. This attempt to calculate the width of one partial dislocation of a dissociated dislocation with a one dimensional PN model seems however questionable: contrary to a perfect dislocation the Peierls relief of a partial dislocation is not symmetric. The solution Eq. 2.13 of the original Peierls-Nabarro model can thus not be directly applied to such a situation.

In general the original Peierls-Nabarro model is not valid for dissociated dislocations, as it assumes slip along one direction only. For partial dislocations, treatment in two dimensions is necessary [23]. Many PN theories like the above mentioned generalized two dimensional Peierls model [24] or the semidiscrete variational PN model [23, 28] have been proposed to study dissociated dislocations in fcc metals. One important insight obtained by the generalized two dimensional Peierls model is that the displacement vectors of mixed dislocations can deviate from the crystallographic Burgers vector, even when it runs along a path of lowest misfit energy [24]. The reason for this is that edge and screw components of the mixed dislocation can adjust independently to the minimum energy configuration, as the elastic

response of the medium is different for the two types of displacements. This statement should be also valid for Shockley partial dislocations.

7.1.2 Peierls stress

The determination of the Peierls stress from model calculations, based on the Peierls-Nabarro model, from experiments, and more recently from atomistic calculations has been the subject of research over half a century [249, 250]. Although the original simple Peierls-Nabarro model has been superseded by more realistic approaches, its qualitative description of the dependence of the Peierls stress on the material properties (Eq. 2.15) are generally recognized to be valid: τ_P is orders of magnitudes smaller than the theoretical shear strength, slip usually takes place on the most widely spaced planes and dislocations with wide, planar cores have lower values for τ_P compared to dislocations with narrow core. For this reason, edge dislocations are generally more mobile than screw dislocations [13].

These qualitative features are also reflected in the results in Tab. 4.4: the Peierls stress of screw dislocations is one order of magnitude higher than for edge dislocations, and between the different fcc metals the Peierls stress decreases with increasing dissociation distance between the partial dislocations. However, large differences in τ_P exist between the different potentials. The Peierls stress depends sensitively on the details of the atomic interactions. Therefore calculations with different potentials – or γ -surfaces in the case of the PN-model – can lead to a wide range of values for τ_P . This is directly reflected in the result of recent calculations of the Peierls stress summarized in Tab. 7.1.

The overall magnitude of the Peierls stresses determined by the atomistic simulations (Tab. 4.4) agrees with the notion of a generally low Peierls stress for face centered cubic metals ($\tau_P \lesssim 10^{-6}\mu'$ to $10^{-5}\mu'$ [13]). For Al_I the values of τ_P are in excellent agreement with the elaborate study on the same potential of Olmsted *et al.* [94]. For Ni_I the values of τ_P agree well with the ones determined by the nudged elastic band method in [97]. The used method therefore seems to provide reliable estimates for τ_P in different potentials. Besides the differences between the used potentials, additional effects due to additional stresses [29, 251], or boundary effects can account for the various values of τ_P . A special case was reported in [99], where two different core structures existed for edge dislocations in Al.

The differences in the γ -surfaces used in the PN-model are the reason for the large variations reported e.g. in [252, 253]. Although the improved Peierls-Nabarro models can directly benefit from accurately determined γ -surfaces from *ab-initio* calculations, it suffers some shortcomings [27, 254]. The problem of using a one dimensional PN model like in [95, 246] has been already addressed in the previous section and is discussed in [23, 27]. The results of such studies can only be considered to be approximate. An important aspect is that in some PN-models the relaxation of the atoms when the dislocation moves across the Peierls energy barrier is not taken into account [254]. I.e. the dislocation displacement profile stays constant during the motion of the dislocation. This can be the cause for the trend in Tab. 7.1 towards higher Peierls stresses in the PN-model compared to the direct atomistic simulations.

When comparing the values for τ_P in Tab. 7.1 with experimental data one has to be aware of a 50-year-old puzzle in materials science: the estimates of τ_P from the Bordoni peak internal friction (IF) measurements or from Harper-Dorn creep show a factor of 100 discrepancy to those obtained from mechanical testing, see [249] and references therein. It has been argued that IF experiments sample the average dislocation population and thus measure the 'true' Peierls stress, whereas low temperature plastic deformation experiments sample only the

	Cu, \perp	Cu, s	Ni, \perp	Ni, s	Al, \perp	Al, s
this study	0.05	6	0.03 - 0.3	5 - 30	5-6	50
direct atomistic simulations	2 [255]	7 [255] 40-270 [29]	1 [95] 0.3 [97]	10 [95] 20 [97]	6 [94] 8 [93] 4-880 [99]	50 [94] 320 [251] 4 [99]
Peierls-Nabarro models		50-350 [252]	5 [95]	8 [95]	7 [246] 11-93 [253]	312-1000 [256] 110-3350 [252]

Tab. 7.1: The Peierls stress of edge (\perp) and screw (s) dislocations in different metals as determined in recent simulations. The Peierls stress is given in units of $10^{-5}\mu$.

weakest areas [250]. The critical resolved shear stress (CRSS) in such weak areas is thought to be caused by internal stresses which modify the partial dislocation separation: when d is an integral multiple na' of the Peierls energy period a' the partial dislocations move in phase and the CRSS represents the Peierls stress. If however $d = (n + 1/2)a'$ the partials are exactly out of phase and the energy of the dislocation remains unchanged under translation. The resulting CRSS should be consequently zero [29, 257, 258]. In his atomistic simulations on screw dislocations in copper Duesbery [29] in fact found a 85% decrease of the Peierls stress depending on the partial dislocation separation.

In the simple version of this model the two partials are rigidly coupled and the Peierls "hills" are symmetric [250, 258]. The effect of the partial dislocation on the downward slope of the Peierls hill pushing the other dislocation uphill should however depend on the shape of the Peierls barrier and on the strength of the interaction between the two partial dislocations. Like the deviation of the displacement vectors of mixed dislocations from the crystallographic Burgers vector and the splitting distance, the cooperative motion and the Peierls stress depend on the details of the *entire* γ -surface. Furthermore, the relaxation of the dislocation core atoms during the motion of the dislocation across the Peierls energy barrier has to be considered. One dimensional models Peierls-Nabarro models like in [248], which rely only on the dislocation width and the fault energy or resistance curves (Fig. A.1), therefore miss features essential for a quantitative determination of τ_P .

As stated in the previous section, atomistic calculations of the Peierls stress with semi-empirical potentials are impaired by the lack of an accurate representation of the γ -surface and the stacking fault energy [27, 245]. Therefore values for the Peierls stress or Peierls energy derived from atomistic simulations can at best be only considered as order of magnitude estimate. However, atomistic simulations in combination with generalized PN-models could provide information on how the shape of the γ -surface influences τ_P e.g. by affecting the cooperative motion of the partial dislocations.

7.1.3 Line energy

In section 4.2 the additional energy due to the presence of a dislocation in the crystal was calculated. The plots of the strain energy per unit length of dislocation as a function of the cylinder radius R (Figs. 4.5 - 4.6) followed the logarithmic relationship predicted by the linear elastic theory for a wide range of R (see also sec. 2.1.1):

$$\frac{E_{\text{el}}}{L} = \frac{Kb^2}{4\pi} \ln \frac{R}{r_0}. \quad (7.1)$$

The fits of straight lines to the linear portion of E_{el} as function of $\ln R$ directly provides the factor $\frac{Kb^2}{4\pi}$ of Eq. 7.1. The values of this factor in Tab. 4.2 are in excellent agreement with the results of anisotropic elastic calculations following [12] using the program DISLOELAST [220], see Tab. 7.2.

Potential	$K_{\text{aniso}}(\perp)$ [GPa]	$K_{\text{aniso}}/K_{\text{fit}}$	r_{dev}^p [b]	$K_{\text{aniso}}(s)$ [GPa]	$K_{\text{aniso}}/K_{\text{fit}}$	r_{dev}^p [b]
Al _I	48.5313	0.9954	2	32.025	1.0006	5
Al _{II}	44.1237	1.0002	3	28.7736	1.0013	5
Ni _I	123.388	1.0003	5	78.6374	1.0024	8
Ni _{II}	121.68	1.0018	3	75.8968	0.9955	5
Cu	73.3253	0.9923	7	40.6169	0.9593	4

Tab. 7.2: Comparison of the anisotropic energy factor K_{fit} for edge (\perp) and screw (s) dislocations determined by atomistic calculations (see Figs. 4.5 - 4.6 and Tab. 4.2) and the result of anisotropic elastic calculations. A rough estimate of the partial dislocation radius r_{dev}^p is also provided.

The energy of a dislocation core is determined by the non-linear interatomic forces between the individual atoms within the core. The local bonding topology is therefore an important quantity and a dislocation could display several metastable core structures. The existence of such different core structures for dislocations in aluminum was recently claimed [99]. The reported core structures, however, were specific to the used potential. In general, experiments are unable to provide precise information on core energies: such data can only be obtained from atomistic simulations [237].

The partitioning of the total (elastic + core) energy is to a large extent arbitrary. Thus the mathematical core radius r_0 is not by itself a physical quantity, but describes only the choice of the partitioning. It is usually set such that the core energy in Eq. 2.1 becomes zero. Its value can then be obtained directly from the intercept of the straight line with the abscissa, see sec. 4.2.

In the literature the radius r_{dev} at which the strain energy deviates from Eq. 7.1 is often identified with the onset of the nonlinear core region and thus identified with the dislocation core radius [13]. For dissociated dislocations, however, the effect of the splitting distance has to be accounted for. A simple way to define the distance r_{dev}^p for onset of nonlinearity for partial dislocations would be $r_{\text{dev}}^p = r_{\text{dev}} - d/2$ (see Tab. 7.2). This value can however be only interpreted as a very rough estimate, as d and r_{dev} each have an error margin of $\pm b$. Furthermore r_{dev}^p does not account for core overlap. The effect of the nonlinear partial dislocation core region on $E_{\text{strain}}(R)$ is furthermore difficult to assess, as the nonlinear regions make up only a certain part of the cylinder volume.

The usual definition of core energy $E_{\text{core}}^{\text{dev}} = E_{\text{strain}}(r_{\text{dev}})$ is also not adequate for dissociated dislocations. It would include not only the core energy of the partial dislocations but also the stacking fault energy, and the linear elastic part of the strain energy between the two partial dislocations. In general, the deviation from *linear* elasticity does not have to correspond to the physical dislocation core, in which elasticity itself no longer provides an adequate description of atomistic topology and bonding.

7.2 Moving dislocations

The motion of dislocations at different temperatures and subjected to varying shear stresses was studied in chapter 5. The dislocation motion is determined by the resolved shear stress acting on the dislocation, its rate of acceleration – the inertia of the dislocation – and the forces opposing the motion of the dislocations. In the following the dislocation inertia and the viscous drag at intermediate stresses will be discussed, and special effects for high-velocity dislocations will be addressed.

As mentioned in chapter 5, molecular dynamics methods are limited to the simulations of small time spans. Therefore dislocation motion dominated by thermal activation, typical for dislocation velocities $\lesssim 10^{-2}c_t$, can not be addressed here. This study focuses on the dislocation motion for $v > 10^{-2}c_t$, sometimes also called the high-velocity region [49], in which the dislocation motion has a viscous character.

7.2.1 Dislocation inertia

Figure 5.9 shows that the time it takes for the dislocation to accelerate at a given temperature clearly depends on the box height L_z . In the setup used here, L_z corresponds to the smallest dimension normal to the dislocation line. The increase of the acceleration period is therefore qualitatively in agreement with the increase of dislocation inertia $m_0^{\perp,s}$ according to continuum theory.

To see whether there is also a quantitative rapport between the acceleration characteristics of the dislocations in the simulations and the theoretical predictions, a method to fit the equation of motion to the dislocation trajectory was developed. It has been shown in sec. 2.1.3.2 that the expressions of Hirth [43] *et al.* and Sakamoto [48] for the dynamic mass of an edge dislocation can be transformed into each other. For practical reasons the definition according to Eq. 2.33 and the following equation of motion for an edge dislocation

$$m_0^{\perp} \cdot \left(\frac{m_1^{\perp}}{m_0^{\perp}} \right) \cdot \frac{\partial}{\partial t} v - F + Bv = 0, \quad (7.2)$$

with m_1^{\perp} defined in Eq. 2.38 are used. For screw dislocations the same equation is used, however, m_1^{\perp} is replaced by m^s from Eq. 2.28, and m_0^{\perp} accordingly with m_0^s .

In the case of an edge dislocation this equation of motion can be solved only numerically. In doing so, the initial conditions $x(t=0) = x_0, v(t=0) = v_0$ as well as $m_0^{\perp,s}, B$ and F can be treated as variable parameters. The solution $x_{\text{fit}}(t)$ of Eq. 7.2 can then be compared to the n discrete points of the dislocation trajectory $x_{\text{MD}}(t)$ obtained from the MD simulations. A minimization algorithm^b can then be used to minimize the difference $\chi = \sum_t \frac{\sqrt{(x_{\text{fit}}(t) - x_{\text{MD}}(t))^2}}{n}$ by varying $x_0, v_0, m_0^{\perp,s}, B$ and F . Physically realistic parameter values for x_0, v_0 and F were enforced by penalty functions.

To get a reasonable estimate of the rest mass m_0 the fits have to be carried out in the low velocity and low damping regime (see Tab. 7.3). The onset of motion from rest ($t \lesssim 2L_z/c_t$) is not considered for the fit, because it might be affected by the starting conditions of the simulations. Due to the periodic boundary conditions the dislocation is interacting with its own radiated phonons. This effect is minimized by only considering the motion during the the

^bNumerical integration and minimization were performed in Mathematica [259], which for numerical minimization uses Brent's principal axis method [260].

first 100-150 ps. The quality of the fit depends on the quality of the trajectory. Typical mean deviations of the fitted solution of Eq. 7.2 from the data points of $x_{\text{MD}}(t)$ were $b/5 \lesssim \chi < b^c$. Examples of the fitted equation of motion to different trajectories in boxes of different heights are shown in Fig. 7.4, the results for $m_0^{\perp,s}$ are summarized in Tab. 7.3.

The ability to fit the dislocation trajectories with Eq. 7.2 shows to a certain extent the validity of the expression for the dynamic mass, Eqs. 2.28 - 2.38. Attempts to fit the trajectory with a constant $m^{\perp,s}$ failed, and applying e.g. the functional form of m^s (Eq. 2.28) to edge dislocations also lead to unacceptable fits. The terms of higher order in γ in Eq. 2.38 make the numerical solution of Eq. 7.2 also sensitive to the correct values of c_t and c_l . Although the numerical method described above leads to good fits, its accuracy does not allow to discern the small difference of the factor $\left(1 + \frac{c_l^4}{c_t^4}\right)$ (Eq. 2.29) between the rest mass of edge and screw dislocations, see Tab. 7.3.

The fits to the dislocation trajectories show a significant deviation ΔF of the force accelerating the dislocation from the applied force, see Tab. 7.3. The differences are rather small, and seem to be correlated with the Peierls stress. It is believed that ΔF is related to “dry radiation friction”, as will be discussed in the next section.

Given the usual time and length scales of MD simulations (ps, Å), the adapted unit of the rest mass per unit length is $\text{pN}\cdot\text{ps}^2/\text{Å}^2 = 10^{-16}\text{Kg/m}$. It can be also expressed in units of mass of the respective atom type per Burgers vector: $m_0(\text{Al}) = 0.51 \text{ atoms}/b$, $m_0(\text{Ni}) = 0.52 \text{ atoms}/b$, $m_0(\text{Cu}) = 0.46 \text{ atoms}/b$ (for the largest box-sizes). These values are in excellent agreement with the notion of a rest mass of about half an atom per Burgers vector [47]. It should however be highlighted, that the inertia of dislocation is *not* caused by the mass of the atoms within the dislocation core, see sec. 2.1.3.2.

With the expression for the rest mass (Eqs. 2.27, 2.29), and an estimate for the outer cut-off radius of $R \approx L_z/2 - 3d_{111}$ one can calculate the appropriate core radius:

$$r_0^m = \exp\left(-\frac{c_l^4 c_t^2 m_0}{(c_l^4 + c_t^4) K}\right) R. \quad (7.3)$$

The values of r_0^m are shown in Tab. 7.3 (the material parameters are taken from Tab. A.1 and Tab. 7.2). In addition to the error in the determination of m_0 the values of r_0^m are subjected to some error caused by the definition of R in the 2D dynamic boundary conditions (which were accounted for by subtracting the 2D dynamic boundary layers from the box height). Within these error margins r_0^m is independent of the simulation box size, indicating that the logarithmic dependence of m_0 of L_z is indeed valid.

Taking into account that the total dislocation strain energy determined from the static simulations in the set-up for dynamic simulations is somewhat higher ($\lesssim 10\%$) than the one from the cylindrical set-up (see sec. 4.2), the appropriate core radius for dislocations without finite size effects should be somewhat (approx. $0.5 - 1b$) larger than the values in Tab. 7.3.

The lower cut-off radius r_0^m determined from the effective rest mass of the dislocations characterizes full dislocations. It can therefore directly be compared with the mathematical core radius r_0 and with the core radius determined from the deviation from linear elasticity r_{dev} from Tab. 4.2. Both r_0 and r_{dev} clearly lie outside the error margin for r_0^m . However,

^cTo examine the robustness of the results from the fitting procedure, the fitting was performed with many different starting points. Furthermore the fitting was repeated on different subsets of the data, and within different parameter subspaces. The error margins in Tab. 7.3 were determined from the range of parameter values found in these different fits.

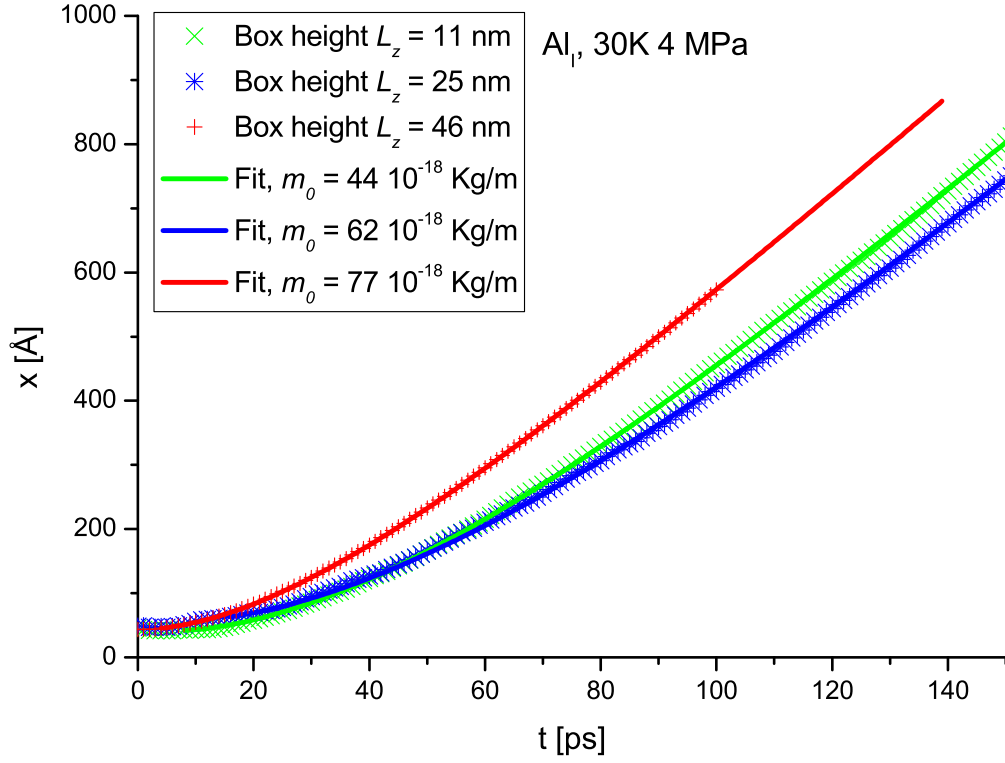


Figure 7.4: Trajectories of edge dislocations in thin films of different heights L_z . The lines correspond to fits of the numerical solution of the equation of motion Eq. 7.2.

for the cases without strong core overlap r_0^m is of the order of magnitude of the partial dislocation width w determined from the FWHM of the energy of the partial dislocation core atoms, Tab. 4.1, and is surprisingly well represented by r_{dev}^p (Tab. 7.2), although this is intended to estimate the radius of one partial dislocation only. It is furthermore interesting to note that within the error margin r_0^m is independent of the potential.

Usually, the total energy E_{total} of a dislocation is seen as the only physically relevant and measurable quantity. The core energy E_{core} and its (mathematical) radius r_0 are in this context "merely parameters in a mathematical partition" of E_{total} [261]. The invariance of E_{total} of a static dislocation is thereby not limited to continuum theory. It can be defined by a thought experiment in which a dislocation dipole is created in an infinite lattice in which atoms near the dislocation cores are allowed to relax [261]. E_{total} then describes the increase in the total atomistic energy due to the presence of a dislocation dipole. The physical core radius r_0^{phys} , defined by the atoms whose local atomic order is drastically different from that of the crystalline lattice, is not addressed in this context.

For a moving dislocation however, the total energy of a dislocation is no more invariant with respect to the partitioning between core energy and strain energy E_{el} . According to the derivation of the dislocation inertia, Eqs. 2.31 - 2.33, only the part of E_{total} which changes

System	m_0 [10^{-18} Kg/m]	r_0^m [b]	$\Delta F/b$ [MPa]
edge dislocation			
Al _I , 4 MPa, (48,19,11)	41 ± 3	2.1 ± 0.5	0.4 ± 0.2
Al _I , 4 MPa, (96,4,25)	62 ± 2	2.1 ± 0.1	0.4 ± 0.1
Al _I , 4 MPa, (48,4,46)	80 ± 5	2 ± 0.3	0.4 ± 0.1
Al _{II} , 4 MPa, (48,4,25)	55 ± 5	1.7 ± 0.5	0.5 ± 0.2
Ni _I , 10 MPa, (42,8,10)	83 ± 5	5.3 ± 0.2	1.6 ± 0.5
Ni _I , 10 MPa, (42,8,22)	155 ± 5	4.9 ± 0.2	2. ± 0.5
Ni _{II} , 10 MPa, (42,4,22)	165 ± 5	4.4 ± 0.4	0.2 ± 0.1
Ni _{II} , 10 MPa, (84,4,40)	205 ± 10	4.8 ± 0.4	0.2 ± 0.1
Cu , 6 MPa, (86,4,41)	190 ± 10	7 ± 1	0.3 ± 0.1
screw dislocation			
Al _I ,12 MPa, (49,5,25)	63 ± 2	1.7 ± 0.1	1.3 ± 0.2
Ni _{II} , 10 MPa, (43,4,22)	160 ± 10	4.5 ± 0.5	1.7 ± 0.1

Tab. 7.3: The dislocation rest mass m_0 and the 'friction force' ΔF as determined by the fits of the numerical solution of the equation of motion 7.2 to the trajectory of dislocations at 30 K (see also Fig. 7.4). From the theoretical expression for m_0 , Eqs. 2.29 and 2.4, and the box height L_z an effective dislocation core radius r_0^m for the mass can be estimated.

with the dislocation velocity contributes to its inertia. According to Eq. 2.25 this is the case for the entire elastic energy.^d The energy of the physical dislocation core – which can not be described by elasticity – will certainly also depend on the dislocation velocity as the dislocation core changes for high velocities [12]. However, there will be a constant minimum energy caused by the locally distorted bonding within the dislocation core.

Therefore the lower cut-off radius r_0^m becomes a physical quantity which (together with R and K) defines the inertia of a dislocation. It follows from the above reasoning that it is closely related, however not necessarily identical, to the physical core radius r_0^{phys} .

It should be noted that the term physical core radius might not be fully adequate for dislocations in fcc metals. Unlike r_0 , r_{dev} or r_0^m the physical core radius is not a mathematical quantity representing characteristics of a 'virtual' perfect dislocation. Dissociated dislocations should therefore be described by two physical dislocation cores – which for mixed dislocations can have different $r_0^{\text{phys,P}}$ – plus the stacking fault. In this context it is not clear how $r_0^{\text{phys,P}}$ is defined in the case of core-overlap. Furthermore, the (partial-) dislocation cores in fcc metals are usually spread out in the glide plane (see e.g. Figs. 4.1 and 4.2), thus not showing a radial symmetry inflicted by the term core radius. The generalized dislocation widths ζ from 2D PN-models seem more adequate for describing dissociated dislocations in fcc metals than r_0^{phys} .

7.2.2 Dislocation drag

The dislocation drag can be separated into a velocity dependent viscous drag characterized by the drag coefficient B and contributions without linear velocity dependence, like the radiation friction, see sec. 2.1.3.4. The fits to the dislocation trajectory in the low-velocity and low-temperature regime (Tab. 7.3) showed indications for the existence of a dynamic friction stress $\tau_r = \Delta F/b$. For the edge dislocation the radiation stress τ_r is about one order of mag-

^dThis statement includes also nonlinear elastic contributions.

nitude smaller than the static Peierls stress τ_P in Al, and about one order of magnitude larger than τ_p in Ni and Cu. The radiation stress for screw dislocations is by one order of magnitude larger than that of edge dislocations, see Tab. 4.4. Fits to dislocation trajectories at higher temperatures and stresses, however, showed no clear indication of a dynamic friction stress. The existence of a "dry friction type" of radiation friction with $\tau_r \approx \tau_P$ was postulated by some models (see e.g. sec. 2.1.3.4 and the review by Alshits [64]). However, no consistent theory of radiation friction currently exists [16,68]. Based on their simulations of dislocation motion at 0 K in square and triangular lattices Koizumi *et al.* [68] stated that even at room temperature the energy loss of moving dislocations is about one order of magnitude larger than the theoretical value estimated by phonon-scattering mechanisms. The present simulations however show that velocity independent radiation friction does not provide a significant contribution to the drag of dislocations in fcc lattices in the investigated velocity regime and at $T \gtrsim 100$ K (see also the following discussion).

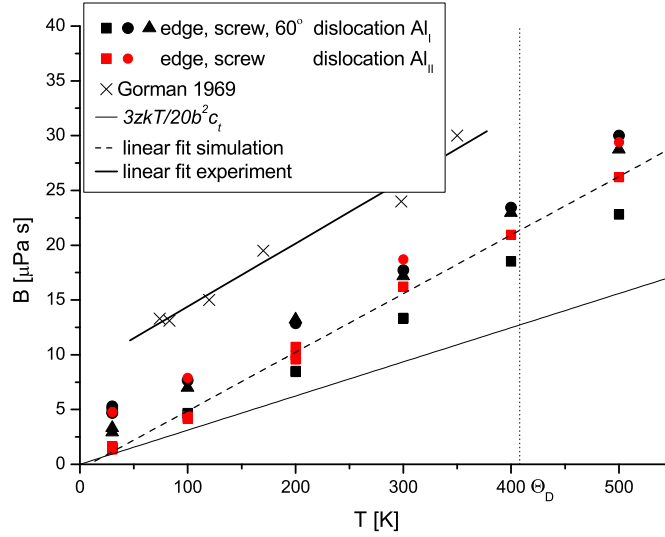


Figure 7.5: Plot of the drag coefficient B as function of the temperature. The simulation results for different types of dislocations and two aluminum potentials are compared with experimental values [262]. Θ_D denotes the Debye temperature.

Therefore in the following the radiation friction is neglected, and the drag coefficient of dislocations moving with steady state velocity v_{ss} in the low velocity regime ($v_{ss} < c_t/3$) is determined in the usual way:

$$B = \frac{\tau b}{v_{ss}} . \quad (7.4)$$

The so obtained drag coefficient is shown for Al, Ni and Cu in Figs. 7.5 to 7.7. These values can be directly used in dislocation dynamics (DD) simulations [263–265]^e. Where available,

^eIt should however be kept in mind that the drag by electrons and in Ni also magnons is not modeled by MD.

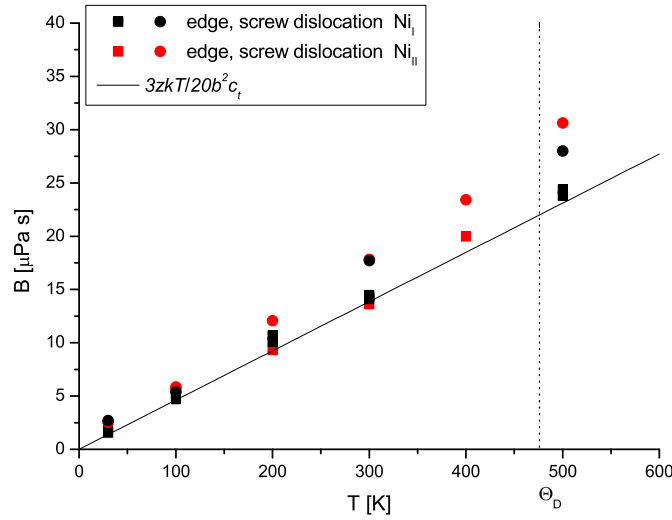


Figure 7.6: Plot of the drag coefficient B as function of the temperature as determined from dynamic simulations of edge and screw dislocations using two different potentials for Ni. Θ_D denotes the Debye temperature.

experimental values are shown. In these figures the following general observations can be made:

- The drag coefficient follows a roughly linear relationship with the temperature
- The magnitude of B is comparable for Al, Ni and Cu
- screw and 60° dislocations have a higher drag coefficient than edge dislocations.

In the following the drag coefficient of dislocations in the different potentials will be analyzed in more detail.

The drag coefficients of edge, screw and 60° degree dislocations in the two aluminum potentials are shown in Fig. 7.5. The dynamics of three types of dislocations were studied with the aluminum potential of Ercolessi (Al_I) [206]. This potential was also used to study the flutter effect, see Fig. 5.10. However, as mentioned in sec. 5.2, the effect was only noticeable at 30 K. The different velocities there translate to a difference in B of only $0.1 \mu\text{Pa s}$. The flutter effect can thus be safely neglected at temperatures above approx. 100 K, in accordance with the theory (see sec. 2.1.3.4). Fig. 7.5 shows that the drag coefficient of screw and 60° dislocations are similar, but edge dislocations have generally a lower drag coefficient. The drag coefficient of edge dislocations in Al_I shows a somewhat lower increase with temperature compared to the other dislocations and is generally lower than B for edge dislocations in Al_{II} . A linear fit to the data of the edge dislocations in Al_I yields a slope of $(4.5 \pm 0.1) \cdot 10^{-8} \text{ Pa s/K}$. This has to be compared to $(5.7 \pm 0.2) \cdot 10^{-8} \text{ Pa s/K}$ for the other dislocations. This slope is in very good agreement with the result of $(5.8 \pm 0.5) \cdot 10^{-8} \text{ Pa s/K}$ from a linear fit to the experimental data by Gorman [262]. The absolute value of the drag coefficient in the experiments is however about $9 \pm 0.5 \mu\text{Pa s}$ higher than in the simulations. The reason for this

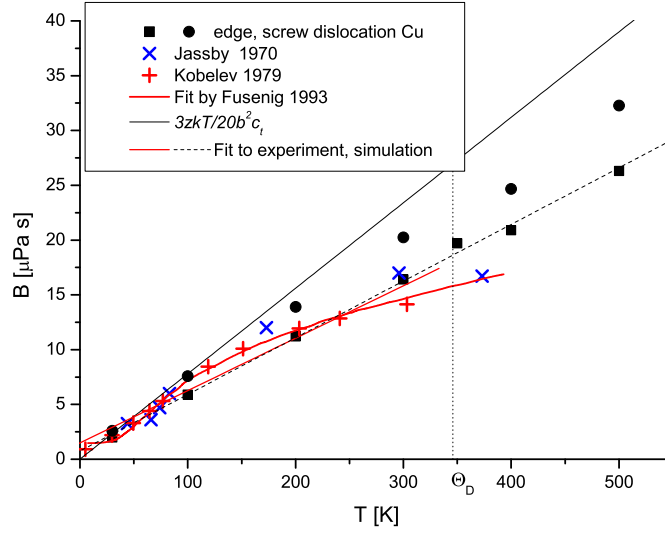


Figure 7.7: Plot of the drag coefficient B as function of the temperature as determined from dynamic simulations of edge and screw dislocations in copper. For comparison experimental values are also plotted. Θ_D denotes the experimental Debye temperature. See text for details.

difference is unclear. Drag by electrons is not included in the MD simulations, but according to the measurements by Hikata *et al.* [266] it should only give a constant contribution of $B_e = 1.4 \mu\text{Pa s}$. Leibfried's estimate, Eq. 2.45, of the drag by phonon wind gives a pre-factor of $3kTz/20c_t b^2 = 3.1 \cdot 10^{-8} \text{Pa s/K}$, which is about 2 times smaller than the one determined from experiment and simulation.

The drag coefficient for edge and screw dislocations in the two Ni potentials is shown in Fig. 7.6. Although the static properties of the dislocations in the two potentials differ significantly, their drag coefficients are very similar. The slope ($4.6 \pm 0.1 \cdot 10^{-8} \text{Pa s/K}$) and absolute value of the drag coefficient of edge dislocations agree very well with the prediction of Leibfried's equation $B_{\text{wind}}/T = 3kTz/20c_t b^2 = 4.62 \cdot 10^{-8} \text{Pa s/K}$. The drag coefficient of screw dislocations, however, shows a somewhat steeper slope: $6 \pm 0.1 \cdot 10^{-8} \text{Pa s/K}$.

The drag coefficient for copper is shown as function of temperature in Fig. 7.7. Linear fits for edge and screw dislocations show somewhat different slopes of $(5 \pm 0.2) \cdot 10^{-8} \text{Pa s/K}$ (edge) and $(6 \pm 0.2) \cdot 10^{-8} \text{Pa s/K}$ (screw). These values are both lower than the slope provided by the Leibfried relation ($B_{\text{wind}}/T = 7.8 \cdot 10^{-8} \text{Pa s/K}$). Up to room temperature, the experimental B by Jassby *et al.* [267] and Kobelev *et al.* [268] agree rather well with the simulations. A linear fit to the experimental data agrees well with the fit to the simulations, see Fig. 7.7. However, the experimental values suggest a nonlinear increase of B with T [267, 268]. Such a nonlinear behavior is predicted for Cu by more elaborate theories of dislocation drag, see [16, 63]. It is unclear why the simulation does not show a similar deviation from the straight line. A possible reason might be that the Debye temperature of the potential does not correspond to the experimental one, or an influence of the use of room temperature properties as potential properties at 0K

The linear relationship between temperature and drag coefficient in the Leibfried approx-

imation, Eq. 2.45, is the simplest approach to describe dislocation drag by phonon processes. In the derivation of the drag by phonon wind, Eq. 2.45, Leibfried furthermore did not calculate the cross section for phonon scattering by dislocations, but assumed it to be of the order of the lattice constant [65]. Therefore Eq. 2.45 applies basically to any scattering mechanism with a diameter of the order of a_0 . Especially it applies also for the flutter effect [63]. However, the phonon scattering diameter due to nonlinear phonon - dislocation interactions depends on the nonlinear region of the dislocation core. It is noteworthy, that the different dislocation core structures and energies in the different potentials for the same material have no significant effect on B . The deviation of the Leibfried estimate from the experimental values by approx. +80% and -40% is however relatively small compared to the possible variations of $1/60 - 1/5$ for the numerical factor in Eq. 2.45, and compared to the experimental scatter, see sec. 2.1.3.4.

More elaborated treatments of dislocation drag than Eq. 2.45 have been subsequently developed, which include different interaction mechanism and more adequate representations of anharmonicity, see e.g. [16, 64]. These models, however, require information on the anharmonicity like the Murnaghan modulus [64] which is not readily available for interatomic potentials. Similarly, the application to experimental data is also not straight-forward. Fusenig [88] for example used a combination of 3rd order series approximation of the integral functions used by Alshits [64] to fit the the dislocation drag in Cu, see Fig. 7.7. The fit describes well the deviations from a straight line for the experimental values. However, the fit was only possible by using an unreasonably small value $\Theta_D = 235$ K for the Debye temperature [88].

The existing theoretical studies of phonon damping do furthermore not offer any explanation of the larger drag for screw dislocations compared to edge dislocations. The more elaborate theories of dislocation - phonon interaction can consider edge and screw dislocations by different anharmonical factors [16]. However, according to the numerical example by Nadgornyi (page 237 in [16]) edge dislocations in Cu should experience *larger* drag than screw dislocations. One could argue that the more compact core of screw dislocations could lead to a stronger scattering of phonons. Further detailed studies are required to address this question.

From a modeling point of view and given the scatter of the obtainable experimental data, the results of the atomistic simulations can be summarized as follows:

- The atomistic simulations agree well with experiments.
- The details of the potential do not significantly influence the drag coefficient - the character of the dislocation has a larger influence.
- For most modeling applications the use of a drag coefficient which is linear with T is adequate, at least up to the Debye temperature.

7.2.3 High velocity dislocations

The simulations of dislocation motion at higher stresses revealed a high velocity regime of dislocation motion where the dislocation velocity increases only slightly with increasing stress, and is less sensitive to temperature. At very high velocities radiation of phonons by the dislocation can be seen (see Fig. 5.16). For screw dislocations, the high velocity regime starts at lower velocities than for edge dislocations. In the high velocity regime the increase of

velocity v with applied shear stress τ is furthermore generally stronger for screw dislocations than for edge dislocations. Nearly stress and temperature independent "velocity plateaus" or "preferred velocities" for edge dislocations have also been reported in the literature [53, 56, 57, 60]. Different velocity regimes were also recently identified for screw dislocations [53, 103]. Olmsted *et al.* [53] found in their detailed atomistic study on dislocation motion in Ni and Al that the velocity of screw dislocations in the high velocity regime could be fitted to the radiation damping form postulated by Eshelby [52]. However, no convincing physical interpretation of the plateau velocity for edge dislocations could be provided, and the existence of a threshold velocity for radiative damping could not be explained [53].

Different theories for the motion of dislocations at high velocities have been proposed and can be compared against the simulation results presented in sec. 5.2. Roos *et al.* proposed that the drag caused by the flutter mechanism becomes velocity dependent and diverges when v approaches the shear wave velocity [232]. Integrating the equation of motion, Eq. 7.2 modified with the proposed functional form of $B(v)$, however does not reproduce the dislocation trajectories from the simulations. Furthermore, the simulations with dislocations of minimal line length showed that the flutter effect does not lead to a significant drag in the high velocity regime (see Fig. 5.10).

In sec. 2.1.3.3 two possible theories which include special subsonic velocities were presented. Eshelby postulated radiative damping for velocities $v > \frac{\omega}{k}$ larger than the phase velocity c_p of the slowest phonon mode. These velocities can be calculated from the frequency ν_t of transverse phonons at the boundary of the first Brillouin zone (see appendix A). The results are given in Tab. 5.2. A comparison of these values with the crossover velocity v_c , Tab. 5.1, or the velocity of the emitted waves, Tab. 5.2, shows no significant correlation, in accordance with the discussion of Olmsted [53].

Bhate [56] determined from phonon dispersion relation in Al the velocities $v_{g=p_1} = 20.7$ Å/ps $v_{g=p_2} = 11.1$ Å/ps and at which phonons have the same phase and group velocity. Based on the model of Celli and Flytzanis [54, 55] Bhate [56] suggested that these velocities represent limit velocities for dislocation motion. As can be seen from Fig. 5.10 this is not the case in the present simulations.

The observations that the high velocity regime is connected with the overlap of the partial dislocation cores (Figs. 5.10-5.12 and Fig. 5.14), and that subsonic high velocity dislocations show radiation (Fig. 5.16) point to an alternative explanation of the high velocity regime. In sec. 2.1.3.4 radiation friction was introduced as drag mechanism. There, periodic changes of the dislocation core configuration lead to radiation. The according theories (see e.g. [16, 49, 64]) however were derived from the motion of perfect dislocations in Frenkel-Kontorova type models. Currently no theory describes the radiation of dislocations moving in realistic crystal structures.

Fig. 5.18d show that during the passage of a fast edge dislocation the atoms above (and below) the glide plane experience a relatively large and fast deflection. This is caused by successive displacement by the rapidly following partial dislocations. It is therefore speculated that the large atomic accelerations lead to the observed radiation. The mode of displacement within the partial dislocation cores is reflected in the atomic velocities within the emitted wave, see Fig. 5.18. The atomic accelerations depend on the velocity of the dislocation and on the spacing of its partial dislocations. It can be therefore hypothesized that depending on the dynamic partial dislocation separation different modes of radiation friction exist. The large distance between the partial dislocations of the edge dislocation in Cu could thus explain the observed high v_c for for this dislocation.

The distance d between the partial dislocations is determined by the stress field of the moving partial dislocations and the stacking fault energy. The stacking fault energy is assumed to be velocity independent, the stress field of a moving dislocation however depends on its velocity [47]. If the attraction between the partial dislocations due to the screw (edge) components of the partial dislocations of an edge (screw) dislocation is neglected, $d(v)$ is proportional to the contraction of the stress field in the glide plane. For screw dislocations this corresponds simply to the relativistic contraction [47]. Therefore the dynamic splitting distance can be written as

$$d(v) \approx d(v=0) \cdot \sqrt{1 - \frac{v^2}{c_t^2}}. \quad (7.5)$$

The situation is more complicated for edge dislocations. Within isotropic linear elasticity theory the stress σ_{xy} within the glide plane of an edge dislocation moving with velocity v is given as [47]:

$$\sigma_{xy}^\perp(v) = \frac{2bc_t^2\mu \left(\frac{\sqrt{1-\frac{v^2}{c_l^2}}\sqrt{1-\frac{v^2}{c_t^2}}}{x^2} - \frac{\left(1-\frac{v^2}{2c_t^2}\right)^2}{x^2} \right) x}{\pi v^2 \sqrt{1-\frac{v^2}{c_t^2}}}. \quad (7.6)$$

This equation can be compared to the usual expression for the stress field of an edge dislocation for $y=0$ [13]:

$$\sigma_{xy}^\perp(v=0) = \frac{b\mu}{2(1-\nu)\pi x}. \quad (7.7)$$

Using the relation

$$\nu = \frac{c_l^2 - 2c_t^2}{2(c_l^2 - c_t^2)} \quad (7.8)$$

the contraction of the stress field of a moving edge dislocation can be determined from Eq. 7.6 and Eq. 7.7, and the following approximation for d can be obtained:

$$d(v) \approx -d(v=0) \cdot \frac{c_l^2 \left(4 \left(\sqrt{1-\frac{v^2}{c_l^2}} \sqrt{1-\frac{v^2}{c_t^2}} - 1 \right) c_t^4 + 4v^2 c_t^2 - v^4 \right)}{2c_t^2 (c_t^2 - c_l^2) v^2 \sqrt{1-\frac{v^2}{c_t^2}}}. \quad (7.9)$$

The curves according to Eq. 7.5 and 7.9 are plotted in Fig. 5.14. It can be seen that at least for velocities smaller than the crossover velocity v_c the determined d follow quite well the above relationships. However, edge dislocations in Ni and Cu show at high velocities deviations from Eq. 7.9. This is most probably due to the neglect of anisotropy in the derivation of Eq. 7.9.

How exactly the partial dislocation distance affects the radiation of phonons requires further investigation. In general, however, for screw dislocations the criterion

$$d(v_c) \approx w \quad (7.10)$$

seems to provide a good estimate for the crossover velocity delimitating the high velocity radiation dominated regime from the low velocity drag controlled region. For edge dislocation the crossover occurs already at somewhat lower velocities. It has to be noted, that the suggested reason for the crossover to the high velocity regime is not directly related to any "special" velocity derived from the phonon dispersion, but rather to the properties of the dislocation.

7.3 Static and dynamic dislocation - obstacle interactions

7.3.1 Static dislocation depinning

The interaction between dislocations and voids has recently attracted renewed interest in the context of multi-scale modeling of irradiation damage [5, 114, 115, 269]. Elasticity theory of dislocations and defects provides a valid description of strengthening, but there are problems when it comes to processes that are controlled by atomic-scale mechanisms. The multi-scale modeling approach wherein the mechanisms and parameters describing the dislocation-obstacle interaction are derived from atomistic simulations and fed into higher level continuum mechanical models is now widely recognized as the method of choice for treating the mechanical response of (irradiated) materials. In this context voids can serve as model obstacles to mutually validate continuum approaches and atomistic modeling [114].

The critical stress required for the unpinning of a (edge) dislocation from a row of voids is usually described using the following relationship by Scattergood and Bacon [234]:

$$\tau_{\text{SB}}^{\perp} = \frac{\mu' b}{2\pi L} (\ln(D^{-1} + L^{-1})^{-1} + \Delta) , \quad (7.11)$$

where $(D^{-1} + L^{-1})^{-1}$ is the harmonic mean of obstacle spacing L and diameter D in units of b . The parameter Δ describes the resisting force caused by the creation of a surface step. It is defined as normalized surface energy [234]:

$$\Delta = \frac{\gamma_{\text{surf}}}{\frac{\mu' b}{4\pi} \ln(R/r_0)} , \quad (7.12)$$

where the factor $\ln(R/r_0)$ is usually taken equal to unity.

The rationale behind this model follows the treatment of the Orowan mechanism where the extension of dislocation dipoles from the obstacles is believed to be the main cause of the Orowan stress [270]. The argument of the logarithm $(D^{-1} + L^{-1})^{-1}$ is thereby interpreted as effective outer cut-off radius for the energy of the dislocation lines making up the dipole [270]. Scattergood and Bacon [234] reported that Eq. 7.11 fits very well the results of their continuum model of a flexible dislocation interacting with a row of voids. The model incorporated the effect of self-interaction of the dislocation, and the boundary condition for a dislocation at a void surface were treated as though the terminating segment is in equilibrium with a flat, infinite surface. The effect of the creation of the surface step was included by a point force tangential to the surface at the intersection point of the dislocation. Equation 7.11 was also recently shown to fit well the critical stress for an edge dislocation interacting with an array of voids in bcc Fe as determined by Osetsky and Bacon using atomistic modeling [114, 236].

The critical stress for a screw dislocation can be calculated by replacing μ' by $\mu'/(1 - \nu_A)$. I.e. a screw dislocation creates an edge dislocation dipole. The elastic anisotropy

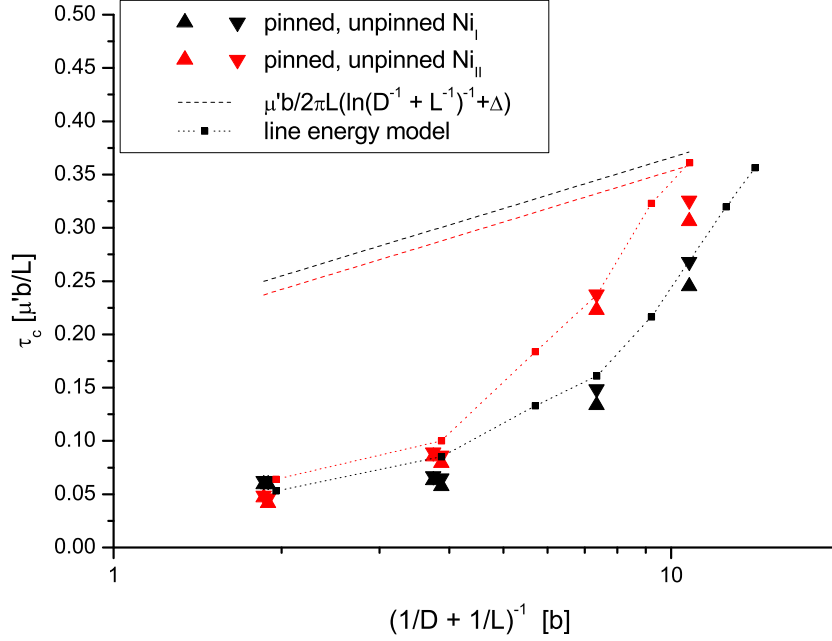


Figure 7.8: Static unpinning stress as function of the harmonic mean of obstacle spacing L and void diameter D , compare also to Fig. 6.2. In addition to the values from the simulations the theoretical estimate from Scattergood and Bacon [114, 234] and the results of a model which assumes that the critical stress is determined by the annihilated dislocation core energy (which is taken from Fig 4.6) is plotted.

is thereby taken into account by using the effective anisotropic shear modulus μ' and the effective anisotropic Poisson ratio $\nu_A = 1 - K_s/K_\perp$ [270].

Eq. 7.11 with the appropriate values of Δ and μ' for the two potentials is plotted in Fig. 7.8 together with the results from the static simulations (Tab. 6.1 and Tab. 6.2). It can be seen that Eq. 7.11 considerably overestimates the critical stress for the simulated void sizes. This behavior was also found in the recent studies of dislocations interacting with voids in copper [114, 116]. There the overestimation is attributed to the effect of dislocation dissociation which is not taken into account in Ref. [234]. Osetsky and Bacon assumed that for voids with diameter D smaller than the splitting distance d the partial dislocations break from the void individually [114]. Since the magnitude of the partial Burgers vectors is less than b , it was reasoned that the individual critical stress values are lower than for a full dislocation [114]. However, Eq. 7.11 in this case does not provide a quantitative description of the stress necessary for the depinning of partial dislocations. Furthermore, also voids with $D > d$ ($R_{\text{void}} = 4, 6b$ in Ni_{II}) show a lower τ_c than predicted by Eq. 7.11. Additionally the constriction of the dislocation can lead to simultaneous trapping of the two partial dislocations by voids with $D < d$. Upto now there is no model that can quantitatively predict the critical stress required for dislocations to unpin from small voids ($D \lesssim d$).

In general, the application of Eq. 2.2 to calculate the line energy is restricted to $R > r_{\text{dev}}$,

see section 4.2. For smaller cut-off radii the line energy can only be calculated atomistically. In order to estimate the critical depinning stress based on the properties of static dislocations obtained in sections 2.2 and 7.1 we propose an ansatz based on energetic considerations. Dislocation-obstacle interactions can be described in terms of the energy which has to be provided to the dislocation to overcome the obstacle [13]. In the case of an dislocation interacting with a void one can assume that the energy barrier is correlated with the dislocation core energy which is annihilated by the void plus the energy $\Delta E_{\text{step}} \approx b\pi D\gamma_{\text{surf}}$ necessary to produce the step of one Burgers vector:

$$\Delta E_{\text{pot}} = \Delta E_{\text{core}} + \Delta E_{\text{step}} \approx DE_{\text{core}} + b\pi D\gamma_{\text{surf}} . \quad (7.13)$$

To overcome the void, the dislocation has to be displaced by a distance $\Delta x = D$. In the static case at 0 K the energy to overcome the obstacle is provided by the mechanical work W done by the applied load

$$\Delta E_{\text{pot}} = W = \tau bL\Delta x . \quad (7.14)$$

The critical stress can thus be estimated by

$$\tau_{c,\text{est.}} = \frac{\Delta E_{\text{core}} + \Delta E_{\text{step}}}{bLD} . \quad (7.15)$$

All the necessary values can be obtained by atomistic calculations. However, to make the connection to the continuum theory, one can use Eq. 2.2 and the effective anisotropic modulus and Poisson contraction, and one gets for $R > r_{\text{dev}}$

$$\tau_{c,\text{est.}} = \frac{\mu' b}{4\pi(1 - \nu_A)L} \ln(D/2) + \frac{\pi\gamma_{\text{surf}}}{L} . \quad (7.16)$$

For $L \gg D$ where $\ln(D^{-1} + L^{-1})^{-1} \approx \ln(D)$ this expression can be directly compared to Eq. 7.11. Considering the usual values for ν_A and $\ln(D/2)/\ln(D) \approx 0.8$ for typical $D \gtrsim 10b$, Eq. 7.16 and Eq. 7.11 lead to similar values for the pre-factor to the logarithm. The difference of $\pi/2$ in the the constant describing the energy of the step is of minor importance as additional parameters due to the lower cut-off radius for the dislocation are usually subsummed into the additional constant.

The advantage of Eq. 7.15 is that it is not limited to the case $D/2 > r_{\text{dev}}$ where Eq. 2.2 can be applied. For small voids $DE_{\text{el}}(D/2)$ can be directly determined from Fig. 4.6 ^f and ΔE_{step} can be taken from ΔE_{cut} of Fig. 6.1b. For the vacancy cluster the potential energy barrier can be estimated by using the value of $\Delta E/E_{\text{coh}}$ from Tab. 4.1 for the high energetic dislocation core atoms. The results of Eq. 7.15 obtained with these values are shown in Fig. 7.8. It can be seen that with the information gained from atomistic simulations Eq. 7.15 provides reasonable estimates for the critical depinning stress from small voids.

In this context it is interesting to note that in the simulations the depinning was always controlled by the trailing partial dislocation, except for the case of the cluster of 6 vacancies where the obstacle strength is significantly degraded after the passage of the first partial dislocation. This can be directly seen from the static simulations for the void with $R_{\text{void}} = 2b$, Fig. 6.3, and from the dynamic simulations, see figures 6.5 to 6.7. Fig. 6.7 e.g. shows that

^fFor the void with $R_{\text{void}} = 2b$ where the partial dislocations interact individually with the void $1/2E_{\text{el}}(D/2)$ was used.

leading partial dislocation can temporarily unpin from the void, whereas the trailing partial dislocation stays pinned. In their quasi-static simulations under constant load rate Osetsky and Bacon [114] see the same behavior for small voids, however for larger voids they report a critical resolved shear stress controlled by the leading dislocation. For voids with $D > d$, however, simultaneous release of both partial dislocations is reported. From an energetic point of view the energy barrier for the leading partial dislocation to leave the void should be lower than for the trailing partial dislocation because a part of the stacking fault energy between the two partial dislocations is annihilated by the void.

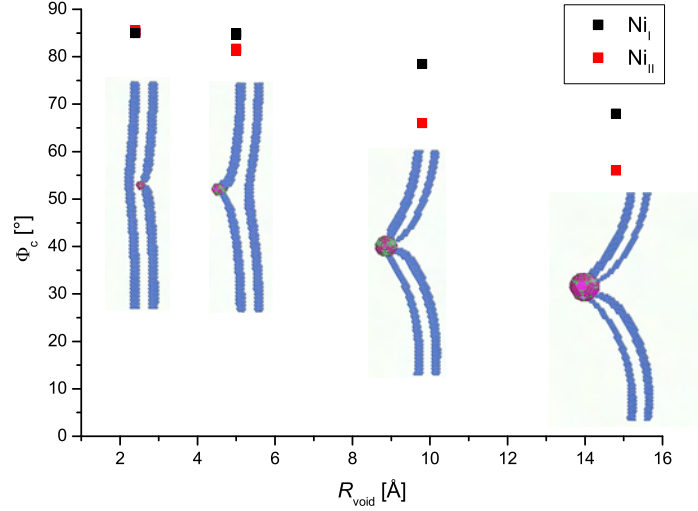


Figure 7.9: Critical angle calculated in the isotropic line tension approximation with the critical stress and the line tension from atomistic simulations. The configuration for the lower boundary of τ_c in Ni_{II} is also shown.

Due to the reorientation of dislocation segments at the void surface and the dissociation into partial dislocations the geometrical determination of a critical angle Φ_c is to a certain degree arbitrary (see sec. 6.2). To provide information on the obstacle strength for the widely used isotropic line tension models an alternative route can be used. Within this model Eq. 2.10 can be used to calculate an effective critical angle for a virtual full dislocation, provided that τ_c , L and Γ are known. For consistency Eq. 2.30 is used here with the dislocation rest mass m_0 from Tab. 7.3 to determine the line-tension. This way the appropriate values for the parameter r_0 and R for the simulations are automatically included. The so determined values for Φ_c are shown in Fig. 7.9. The Φ_c are within the typical range for weak ($\Phi_c \simeq 90^\circ$) to medium obstacles ($\Phi_c \simeq 45^\circ$). The definition of the obstacle strength by the breaking angle Φ_c calculated by equation 2.10 is used in many models of strengthening. It should however be kept in mind that the line tension used in Eq. 2.10 depends logarithmically on the simulation box size. With information on the appropriate K and r_0 (see Tab. 7.2 and Tab. 7.3) the Φ_c can be scaled according to experimentally reasonable R . The Φ_c can then e.g. be used in an isotropic line tension model where the obstacle is assumed to be point like and the dislocation segments on both sides of the obstacle do not interact with each other.

Dislocation dynamics (DD) simulations divide the dislocation line into segments which interact with each other. They therefore automatically include the interaction of dislocation segments at both sides of the obstacle. The simple definition of Φ_c by a constant line tension is therefore not adequate for DD simulations which have to use the full information on D, L, τ_c .^g In providing information on the strength of individual obstacles, atomistic simulations play an important role in multi-scale modeling, as such information e.g. on obstacles caused by irradiation is difficult to obtain experimentally. Transmission electron microscopy (TEM) observation of in-situ strained irradiated metals seem in this context a promising method to determine critical angles of obstacles [271]. Further studies in this direction trying to compare experimental and atomistic results are important to clarify whether the mechanisms observed in atomistic simulations are still dominating under experimental conditions, or whether other mechanisms, e.g. dislocation climb, become important at realistic strain rates and temperatures.

7.3.2 Dynamics of dislocation - void interactions

In section 6.3 it was shown that the critical stress τ_d to pass an array of voids is significantly smaller for moving dislocations compared to the critical stress τ_c necessary to depin a static dislocation from the same array of voids. The dependence of τ_d on the initial distance of the dislocation from the voids (Tab. 6.2) and its decrease with increasing temperature are clear indications for inertial effects. Thermal effects like thermal activation or the change of dislocation- or obstacle properties, e.g. due to the change of the elastic constants, can not explain these effects.

The theory of inertial overshooting was introduced in section 2.1.3. In contrast to the complex situation in experiments which has to be modeled by mesoscopic models of dislocations interacting with an array of random obstacles [73–80], atomistic simulations can provide direct evidence and a quantitative description of inertial effects for individual dislocation-obstacle interactions. Such studies are important to provide the parameters for meso-scale models which include dynamic effects [77, 79, 80, 263, 265] and to provide a testing ground for these models. Furthermore the study of dynamical dislocation effects is useful for the interpretation of atomistic simulations of plasticity at high strain rates. The present work presents the first detailed atomistic study of dynamical effects during dislocation-obstacle interaction.

In the following the dynamical effects are analyzed with respect to the energies involved in the dislocation-void interaction (sec. 7.3.2.1) and a simple line tension model is developed to assess the magnitude of inertial effects in the interaction of dislocations with a regular array of localized obstacles (sec. 7.3.2.2). Results of dislocation dynamics (DD) simulations which take the dislocation inertia into account are presented in sec. 7.3.2.3. Implications from the analysis of individual overshooting events for the study of dynamical effects of dislocations moving in a random array of obstacles will be discussed in sec. 7.3.2.4.

7.3.2.1 Dynamic overcoming of energy barriers

The description of the interaction of dislocations with obstacles in terms of the energy barrier ΔE_{pot} and the work W provided by the applied load was already used in section 7.3.1 to estimate the critical stress in the case of dislocation depinning from the voids in the static

^gThe determination of Φ_c in DD simulations furthermore has to be calibrated with τ_c and L to account for the discretization of the dislocation line.

simulations. By including the kinetic energy E_{kin} and the dissipated energy E_{dis} this concept can be extended to study the dynamic interaction of moving dislocations with obstacles (see also [263, 272]).

For simplicity in the following the potential energy of the system instead of the Gibbs free energy is used, and thermal activation is neglected. Passing the obstacle then requires to surmount an energy barrier of height ΔE_{pot} . In the static case, corresponding to the balance of forces (Eq. 2.9) for Φ_c , the energy required to pass the barrier is provided by the work W_c done on the dislocation by the applied stress τ_c . If a fast moving dislocation has enough kinetic energy $E_{\text{kin}} = \frac{1}{2}m(v)v^2L$ to outweigh the energy E_{dis} which is dissipated during the process of the dislocation bow-out, the dislocation can overshoot its equilibrium position and eventually pass the energy barrier ΔE_{pot} dynamically. Dynamical obstacle passing in a purely mechanical model is thus possible at stresses $\tau_d < \tau_c$ when the work W_d done by this stress is larger than the barrier height lowered by the kinetic energy:

$$W_d > W_c - (E_{\text{kin}} - E_{\text{dis}}) . \quad (7.17)$$

The contributions of the terms in Eq. 7.17 are path dependent and not easily accessible. If one assumes that the critical depinning configuration is the same for the dynamic case and the static case, the critical depinning configuration can be characterized by the critical angle Φ_c and the area A_c swept by the dislocation between the first contact till the depinning. The work done in the static case can thus be estimated to be $W_c^{\text{est.}} = \tau_c b A_c$. In the dynamic case, the work done by the dynamic passing stress τ_d to reach the critical configuration is $W_d^{\text{est.}} = \tau_d b A_c$. The dissipated energy during bow-out can be estimated to $E_{\text{dis}}^{\text{est.}} = \frac{1}{2}v_i B A_c$, which, just like the kinetic energy, depends on the velocity $v_i(\tau_d, B)$ at which the dislocation impinges on the obstacle. This velocity can directly be determined from the atomistic simulations or by solving the equation of motion (Eq. 7.2) with τ_d, l, m_0^\perp and B as determined from above. In sec. 7.3.1 the critical area A_c was approximated by LD to determine τ_c . For the study of the different energy contributions in Eq. 7.17, however, the area swept by the dislocation to reach the critical configuration in the static case at τ_c is known and can be directly determined from the atomistic simulations.^h

These contributions were calculated for a void ($R_{\text{void}} = 4b, L=276\text{\AA}$) in Ni_{III}, see Fig. 7.10. The estimated work in the static case agrees reasonably well with the estimated energy barrier from section 7.3.1 $\Delta E_{\text{pot}} = 2R_{\text{void}}E_{\text{el}}(R_{\text{void}}) + \Delta E_{\text{cut}}(R_{\text{void}}) = 13.2$ eV with the values from Fig. 6.1b and Fig. 4.6. It can be seen in Fig. 7.10 that the sum $W_d + E_{\text{kin}} - E_{\text{dis}}$ in all of the dynamic cases is – within the error margins – comparable to the work in the static case. It can also be seen that the increase of the dissipated energy with temperature has to be balanced by an increase in the work done on the dislocation. The large contribution of the kinetic energy of the dislocation to the obstacle passing clearly indicates that the dynamical obstacle passing at $\tau_d < \tau_c$ is indeed an *inertial* effectⁱ. Furthermore, the kinetic energy of the whole dislocation line needs to be considered. The effect can therefore be considered as a weak dynamic effect (see sec. 2.1.3.5).

^hFor this purpose the atomistic slip vector (see sec. 3.3) was determined and the number of slipped atoms above the glide plane was multiplied with the area per atom on a {111} plane.

ⁱThe same kind of study was also performed using a mono-atomic step on a surface as obstacle [272], where the same conclusions were reached. Although not representing a realistic obstacle, the surface step has the advantage that its energy barrier is well defined by the energy to increase the dislocation line length by one atomic layer plus the energy to produce the kink in the surface step.

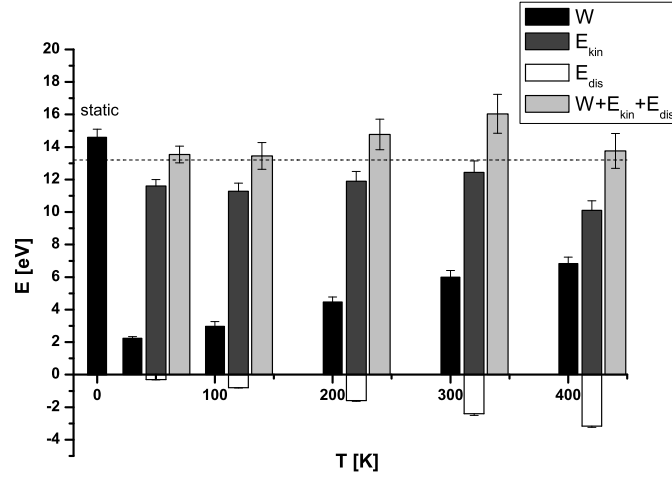


Figure 7.10: Estimated energy contributions of the applied stress acting on the dislocation (W), of the dislocation inertia (E_{kin}) and the drag forces (E_{dis}) for overcoming a void ($R_{\text{void}} = 4b$, $L=276\text{\AA}$) in Ni_{II}. The dashed line shows the estimated energy barrier ΔE_{pot} from sec. 7.3.1.

The description of inertial effects in an energy framework allows to easily derive qualitative implications of parameters like obstacle strength, spacing, etc. on dynamic effects in general.

The kinetic energy of a dislocation is a function of the square of its velocity, therefore inertial effects depend sensitively on the impinging velocity v_i . Inertial effects are therefore of course expected for dislocations subjected to high shear stresses and low temperatures. However, the dislocation also requires a certain free flight distance l between the obstacles to accelerate, and the magnitude of inertial effect is furthermore limited by the reduced stress sensitivity of the dislocation velocity in the high velocity regime, see sec. 7.2.3. The lack of adequate acceleration distance l is for example the cause for the less pronounced dynamic effect at the large voids at low temperatures compared to the smaller voids, see figures 6.9 and 6.10. At 30K and $\tau_d = 42$ MPa (for $R_{\text{void}} = 6b$) for example, the dislocation reaches only a velocity of $v_i \approx 11$ $\text{\AA}/\text{ps}$ after $l = 300$ \AA compared to $v \approx 15$ $\text{\AA}/\text{ps}$ which would be reached after 200 nm.^j The dislocation velocity required for large inertial effects, i.e. small τ_d/τ_c ratios, require large stresses τ_d and accordingly large τ_c . Dislocations overcoming closely spaced, strong obstacles are therefore candidates for inertial effects.

The antagonist of the kinetic energy is the dissipation of energy during the process of dislocation bow-out. This of course depends on temperature via the drag coefficient B , but also on the area swept by the dislocation until it reaches the critical configuration. Therefore at the same critical stress and same L , larger obstacles^k should show less pronounced inertial effects than small obstacles. This provides a physical reason for the increase of $\tau_{d,c}$ with η_0 in the model of Schwarz and Labusch [73], see sec. 2.1.3.5.

^jThe steady state velocity $v_{ss} = \frac{\tau b}{B}$ in this case would be higher than c_t .

^kMore general obstacles with large extension in the direction of motion of the dislocation, e.g. platelets.

7.3.2.2 Dynamic line tension model

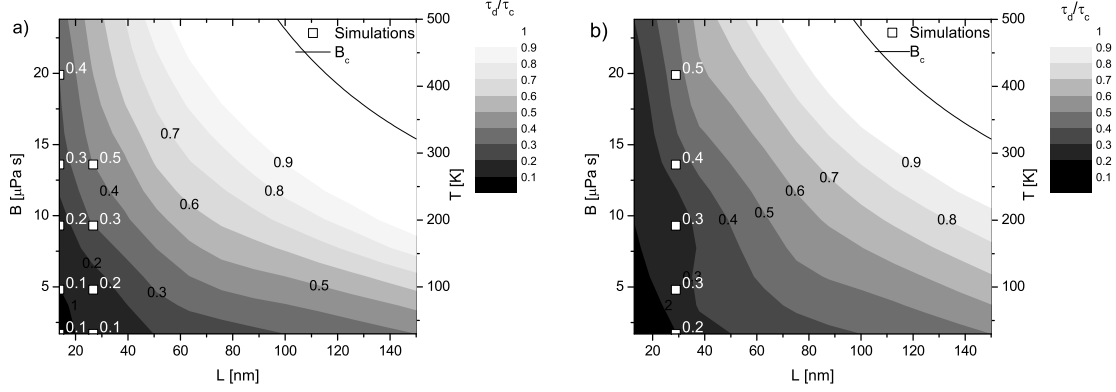


Figure 7.11: Magnitude of the inertial effect τ_d/τ_c as function of obstacle spacing L and drag coefficient B , estimated with a dynamic line tension model with B and m_0 as determined from the atomistic simulations. The critical angle is in a) $\Phi_c = 81.5^\circ$ and in b) $\Phi_c = 56^\circ$, the acceleration distance of the dislocation is in both cases $l = 30$ nm. The solid line represents the classical criterion for overdamped motion Eq. 2.50, the white points indicate the results of the dynamic simulations of dislocation-void interaction.

The previously introduced description of inertial effects in terms of the different contributions to pass the potential energy barrier does not provide a valuable mean to estimate the magnitude of inertial effects as it requires knowledge of v_i and A_c . The usual criterion Eq. 2.49 provides the critical drag coefficient B_c below which the dislocation motion is underdamped. It provides however no way to estimate how large the effect of inertia would be.

The use of a simple *dynamic* line tension model is suggested to obtain an quantitative estimate of the ratio τ_d/τ_c for a gliding dislocation interacting with an equally spaced row of obstacles (see also [273]). Such a dynamic line tension model can be used to map out the parameter space in which dynamical effects are expected by determining the critical stress to overcome the obstacles for a wide range of different B, L, l and Φ_c . In this way it can also provide rough estimates of τ_d/τ_c for obstacle configurations whose study by MD is computationally prohibitive. The dynamic line-tension model corresponds to a simplified version of the model used by Schwarz and Labusch [73]. It uses however non-normalized parameters and a grid of equally spaced point obstacles. This allows a direct comparison to the MD simulations. According to Schwarz and Labusch [73] using point-like obstacles is justified because $\eta_0 = 2R_{\text{void}}/L \cos \Phi_c^{-1/2} \ll 1$.

To study the time evolution of a dislocation line of length L pinned at the end points and subjected to a stress τ the dislocation line is discretized into straight segments for which the equation of motion

$$\frac{\partial}{\partial t} \left(M \frac{\partial y}{\partial t} \right) + B \frac{\partial y}{\partial t} - \Gamma \frac{\frac{\partial^2 y}{\partial x^2}}{\left(1 + \left(\frac{\partial y}{\partial x} \right)^2 \right)^{3/2}} = \tau b \quad (7.18)$$

is solved using a leap-frog integrator [189].¹The line tension Γ is assumed to be isotropic and

¹For the calculation of the partial derivatives the usual numerical methods with errors of $O(4)$ were used.

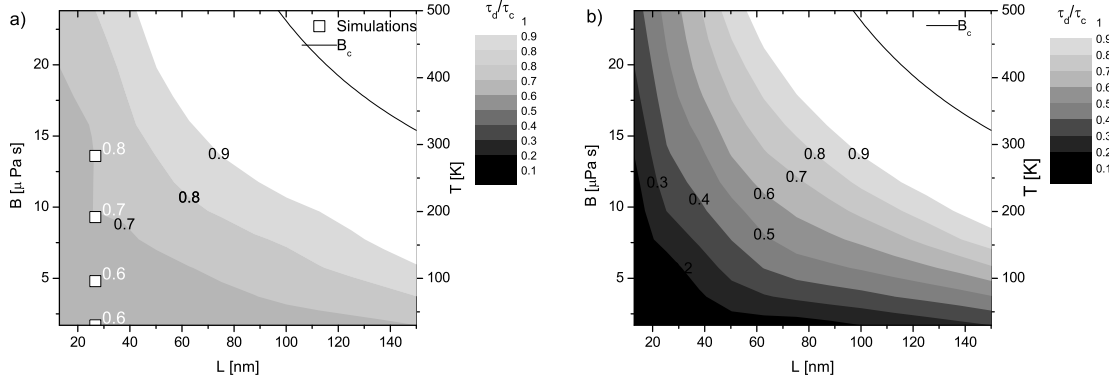


Figure 7.12: Same as Fig. 7.11 for $\Phi_c = 81.5^\circ$ and $l = 0$ nm (a), and $l = L$ (b).

independent of the velocity.^m The increase of the dislocation velocity is limited in the high velocity regime. For practical reasons, a limit velocity $v_{\text{lim}} \approx v_c$ (see sec. 7.2.3) can therefore be introduced. The boundary and initial conditions are: $x(0, t) = x(L, t) = 0, x(y, 0) = 0, \dot{x}(y, 0) = v_i$.ⁿ The impinging velocity v_i is determined by calculating the velocity which is reached by a dislocation after an acceleration distance l using a one dimensional version of Eq. 7.18. The time evolution of Eq. 7.18 is calculated for a range of τ . At each time step the angle Φ is compared to Φ_c , thus allowing to detect inertial overshooting events at $\tau_d < \tau_c$. This method can also be used to study e.g. the dynamical detachment of dislocations from pinning points under high frequency agitation or the effect of inertia on the depinning of pinned dislocations at different loading rates $\dot{\epsilon}$. The parameters $m_0, \Gamma, B, v_{\text{lim}}$ ^p for the dynamic line tension model can be taken from atomistic simulations, theory or experiment.

The estimates of τ_d/τ_c as a function of B and L of the dynamic line tension model for different materials, initial conditions and obstacle strengths are shown in form of contour plots in Figs. 7.11 to 7.13.^q Although the drag coefficient $B(T)$ is not necessarily a linear function of T , a temperature scale is added to indicate the covered temperature range. In addition the criterion $B_c = \frac{2\pi m_0 c t}{L}$ for overdamped vs. underdamped dislocation motion calculated with the parameters used in the dynamic line tension model (see also Eqs. 2.49 and 2.50) is shown in the figures.

The comparison in Fig. 7.11 of τ_d/τ_c as determined from the MD simulations with the range calculated by the dynamic line tension model show that with the atomistic information (m_0 and Γ determined from Tab. 7.3, B from Fig. 7.6, $l = 30$ nm) the simple dynamic line tension model provides reasonable estimates of the inertial effect. This is also the case

^mThe line tension depends in principle also on the velocity [48]. As detailed in [16,17] the line tension is caused by the dislocation self interaction. Its value in the relativistic regime thus depends on the velocities of all dislocation segments. The simple concept of constant line tension therefore does not apply for curved high velocity dislocations with locally different velocities and accelerations.

ⁿWith this velocity profile as starting condition and typical Γ, m_0, B relatively small time steps Δt of the order of 10 fs and discretization lengths $\Delta y \approx 1b$ have to be used for numerical stability.

^o Φ_c is determined directly in the program using isotropic line tension approximation (see e.g. [19]) and τ_c .

^pWhere m_0 and Γ are related by Eq. 2.28 or Eq. 2.30.

^qThe determination of the contours of equal τ_d/τ_c is performed on a non-equidistant grid. The rounding of τ_d to the contour lines and the interpolation between the discrete τ_d can introduce some irregularities in the plots.

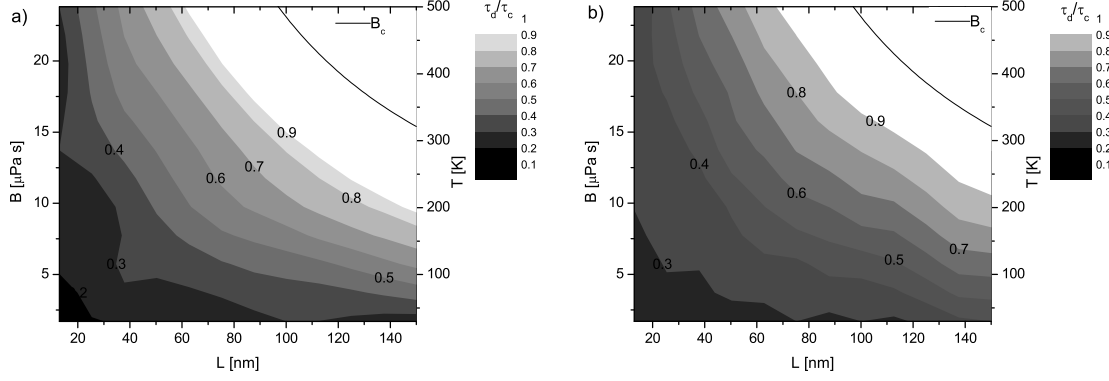


Figure 7.13: Same as Fig. 7.11 for a) $\Phi_c = 56^\circ, l = L$, b) $\Phi_c = 45^\circ, l = L$.

for the voids in Ni_I and Al (not shown). As expected the inertial effects are highest for low temperatures and narrow obstacle spacing (high E_{kin} , low E_{dis}). For small L inertial effects can still be of importance at room temperature.

The effect of the acceleration distance l on τ_d can be seen by comparing Fig. 7.11a ($l = 30$ nm) with Figs. 7.12a ($l = 0$ nm) and 7.12b ($l = L$). Even when the dislocation has no initial velocity, its acceleration during the bow-out under instantaneously applied stress can lead to a weak inertial effect, explaining the values of τ_d in brackets in Tab. 6.2. The differences in l show only up in the very low temperature regime where the relaxation time $t_r = m_0/B$ is correspondingly longer. There, the longer l is the lower is τ_d .

The effect of obstacle strength Φ_c on the inertial effect can be rationalized by comparing Fig. 7.12b and Figs. 7.13a and 7.13b. The maximally possible decrease of the critical passing stress by inertial effects (smallest possible ratio τ_d/τ_c) is significantly influenced by the obstacle strength. For very strong obstacles the inertial effect is limited by the maximum impinging velocity which is determined by l and the limit velocity. Due to the higher involved shear stresses which lead to generally higher velocities, the extend of the region of inertial effects is larger for stronger obstacles.

Many aspects of the material properties affect the inertial effects. Of course the dislocation rest mass and the drag coefficient are important parameters for dynamical effects, but also the sound velocity and the limiting dislocation velocity directly affect the maximal kinetic energy available to a dislocation. Furthermore the line tension Γ is related by the sound velocity c_t to the rest mass m_0 . For the same Φ_c metals with higher m_0 will also have higher τ_c , thus higher driving forces on the dislocations. The dynamic line tension model was also used with the parameters for the Al_I and Cu potentials. For copper the inertial effects are qualitatively and quantitatively similar to Ni. The differences in the line tension due to the different elastic moduli are leveled off for m_0 by the differences in the sound velocity, see also Tab. 7.3. The differences in the drag coefficient become only important in the high temperature region. For aluminum, however, the inertial effects are less pronounced compared to Ni, in agreement with the criterion for over/underdamping Eq. 2.49.

With correct parameters, the dynamic line tension model can thus provide an estimate for the magnitude of inertial effects during the interaction of a straight moving dislocation line and a row of equally spaced identical obstacles. This kind of information is not provided by Eq. 2.49 which is used to characterize underdamped versus overdamped dislocation motion.

The model can in principle also be used to study dynamical effects for pinned dislocations subjected to a constant load rate. However, it will suffer similar limitations to high strain rates like DD simulations. The model can not be used to determine the upper critical resolved shear stress (CRSS) $\tau_{d,c}$ as defined by Schwarz and Labusch [73]. As detailed in sec. 2.1.3.5 this would be the CRSS measured experimentally. However, the deviation of dynamical upper critical CRSS from the overdamped CRSS (τ_c) is correlated with the deviation of the lower CRSS ($\tau_{d,l}$) from τ_c , see Fig. 2.6. In the context of the Schwarz-Labusch model the ratio τ_d/τ_c can therefore be seen as an indicator under which conditions inertial effects on $\tau_{d,c}$ can be expected.

The simplifications inherent to the dynamic isotropic line tension model neglect effects due to the dislocation self interaction or due to the splitting into partial dislocations. The assumption of point-like obstacles furthermore does not allow to study the influence of obstacle size and of long range stress fields. To study the dynamics of the interaction of dislocations with realistic obstacles (and obstacle distributions) and to determine directly measurable effects of inertia on the CRSS, dislocation dynamics (DD) simulations which include the dislocation mass and use realistic drag coefficients are the method of choice, these are presented in the next section. The dynamic line tension model can however serve as guidance to decide under which conditions DD with inertia should be used, and when standard overdamped DD simulations are fully adequate.

7.3.2.3 Dislocation dynamics simulations with inertia

Dislocation dynamics (DD) simulations which include the inertia of dislocations and use realistic drag coefficients can be used on the one hand to study in detail aspects of dynamic dislocation-obstacle interaction which are not accessible by MD simulations, and on the other hand large scale DD simulation can be used to model experimental situations in which dynamic effects are likely to occur. Such studies are not possible with the quasi-static, overdamped dislocation motion according to $v = \tau b/B$ used in most of the DD codes [4, 274, 275].

Weygand [263] recently implemented an inertia based equation of motion for dislocations into a discrete dislocation dynamics model. The DD model of Weygand *et al.* [276] is based on a discretization of the dislocation line using straight segments connected at nodal points. The motion of the dislocation is then described by the positions and velocities of the nodal points. The appropriate equation of motion for the nodal points was derived using the principle of virtual work. The interaction between dislocations is calculated using linear elasticity theory, neglecting relativistic effects. The maximum velocity of a dislocation segment (not a nodal point) must therefore be restricted to about $c_t/2$. Further details of the implementation of inertia into the DDD model are given in [263].

The small vacancy cluster ($R_{\text{void}} = 1b$) of Tab. 6.1 was used as test case [263]. In the DDD simulation, the row of vacancy clusters were translated into finite size obstacles of similar diameter. After detection of the pinning event, two pinned nodal points, representing the two intersection points of the dislocation with the vacancy cluster, are introduced on the dislocation line. The depinning event is controlled by a critical curvature/angle of the dislocation at the pinning center set to fit τ_c of the static atomistic simulations. ^r

^rThe critical stress in the DD simulations has to be independent from the regularization scheme for the local self-interaction. This was achieved by controlling the minimum and maximum length of the dislocation segments.

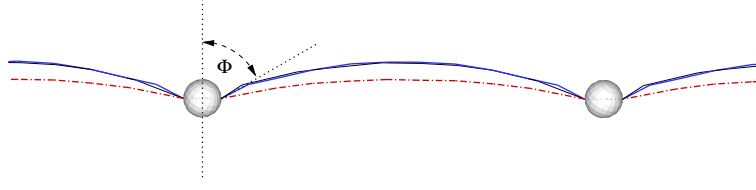


Figure 7.14: Results of different DD simulations: the thick line corresponds to the configuration before unpinning of the underdamped dislocation at τ_d ; the dashed line represents the final configuration of an overdamped dislocation at τ_d ; the thin black line represents the critical configuration at $\tau_c > \tau_d$ in a quasistatic simulation. DD calculations by D. Weygand [263].

Simulation	τ_c^{MD} [MPa]	τ_c^{DDD} [MPa]
static	75 - 80	75 \pm 2
100 K	15 - 16	13 \pm 1
300 K	30 - 33	30 \pm 2

Tab. 7.4: Lower and upper bound for the stress required for the edge dislocation to pass an array of obstacles separated by $L = 15$ nm at different temperatures T . The obstacles in the MD simulations consist of 6 clustered vacancies in the Ni_I potential. For the DD simulations a pinning center with similar diameter was chosen (see text). The initial distance between dislocation and obstacle was in both cases $l = 15$ nm.

To validate the implementation of the dislocation inertia into the DD model, overdamped and underdamped simulations with $m_0, l, B(T)$ according to the atomistic simulations were performed. Fig. 7.14 shows three different dislocation configurations. It can be seen that the critical configuration from the quasi-static calculation at τ just below τ_c is attained during the dynamic simulations at $\tau_d < \tau_c$, whereas the final configuration in the overdamped quasistatic simulation at τ_d is far from the critical configuration. The inertial overshooting can thus also be seen in DD simulations. With the appropriate $B(T)$ and m_0 the DD simulations with inertia can also quantitatively reproduce the MD results of dynamic unpinning, see Tab. 7.4.

With the model of Weygand dynamic effects in dislocation - obstacle interactions can be studied on a large scale, including different kinds of obstacles and -distributions. The model has already been applied to the study of the formation and stability of Lomer locks [264], where, depending on the loading conditions, considerable inertial effects have been found for short dislocation lengths. It has furthermore been used to study dislocation damping under high-frequency agitation [265], where for typical B and dislocation loop lengths the inertia of a dislocation was found to become important for frequencies in the GHz regime.

Also other groups are currently implementing inertial effects in their DD simulations. For example Pilon *et al.* recently used two dimensional DD simulations including inertia to show the importance of inertial effects for the formation of dislocation dipoles [277].

7.3.2.4 Relationship to experiments and mesoscale modeling

An important difference between the present MD simulations and the experimental situation is the neglect of the obstacle randomness. Except for special situations like solid solutions [109], current atomistic simulations can not take into account the effect of obstacle randomness in dislocation-obstacle interactions. Atomistic simulations of dislocation-obstacle interaction

therefore can usually not provide statements directly relevant to experiments. However, in the framework of multi-scale modeling [278] atomistic simulations of idealized dislocation-obstacle interactions can be used to inform mesoscopic models. Atomistic simulations are especially valuable to provide parameters for meso-scale models, to validate these models and to suggest refinements of the models based on the observed microscopic interaction mechanisms.

In sec. 2.1.3.5 the model by Schwarz and Labusch [73] of a dislocation interacting with a random array of weak obstacles was introduced. In the following the simulation results are compared with the results of Schwarz and Labusch [73]. It is furthermore shown how the inclusion of atomistic information into this model can lead to a better agreement with experimental data [88].

As stated in sec. 6.3, the dynamical depinning stress τ_d in the simulations corresponds to the lower critical resolved shear stress (CRSS) $\tau_{d,l}$ in the model of Schwarz and Labusch [73]. According to their model, for the case of point obstacles (normalized obstacle width $\eta_0 = 0$), the dependence of the normalized $\tau_{d,l}$ on the normalized drag coefficient γ should be independent of the obstacle arrangement [73]. The slope of $\tau_{d,l}$ in Fig. 2.6 should in this case be equal to γ [73]. With the definitions of the normalized parameters of the Schwarz-Labusch model (Eqs. 2.52 - 2.54) this can be expressed as

$$\frac{\tau_d b L}{2\Gamma(\cos \Phi_c)^{3/2}} = \frac{BL}{\sqrt{4\Gamma m_0 \cos \Phi_c}}. \quad (7.19)$$

Using the definition of τ_c , Eq. 2.11, and the expression for the mass of an edge dislocation, Eq. 2.30, the above equation can be written as

$$\frac{\tau_d}{\tau_c} = B(T) \frac{L}{2m_0 c_t} \sqrt{(1-\nu)(1-c_t^4/c_l^4)}. \quad (7.20)$$

The drag coefficient $B(T)$ of Ni_{II} has been determined in sec. 7.2.2. The appropriate dislocation mass m_0 for the simulation set up is given in Tab. 7.3. With these values Eq. 7.20 yields $\tau_d/\tau_c = 0.0014 \text{ K}^{-1}$ for $L = 267 \text{ \AA}$ and $\tau_d/\tau_c = 0.0007 \text{ K}^{-1}$ ($L = 138 \text{ \AA}$). Given the errors of the fits involved in the determination of m_0 , $B(T)/T$ and τ_d/τ_c , these values are in good agreement with the slopes determined from the simulations, Tab. 6.3. The model of Schwarz and Labusch [73] thus provides an adequate description for the functional dependence of $\tau_{d,l}$ for point obstacles. The qualitative trend of less steep slopes for larger obstacle sizes in Tab. 6.3 is also captured by Fig. 2.6. The absolute values of τ_d (Tab. 6.2) are however underestimated by Fig. 2.6. Furthermore, the detailed analysis of the kinetic energy involved in the dislocation-void interaction showed no strong dynamic effects at $\gamma = 0.08$, which were predicted by Schwarz and Labusch for $\gamma \ll 1$ [73].

The model of Schwarz and Labusch was also used by Fusenig and Nembach to interpret their data on the temperature dependence of the CRSS of precipitation hardened copper [88]. The CRSS determined by compression tests are shown in Fig. 7.15a for different temperatures T and different volume fractions f of cobalt precipitates. The normalized damping coefficient γ calculated with Eq. 2.53 by Fusenig and Nembach [88] is shown for $f = 0.023$ in Fig. 7.15b (dashed line).^s The experimental CRSS corresponds in this case to the upper CRSS $\tau_{d,c}$ in the Schwarz-Labusch model [88]. The appropriate obstacle width was determined to $\eta_0 \approx 0.1$. Therefore the curve for $\eta_0 = 0$ in Fig. 2.6 was used for the discussion [9, 88], it is shown

^sThe matrix in the system Cu-Co is nearly pure Cu [9], damping of the dislocation motion by solute atoms can therefore be neglected.

separately in Fig. 7.15c. With the γ -values determined by Fusening and Nembach (Fig. 7.15b), the Schwarz-Labusch model (Fig. 7.15c) however does not match the experimental data. With these values Fig. 7.15c predicts significant inertial effects at room temperature (RT), whereas below 100 K no changes of the CRSS are expected (see the black lines in Fig. 7.15). This discrepancy can be resolved by using in Eq. 2.53 the appropriate value of m_0 instead of $m_0 = \rho b^2$ as used in [88]. The line-tension Γ was calculated by Fusening and Nembach using the factor $\log(L/b)$ with $L \approx 30$ nm [88]. Determining m_0 by using this value in Eq. 2.30 leads to a factor of about 1.8 by which the results of Eq. 2.53 in Fig. 7.15b have to be multiplied. Considering further as lower cut-off radius $7b$ as determined in Tab. 7.3 instead of b , the γ used in [88] (dashed line in Fig. 7.15b) should be multiplied by 2.3, resulting in the red curve in Fig. 7.15b. With the rescaled γ , the Schwarz-Labusch model (Fig. 7.15c) describes well the temperature dependence of the experimentally determined CRSS. Especially only relatively small inertial effects are expected at room temperature.

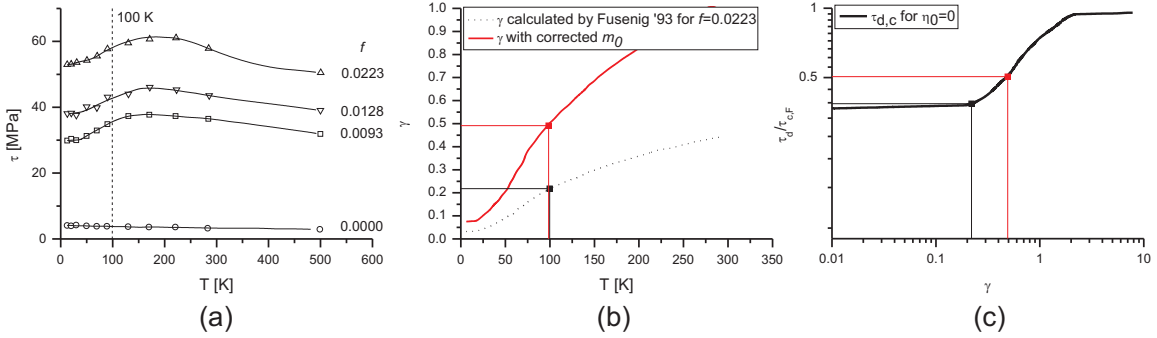


Figure 7.15: a) Experimentally determined CRSS of copper-rich copper-cobalt single crystals versus the temperature T_D at which the specimens have been deformed (from [88]). The average particle radius is $r \approx 2.9$ nm, f indicates the volume fraction of the precipitates. b) Reduced damping constant γ calculated from experimental values with Eq. 2.53 (dashed line, according to [88]) and rescaled by the appropriate dislocation mass (red line). c) Normalized CRSS vs γ according to [73], see also Fig. 2.6.

Figure 7.15a shows that the relative reduction of $\tau_{d,c}$ by inertial effects from $T = 200$ K to 12 K is about 15% (for $f = 0.0223$, 20% for $f = 0.0093$). This is much less than the reduction of about 40% predicted by the model of Schwarz and Labusch, Fig. 7.15c. This discrepancy can be explained by resorting to recent MD simulations by Shim and Wirth [279]. Their simulations of the interaction between an edge dislocation and a coherent cobalt precipitate in Cu revealed that at temperatures below about 250 K a new interaction mechanism becomes active: at low temperatures, the trailing partial bypasses the precipitate with the Orowan mechanism, whereas it shears the precipitate at high temperatures. As actually the strength of the precipitates increases with lower temperature, the inertial effect is significantly larger than the above estimated 15% which is obtained with the lower, high temperature obstacle strength.

From the comparison with the experiment [88] and the MD simulations it can be concluded that the model by Schwarz and Labusch [73] captures essential aspects of inertial effects in the interaction of underdamped dislocations with a random array of obstacles. The comparison furthermore shows the importance of the choice of appropriate values for Γ , c_t , m_0 and B in modeling dynamic dislocation effects. The line tension Γ should be calculated by using in

Eq. 2.4 the mean obstacle spacing L as outer cut-off radius (see also [9]) and a reasonable estimate for the lower cut-off radius. The effective mass of the dislocation can then be obtained by Eqs. 2.27 and 2.30. The quantitative results of Hiratani *et al.* [77, 79, 80] obtained with $m_0 = \rho b^2/2$ should therefore be regarded with caution.

The used simulation set-up does not allow to make direct predictions for experiments. However, according to [73] the deviation of the measured CRSS $\tau_{d,c}$ from the overdamped CRSS τ_c is correlated with the deviation of $\tau_{d,l}$ from τ_c , see Fig. 2.6. The existence of dynamical effects in our simulations therefore suggest that inertial effects could be measured at relatively high temperatures in fcc metals irradiated under conditions favoring the formation of closely spaced voids. Under such conditions dynamic effects in dislocation-obstacle interactions might be of importance for the explanation of plastic instability and creation of cleared channels in irradiated metals [113, 271].

Besides from the interaction of dislocations with localized obstacles like voids and precipitates dynamic effect might also be important in the deformation of micro- to nanoscale samples or nanocrystalline metals. These show usually a significantly increased yield stress [280] compared to their bulk or coarse-grained counterparts. When these samples deform plastically, the dislocations in the samples are subjected to high stresses, and therefore can attain the high velocities required for inertial effects. For example, recent analysis of the velocity distribution in DD simulations modeling micro compression test (see e.g. [281–283]) showed that a significant fraction of the dislocations participating in strain burst have velocities which are in the relativistic regime [284]. Furthermore the length of dislocation segments is limited by the dimensional constraints. The probability of underdamped motion of dislocation segments is therefore increased. Compared to the deformation of large scale samples where the plasticity is carried by many dislocations, the effect of the individual dislocation-obstacle or dislocation-dislocation interactions should become more pronounced at small scales. Individual strain burst events therefore could show signs of inertial effects. This could for example be studied by performing micro compression tests at low temperatures.

Chapter 8

Conclusion I: Dislocation Motion and Interaction with Obstacles

The properties of static and dynamic dislocations were studied in atomistic simulations using different potentials for Al, Ni and Cu. This large scale study provides a database of dislocation properties which can be used directly in mesoscale simulations of plasticity [263–265]. It furthermore enabled the correlation between properties of static dislocations and dynamic dislocation properties, thus leading to new physical insights.

From the static calculations of straight dislocations the following conclusions could be drawn:

- The dissociation distance d between the partial dislocations was found to be consistently larger than the one calculated by anisotropic elasticity theory using the stacking fault energy γ_{sf} of the potentials. It could be shown that the generalized Peierls model by Schoeck [25] using an adequate representation of the generalized stacking fault (GSF) curve of the potential provides the same results as the atomistic simulations. The necessity to include information on the GSF for a correct calculation of d has important consequences for the calculation of stacking fault energies from experiments and subsequently for the quantitative interpretation of results obtained by atomistic simulations.
- Evaluation of the Peierls stress τ_P revealed large differences among the different EAM potentials for the same material. The current EAM potentials which use experimentally determined γ_{sf} can only provide an order of magnitude estimate of the Peierls stress of the modeled material.

In addition to the determination of the drag coefficient of dislocations in Al, Ni and Cu, the study of moving dislocations under various stress and temperatures revealed the following:

- Moving dislocations exhibit two distinct velocity regimes. Whereas no qualitative differences between edge and screw dislocations exist in the low velocity regime, the onset of the temperature insensitive high velocity regime and the stress dependence of the dislocation velocity in the high velocity regime is different for edge and screw dislocations.

- In the low velocity, drag controlled regime the drag coefficient B shows an approximately linear increase with temperature up to the Debye temperature. The simulated values are comparable to experimental values. Although the different potentials lead to significantly different core properties, no significant differences in the dislocation drag could be found between the potentials modeling the same material. Screw dislocations however showed a consistently larger B than edge dislocations. To the authors knowledge no current dislocation theory can explain this difference.
- By fitting the equation of motion to the dislocation trajectories it was possible to determine the effective dislocation rest mass m_0 from atomistic simulations. A core cut-off radius r_0^m was defined to determine m_0 . Contrary to the usual mathematical core radius r_0 , motivated by the partition of the dislocation energy into strain energy and core energy, m_0 has direct physical relevance.
- The crossover between the the low velocity drag controlled regime and the high velocity regime is attributed to the onset of phonon radiation leading to strong energy dissipation of the moving dislocation. It is speculated that the overlap of the partial dislocation cores at high velocities leads to a new mode of radiation friction. The dislocation velocity at which the dynamic dissociation distance is about the same as the partial dislocation width can be calculated from the relativistic contraction of the stress field. It gives a good estimate for the onset of the high-velocity regime.

The discussion of the simulation of the interaction of edge dislocations with rows of equally spaced voids of different sizes lead to following conclusions:

- For the voids studied, the critical stress τ_c necessary to pass the voids as determined from the static calculations is significantly lower than the prediction of the model by Scattergood and Bacon [234]. A model, based on the work necessary to recreate the annihilated line energy, was developed to explain the atomistic results. For large voids and typical spacing the model provides approximately the same results as the equation by Scattergood and Bacon.
- The simulation of dynamic dislocation - obstacle interactions at different temperatures showed direct evidence of inertial overshooting. Dynamical passing of the obstacles was possible at significantly lower stresses than the static critical stress [263,272]. A detailed analysis of the energetic contributions affirmed that the kinetic energy is indeed the cause of the dynamic effect. A dynamic line tension model was subsequently developed to estimate the importance of inertial overshooting for different obstacle strengths, - spacings and temperatures [273]. This model as well as dislocation dynamics simulations which include atomistic information of dislocation inertia and drag reproduced very well the atomistically determined τ_d [263, 273].
- The temperature dependence of the dynamical depinning stress agrees well with the model of Schwarz and Labusch [73] for the lower critical resolved shear stress. The atomistic information on the dislocation mass can be used to provide a better estimate for the normalized drag coefficient in the experiments of Fusenig and Nembach [88]. The corresponding rescaling of the drag coefficient lead to a better quantitative agreement between the experimentally observed temperature dependence of the CRSS with the Schwarz-Labusch model. The model of Schwarz and Labusch [73] therefore captures

essential aspects of inertial effects in the interaction of underdamped dislocations with a random array of obstacles.

Chapter 9

Outlook I

Several ideas how this work could be extended have already been presented in the respective sections. They will be summarized here, together with open questions and possible areas of future investigations.

Properties and modeling of static dislocations In the light of the present study, experimental values of the stacking fault energy determined by measurement of the dissociation distance d by TEM observation and then analyzed simply by the Eq. 2.18 might need some correction. Accurate first-principles calculations of the generalized stacking fault (GSF) curve used in generalized Peierls-Nabarro (PN) type models can lead to more accurate calculations of d and would allow a reinterpretation of the experimental data [243]. As the amount and accuracy of ab-initio calculations increases, fitting of EAM potentials to first-principle GSF data should become more common, thus e.g. allowing a more accurate determination of the Peierls stress from atomistic simulations.

A concerted study with atomistic methods and the generalized PN model using the same *model* GSF curves could provide valuable insights into the processes during the surmounting of the Peierls barrier. A question of particular interest would be how the details of the GSF curve influence the cooperative motion of the partial dislocations over the Peierls barrier [250, 258].

Moving dislocations Compared to the study of the properties of static dislocations, detailed atomistic investigations of moving dislocations are relatively recent. There are therefore still many open questions, concerning for example the reason for the higher drag coefficient of screw dislocations. The present study could be directly extended to investigate in more detail the dynamics of mixed dislocations. It would for example be interesting to study whether the drag coefficient of mixed dislocations depends on the direction of motion, like it is the case for the Peierls stress [94]. Further studies are also necessary to analyze in more detail the nature of the radiation friction stress at low temperatures and velocities. Here a combination of the fitting procedure for the equation of motion to the dislocation trajectory and a detailed analysis of the emitted waves (following e.g. [68]) in realistic crystal structures could provide valuable information for models of radiation friction.

The existence of a high velocity regime has only recently been reported. Further atomistic and especially experimental studies of the high velocity regime are highly desirable to verify the suggested mechanism of crossover and to further elucidate the exact mechanism behind the observed strong radiation of phonons below c_t .

High velocity dislocations can be expected under shock loading conditions. However, the dynamic properties of dislocations at high volumetric compressions leading to hydrostatic pressures P of upto several tens of GPa are still poorly studied. Preliminary simulations of dislocation motion in Cu under shock loading conditions [231] showed significant differences in the dislocation motion compared to $P \approx 0$. For example the stacking fault energy and the elastic constants change in a way that the motion of the partial dislocations is only very weakly coupled. Further studies in this direction seem promising, are however complicated by the required very large systems and small time steps.

In the present study the drag on single, straight dislocations was studied. This situation is comparable to the experimental situation where the displacements of single dislocations after a stress pulse is measured [16]. Under usual experimental conditions, however, other extrinsic damping mechanisms come into play [16]. When a dislocation encounters a local obstacle, additional phonon radiation and waves on the dislocation are induced which can lead to additional dragging of the dislocation. A possible way to study this effect is to fit the equation of motion to the trajectory of dislocation after its interaction with an obstacle. The strain field of a moving dislocation can induce oscillations on pinned [285] and moving dislocations, leading to a kind of flutter effect. New statistical physics approaches to describe collective phenomena of dislocations [286] open up new ways to provide information on the stress fluctuations at a dislocation caused by the surrounding moving dislocations necessary to develop a theory of this effect.

Dynamics of dislocation - obstacle interactions Most aspects related to inertial effects like the existence of dynamic unzipping events have to be studied by mesoscopic models. Only models which take the random obstacle distribution into account can provide experimentally verifiable conclusions. Atomistic simulations can however be used to study fundamental aspects of inertial effects. For example the influence of obstacle size on inertial effects could be studied by modeling equally spaced coherent precipitates of different sizes but equal obstacle strength by adequately modifying the atomic interaction potential. This allows also to study the influence of attractive compared to repulsive obstacles on the inertial effect.

Further areas of research Dynamic effects can be expected whenever the driving forces for dislocation motion vary abruptly. As discussed, this is the case when a moving dislocation meets with obstacles. However, the dislocation inertia can become important also in other situations. This outlook is closed by pointing out some areas of research which could benefit from the present study on dislocation drag and inertia.

The *interaction of dislocations with elastic waves* has recently attracted renewed interest from both the theoretical [265, 287, 288] and from the experimental side [289, 290]. For the study of such interactions the use of realistic values for the drag coefficient, dislocation line tension and -mass are important. The study of Walcker *et al.* suggests that for typical application condition of surface acoustic wave (SAW) filters [290] at frequencies in the GHz range, dislocation motion is underdamped and the dislocation mass has to be taken into account. Under special conditions the dislocation can attain relativistic velocities under the subtle strains introduced by SAWs [289] so that the velocity dependence of the mass should not be neglected. At higher stresses dynamic depinning and repinning as observed in Fig. 6.7 could be possible for pinned dislocations vibrating at high frequencies.

The monitoring of *acoustic emission* by fast moving, underdamped dislocations recently

proved a promising tool to study the intermittent character of plastic flow caused by dislocation avalanches [291, 292]. The interpretation of the amplitude and energy of the acoustic wave in terms of dislocation dynamics and plastic deformation is however based on a model by Rouby *et al.* [293] which assumes instantaneous acceleration of dislocations. A more realistic treatment of underdamped dislocation motion including acceleration and deceleration phases could eventually lead to more precise models of acoustic emission sources.

The use of realistic mobility laws including dislocation acceleration might also be useful in the modeling of *dislocations near cracks*. At high loading rates the inertia of dislocations could have an influence on the size of the plastic zone around a crack tip. This might be of special relevance for transition metals or semiconductors which show a temperature and loading rate dependent transition from brittle to ductile failure.

Part II

Dislocation Nucleation and Multiplication at Crack Tips

The processes involved in the generation of dislocations at crack tips were studied for dynamically propagating cracks and their interaction with obstacles as well as for static cracks and their interaction with preexisting dislocations. Whereas the nucleation of dislocations from undisturbed static and dynamic cracks has already been the subject of several simulation studies, the interaction of cracks with defects, and especially dislocations, has not yet been investigated in full three dimensional detail. The study of the processes during the interaction of dislocations with a crack front is at the center of the second part of this thesis.

The following fracture simulations were performed on the so called γ -orientation shown in Fig. 9.1. It provides two sets of symmetrically arranged slip planes (a) and (b) (in Thompson tetrahedral notation). These planes contain a Burgers vector normal to the (110) cleavage plane. A second symmetric set of slip planes (c) and (d), oblique to the cleavage plane and the crack front, contain the crack propagation direction which is parallel to a possible slip direction.

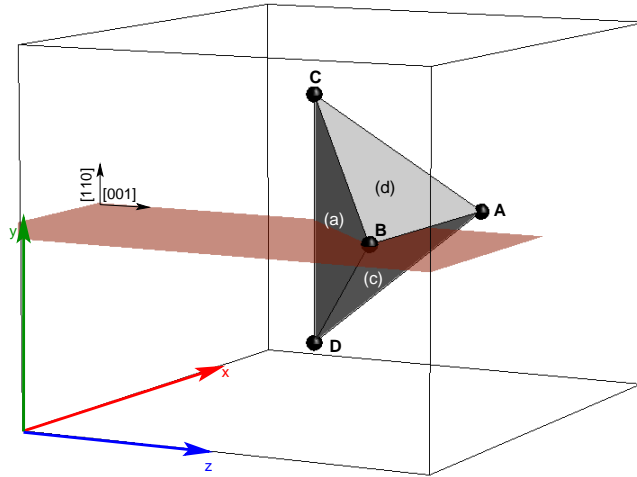


Figure 9.1: Orientation of the slip planes with respect to the crack front in the γ -orientation. The Thompson tetrahedron notation is applied to identify the Burgers vectors and glide planes.

As described in the methods section 3.2.2, two different loading conditions were used: plane strain deformation along the y -axis and straining along the y -direction combined with the Poisson contraction in z direction, which models the plane stress case. All simulations were performed using the Ni_{II} potential by Mishin [213]. Most large scale simulations were preceded by simulations on smaller systems. They allowed to develop and test the simulation methods. These simulations will frequently also be presented, as in combination with the large scale simulations they provide a possibility to assess finite size effects in the interaction mechanisms between cracks and dislocations. The effect of the boundary conditions on the dislocation - crack interactions are also addressed in appendix C.

Chapter 10

Properties of straight cracks

10.1 Griffith load

Atomically sharp cracks were introduced at the predetermined Griffith load according to the method outlined in sec. 3.2.2 and subsequently relaxed. Except for the small configuration under plane stress like conditions, this method produced stable cracks. The displacement field of the relaxed cracks was subsequently rescaled and added to the original sample to produce an over- or underloaded crack. Table 10.1 shows the Griffith strain and loading at which a stable relaxation of the crack became impossible.

This stability range is relatively small compared to the lattice trapping range of 1-6% in 2D simulations [294]. This is most probably due to the fact that in the region of the 2D dynamic boundary conditions the position of the crack front differs from the position of the crack within the bulk of the sample, see Fig. 10.1. The advance of the crack front by about $3b$ indicates that the net force in the crack opening mode on the atoms in the 2D dynamic boundary region is larger than the net force acting on the atoms within the box. The constrained motion in the boundary layers results in plane strain conditions at the surface – like within the sample.

However, atoms at the surface have also less bonds, which in the EAM-framework are stronger [201]. In the present case the net effect leads to a reduced resistance towards crack opening within the 2D dynamic boundaries. This boundary effect can constantly provide kinks necessary for the crack propagation by kinks, thus significantly reducing the lattice trapping.

Blunted cracks were produced by the removal of one or three (110) layers. Although blunting provided stability against crack closing, it did not significantly increase the stabil-

size [nm ³]	stress state	ϵ_G	stability range [ϵ_G]
$25 \times 25 \times 25$	plane strain	0.0343	0.99 - 1.01
$25 \times 25 \times 25$	plane stress	0.0433	-
$75 \times 75 \times 75$	plane strain	0.01896	0.99 - 1.002
$75 \times 75 \times 75$	plane stress	0.02738	0.99 - 1.005

Tab. 10.1: Griffith load ϵ_G and the loading under which an atomically sharp crack became unstable upon relaxation. The sharp crack in the small sample could not be stabilized under conditions modeling plane stress loading because dislocations were emitted at all loads.

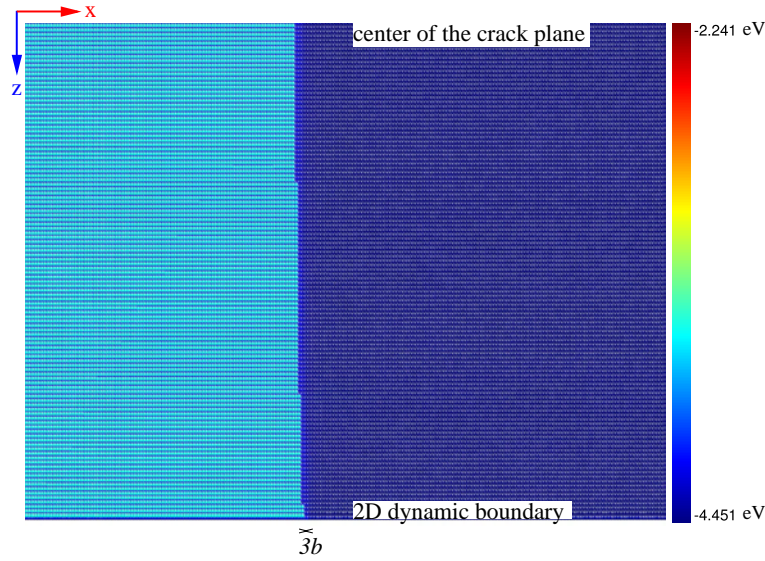


Figure 10.1: Top view on a part of the cleavage plane of an atomically sharp crack relaxed at ϵ_G (plane strain). The atoms are colored according to their potential energy. In the 2D dynamic boundary region the crack has advanced by $3b$ relative to the crack front in the middle of the box.

ity against crack advance. The reason can be seen in Fig. 10.2a. During the relaxation of the blunted crack tip at loads close to ϵ_G atomically sharp cracks develop from the blunted crack tip. This re-initiation of a sharp crack from blunted crack tips by unequal stretching of the crack tip bonds has also been observed in two dimensional calculations [294]. This phenomenon is attributed to the nonlinearity of the atomic interaction at high strains [294]. In three dimensions the breaking of the crack tip symmetry does not need to occur homogeneously along the crack front. Therefore atomic steps on the sharp cracks frequently formed upon relaxation of blunted cracks close to ϵ_G , see Fig. 10.2b.

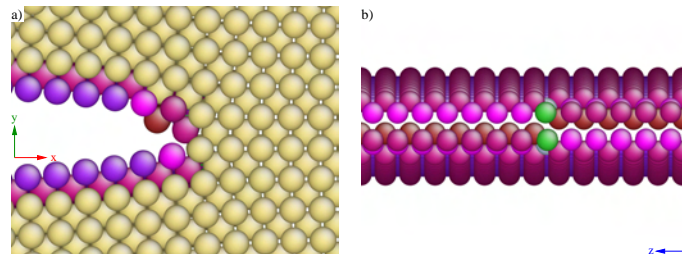


Figure 10.2: Relaxed structure of a crack blunted by removal of one (110) layer at $0.96\epsilon_G$ (small sample, plane strain). During the relaxation an atomically sharp crack developed from the initially blunted pre-crack (a). Monoatomic steps on the sharp crack as shown in b) were frequently produced during this process. The atoms are colored according to their coordination number. In a) all atoms are shown, in b) only atoms in imperfect coordination are displayed.

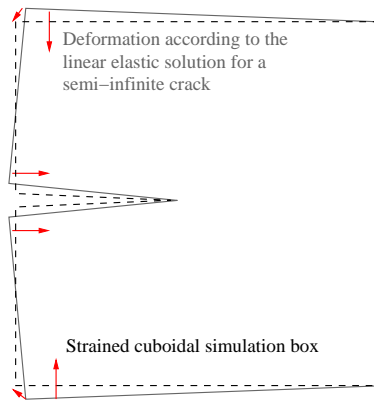


Figure 10.3: Sketch of the relationship between the linear elastic solution of a semi-infinite crack in an infinite continuum (solid line) and the finite simulation box (dashed line). The boundary conditions lead to a modification of the stress field.

10.2 Stress field of the cracks

The local atomic stress tensor (see sec. 3.3) was calculated from the relaxed configurations of blunted cracks. Fig. 10.4 shows the different stress components as interpolated from a vertical slice of atoms from the middle of the sample. The figure shows also the plane strain stress field of a semi-infinite sharp crack in a infinite medium calculated from anisotropic elasticity theory [295]. The stress field obtained by the atomistic calculations was nearly constant in crack front direction. From $L_z/2$ to $L_z - 5b$ the main stress components changed by less than 1%.

Ideal plane stress conditions are characterized by $\sigma_{zz} = 0$. This stress state is a mathematical idealization. A vanishing σ_{zz} can thus not be expected for the boundary conditions used to model plane stress loading. However, by allowing for the Poisson contraction the σ_{zz} stress component is significantly reduced compared to the plane strain loading, see Fig. 10.4. Of course also the other components of the atomistic calculations under plane strain and plane stress loading differ from the anisotropic elastic calculations. The reason is that the boundary conditions of the simulation box lead to a superposition of additional stress fields. The displacement field of the semi-infinite sharp crack in the infinite medium would lead to a deformation of the initially cuboidal simulation box. The fixed boundary conditions enforce orthogonal side surfaces and lead amongst others to a compressive stress field on the crack surfaces, see the sketch in Fig. 10.3.

These differences are clearly visible in the stress field of the simulated cracks, Fig. 10.4. For the small system, the difference from the anisotropic elastic solution was more pronounced than for the large system displayed in Fig. 10.4. However, in the immediate surroundings of the crack tip, the characteristics of the atomistic stress field corresponds to the K -dominated field of the linear elastic solution.

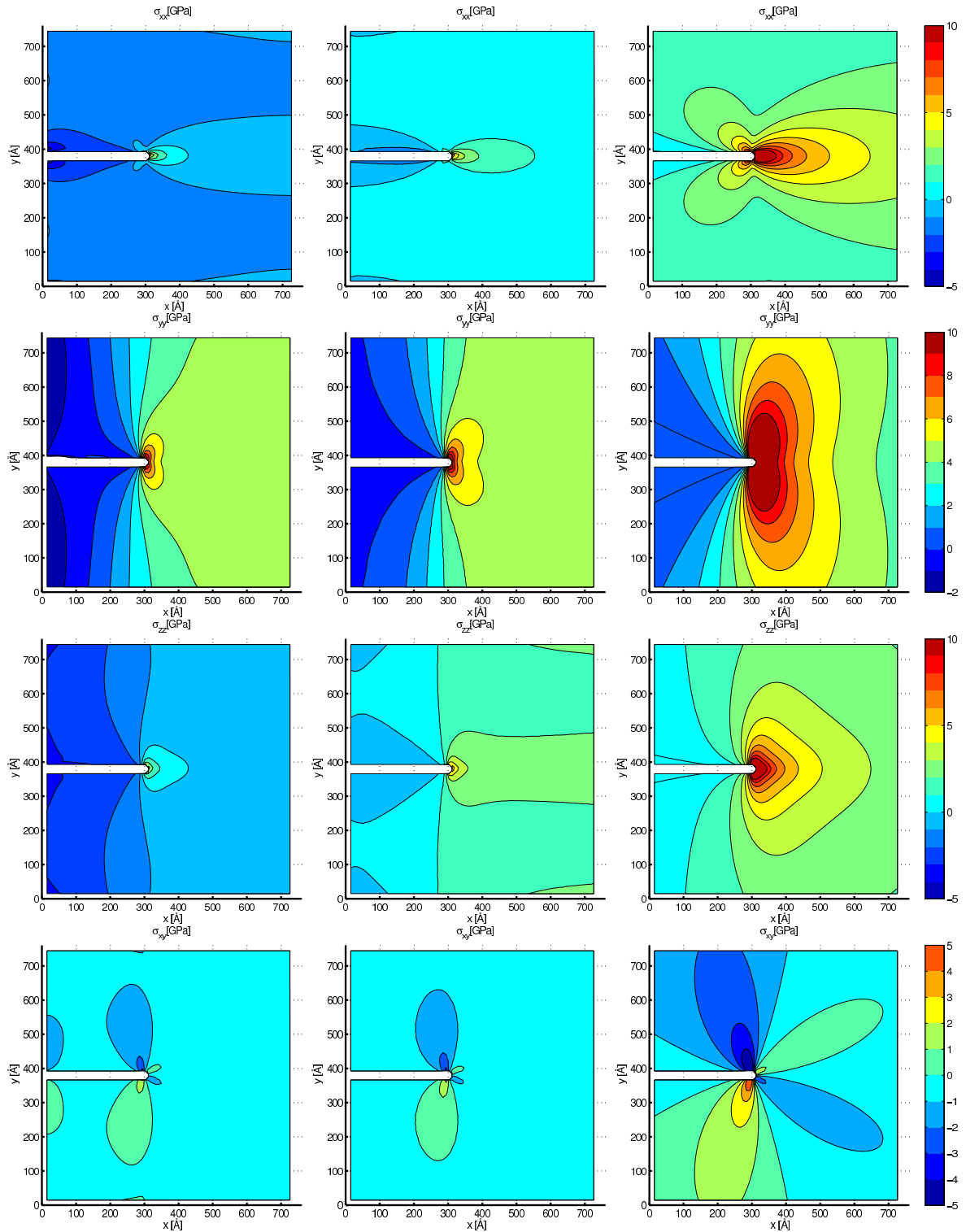


Figure 10.4: The components of the stress field of the crack in the large sample relaxed under conditions modeling plane stress at $\epsilon = 0.024$ (left) and relaxed under plane strain conditions at $\epsilon = 0.018$ (center) compared to the anisotropic plane strain solution with K_I for $\epsilon = 0.018$ (right). Note the different color scales for the different stress components (from top to bottom: σ_{xx} , σ_{yy} , σ_{zz} , σ_{xy}).

10.3 Stability of imperfect crack fronts

In addition to the study of the stability of perfect, sharp and blunted crack tips, some examples of crack fronts containing defects like steps or kinks were simulated. Most of the simulations were performed on the small system under plane stress loading, which showed a strong tendency to dislocation emission.

A first set of simulations consisted of crack fronts blunted by removal of one (110)-layer in which a step was introduced by displacing the atoms on two sides according to the passage of a dislocation with Burgers vector $\mathbf{b} = BC(d)$ or $\mathbf{b} = DB(a)$ (Thompson tetrahedral notation). The configurations resulting from the relaxation at a load of $0.95\epsilon_G$ are shown in Fig. 10.5. Upon relaxation, steps created according to the passage of one dislocation remained stable. A step of $2\mathbf{b}$ remained stable when the cut was made along the (d)-plane (Fig. 10.5c). The $2\mathbf{b}$ step was however unstable when it formed an acute angle with the crack front (Fig. 10.5d). Dislocation were emitted in both cases when the crack surfaces were displaced by $3\mathbf{b}$ (Fig. 10.5e,f).

Steps on atomically sharp cracks were frequently produced during relaxation of blunted crack at loads close to ϵ_G , like in Fig. 10.2b. Like the artificially created steps, these monoatomic steps did not lead to dislocation emission upon relaxation. Even during dynamic crack propagation these steps could remain stable for some time. This will be followed up in sec. 10.4.

Relaxation of $3 - 6\mathbf{b}$ wide kinks on atomically sharp cracks in the small sample under homogeneous plane strain loading at $0.96\epsilon_G$ resulted in perfect straight cracks. No dislocations were emitted during the relaxation of kinked cracks.

The dynamics of the interaction between lattice dislocations and cracks will be presented in detail in the next chapter. However, if the dislocation is initially positioned close to the crack tip, also static calculations can be performed. Fig. 10.6a shows the relaxed configuration of a 60° dislocation $DB(a)$ at the crack tip of a blunted crack at $0.95\epsilon_G$ on plane stress loading. The dislocation processes will be analyzed later, however one can note that the relaxation of a dislocation intersecting the crack front did not lead to the emission of dislocations. The relaxed configuration was subsequently equilibrated at 100 K. Also during this equilibration period no dislocations were nucleated at the crack tip. However, the dislocation $DB(a)$ cross-slipped at a distance from the crack front onto the (c)-plane and later cut the crack front, see Fig. 10.6b.

10.4 Dynamic fracture and dislocation emission

To study crack instability and dislocation emission during dynamic fracture, the displacement field of sharp cracks under plane strain conditions were rescaled to produce an overloaded starting configuration for MD simulations at 0 K. The present simulation set-up is clearly not intended for the study of dynamic fracture, as the running distance is very short, and sound waves are reflected by the boundaries (see e.g. [296] for more adequate boundary conditions). However, in order to be able to later compare dislocation generation during dislocation-crack interactions with the dislocation emission from dynamic cracks, the same set-up was used for both studies. The relevant wave velocities for the study of dynamic fracture in the γ -oriented Ni are $c_l = 60.14 \text{ \AA/ps}$, $c_{t_1} = c_{t_2} = 37.74 \text{ \AA/ps}$, and $c_R = 32.97 \text{ \AA/ps}$, see Eqs. 2.41 and 2.43.

At an overload of $1.1\epsilon_G$ brittle crack propagation with a steady state velocity of $v \approx$

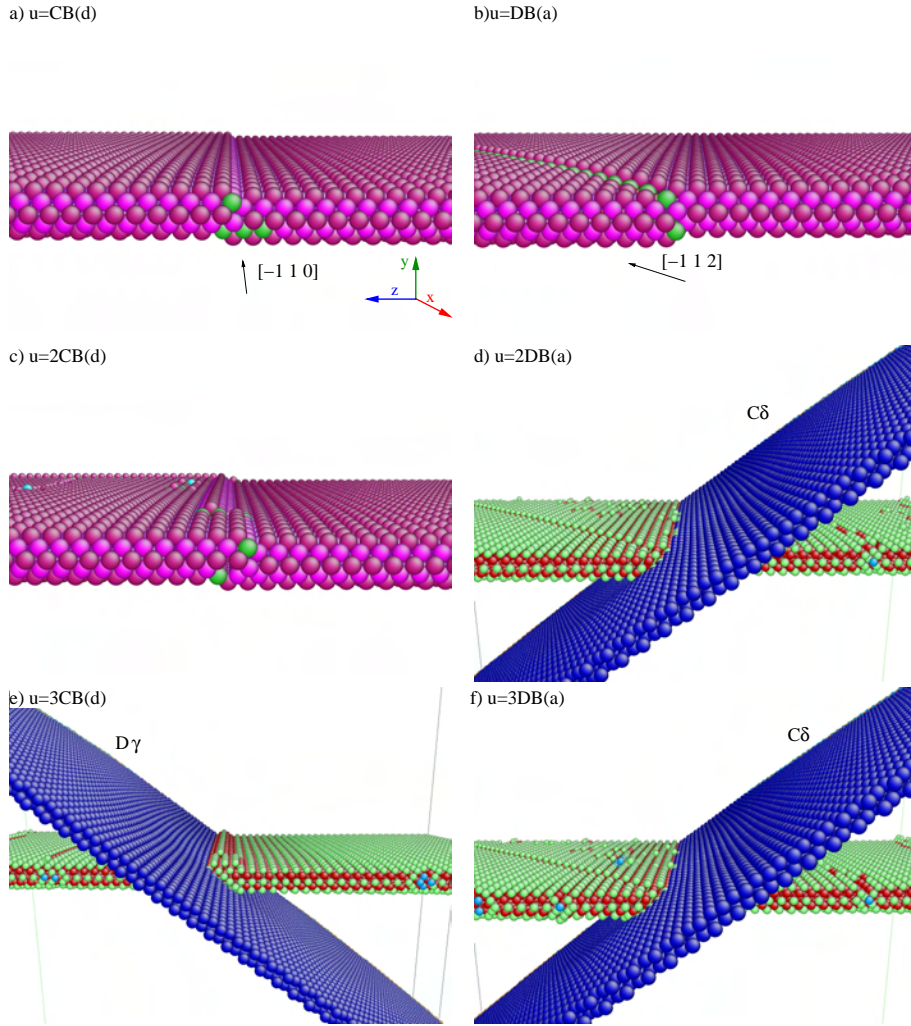


Figure 10.5: Final configurations after relaxation of crack fronts cut according to the passage of a dislocation with Burgers vector $\mathbf{b} = u$ (small sample, plane stress loading at $0.95\epsilon_G$). In a)-c) no dislocation has been nucleated and only atoms with coordination number $\neq 12$ are shown. In the configurations d)-f) a dislocation has been nucleated during relaxation. The atoms are colored according to their CNA-value, thus showing the stacking fault produced by the nucleated dislocations.

$10\text{\AA}/\text{ps} \approx 0.3c_R$ took place. At an overload of $1.2\epsilon_G$ the crack propagated only for about 12 ps before emitting dislocations. The crack velocity attained just before dislocation emission was close to $0.4c_R$. This is in good agreement with the 2D simulations of dynamic fracture in Ni of Gumbsch *et al.* [175] where the maximum steady-state velocity is found to be limited to 40% of the Rayleigh wave speed.

Snapshots from the dislocation nucleation process are shown in Fig. 10.8. The first dislocations were generated at the boundary of the 2D-dynamic region. However, about 1 ps later homogeneous dislocation nucleation occurred on all slip planes along the entire crack front. Only partial dislocations were formed during the simulation run. According to Van Swygenhoven *et al.* [31] such a behavior can be expected for low ratios of stacking fault energy to unstable stacking fault energy, which is the case in Ni_{II} ($\gamma_{sf}/\gamma_{usf} = 0.45$, see appendix

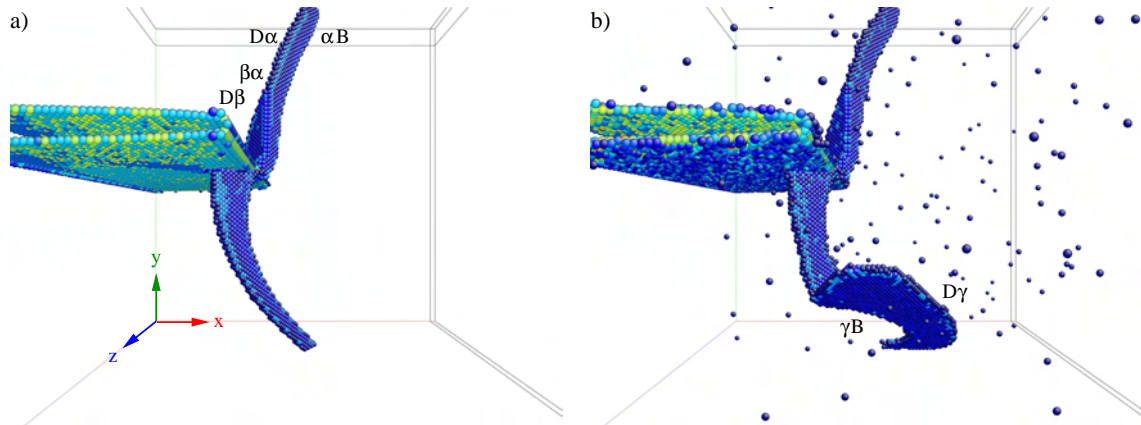


Figure 10.6: Blunted crack with 60° dislocation $DB(a)$ at $0.95\epsilon_G$ (plane stress, small sample). The atoms are colored according to the centro-symmetry parameter. The final configuration after relaxation is shown in a). b) is a snapshot from the equilibration of the sample at 100 K showing cross-slip of the dislocation. No dislocations were emitted from the crack front during relaxation and thermalization. The details of the dislocation processes will be presented in chap. 11.

A). A distinctive feature of the nucleation process is that the partial dislocations on oblique and vertical slip planes form together in most cases. This leads to the formation of stair-rod partial dislocations. This can best be seen in the back view at $t = 19$ ps in Fig. 10.8.

To the authors knowledge such "co-nucleation" has not yet been reported in the literature. The studies on the γ -crack of Kimizuka *et al.* [187] in Al and Cu and the studies by Abraham *et al.* [35, 183] using a Lennard-Jones (LJ) potential however show that for the same crystal structure and crack orientation dislocation emission can exhibit very different characteristics for the same loading conditions. These differences probably arise due to different degrees of elastic anisotropy and differences in the atomic bonding. The simulation conditions used in [187] (constant loading at $\dot{\epsilon} = 2 \cdot 10^9$ 1/s) and in [35, 183] (4% strain) can however also be the cause for the observed differences in the characteristic of dislocation nucleation.

Fig. 10.7 shows the same type of co-nucleation in case of a propagating crack containing a step in the crack front. The step resulted from the relaxation of the blunted pre-crack. Contrary to the homogenous dislocation nucleation, localized dislocation nucleation close to the step occurred at relatively low overload. By the emission of the blunting dislocations αC and αD the local crack front orientation became parallel to $B\alpha$.

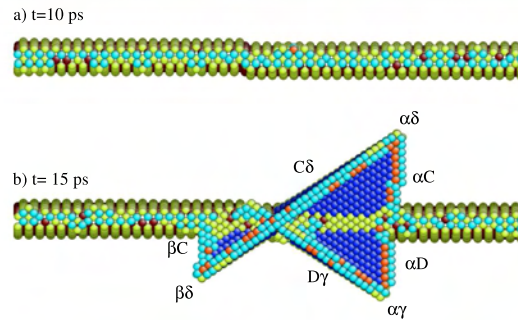


Figure 10.7: Emission of dislocations from a propagating sharp crack containing a monoatomic step ($1.025\epsilon_G$, small sample, plane strain). The atoms are colored according to their CNA value. From the different crack tip structure it can be seen that the emission of the blunting dislocations αC and αD led to a crack front orientation parallel to $B\alpha$.

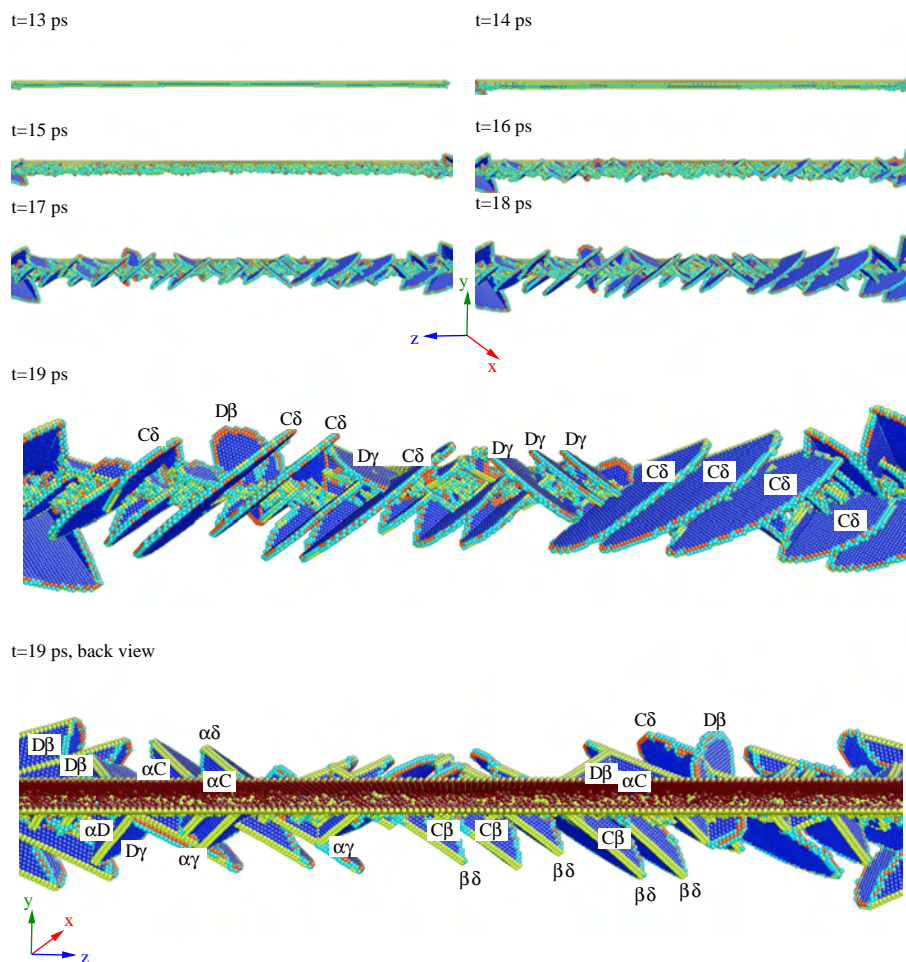


Figure 10.8: Emission of dislocations from a propagating sharp crack ($1.2\epsilon_G$, large sample, plane strain). The atoms are colored according to their CNA value.

10.5 Dynamic crack interacting with a void

To be able to compare the processes during dislocation-crack interaction with the interaction processes of a crack with an other defect, the interaction of a propagating crack with a void was studied. For this purpose the displacement field of a sharp crack at $1.1\epsilon_G$ was added to a configuration containing a relaxed void of radius $R_{\text{void}} = 10\text{\AA}$. As can be seen in Fig. 10.9 the void effectively pins the advancing crack front by causing the massive emission of dislocations. The process of partial dislocation emission corresponds to the previously described co-nucleation. The symmetric upwards and downwards emission of dislocations on the (a) and (b) -plane leads to a blunting of the crack tip by one Burgers vector. The crack front assumes a 'V'-shape with local crack front directions of βA and $B\alpha$. The crack front outside the 'V' can still propagate. It can penetrate the 'V' in a zipper-like way by subsequent emission of further dislocations on (a) and (b) . The consecutive creation of stacking faults leads to twined areas. It is interesting to note that no dislocations are nucleated at the void prior to its contact with the crack. Although the crack cleaved the surrounding material, the atoms on the void circumference were still partially in contact (not shown).

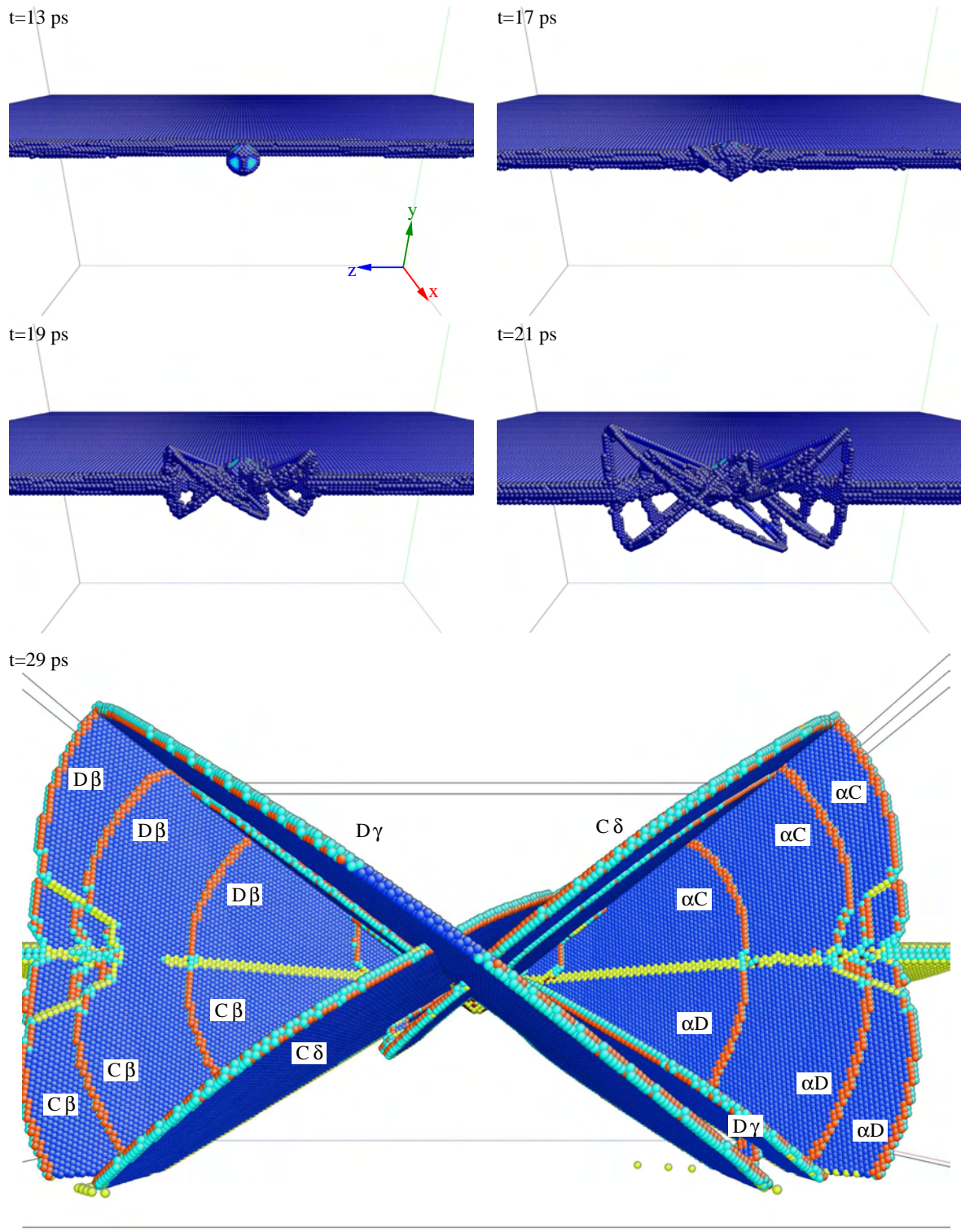


Figure 10.9: Interaction of a propagating crack with a void ($R_{\text{void}} = 10\text{\AA}$, $1.1\epsilon_G$, large sample, plane strain). For $t = 13 - 21$ ps only atoms with increased potential energy are shown, for $t = 29$ ps the atoms are colored according to their CNA value. The partial dislocations on the (b) and (c) as well as the partial dislocations on the (d) and (a) planes are connected by the respective stair-rod partial dislocations.

Chapter 11

Dislocations interacting with cracks

The interaction between dislocations and cracks is of course determined by the nature of the dislocation, i.e. its Burgers vector and glide plane, and the characteristics of the crack, e.g. blunted versus sharp. It is furthermore determined by the stress state, i.e. the loading with respect to the Griffith load ϵ_G and whether plane stress or plane strain conditions prevail. In addition, the relative orientation of the dislocation with respect to the crack and its impinging velocity can influence the dislocation-crack interaction.

The need of finite size simulation boxes has a number of consequences for the study of dislocation-crack interactions. The introduced dislocation is pinned at the boundaries. The initial distance of the dislocation from the crack therefore determines if, and with which curvature, the dislocation reaches the crack. The box boundaries furthermore put a limit to the dislocation motion and cause image forces on the dislocations. The rather small systems which can be simulated by MD lead to high Griffith strains. Therefore not only the loading relative to ϵ_G is important, but also the absolute strain. In highly strained samples artefacts due to nonlinear effects are possible.

Given the computational costs of the large scale simulations, it is clear that extensive parameter studies can not be performed. However, the influence of all the above parameters were at least studied in exemplary simulations. Other important factors like temperature or the effect of multiple dislocations on the same glide plane could however not be addressed.

The remainder of this chapter is organized as follows. First the simulation set-up is presented and symmetry considerations are used to reduce the number of dislocations which have to be included in the study. Next the simulations of dislocations interacting with static, blunted cracks and atomically sharp cracks will be presented in separated sections, followed by exemplary simulations of dislocations interacting with propagating cracks. Preliminary studies on small samples were used to quickly assess the most important features of the particular configuration for each dislocation orientation. The chapter closes with a summary of the simulation results. The simulation resulted often in very complex dislocation structures. For the sake of clarity, however, a detailed analysis is only presented for prevalent, characteristic processes.

11.1 Simulation set-up and symmetry considerations

To study the interaction of preexisting lattice dislocations with cracks, the displacement field of straight relaxed dislocations was added to the configuration of a stable crack as described

in section 3.2.2. In most of the simulations, the crack was blunted by removal of one (110) layer. Some simulations, however, were performed on sharp cracks or cracks blunted by removal of 3 (110) layers. To model the situation in the experiments by the Michot group (see sec. 2.2.2.1) most simulations were performed by modeling a similar "plane stress like" situation as described in sec. 3.2.2.

A typical example of a starting configuration is shown in Fig. 11.1. Only the atoms which have an increased potential energy and do not belong to the box boundaries are shown. Similar figures will be frequently used in the following. The initial position of the relaxed dislocation is indicated by its distance Δx from the crack front, measured within the cleavage plane. In Fig. 11.1 the dislocation will have to move a distance $l \approx 1.73\Delta x$ till it intersects the crack front.

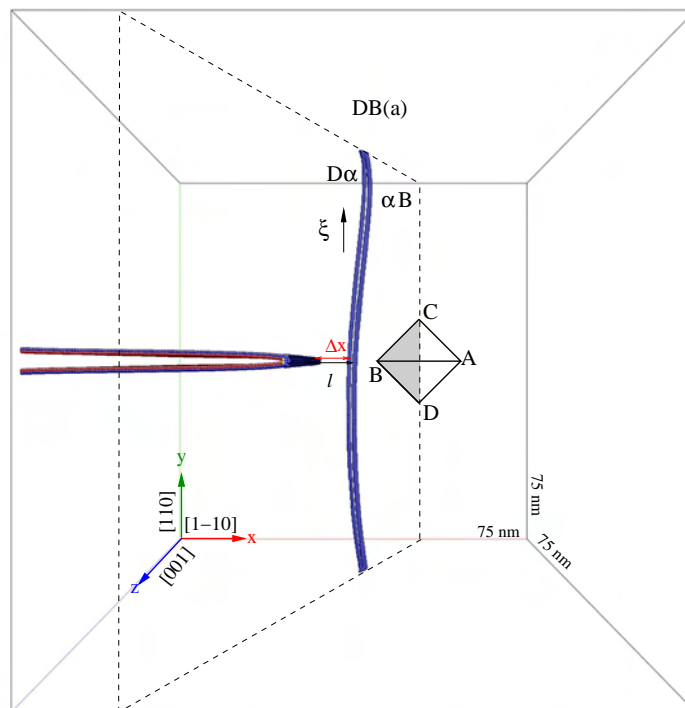


Figure 11.1: Set-up for the simulation of a straight 60° dislocation $DB(a)$ with a crack in the γ -orientation. The box marks the edges of the simulated atomistic cube, from which only the inside atoms with increased potential energy are shown. The Thompson tetrahedron and the glide plane, which is viewed from inside the Thompson tetrahedron, are also drawn. The distance between dislocation and the crack tip is denoted by Δx , whereas l is the distance between the dislocation and its intersection point with the crack front (at $z = 37.5$ nm).

Symmetry considerations allow to limit the study to a subset of possible slip systems. The analysis of the driving forces caused by the stress field of a crack on the various slip system in the γ orientation show three different groups of slip systems. The slip systems of these groups are summarized in Table 11.1. The details of this analysis are worked out in sec. 12.3. However, simple geometrical reasoning can be used to confirm the classification in Tab. 11.1. For example it can be seen in Fig. 9.1 or Fig. 11.1 that the glide planes (c) and (d) are mirror symmetric with respect to the crack plane. Similarly, the behavior of dislocations

I	$AC(b) \equiv BD(a)$	$BC(a) \equiv AD(b)$
II	$AC(d) \equiv BD(c)$	$BC(d) \equiv AD(c)$
III	$AB(d) \equiv DC(a)$	$AB(c) \equiv DC(b)$

Tab. 11.1: Symmetry relations between slip systems for the γ oriented crack. Dislocations in the same class experience the same forces in the stress field of the crack. Within the same class, the behavior of dislocations on the right and on the left side of the table is mirror symmetric with respect to the crack plane.

on the (a)-plane with $\mathbf{b} = BD$ and $\mathbf{b} = BC$ is mirror symmetrical with respect to the cleavage plane. Only dislocations belonging to class I and II are observed in experiments, see sec. 2.2.2.1. To compare with the experimental study of Scandian [153] the focus of the present study is on incoming dislocations on the (a)-plane with Burgers vector $\mathbf{b} = \pm DB$. Only some simulations were performed with dislocations with Burgers vector $\mathbf{b} = \pm DC(a)$ and with dislocations on the (c)-plane. Dislocations with these Burgers vectors and various line orientations were simulated starting from different distances from the crack front.

In this context it is important to point out that due to the anti-mirror symmetry of the σ_{xy} stress component (see Fig. 10.4) there is *no* general mirror symmetry with respect to the crack plane for the driving forces on dislocations. E.g. a straight horizontal dislocation line above the crack will in general not experience the same forces as the same dislocation situated below the crack

The simulations are performed at high strains and near to the critical load for fracture. It is therefore important to assess the sensitivity of the processes during dislocation-crack interaction to (small) changes of the initial conditions. Mechanisms which are observed in both the large and the small samples can be considered to be rather robust. Test on small samples at high strains using symmetrically equivalent initial conditions showed furthermore that the solutions diverged from each other only after multiple dislocation reactions took place.

11.2 Blunted cracks

11.2.1 Incoming dislocations on the (a)-Plane

The orientation of the (a)-plane with respect to the crack front is shown in Figs. 9.1 and 11.1. In addition to the dislocation normal to the fracture plane shown in Fig. 11.1, horizontal dislocations and dislocations inclined to the crack front were studied. Symmetry arguments can be used to rationalize that a straight screw dislocation with $\mathbf{b} = \pm DC$ perpendicular to the crack plane does not experience a net driving force. Therefore, this kind of dislocations were not subjected to further studies.

11.2.1.1 Perpendicular 60° dislocation

Small system, plane stress

Straight dislocations with line direction $\xi = DC$ and Burgers vector $\mathbf{b} = \pm DB$ were simulated in a small sample ($25 \times 25 \times 25 \text{ nm}^3$, plane stress, $\epsilon_G = 0.0433$) at different strains (0.8, 0.9

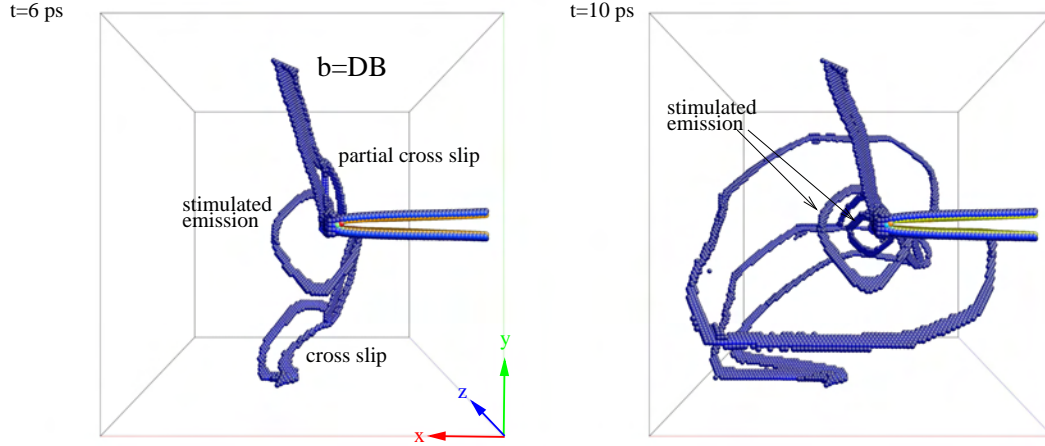


Figure 11.2: Processes during the interaction of an initially straight 60° dislocation with Burgers vector $\mathbf{b} = DB(a)$ with the crack front ($0.95\epsilon_G$ plane stress loading, small sample, $\Delta x = 2$ nm, crack blunted by one layer). Only atoms with increased potential energy are shown.

and $0.95\epsilon_G$). The distance of the dislocations from the crack front was in all cases $\Delta x = 2$ nm, and the crack was blunted by removal of one (110)-plane.

Dislocations with Burgers vector $\mathbf{b} = BD$ and $\boldsymbol{\xi} = DC$ were simply repelled from the crack front. Dislocations with the opposite Burgers vector $\mathbf{b} = DB$ were attracted towards the crack. For these dislocations, three typical processes could be identified (see Figs. 11.2 - 11.4):

1. Change of glide plane of the upper part of the leading partial dislocation at the crack front: $D\alpha \rightarrow D\beta + \beta\alpha$. This mechanism is already active at low loads of $0.8\epsilon_G$.
2. Stimulated nucleation of (partial and full) dislocation loops on the inclined glide planes (c) and/or (d), at the intersection of the incoming dislocation with the crack front (starting at $0.9\epsilon_G$).
3. Cross-slip on (c) of a part of the incoming dislocation which had attained screw character: $D\alpha + \alpha B \rightarrow D\gamma + \gamma B$ (starting at $0.9\epsilon_G$).

The stimulated emission of dislocations from the crack front did not take place in all simulations. In addition to a critical loading of the crack necessary for stimulated emission, the dislocation nucleation process depended on the velocity of the incoming dislocation. Fig. 11.3 compares two series of snapshots of simulations with the same starting configuration and boundary conditions ($0.95\epsilon_G$). In one simulation, however, the velocity of all atoms was set to zero shortly before the dislocation met the crack front ($t = 2$ ps). The impinging velocity v_i of the dislocation was thus reduced to $v_i \approx 8 \pm 5 \text{ \AA/ps}$ instead of $v_i \approx 22 \pm 5 \text{ \AA/ps}$. During the entire simulation time dislocation emission from the crack tip did not occur. However, change of glide plane and cross-slip were observed.

The cross-slip processes started close to the box boundary, where the dislocation is already constricted. Cross-slip occurred by the Fleischer mechanism. The details of this mechanism will be analyzed in sec. 11.2.1.2 on other simulations. By increasing the size of the simulation box in crack front direction the cross-slipped dislocation can cut the crack front, see Fig. 11.4.

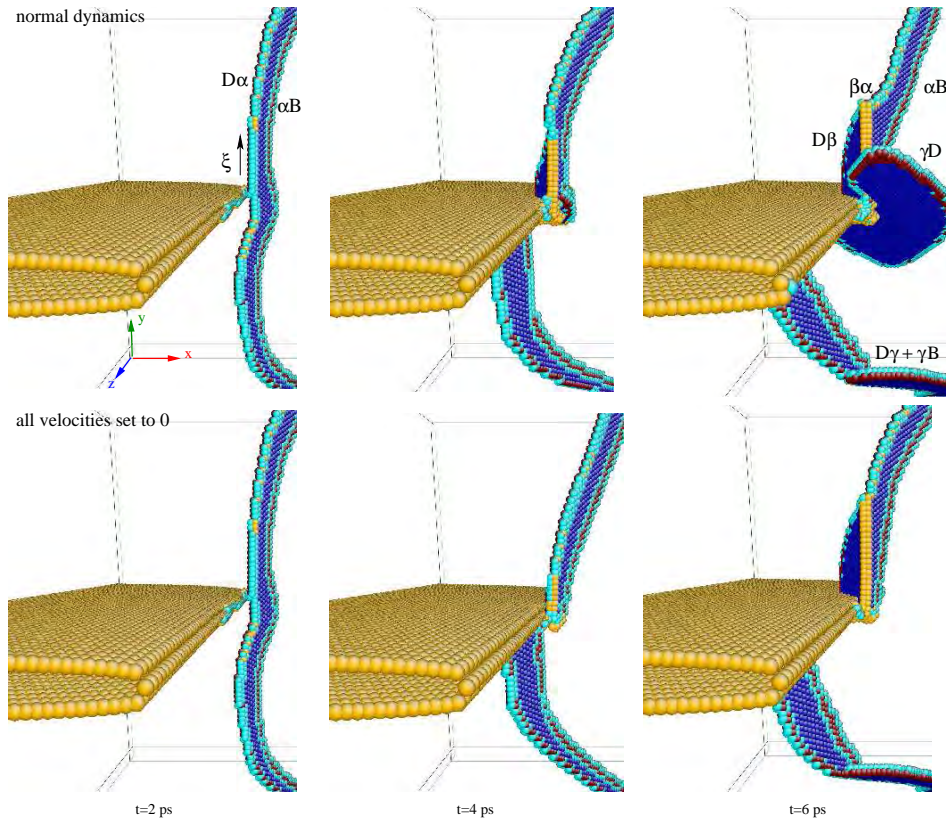


Figure 11.3: Time series of the process of stimulated emission in Fig. 11.2. Upper and lower row show simulations with the same starting configuration and boundary conditions. However, in the lower row the velocities of all atoms is set to 0 at $t = 2$ ps. Contrary to the simulation without freezing (upper row), no stimulated dislocation nucleation is observed in this simulation. The defects are identified using their CNA value.

It can be seen in Fig. 11.4d that a partial dislocation loop nucleated at the intersection of the cross-slipped dislocation and the crack. The nucleation took place some time after the leading partial dislocation $D\gamma$ had cut the crack front, but before the trailing partial touched the crack tip. Like the second partial dislocation loop on (d) emitted at the first intersection point, this dislocation loop was nucleated on top of a stacking fault, leading to a two layer thick "twin".

According to Tadmor and Hai [297] materials with low ratios of stacking fault energy γ_{sf} to unstable stacking fault energy γ_{usf} combined with a high ratio of the unstable twinning energy γ_{utf} to γ_{usf} have a high tendency to twinning. This is the case for the Ni_{II} potential used in this study ($\gamma_{sf}/\gamma_{usf} = 0.45$, $\gamma_{utf}/\gamma_{usf} = 0.83$, see appendix A). According to [297,298] two layer thick micro-twins are precursors to deformation twinning.

The stacking faults are obstacles to the dislocation motion on intersecting planes. However, as can be seen in Fig. 11.4d the dislocations could penetrate through these twins. Using the centro symmetry parameter, the inset in Fig. 11.4e shows how the two layer thick twin was cut by $CB(d)$. The trailing partial δB stayed at the twin boundary, whereas the leading partial continued to glide on a plane one atomic layer below the original glide plane. Similarly the twin boundary was displaced by one atomic layer.

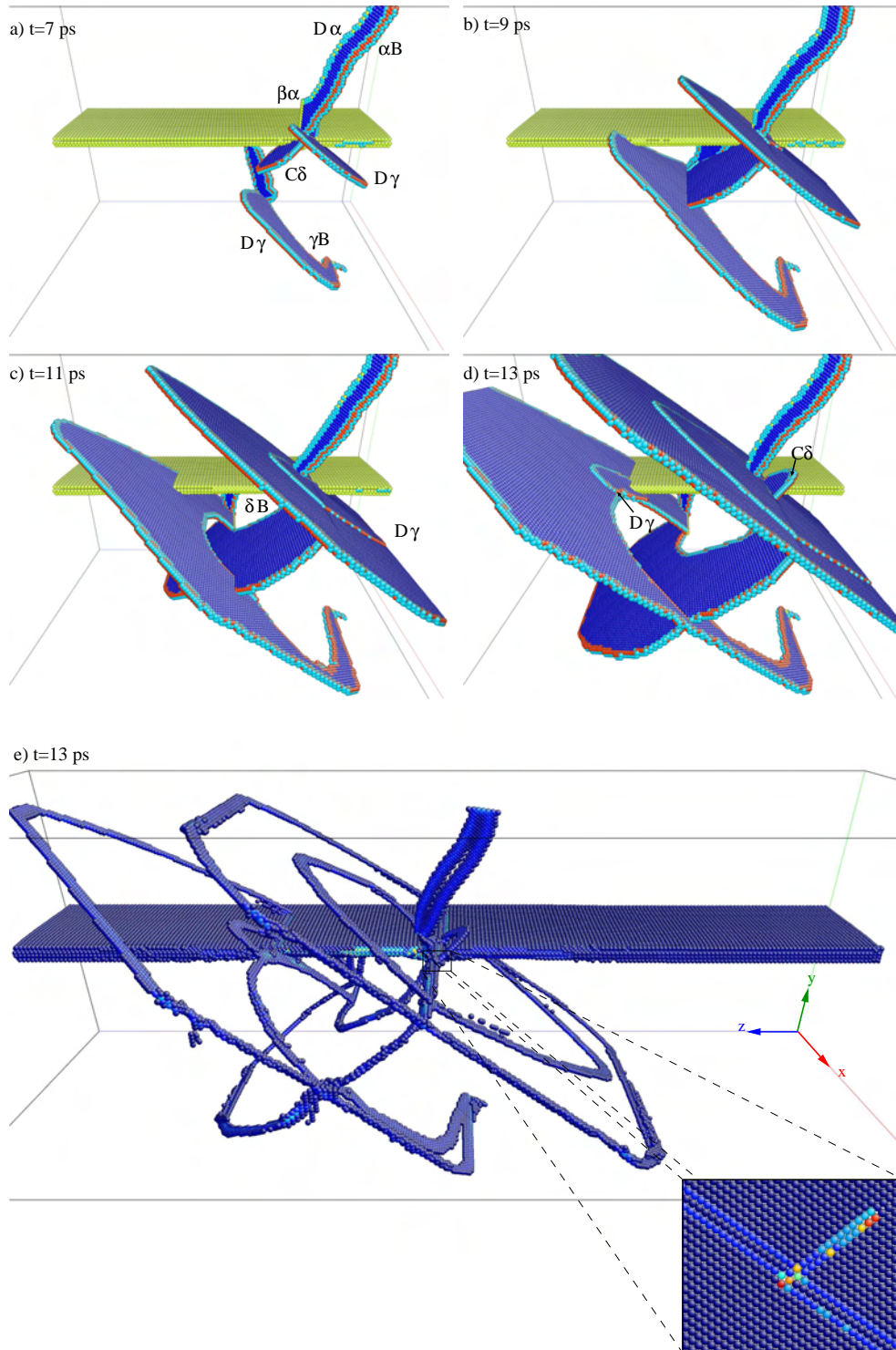


Figure 11.4: Snapshots of the simulation of a crack blunted by 1 layer and a 60° dislocation with Burgers vector $\mathbf{b} = DB(a)$ in the $25 \times 25 \times 75$ nm sample at $0.95\epsilon_G$ (plane stress, $\Delta x = 2$ nm³). The top frames a)-d) show only a part of the system, in which defects are identified using their CNA value. The lower frame e) shows the entire sample in which the defects have been filtered out by their potential energy. The inset in e) shows how a partial dislocation has penetrated through a micro twin (color encodes the centro symmetry parameter).

Large scale simulations, plane stress

The interaction of the straight 60° dislocation with $\xi = DC$ and Burgers vector $\mathbf{b} = BD$ with a crack blunted by removal of one (110) layer was studied at $0.82, 0.84, 0.92$ and $1.01\epsilon_G$. For these simulations in the large system ($75 \times 75 \times 75 \text{ nm}^3$, $\epsilon_G = 0.0274$) the distance to the crack tip was $\Delta x = 6 \text{ nm}$. Depending on the load, the dislocation reached the crack tip after 7-9 ps. Its velocity at that time was about $v_i \approx 21 \text{ \AA/ps}$. An additional simulation at $0.92\epsilon_G$ was performed with a starting distance of $\Delta x \approx 13 \text{ nm}$ to study the influence of Δx on the dislocation-crack interaction. Furthermore, the influence of additional blunting by removal of three (110) layer on the dislocation-crack interaction was studied at $0.97\epsilon_G$ and $1.01\epsilon_G$ ($\Delta x = 6 \text{ nm}$).

The change of glide plane of the leading partial dislocation $D\alpha$ upon contact with the crack front was observed in *all* configurations, see Fig. 11.5 to Fig. 11.10. In some cases this process was followed by the creation of partial dislocations on the (*a*) and (*b*)-planes, e.g. Fig. 11.5. Stimulated dislocation emission occurred at loads of $0.92 \epsilon_G$ and above. At these loads a sharp crack developed and propagated in the anti-shielded region of the crack front. In contrast to the simulations in the small system, no cross-slip was observed.

The processes during the interaction of the dislocation with the crack at a load of $0.82\epsilon_G$ are shown in Fig. 11.5. Upon contact with the crack front the leading partial dislocation changed the glide plane and created thereby a stair rod dislocation: $D\beta(a) \rightarrow D\beta(b) + \beta\alpha$. About 3 ps later a partial dislocation loop with Burgers vector $\beta C(b)$ nucleated where $D\beta(a)$ had intersected the crack front. This dislocation annihilated the stacking fault created by $D\beta(b)$, and together they form the full dislocation $DC(b)$. It also reacted with the stair rod dislocation $\alpha\beta + \beta C \rightarrow C\alpha$. With the trailing partial of the incoming dislocation this reaction led to the full dislocation $CB(a)$. This "unzipping" of a dislocation thus creates two dislocations with new Burgers vectors: $DB(a) \rightarrow DB(c) + CB(a)$. During the whole process the lower part of the incoming dislocation $DB(a)$ proceeded on its glide plane. The same mechanism occurred at $0.84\epsilon_G$.

At a load of $0.92\epsilon_G$ a sharp crack developed during the approach of the dislocation within the anti-shielded part of the blunted crack front, see Fig. 11.6. This sharp crack advanced by roughly $3b$ at the outermost (2D dynamic) boundary. Upon intersection, the upper part of the leading partial changed the glide plane as in the other simulations. After 12 ps, however, a dislocation loop with Burgers vector $C\delta$ has formed at the intersection between the dislocation and the crack front. This process is connected with the creation of a partial dislocation $\beta C(b)$. At the intersection between both dislocations, the stair rod dislocation $\beta\delta$ was formed, see Fig. 11.6b. The growth of the loop $C\delta(d)$ led to the closing of opened up part of the crack front. After 48 ps the trailing partial δB of the nucleated loop was emitted. The full dislocation $CB(d)$ cut the lower part of the original $DB(a)$. Due to the screw component of $DB(a)$ the arms of the dislocation $CB(d)$ could not directly annihilate and formed a long dislocation dipole. The dislocation dipole subsequently collapsed into two dipole loops.

In the simulation at $1.01\epsilon_G$ a sharp crack developed on the both sides of the blunted crack tip and propagated towards the dislocation. Like in the simulations at lower loads the leading partial dislocation changed its glide plane from (*a*) to (*b*). The stimulated emission of $D\gamma$ on the (*c*)-plane was connected with the generation of $C\alpha(a)$, see Fig. 11.7a. The following processes included the nucleation of the trailing partial dislocations on the (*a*) and (*b*)-plane and the emission of the trailing partial of the stimulated loop on (*c*), see Fig. 11.7b.

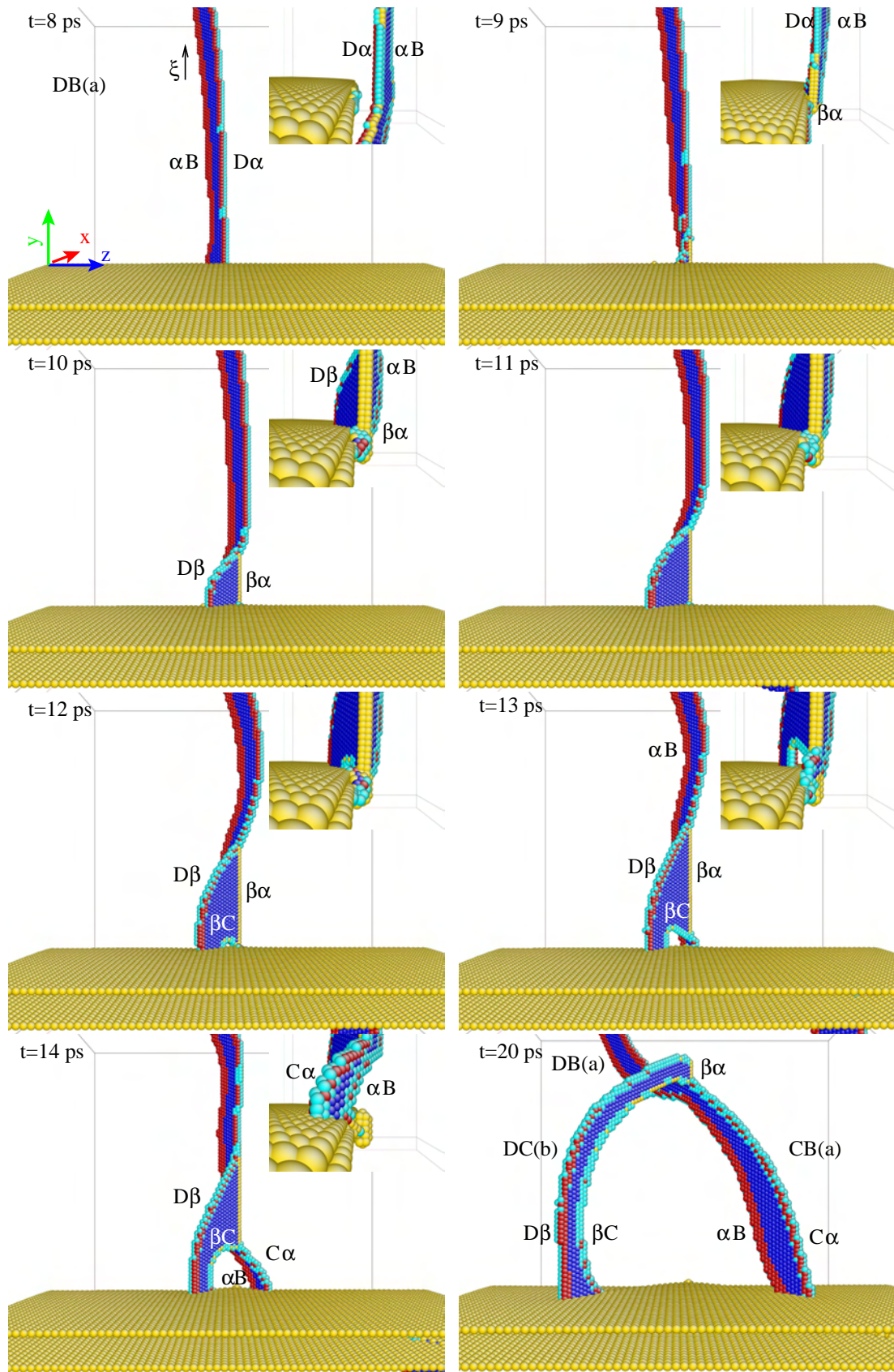


Figure 11.5: Series of snapshots from the simulation of a crack blunted by one layer and a 60° dislocation with Burgers vector $\mathbf{b} = DB(a)$ at $0.82\epsilon_G$ (large system, plane stress, $\Delta x = 6$ nm) which show the initial change of glide plane of the leading partial dislocation and the subsequent "unzipping"-processes leading to the new dislocations: $DB(a) \rightarrow DB(c) + CB(a)$. The insets show a view along the crack front ($-z$) of the same configurations. The defects are identified using their CNA value.

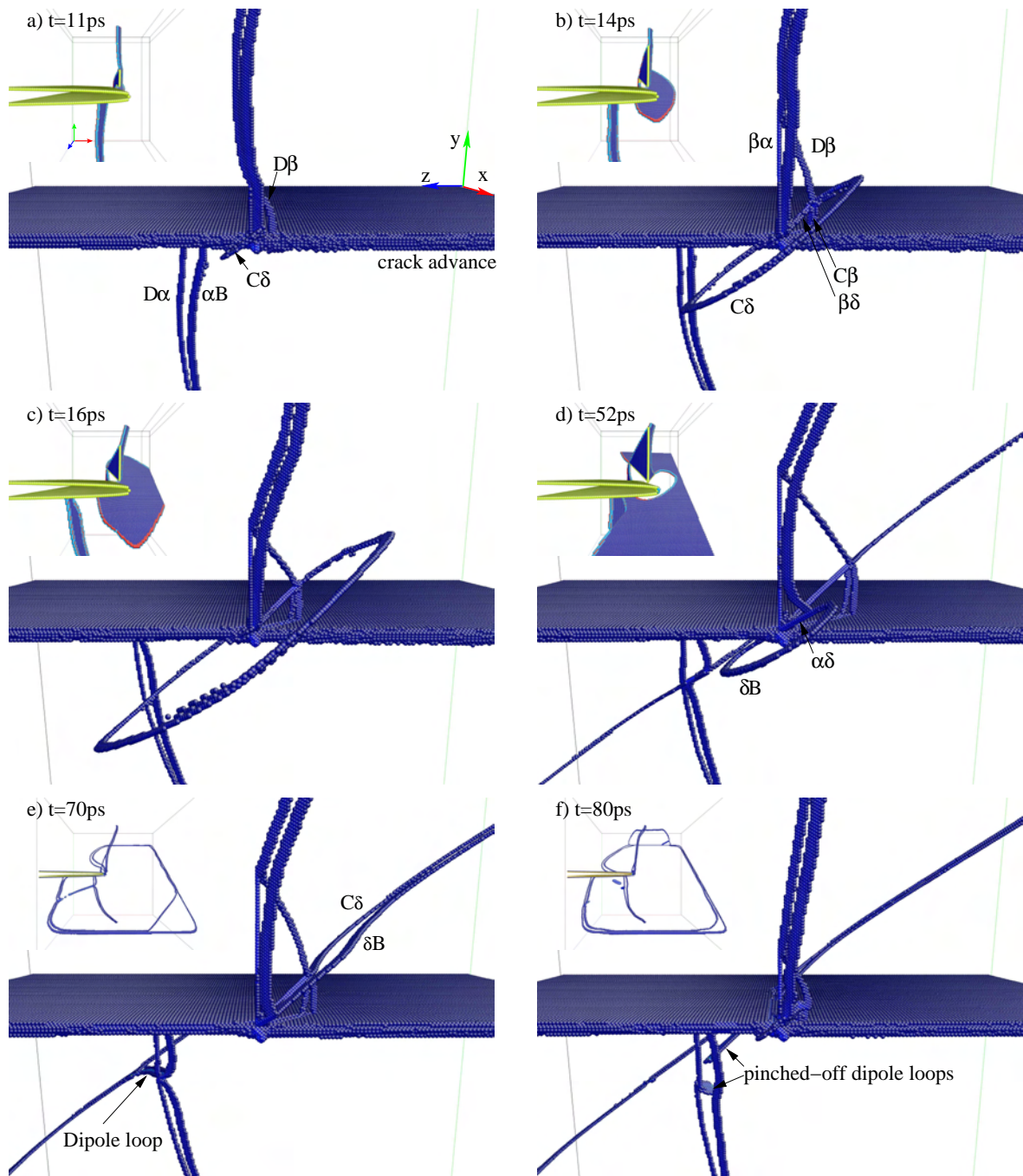


Figure 11.6: Snapshots from the simulation of a crack blunted by one layer and a 60° dislocation with Burgers vector $\mathbf{b} = DB(a)$ at $0.92\epsilon_C$ (large system, plane stress, $\Delta x = 6$ nm) showing the stimulated emission of a full dislocation loop on the (d)-plane. Only atoms with increased potential energy are shown, except for the insets in a)-d) which show atoms colored according to their CNA-value. The insets in e) and f) show the entire simulation box.

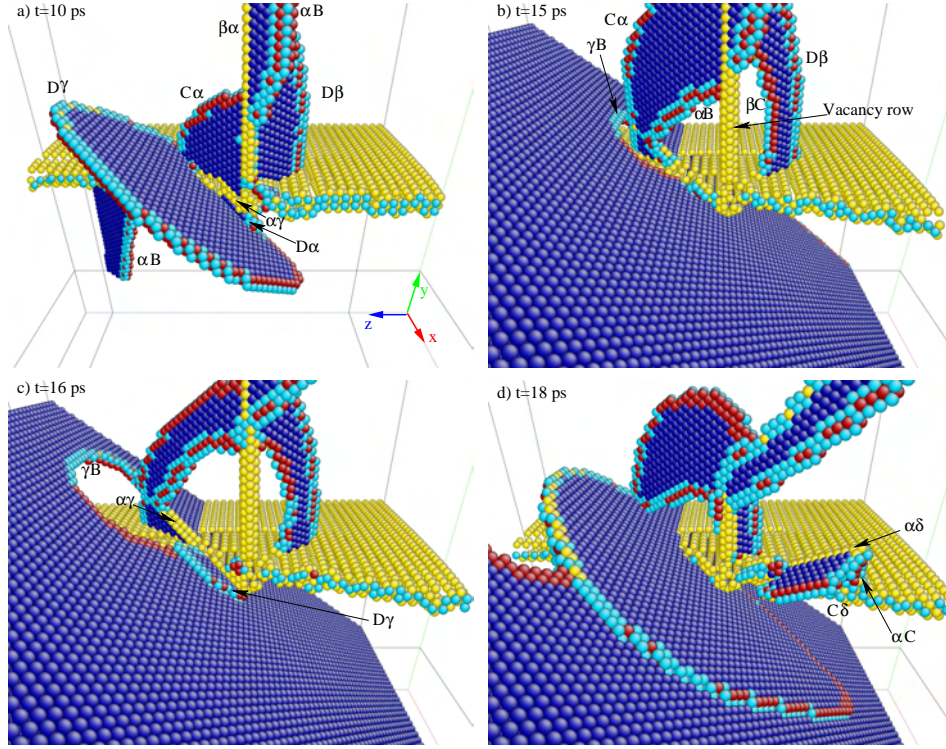


Figure 11.7: Details of the dislocation processes of a crack blunted by one layer and a 60° dislocation with Burgers vector $\mathbf{b} = DB(a)$ at a load of $1.01\epsilon_G$ (large system, plane stress, $\Delta x = 6$ nm). The CNA is used to identify defects within a small region of the entire simulation box. The dislocations involved in the processes are indicated. The processes include the change of the glide plane by $D\alpha$, stimulated emission of dislocation loops on the (c) -plane, nucleation of $CB(a)$ and $\beta C(b)$ leading to the formation of a vacancy row, and the simultaneous nucleation of $C\delta$ and αC from the moving crack front.

The process is similar to the "unzipping" in Fig. 11.5, however, the sequence and location of the nucleated dislocations were different. This led to the formation of a vacancy row. The propagating crack front additionally caused the simultaneous nucleation of $C\delta$ and αC partial dislocations, connected by the stair-rod $\alpha\delta$. This later process is similar to the emission of dislocations by running cracks, see sec. 10.4.

Effect of increased initial distance Snapshots from the simulation run at $0.92\epsilon_G$ with the dislocation initially placed $\Delta x = 13$ nm in front of the crack are shown in Fig. 11.8. Three main differences to the simulation at the same load but with the dislocation starting from $\Delta x = 6$ nm (Fig. 11.6) can be seen. The absence of stimulated dislocation emission is probably caused by the reduced velocity of the dislocation at contact with the crack front ($v_i \approx 17\text{\AA}/\text{ps}$ compared to $v_i \approx 21\text{\AA}/\text{ps}$ for $\Delta x = 6$ nm). The absence of crack advance could be due to a decrease of the shielding or anti-shielding of the crack front. This aspect is illustrated in Fig. 11.9. It can be seen that the curvature due to the pinning of the dislocation also decreased the portion of the dislocation line which can effectively shield or anti-shield the crack front. Finally, the dislocation line swung back and oscillated, which can be attributed to the line tension of the dislocation. These observations highlight the importance of the initial position of the dislocation as parameter determining the possible reactions.

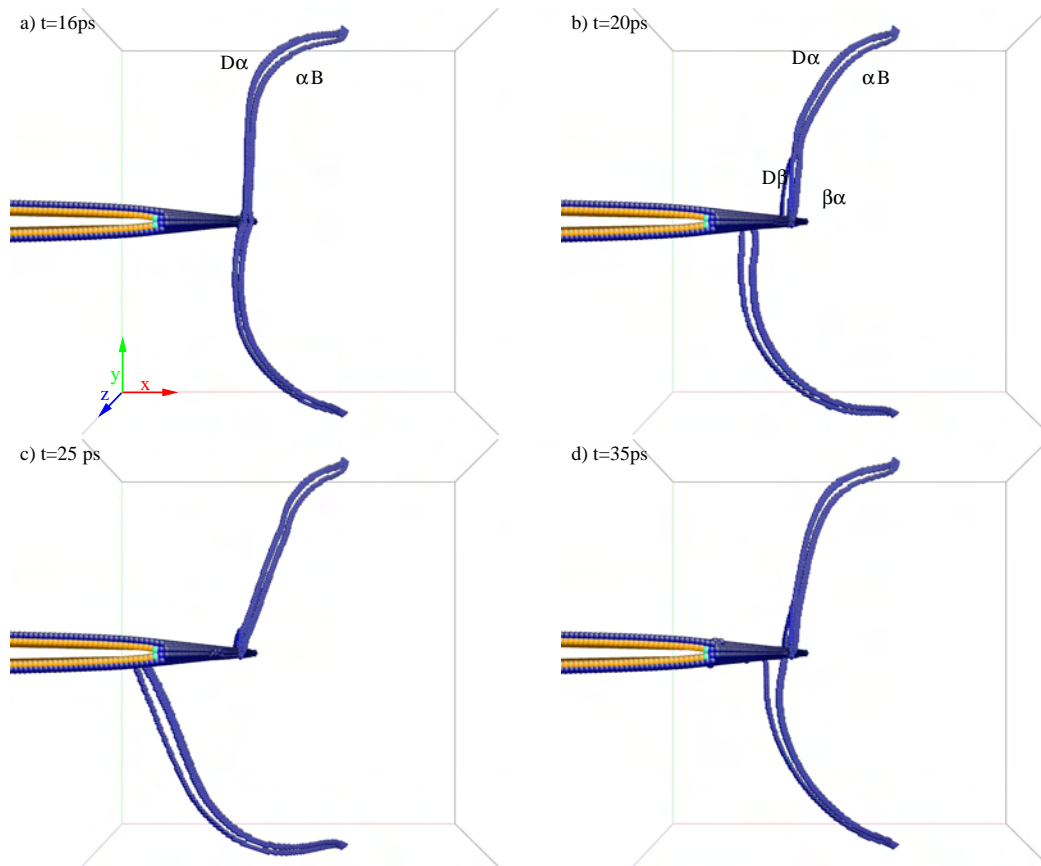


Figure 11.8: Snapshots from the simulation of a crack blunted by one layer and a 60° dislocation with Burgers vector $\mathbf{b} = DB(a)$ at a load of $0.92\epsilon_G$ (large system, plane stress) with the dislocation starting further away ($\Delta x = 16\text{ nm}$) than in Fig. 11.6. The pinning points exert a force acting against the bow-out, thus leading to a reduced impinging velocity and an oscillatory behavior. Stimulated dislocation emission did not take place. Only atoms with increased potential energy are shown.

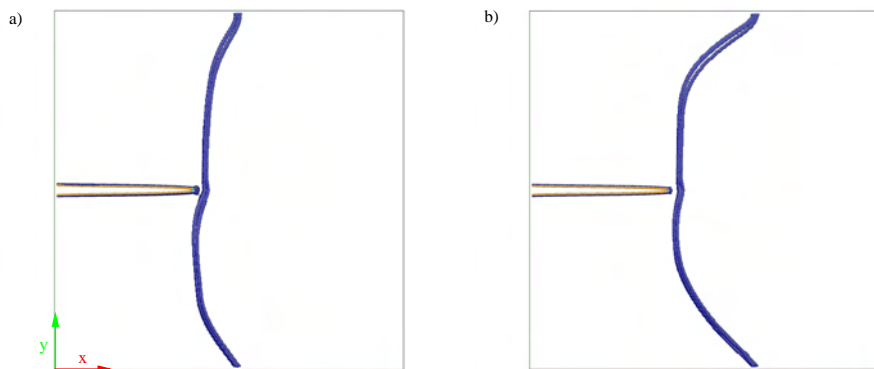


Figure 11.9: Plane view projection of the dislocation in the simulations at $0.92\epsilon_G$, Figs. 11.6 and 11.8, before intersection of the crack front. a) snapshot at $t = 7\text{ ps}$ with the dislocation starting at $\Delta x = 6\text{ nm}$ apart from the intersection point. b) snapshot at $t = 15\text{ ps}$ from the simulation with $\Delta x = 13\text{ nm}$. The bow-out leads to a reduction of the shielding/anti-shielding of the crack.

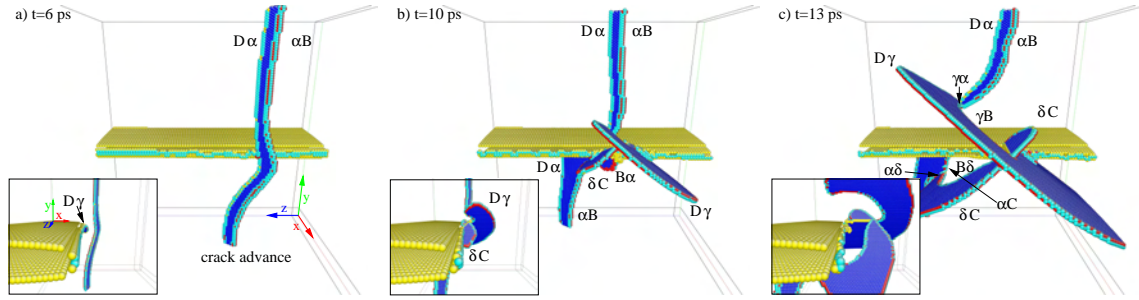


Figure 11.10: Details from the simulation of a dislocation interacting with a crack blunted by removal of 3 (110) layers 60° and a dislocation with Burgers vector $\mathbf{b} = DB(a)$ at $0.97\epsilon_G$ (large sample, plane stress, $\Delta x = 6$ nm). Only a part of the simulation box is shown, the atoms are colored according to their CNA value. In a) a sharp crack had developed which moved within the anti-shielded region and emitted a dislocation towards the dislocation. Stimulated emission of dislocations is shown in b); c) shows the subsequent reactions.

Effect of increased crack blunting At loads of 0.97 and $1.01\epsilon_G$ additional blunting of the crack tip by removal of 3 (110) layers did not prevent the formation of an atomically sharp crack in the stress field of the dislocation, see also sec. 10.1. Like in the studies with the crack blunted by one layer, the crack front propagated in the anti-shielded region at $0.97\epsilon_G$, and at $1.01\epsilon_G$ the entire crack front moved towards the dislocation. In both simulations a new process was observed: the advancing crack emitted a partial dislocation loop ($D\gamma(c)$) towards the dislocation *before* the dislocation cut the crack front, see Fig. 11.10a. This partial dislocation loop originated in both cases from an atomic step on the crack front which had developed in the stress field of the dislocation. The partial dislocation reacted with the incoming dislocation. As a result one part of $DB(a)$ cross-slipped onto (c). The subsequent reactions are shown in Fig. 11.10b,c. The processes at $1.01\epsilon_G$ were basically the same as in Fig. 11.10, except that the crack front kept moving and thus emitted further dislocations like the running cracks in sec. 10.4.

Large scale simulations, plane strain

The interaction of $DB(a)$ with a crack blunted by one (110) layer was studied under plane strain conditions at loads of $0.85\epsilon_G$ and $0.95\epsilon_G$. Contrary to the simulations under plane stress conditions, no stimulated emission took place. The observed processes were variations of the unzipping mechanism of Fig. 11.5. The details of the resulting structure thereby depend on whether the nucleation of $C\alpha(a)$ takes place on the same plane as the glide plane of the incoming dislocation $DB(a)$ or on a neighboring plane.

11.2.1.2 Horizontal 30° dislocations

Small system, plane stress

Studies on the small samples under conditions modeling plane stress were performed on the four possible orientations of 30° dislocations with $\mathbf{b} = \pm DB(a)$ relative to the crack. The dislocations were initially separated from the crack by $\Delta y = 5$ nm, and the crack was blunted by removal of one (110) layer. The starting configurations and their evolution during the first picoseconds of the simulations is shown in Fig. 11.11.

The blunting dislocation $DB(a)$ was drawn towards the crack independent of its location relative to the crack plane. However, the attraction differed in strength and direction, the first contact between dislocation and crack therefore occurred on different parts of the crack. Furthermore when the upper dislocation met the crack, the crack was first cut by the screw-like partial dislocation αB , whereas the lower dislocation cut the crack with a leading partial dislocation of edge character. Similarly, repulsion of $BD(a)$ varied between upper and lower dislocation. The forces on the dislocations arising from the stress field of the crack will be analyzed in detail in sec. 12.3 The horizontal 30° dislocations are closer to the screw orientation than the 60° dislocations. Significant parts of the initially horizontal dislocation can thus assume screw character, enabling cross-slip of the repelled as well as of the attracted dislocation, see Fig. 11.11b and c.

Typical processes observed in the small scale simulations at $0.95\epsilon_G$ include the stimulated emission of partial dislocations on the (c) and (d)-plane when the incoming dislocation intersected the crack front, see Fig. 11.11a, and the cross-slip of parts of the incoming dislocation towards or away from the crack front, see Fig. 11.11b and c. Also simple dislocation bow out in the stress field of the crack and swinging back and forth of the dislocation were observed, see Fig. 11.11d.

Fig. 11.12 shows the cross-slip process of Fig. 11.11c in more detail. As can be seen, no constriction of the dislocation took place, instead the leading partial dislocation αD dissociated into $\alpha D \rightarrow \gamma D + \alpha \gamma$, according to the cross-slip mechanism proposed by Fleischer. Subsequently, the trailing dislocation reacted with the stair rod dislocation, forming the trailing dislocation on the cross-slip plane: $B\alpha + \alpha \gamma \rightarrow B\gamma$. In this process, however, kinks on the incoming dislocation transformed into jogs on the cross-slipped dislocation $BD(c)$. Upon slip of $BD(c)$ the jogs led to the formation of a vacancy tubes.

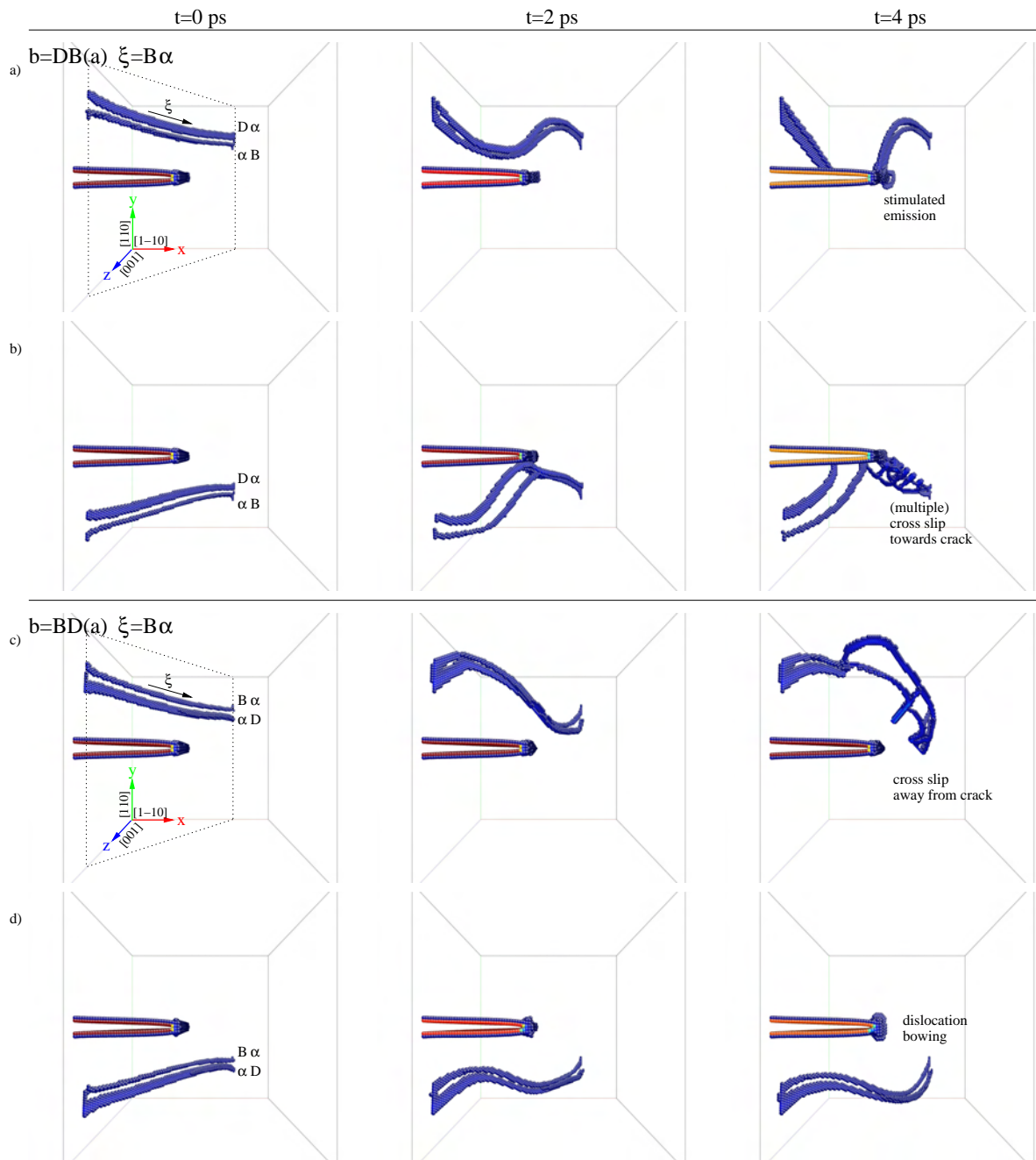


Figure 11.11: Starting configurations for the simulation of horizontal 30° dislocations and their evolution in the small sample at $0.95\epsilon_G$ (small sample, plane stress, $\Delta y = 5$ nm, crack blunted by one layer). The characteristic processes are indicated. Only atoms within the sample with increased potential energy are shown. The view on the glide plane is from inside the Thompson tetrahedron. Note that the compact core of partial dislocations with pure screw character $\pm\alpha B$ can be distinguished from the core of the partial dislocation with edge character.

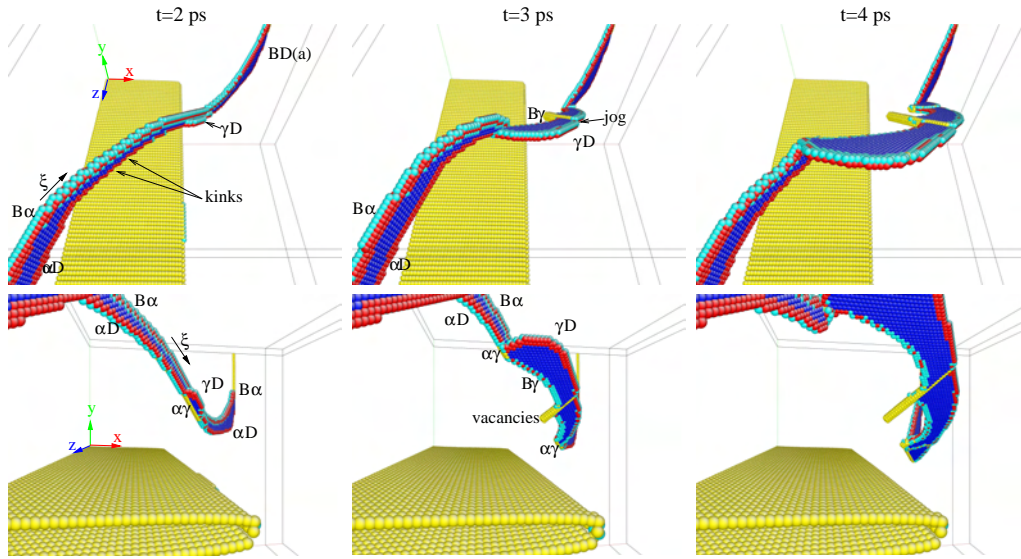


Figure 11.12: Snapshots of the cross-slip process of Fig. 11.11c. The view in the upper row shows both glide planes from inside the Thompson tetrahedron, whereas in the lower row the cross-slip plane is viewed from outside the Thompson tetrahedron. The color coding is according to the CNA parameter of the atoms. The Fleischer mechanism of cross-slip through an acute angle can be clearly seen ($t = 2$ to $t = 3$ ps). A jog in the cross-slipped part of the dislocation caused the creation of a vacancy tube behind the dislocation. Note the change of angle the incoming dislocation and the cross-slipped dislocation from acute to obtuse between $t = 3$ and $t = 4$ ps.

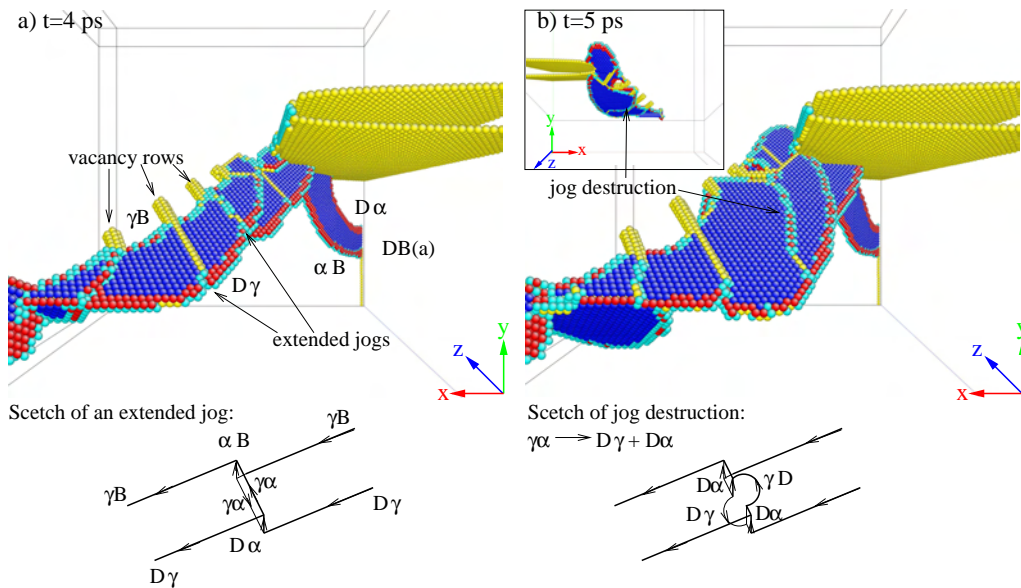


Figure 11.13: Details from the simulation of $DB(a)$ in the small sample at $0.95\epsilon_G$. The atoms are color coded according to their CNA value. The multiple cross-slip process of Fig. 11.11b) is shown in a). The cross-slip of subsequent screw dislocation segments leads to a jogged dislocation on the cross-slip plane. The sketch in a) shows the configuration of such a jog on an extended dislocation. Within the stress field of the crack the jogs dissociate as shown in b). The inset shows that the same process in the opposite direction takes place below the glide plane. The sketch shows a possible mechanism of jog dissociation (only the newly developed dislocations are labeled, please note the indicated line directions). This mechanism led to the formation of a four layer thick twin.

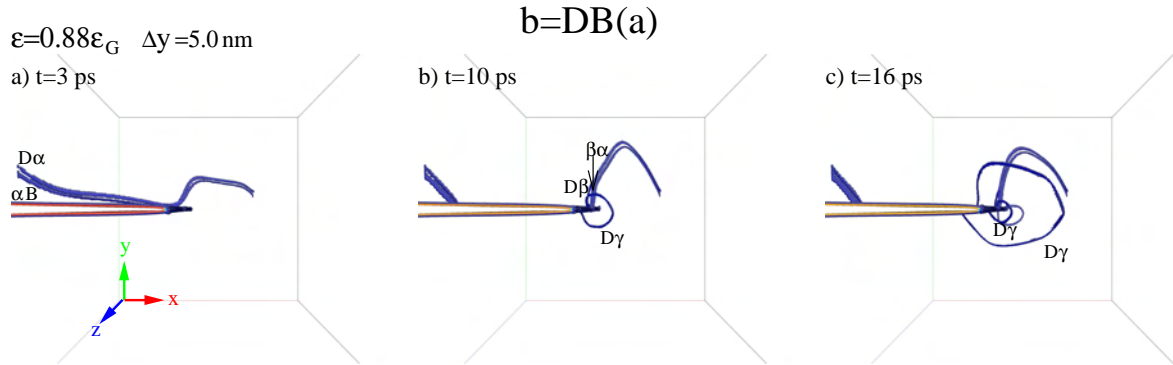


Figure 11.14: Interaction of the 30° dislocation $DB(a)$ coming from above with the crack at $0.88\epsilon_G$ (large sample, plane stress, $\Delta y = 5.0$ nm, crack blunted by one layer). Only atoms with increased potential energy are displayed. Upon contact of the dislocation with the crack tip, a partial dislocation loop was nucleated, and the trailing partial $D\alpha$ changed its glide plane.

Kinks on dislocations naturally arise when the dislocation is not aligned with a close-packed crystallographic orientation. Dislocations oriented close to the screw orientation can thus have several segments with screw orientation separated by monoatomic kinks. The cross-slip of the kinked dislocation $DB(a)$ led to dislocation segments on neighboring planes connected by extended jogs. see Figs. 11.11b and 11.13. The extended jogs were however not stable within the stress field of the crack. A possible mechanism of jog destruction is proposed in Fig. 11.13. The jog destruction led to the formation of a 4 layer thick twin.

Large scale simulations, plane stress

Simulations in the large sample with a crack blunted by one layer were carried out with all the four orientations of dislocations to the crack shown in Fig. 11.11. Starting with various initial distances Δy of the dislocation from the crack simulations were performed at loads $0.82\epsilon_G$ and $0.88\epsilon_G$.

Fig. 11.14 shows the typical processes during the interaction of the 30° dislocation $DB(a)$ with the crack underneath. The dislocation started at a distance $\Delta y = 5$ nm from the crack tip. After the initial intersection of the dislocation and the crack a large part of the dislocation was annihilated at the crack surface. The remaining parts of the dislocation moved in opposite directions, towards and away from the crack tip, and produced a step on the crack surface. When the trailing partial dislocation $D\alpha$ intersected the crack front, it changed its glide plane: $D\alpha \rightarrow D\beta + \beta\alpha$. At about the same time a partial dislocation loop $D\gamma$ was emitted on the (c) -plane. Later a second partial dislocation loop with $\mathbf{b} = D\gamma$ was emitted on top of the stacking fault created by the first stimulated dislocation. The same processes – stimulated emission of a dislocation loop and partial cross-slip of $D\alpha$ – took also place when the dislocation started further away from the crack ($\Delta y = 16$ nm) and at lower loads ($0.82\epsilon_G$).

The same dislocation $DB(a)$ positioned underneath the crack (at $\Delta y = 24, 17, 8$ and 5 nm) showed a different behavior, see Fig. 11.15. Upon contact with the crack tip, the part in front of the crack cross-slipped onto the (c) -plane, where it propagated along the crack flank. The other part of the dislocation was annihilated at the crack surface. The cross-slip process itself took place according to the Fleischer mechanism through an obtuse angle:

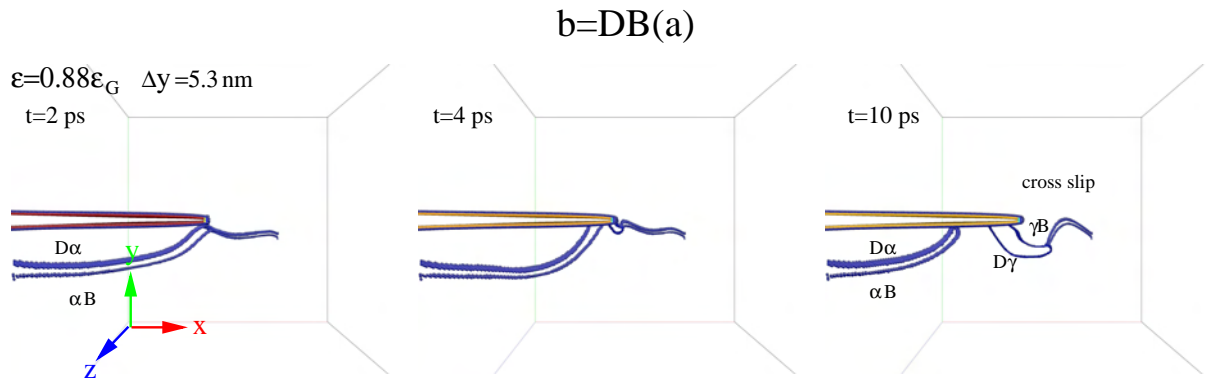


Figure 11.15: Snapshots from the interaction of 30° dislocations $DB(a)$ starting from $\Delta y = 5$ nm below the crack at 0.88ϵ (large sample, plane stress, crack blunted by one layer). Only atoms with increased energy are shown. Cross-slip of the incoming dislocation upon contact with the crack tip occurred also at lower loads and larger Δy .

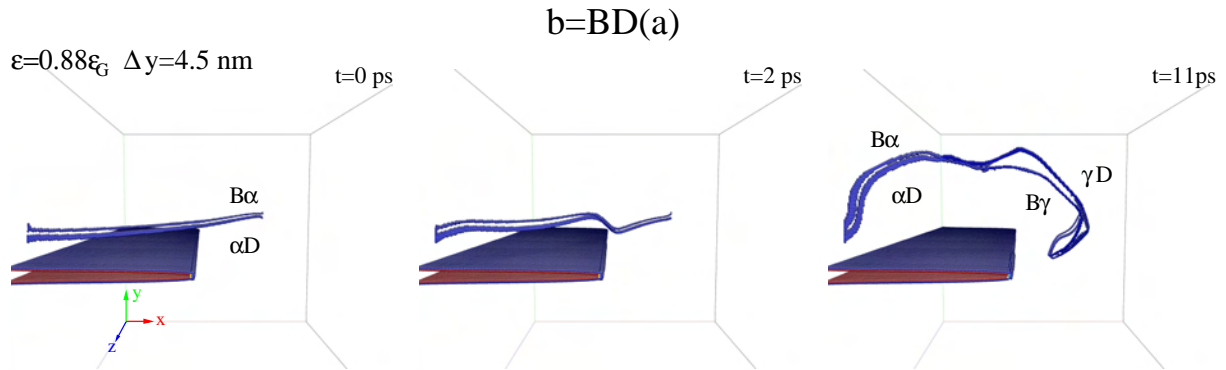


Figure 11.16: Snapshots from the interaction of 30° dislocations $BD(a)$ starting from $\Delta y = 5$ nm above the crack ($0.88\epsilon_G$, large sample, plane stress, crack blunted one layer). Only atoms with increased energy are shown. Cross-slip occurred only when a segment with screw character came sufficiently close to the crack tip. In the other cases the dislocations just swung back and forth.

$\alpha B \rightarrow D\gamma + \alpha\gamma/BD$. The Hirth dislocation lock reacted subsequently with $D\alpha$ to form the trailing partial on (c): $D\alpha + \alpha\gamma/BD \rightarrow \gamma B$. The interaction processes were independent of the load and the initial distance. The impinging velocity was in all cases about $v_i \approx 22 \text{ \AA/ps}$. Stimulated emission of dislocations was *not* observed.

Dislocations $BD(a)$ coming from above were strongly repelled above the crack. In front of the crack tip they experienced a downwards driving force. Dislocations placed further away from the crack (at $\Delta y = 23$ nm and $\Delta y = 16$ nm, $0.82\epsilon_G$) therefore adopted an "S" shape. Dislocation cross-slip away from the crack was only observed for an initial distance of $\Delta y \approx 5$ nm and $0.85\epsilon_G$, see Fig. 11.16.

Dislocations with Burgers vector $BD(a)$ coming from below the crack were strongly repelled by the crack tip. When the dislocation was initially situated close to the crack ($\Delta y = 6$ nm), a part of the dislocation annihilated at the crack surface, see Fig. 11.17. The remaining parts of the dislocation were bound to the crack surface. Due to the repulsion, no direct interaction between the dislocation and the crack tip was possible. Contrary to the

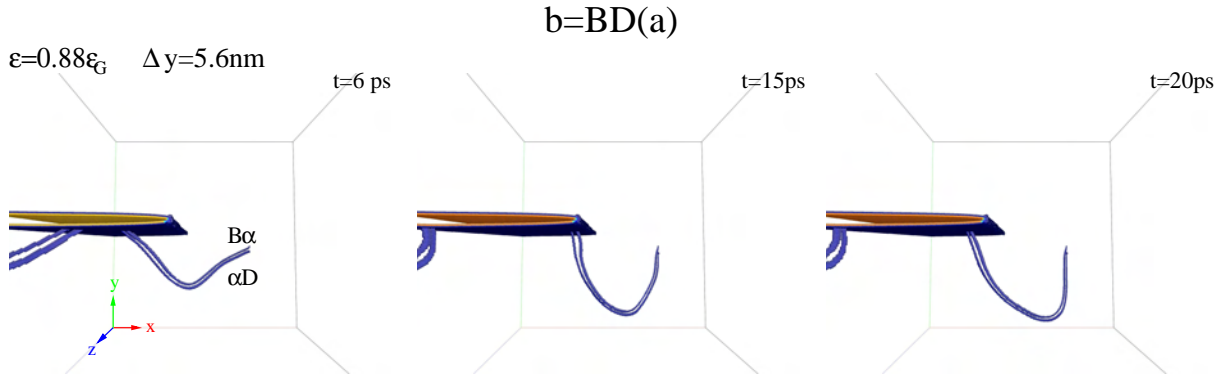


Figure 11.17: Snapshots from the interaction of a 30° dislocation $BD(a)$ starting at a distance $\Delta y = 5.6$ nm below the crack ($0.88\epsilon_G$, large sample, plane stress, crack blunted by one layer). Only atoms with increased energy are shown. The dislocation is strongly repelled by the crack tip, and no direct interaction between crack tip and dislocation takes place.

simulations of the same dislocation situated above the crack, the dislocation could not reach screw orientation, and consequently cross slip was impossible in this configuration.

Each of the four configurations of 30° dislocations showed a different behavior in the stress field of the crack. This allows to determine how the potential energy of the system is influenced by the different processes. Therefore simulation runs with the same load and approximately the same Δy have to be compared. This is done in Fig. 11.18 for $\epsilon = 0.88\epsilon_G$ and $\Delta y \approx 5$ nm. Fig. 11.18 shows that as expected the configuration with attracted dislocations ($\mathbf{b} = DB$, \circ , \diamond in Fig. 11.18) has a lower energy than the configuration containing repelled dislocations ($\mathbf{b} = BD$, $+$, \times). It shows furthermore that the relative decrease of the potential energy of the system depends on the dislocation process: only processes leading to a significant dislocation line length unloading the strained region in front of the crack tip led to a significant reduction of potential energy. This was the case for the stimulated emission of a partial dislocation loop (\diamond), but also for the expansion of the cross-slipped dislocation in front of the crack ($+$). The cross-slip at the crack surface without significant increase in dislocation line length in front of the crack (\circ) and the the partial annihilation of the dislocation at the crack surface and the bowing out of the remaining part of the dislocation (\times) led to nearly no reduction of the total energy.

Large scale simulations, plane strain

Simulations without Poisson contraction were also performed on the dislocation $DB(a)$. Fig. 11.19a shows the equivalent setup to Fig. 11.14 with plane strain conditions and at higher load ($0.95\epsilon_G$). No stimulated emission took place. Instead the same unzipping mechanism as for the dislocation oriented normal to the crack, displayed in Fig. 11.5, was active. For the dislocation $DB(a)$ situated below the crack, only the change of glide plane of the leading dislocation was observed, see Fig. 11.19. The cross-slip process observed under plane stress conditions, Fig. 11.15, was not activated.

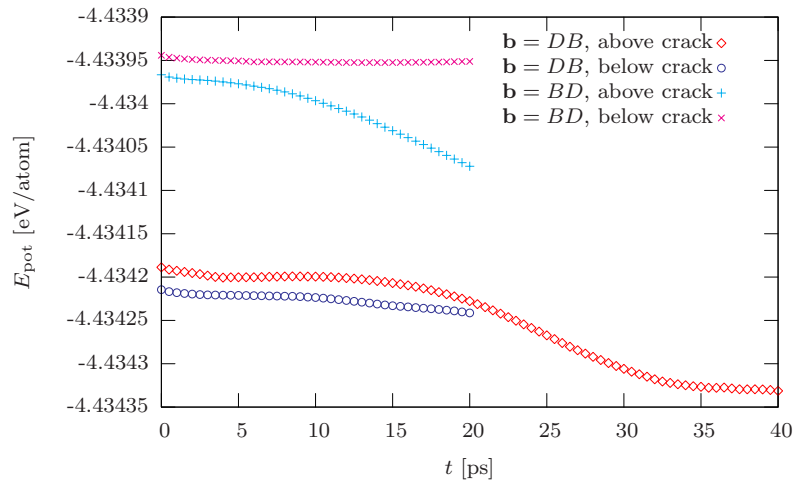


Figure 11.18: Potential energy per atom as function of time for the different configurations of horizontal 30° dislocations at $\epsilon = 0.88\epsilon_G$ and $\Delta y \approx 5$ nm. Dislocations with Burgers vector DB are attracted towards the crack and lead therefore to lower potential energy than the dislocations of opposite sign.

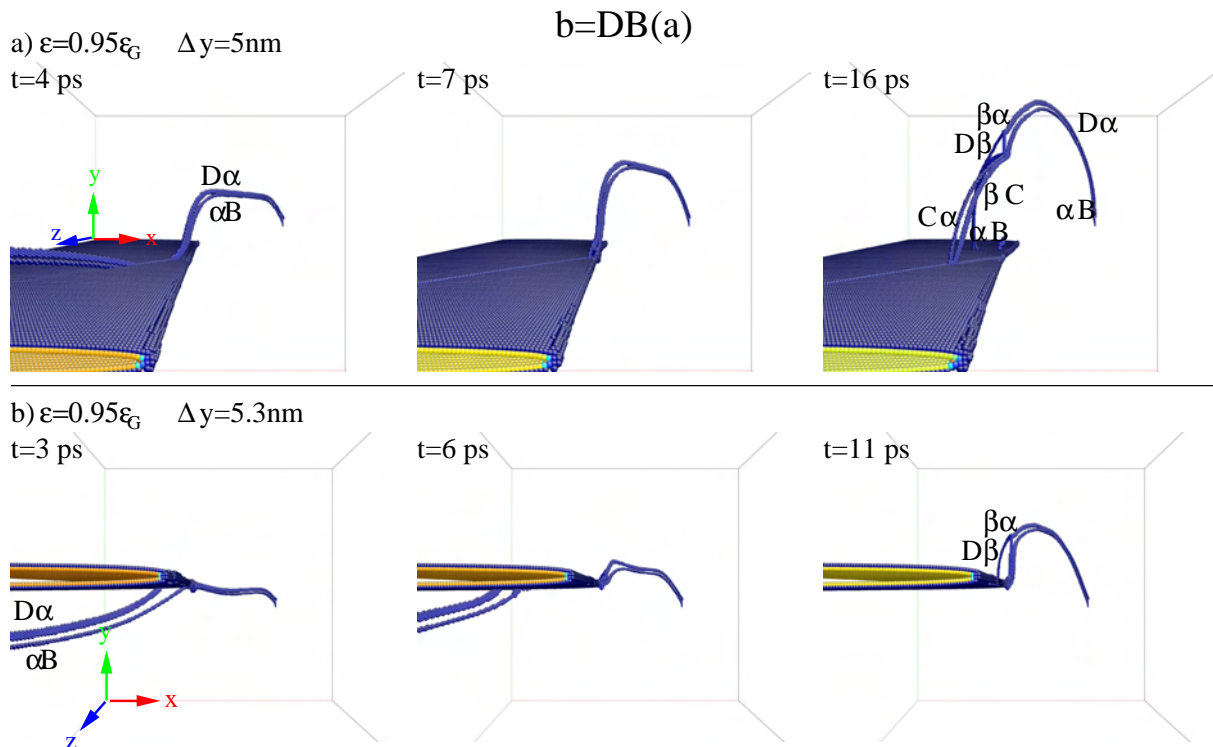


Figure 11.19: Snapshots from the interaction of 30° dislocations $DB(a)$ with a crack at $0.95\epsilon_G$ (large sample, plane strain, crack blunted by one layer). Only atoms with increased energy are shown. The starting configuration in a) is identical to that of Fig. 11.14 ($\Delta y = 5$ nm). For b) the set-up is equivalent to that of Fig. 11.15 ($\Delta y = 5.3$ nm). Neither cross-slip nor stimulated emission takes place.

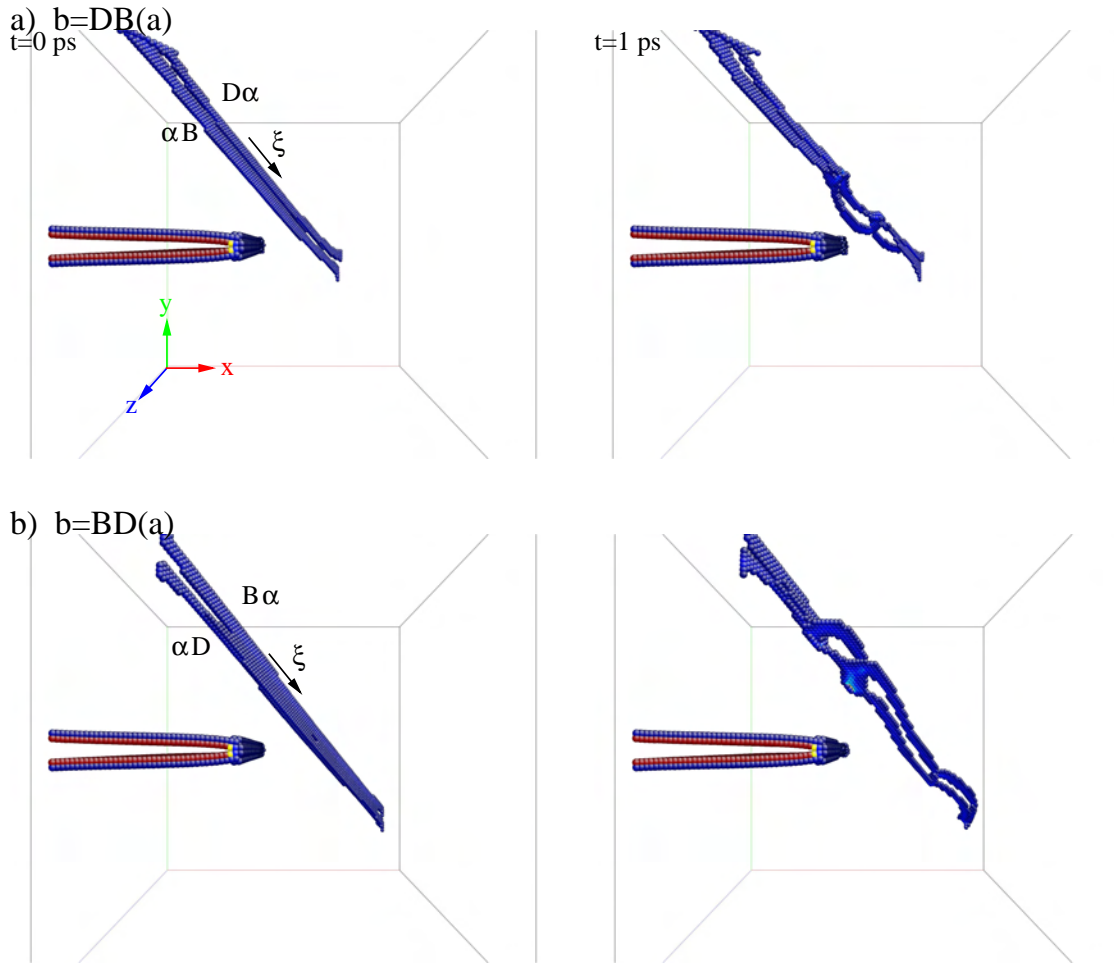


Figure 11.20: Starting configurations ($t = 0$ ps) for the small scale study of screw dislocations and their immediate reaction ($t = 1$ ps) on the stress field of the crack at $0.95\epsilon_G$ (small sample, plane stress, $\Delta x = 5$ nm crack blunted by one layer). Only atoms with increased potential energy are shown. Burgers vector a) $\mathbf{b} = DB(a)$ and in b) $\mathbf{b} = BD(a)$.

11.2.1.3 Inclined screw dislocations

Small sample, plane stress

Screw dislocations with Burgers vector $\mathbf{b} = \pm DB$ are inclined to the crack front. In an infinite body, a straight, infinite screw dislocation can not be positioned below a semi-infinite crack without cutting the crack surface. This is only possible, when the dislocation comes from above the crack. Therefore only screw dislocations with $\mathbf{b} = \pm DB$ were studied in initial configurations like the ones shown in Fig. 11.20. The basic set-up is similar to the situation in the experiments of Scandian [153], see also Fig. 2.10.

All the simulations in the small sample showed cross-slip of the dislocation. Depending on the Burgers vector, the cross-slip was directed either towards the crack tip ($\mathbf{b} = DB$) or away from the crack ($\mathbf{b} = BD$), see Fig. 11.20.

Large scale simulations, plane stress

The interaction of the screw dislocation with a crack blunted by removal of one atomic layer was studied at a load of $0.88\epsilon_G$ and initial distances of $\Delta x = 16, 11$ and 8 nm. An additional simulation was performed at $0.96\epsilon_G$ using a crack tip which was blunted by removal of three (110)-layers.

The initial distance determines the location of the pinning points of the dislocation at the box boundaries. The initial distance thus not only determines the distance of the dislocation from the crack tip, but also the relative length of dislocation which is situated above the crack and in front of the crack tip. The screw dislocation with $\mathbf{b} = DB$ is attracted above the crack surface and repelled in front of the crack (vice versa for $\mathbf{b} = BD$). The position of the pinning points therefore has a large effect on the dislocation bow out. At an initial distance of $\Delta x = 16$ nm for example, the screw dislocation $DB(a)$ could not reach the crack tip and just swung back and forth.

At an initial distance of $\Delta x = 11$ nm the dislocation bowed out to an "S"-shape, and came into contact with the crack, see Fig. 11.21. Upon contact with the crack tip, the trailing partial dislocation changed the glide plane $D\alpha \rightarrow D\beta + \beta\alpha$ and a partial dislocation loop with $\mathbf{b} = \delta C$ was emitted on the (d)-plane. In the following the emitted dislocation interacted with both the partially cross-slipped dislocation and the incoming dislocation, see Fig. 11.21c. With the trailing partial βC it formed a stair rod dislocation $\beta\delta$. More important, however, is the cutting process with the incoming dislocation $DB(a)$ which led to cross slip to $DB(c)$, see Fig. 11.21d. The cross slipped part was attracted to the the crack tip which it cut in Fig. 11.21f. During this process the original part of the dislocation attached to the crack tip acted as "pole" around which $DB(C)$ revolved, see Fig. 11.21d-f. Basically the same mechanisms were observed when the crack was blunted by removal of three atomic layers instead of one as in Fig. 11.21. Also in this case a pinned arm of the original dislocations acted as pole or shaft around which the cross-slipped dislocation gyrated.

At a closer spacing of the dislocation ($\Delta x = 8$ nm), the bow out was not so pronounced as in the case of of $\Delta x \approx 11$ nm, see Fig. 11.22. The absence of a dislocation on the (d)-plane which in the previous simulation triggered the cross-slip and the smaller dislocation bow-out led to the qualitatively different reactions showed in Fig. 11.22 compared to the previous simulation. In particular, no pole around which a cross-slipped dislocation could revolve was created.

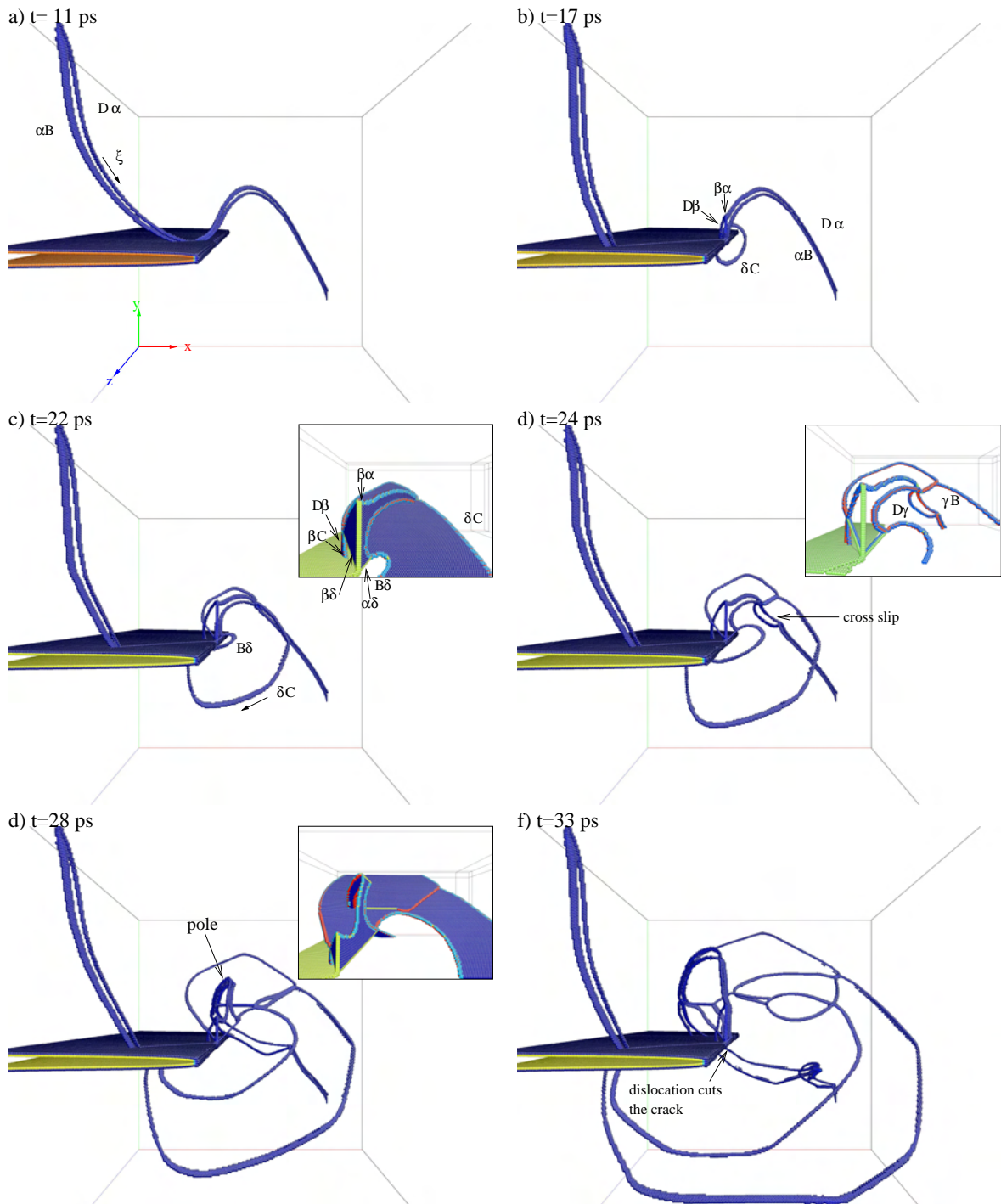


Figure 11.21: Snapshots from the simulation of the screw dislocation DB (a) initially positioned $\Delta x = 11$ nm in front of the crack tip at $0.88\epsilon_G$ (large sample, plane stress, crack blunted by one layer). The "pole" around which the cross-slipped dislocation revolves is indicated in d). The revolving dislocation later cuts the crack front. Only atoms with increased potential energy are shown. The insets show details of the structure using the CNA analysis.

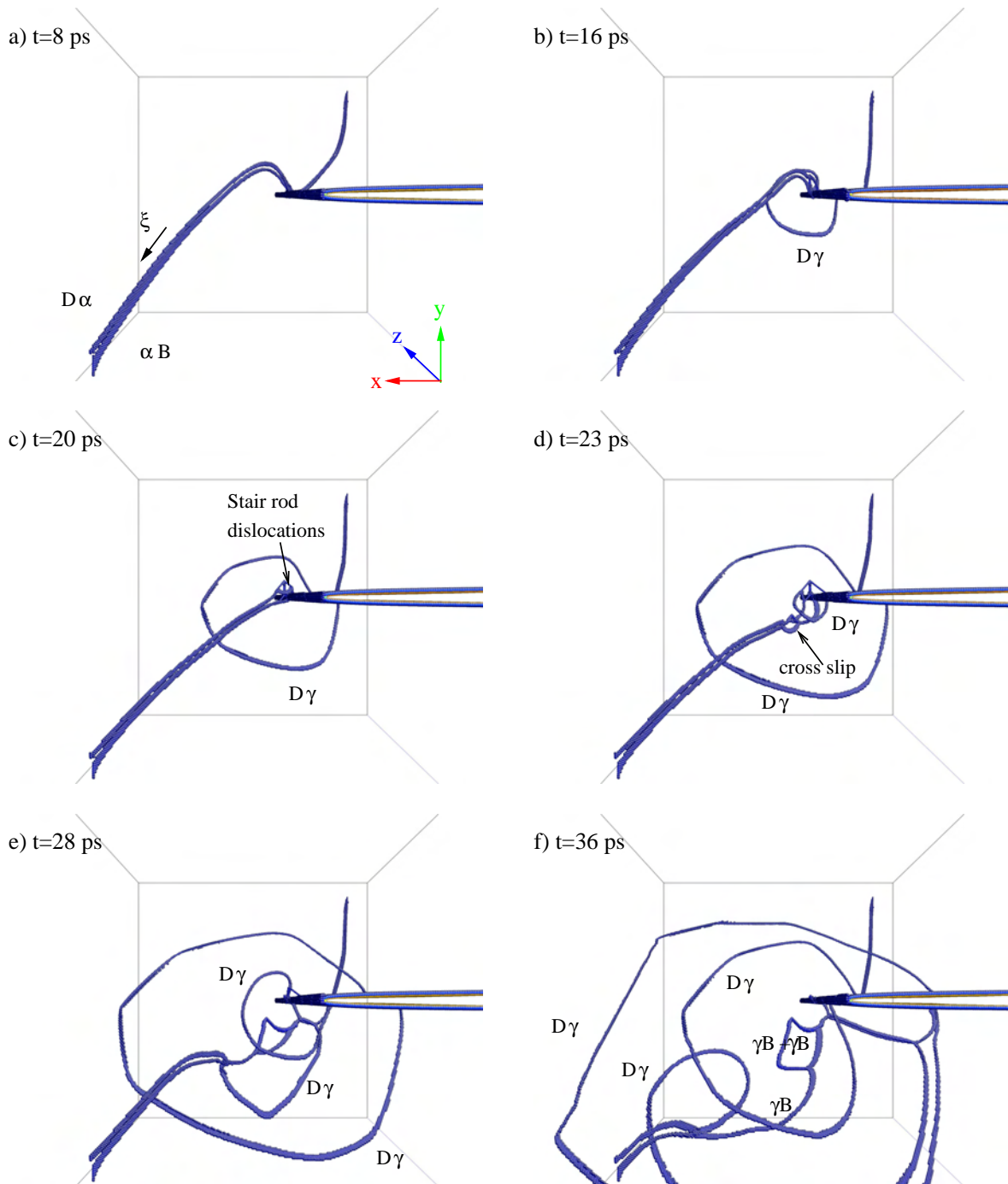


Figure 11.22: Snapshots from the simulation of a screw dislocation $\mathbf{b} = DB(a)$ initially positioned $\Delta x = 8$ nm in front of the crack tip at $0.88\epsilon_G$ (large sample, plane stress, crack blunted by one layer). Only atoms with increased potential energy are shown. New dislocations are created by stimulated emission (b) and cross-slip.

The screw dislocation with $\mathbf{b} = BD$ did neither cross-slip nor reach the crack when it was started from $\Delta x \approx 11$ nm in front of the crack. At an initial distance of $\Delta x = 8$ nm, however, the dislocation immediately cross-slipped on the (c) plane, see Fig. 11.23. Cross-slip took place by the Fleischer mechanism. The local curvature of $BD(a)$ before cross-slip led to one acute and one obtuse angle with the cross-slipped dislocation.

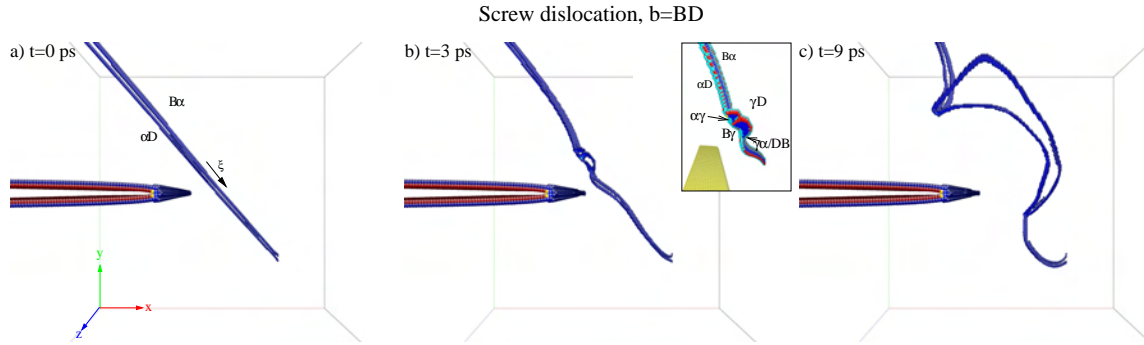


Figure 11.23: Snapshots from the simulation of a screw dislocation with $\mathbf{b} = BD(a)$ initially positioned $\Delta x = 8$ nm in front of the crack tip at $0.88\epsilon_G$ (large sample, plane stress, crack blunted by one atomic layer). Only atoms with increased potential energy are shown. The dislocation cross-slips on the (c) plane by the Fleischer mechanism. However, the cross-slip initially occurs on two adjacent planes, forming an acute and an obtuse angle with the primary plane, see inset in b). The smaller section of the cross slipped dislocation shrinks and the dislocation moves only on one cross-slip plane, see c).

Screw dislocations were also simulated in configurations under plane strain conditions. However, even at an initial distance from the crack tip of $\Delta x = 8$ nm and $0.95\epsilon_G$ the screw dislocation with $\mathbf{b} = DB$ did not reach the crack tip, but swung only back and forth.

11.2.1.4 Inclined 15° dislocations

Inclined 15° dislocations with $\mathbf{b} = \pm DB$ were simulated in the large sample under plane stress conditions at $0.88\epsilon_G$ and initial distances of $\Delta x = 10$ nm and $\Delta x = 5$ nm.

At $\Delta x = 10$ nm, the dislocation $DB(a)$ was just swinging in the stress field of the crack. At $\Delta x = 5$ nm, the dislocation started to cross-slip relatively far away from the crack tip, as shown in Fig. 11.24. When the dislocation cut the crack front the lower part of the dislocation also cross-slipped on (c) , where it merged with the previously cross-slipped part of the dislocation.

The same dislocation with opposite Burgers vector is shown in Fig. 11.25. The dislocation also cross-slipped relatively far away from the crack tip. The cross-slipped part of the dislocation cut the crack tip and expanded along the upper crack surface. The non cross-slipped part of the dislocation normal to the crack front was subjected to the "unzipping" mechanism, as displayed in Fig. 11.5

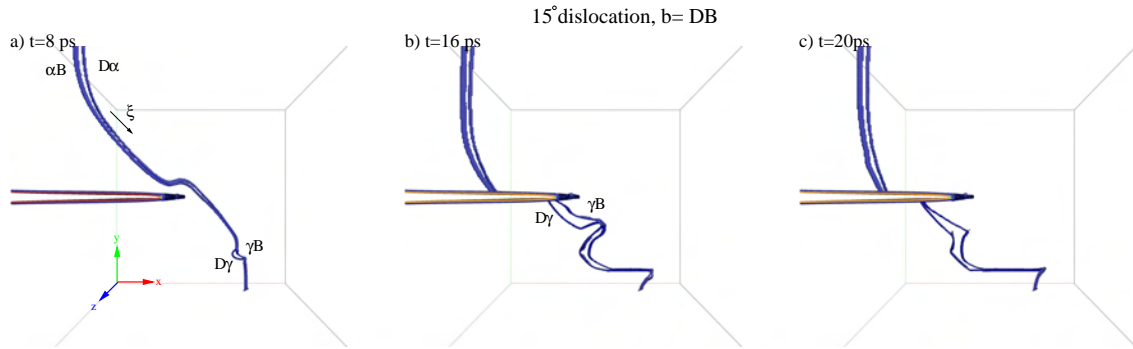


Figure 11.24: Snapshots from the simulation of a 15° dislocation with $\mathbf{b} = DB$ (a) initially positioned $\Delta x = 5$ nm in front of the crack tip at $0.88\epsilon_G$ (large sample, plane stress, crack blunted by one layer). Cross-slip by the Fleischer mechanism started relatively far away from the crack front (a), however, the dislocation also cross-slipped at the crack surface (b). The two cross-slipped dislocations merge in (c). Only atoms with increased potential energy are shown.

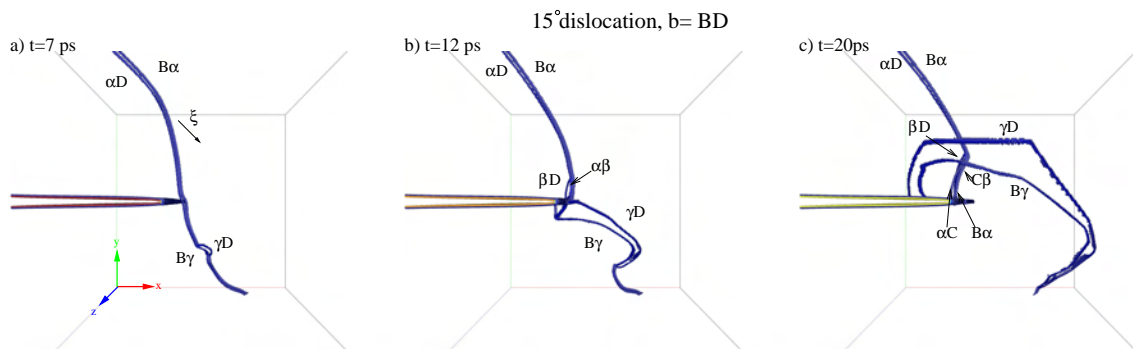


Figure 11.25: Snapshots from the simulation of a 15° dislocation with $\mathbf{b} = BD$ (a) initially positioned $\Delta x = 5$ nm in front of the crack tip at $0.88\epsilon_G$ (large sample, plane stress, crack blunted by one layer). In a) the dislocation cross-slips on the (c) plane towards the crack. Cutting of the crack front by the cross-slipped part of the lower dislocation did not lead to any further dislocation generation. Only atoms with increased potential energy are shown.

11.2.1.5 Horizontal edge dislocation, $\mathbf{b} = \pm DC$

All previously simulations were performed on dislocations with Burgers vector $\mathbf{b} = \pm DB$. Simulations with $\mathbf{b} = \pm DC$ are reported here and in sec. 11.4. Note that these Burgers vectors have *not* been observed in the experiments on γ -oriented cracks in thin silicon wafers [153].

The results of the simulation of an horizontal edge dislocation with Burgers vector $\mathbf{b} = DC$ initially positioned $\Delta y = 5$ nm below a blunted crack in the large sample at a plane stress load of $0.88\epsilon_G$ are shown in Fig. 11.26. The starting configuration of the dislocation was already strongly bowed by the action of the image forces caused by the fixed box walls. The characteristic features of this simulations were the change of the glide plane of the leading partial dislocation $D\alpha \rightarrow D\gamma + \alpha\gamma$ upon contact with the crack tip, and the stimulated emission of δC partial dislocations onto the (d) -plane, see Fig. 11.26.

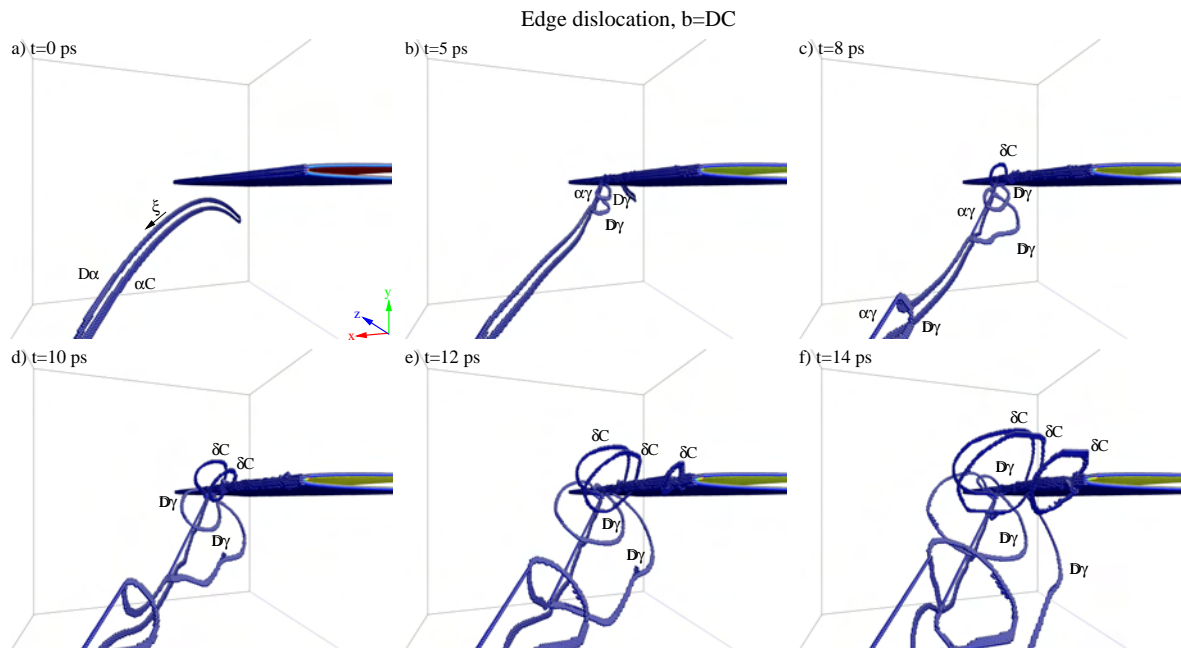


Figure 11.26: Snapshots from the simulation of the edge dislocation with $\mathbf{b} = DC$ (a) initially positioned $\Delta y = 5$ nm below the crack tip at $0.88\epsilon_G$ (large sample, plane stress conditions, crack blunted by one layer). Only atoms with increased potential energy are shown. In b) the leading partial dislocation changed its glide plane to the (c) plane, leaving a stair rod dislocation behind. Stimulated emission on the (d) plane can be seen in c) and d).

11.2.2 Incoming dislocations on the (*c*)-plane

The interaction of dislocations on the (*c*)-plane with a crack were studied in the large sample under plane stress conditions for 30° and 60° dislocations with $\mathbf{b} = DB$. An additional simulation was performed with the 30° dislocation under plane strain conditions. The 30° dislocation was initially positioned at a distance $\Delta x = 9$ nm in front of the crack, the 60° dislocations $BD(c)$ were initially placed at a distance $\Delta y = 6$ nm above and below the crack.

Fig. 11.27 shows the results for the 30° dislocation and for the 60° dislocation $BD(c)$ situated above the crack. Like in the simulation of the 60° dislocation positioned below the crack (not shown), *no* stimulated dislocation emission, cross-slip or other dislocation reaction occurred. This was also the case for the 30° dislocation under plane strain conditions at $0.95\epsilon_G$. The dislocations were however subjected to large driving forces leading even to *transonic velocities* for the 30° dislocations.

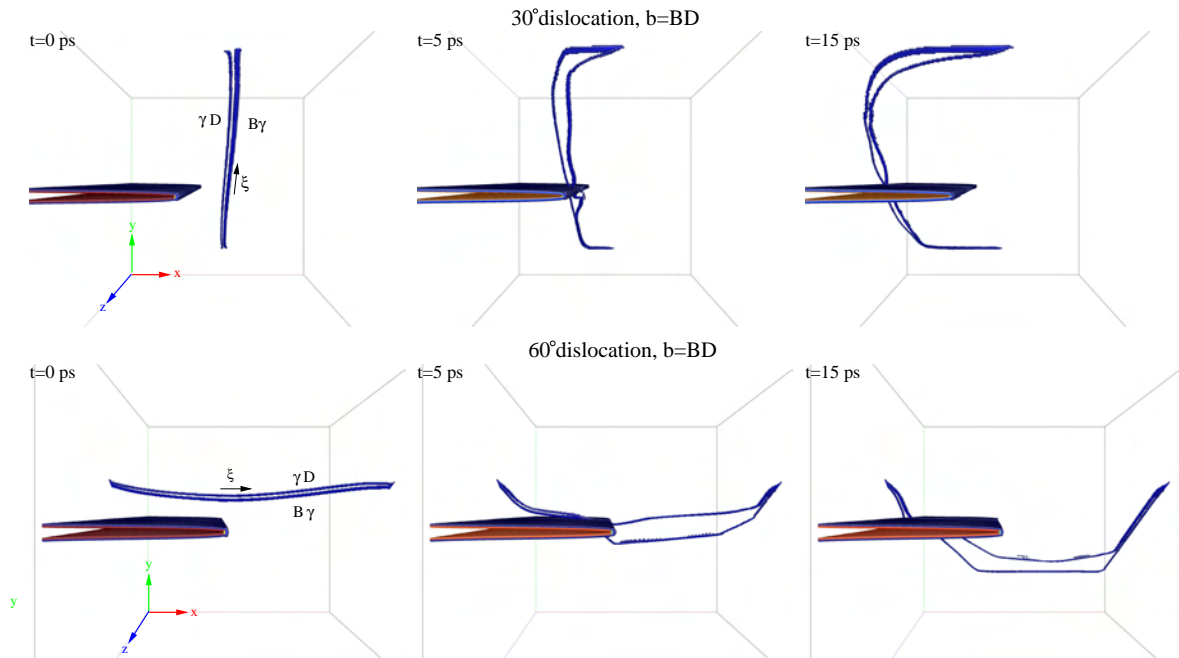


Figure 11.27: Snapshots from simulations of dislocations $\mathbf{b} = BD(c)$ interacting with the crack at $0.88\epsilon_G$ (large sample, plane stress, crack blunted by one layer). Only atoms with increased potential energy are shown. No cross-slip or stimulated dislocation emission occurred. a) 30° dislocation and $\Delta x = 9$ nm b) 60° dislocation and $\Delta y = 6$ nm

11.3 Sharp cracks

Atomically sharp cracks are stable within a very narrow loading range, see chapter 10.1. Sharp cracks can thus react to the stress field of a dislocation by opening up and propagating or by closing. The crack front usually becomes curved when subjected to the inhomogeneous stress field of a dislocation. Sharp cracks should therefore add to the complexity of the dislocation-crack interaction. Only a few exemplary simulations were performed on sharp cracks.

11.3.1 Large sample, plane stress

Simulations under plane stress conditions were performed with a 60° and a screw dislocation with $\mathbf{b} = DB(a)$ at $0.995\epsilon_G$ and $\Delta x = 6$ nm.

Fig. 11.28 shows the snapshots from the simulation of the 60° dislocation $DB(a)$. At the beginning the same processes as in case of a blunted crack (see e.g. Fig. 11.6) took place: The leading partial dislocation changed its glide plane ($D\alpha \rightarrow D\beta + \alpha\beta$) and the emission of a partial dislocation loop $D\gamma(c)$ was stimulated. However, as the crack advanced in the anti-shielded region of the crack front, $D\beta$ slipped back. At the intersection point of the advancing crack front and $DB(a)$ a partial dislocation loop $B\delta(d)$ was nucleated. This dislocation reacted with αB to a stair rod dislocation $\alpha\delta$. The crack closed in the region shielded by $D\gamma$, and further dislocations ($B\delta(d)$ and $D\gamma(c)$) were emitted by the moving crack.

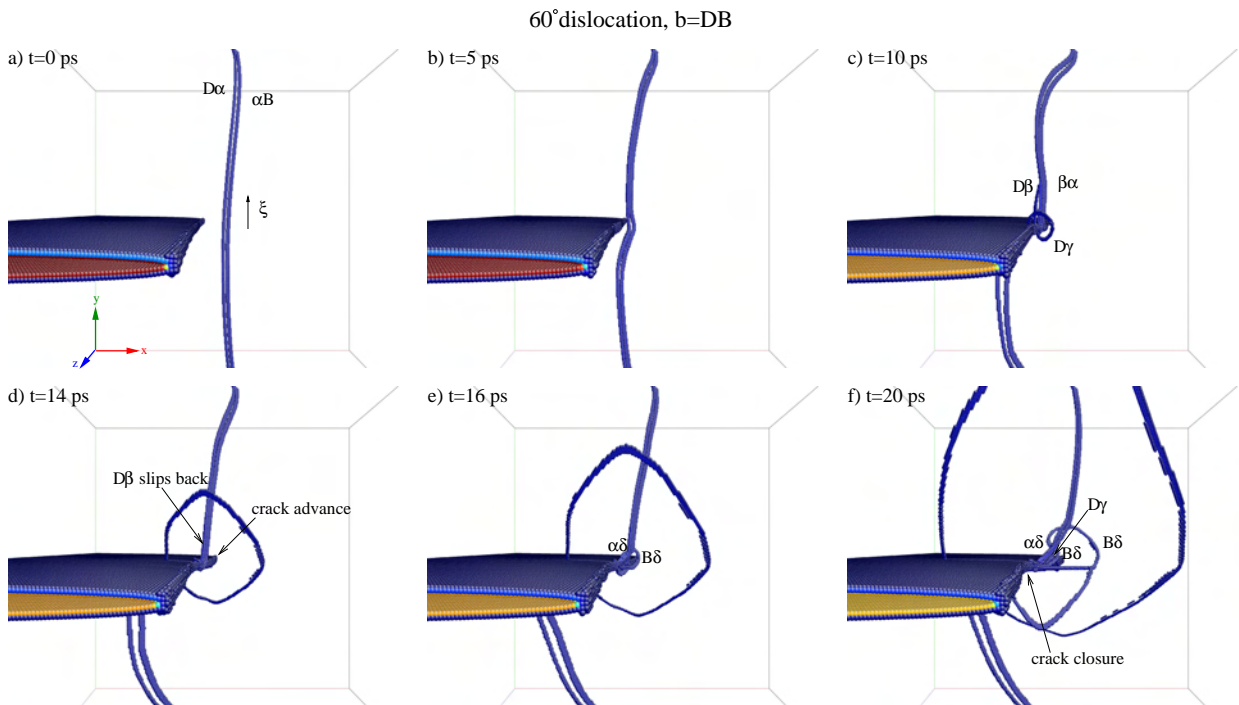


Figure 11.28: Snapshots of the 60° dislocation DB interacting with a sharp crack at $0.995\epsilon_G$ (plane stress, $\Delta x = 6$ nm). Only atoms with increased potential energy are shown.

The interaction of a screw dislocation with $\mathbf{b} = DB$ initially placed $\Delta x = 6$ nm in front of the sharp crack tip at a plane stress load of $0.995\epsilon_G$ is shown in Fig. 11.29. As in the

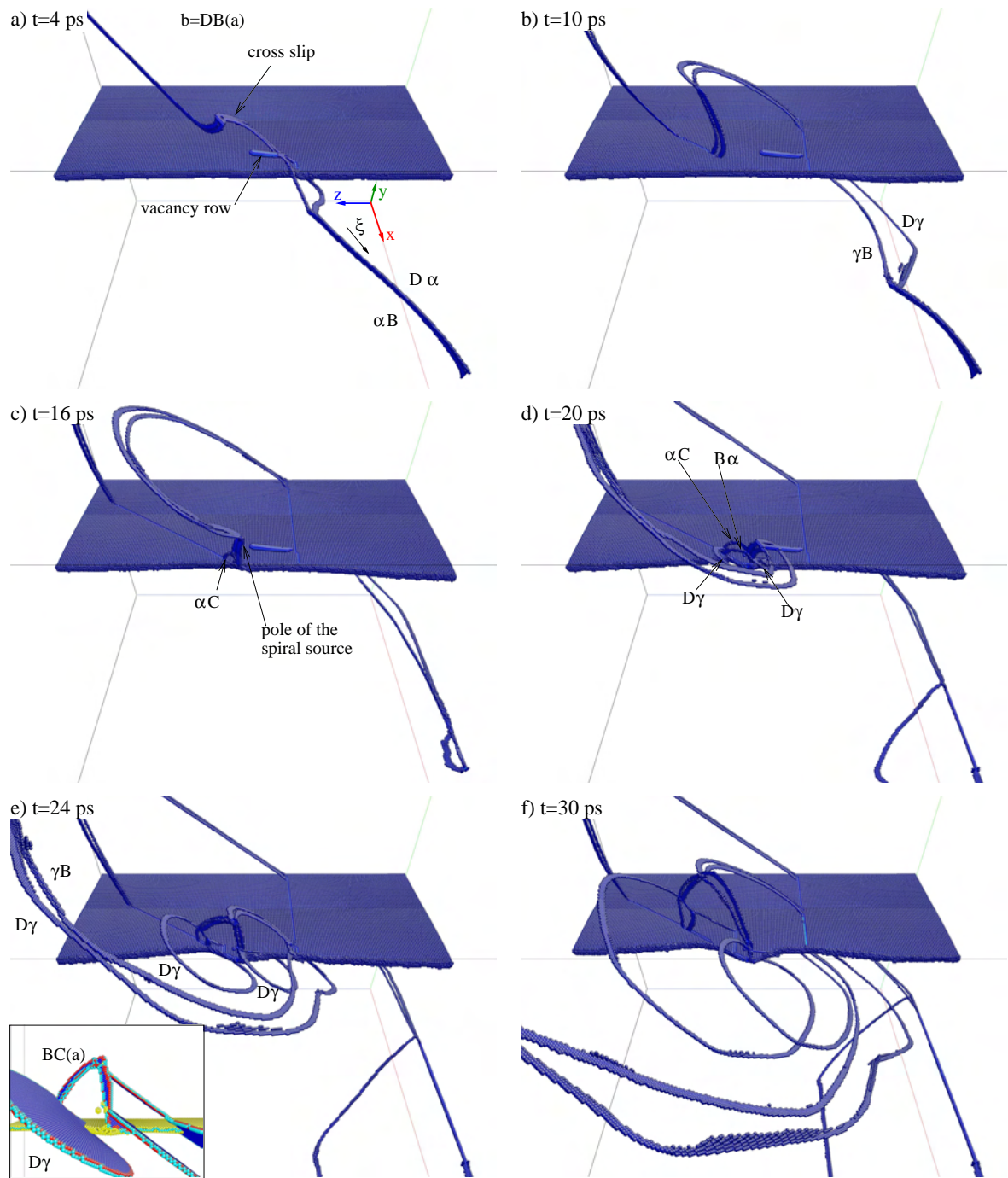


Figure 11.29: Snapshots of the screw dislocation DB interacting with a sharp crack at $0.995\epsilon_G$ (plane stress, $\Delta x = 6$ nm). One arm of the non cross-slipped part of the incoming dislocation is pinned at the crack tip and acts as pole of a spiral source.

previous simulations with blunted cracks (Figs. 11.21 - 11.23), the dislocation was attracted by the crack surface. However, at the high stress caused by the loading close to the Griffith load the dislocation cross-slipped towards the crack. Like in Fig. 11.12 the cross-slip occurred on two adjacent slip planes, and the so created jog produced a row of vacancies, Fig. 11.29a. The cross-slipped dislocation cut the crack surface while a part of the incoming dislocation annihilated at the crack surface, Fig. 11.29b. The non cross-slipped part of the dislocation moved towards the crack tip where it triggered the nucleation of new dislocations; amongst others two partial dislocations $D\gamma$ on the (c) -plane and $BC(a)$ on the same glide plane as the incoming dislocation. More important, however, is the fact that the cross-slipped dislocation which cut the crack front bowed over its non-cross-slipped arm and cut the crack front again. The non-cross-slipped arm of the original dislocation at the crack tip thus served as pinning point of a *spiral source*, see Fig. 11.29b-c. A possible configuration for a similar spiral source can also be seen in Fig. 11.23, however in the Fig. 11.29 the spiral source operated for more than one entire cycle and repeated operation could have been possible.

11.3.2 Large sample, plane strain

Simulations under plane strain conditions were performed in the large system at $0.998\epsilon_G$ with 30° dislocations with $\mathbf{b} = DB$ situated $\Delta y = 24$ nm below and $\Delta y = 9$ and 24 nm above the crack and with $\mathbf{b} = BD$ situated $\Delta y = 16$ nm above the crack. Furthermore a screw dislocation with $\mathbf{b} = DB$ situated $\Delta x = 9$ nm in front of the crack was simulated.

The screw dislocation at $\Delta x = 9$ nm and the 30° dislocations $\mathbf{b} = DB$ at $\Delta y = 9$ nm and $\Delta y = 24$ nm did not reach the crack front. Instead the dislocations swung in the stress field of the cracks, which in turn reacted onto the stress field of the dislocation. Such a process is shown in Fig. 11.30 for the screw dislocation.

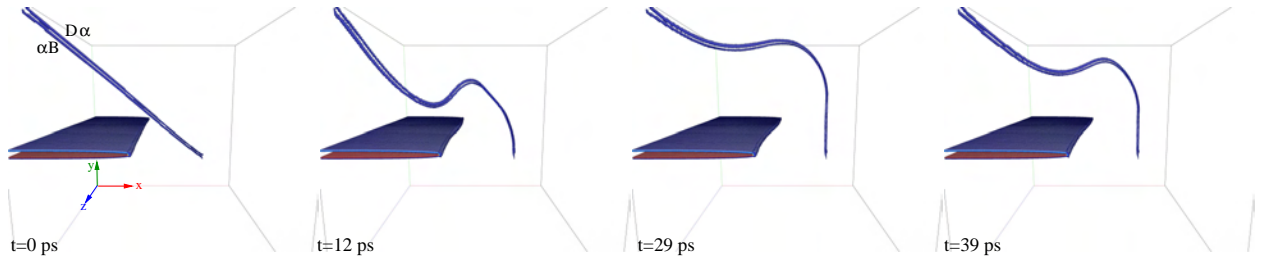


Figure 11.30: Snapshots of the screw dislocation DB interacting with a sharp crack at $0.998\epsilon_G$ (plane strain, $\Delta x \approx 8$ nm). The motion of the dislocation and the crack are coupled by their stress fields.

The processes during the interaction of the 30° dislocation DB starting from $\Delta y = 24$ nm below the crack are shown in Fig. 11.31. The behavior of the dislocation, including the change of the glide plane of $D\alpha \rightarrow D\beta + \alpha\beta$, is the same as in the case of a blunted crack tip, see Fig. 11.19. However, the significant crack closure led to a local crack front orientation parallel to $B\alpha$. There the dislocation loops αC and αD were emitted on the (a) -plane. The nucleation of this dislocations is combined with the emission of $C\delta$ and $D\gamma$ which led to the creation of stair rod dislocations, see the inset in Fig. 11.31c. This process corresponds to the process in Fig. 10.9 during the interaction of a sharp crack with a void.

Figure 11.32 shows snapshots from the simulation of the 30° dislocation $BD(a)$ starting

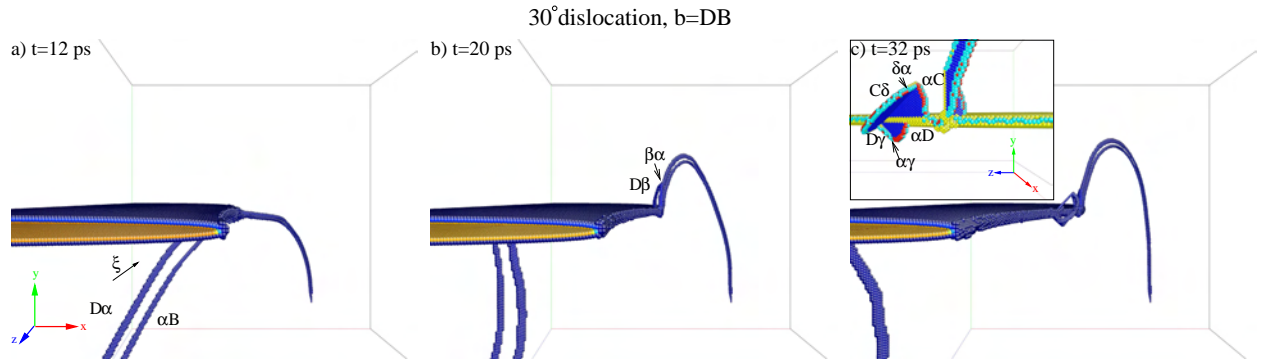


Figure 11.31: Snapshots of the 30° dislocation DB interacting with a sharp crack at $0.998\epsilon_G$ (plane strain, $\Delta y = 24$ nm). Only atoms with increased potential energy are shown. Crack closure in the shielded region leads to a local $[1\bar{1}2]$ orientation of the crack front. On this part of the crack front blunting dislocation half loops are emitted which are linked to dislocation on the inclined plane, see inset in c) in which the atoms are colored according to their CNA value.

at $\Delta y = 16$ nm above the crack. The dislocation came very close to the crack tip where it reached screw orientation and cross-slipped. This cross-slip at a sharp crack and $0.998\epsilon_G$ was the only time that cross-slip occurred under plane strain loading. As stated at the beginning of this chapter the cross-slip tendency is higher when the stress state is not pure plane strain. The cross slip in Fig. 11.31 indicates that cross slip onto the inclined planes can occur also under plane strain conditions.

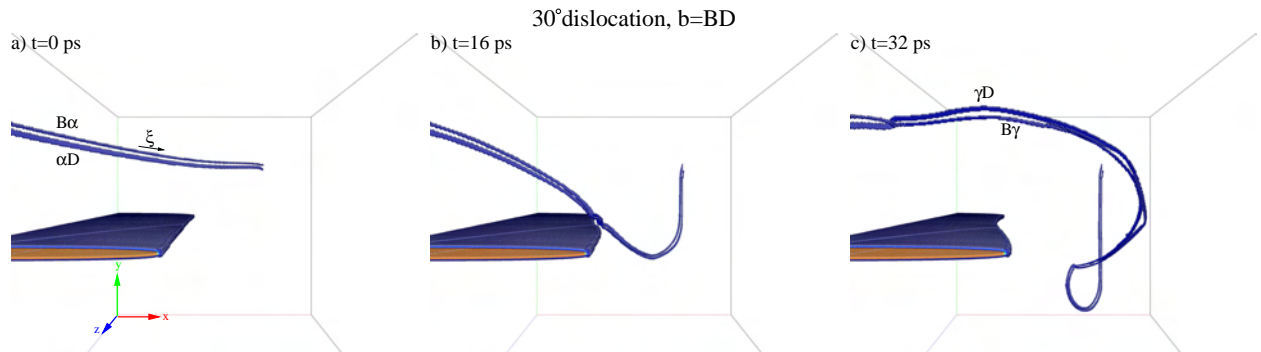


Figure 11.32: Snapshots of the 30° dislocation BD interacting with a sharp crack at $0.998\epsilon_G$ (plane strain, $\Delta y = 16$ nm). Only atoms with increased potential energy are shown. This example shows that cross-slip onto the inclined glide planes is also possible under plane strain conditions where the resolved shear stress on the (c) and (d) -planes is not as high as in the plane stress case.

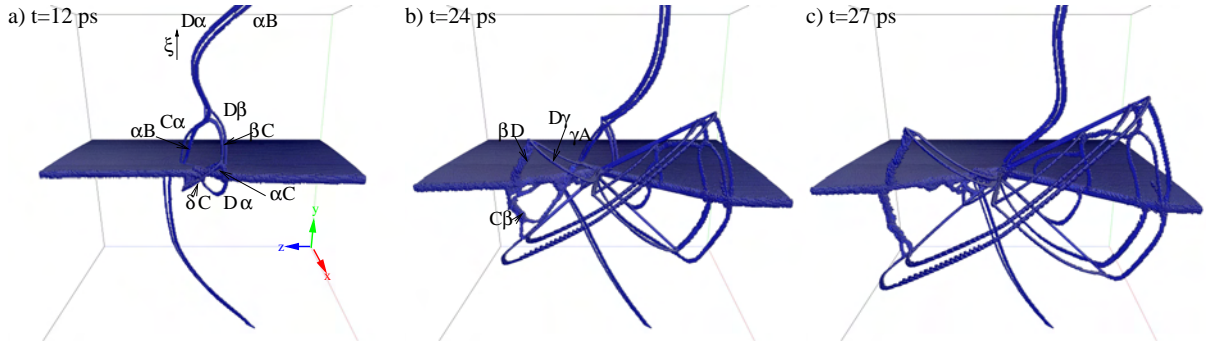


Figure 11.33: Snapshots of the interaction between a running crack and the 60° dislocation $DB(a)$ at a plane strain of $1.04\epsilon_G$ ($\Delta x = 8$ nm). Only atoms with increased potential energy are shown. The intersection of the crack with the dislocation leads to crack front segments with orientations along $B\alpha$ and βA , from which partial dislocation half loops like $D\alpha$ are emitted. The process of dislocation emission is the same as in Fig. 10.9.

11.4 Dynamic cracks and dislocations

The interaction of a propagating crack with the 60° dislocation $DB(a)$ placed at $\Delta x = 8$ nm in front of the crack was studied in the large sample under plane strain conditions and an overload of $1.04\epsilon_G$. The interaction of a sharp crack at an overload of $1.05\epsilon_G$ with a vertical screw dislocation with $\mathbf{b} = DC$ ($\Delta x = 10$ nm) was studied under plane strain conditions in the small sample ($50 \times 25 \times 25 \text{ nm}^3$). These studies were motivated by the observation that sharp propagating cracks can develop from blunted crack tips in the stress field of dislocations, and that these cracks can emit dislocations towards the incoming dislocation (see e.g. Fig. 11.10).

The interaction of an atomically sharp crack with the 60° $DB(a)$ at an overload of $1.04\epsilon_G$ is shown in Fig. 11.33. The simulation is equivalent to the one shown in Fig. 11.28 just at higher load. The initial processes (Fig. 11.33a) were similar to the "unzipping" process in Fig. 11.28 and Fig. 11.5. The velocity with which the dislocation approached the crack ($v_i \approx 17 \pm 5$ Å/ps) was about three times faster than the crack velocity at that time ($v \approx 5 \pm 2.55$ Å/ps). By the interaction with the dislocation and the emission of dislocations the crack front was locally arrested. The rest of the crack front, however, kept propagating. The crack front direction thus became locally parallel to the $B\alpha$ and βA directions. This enabled multiple emission of dislocation half loops on the (a) and (b) planes, which were coupled by stair rod dislocations to partial dislocations on the (c) and (d). This process is almost identical to the emission of dislocations in the simulation of the crack-void interaction, Fig. 10.9.

The vertical screw dislocation with $\mathbf{b} = DC$ does not experience any driving force in the stress field of the γ -crack. This dislocation was therefore used to study how the presence of the dislocation would affect a propagating crack. Fig. 11.34 shows that the stress field of the dislocation led to an instability of the crack front which caused the emission of a partial dislocation on the (c)-plane towards the dislocation. The emitted dislocations reacted with $D\alpha$ of the screw dislocation forming $\gamma\alpha$, which allowed $D\alpha$ to interact with the crack front. Emission of the trailing partial dislocation γB and the subsequent development of a full dislocation loop unloaded the whole small sample, and crack propagation stopped. No emission of dislocations on the blunting planes (a) and (b) was observed. The same crack under the same load without dislocation propagated at a constant velocity $v \approx 3 \pm 0.25$ Å/ps without showing signs of instability or dislocation emission.

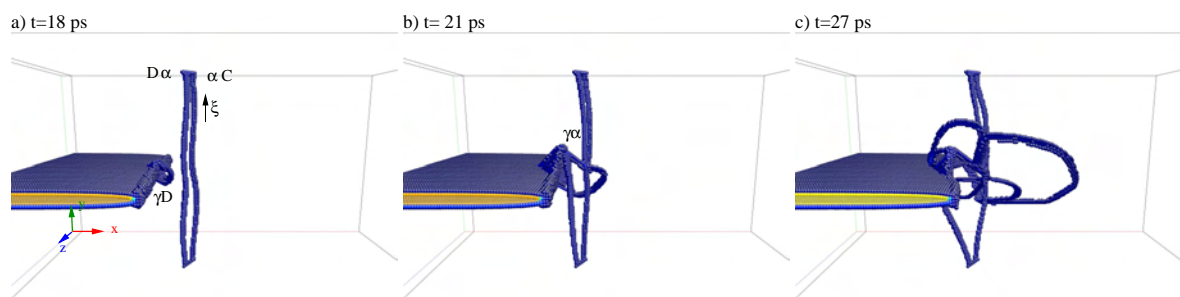


Figure 11.34: Snapshots of the interaction between a running crack and the screw dislocation $DC(a)$ at a plane strain of $1.05\epsilon_G$ (small sample: $50 \times 25 \times 25 \text{nm}^3$, $\Delta x = 10 \text{nm}$). Only atoms with increased potential energy are shown. In the stress field of the dislocation the running crack emits a partial dislocation. The same crack without dislocation propagated without emission of dislocations.

Chapter 12

Discussion

The study of crack front stability, the simulations of propagating cracks and their interaction with obstacles, and the analysis of the interactions between preexisting dislocations and cracks showed a plentitude of different phenomena. The aim of this discussion is not to provide detailed explanations for the specific effects, but rather to deduce generic principles which can be applied to mesoscopic models. Furthermore, the limitations of the MD method only allow for a qualitative comparison with the – upto now scarce – experimental literature.

The discussion is organized as follows: The next section critically reviews the consequences of various aspects of the present simulations for the discussion of the results. Sec. 12.2 summarizes and classifies the observations from the atomistic simulations. The driving forces on dislocations in the stress field of a semi-infinite crack are analyzed in sec. 12.3. These can be used to discuss the observed mechanism independent of the specific simulation set-up. Atomistic details of the dislocation-crack interactions are discussed in sec. 12.4. The differences between the model material and the experiments in Si are addressed in sec. 12.5, which closes with a qualitative comparison of the simulations to experiments.

12.1 Simulation specific aspects

It is clear that MD simulations are not able to model the full complexity inherent to the different time and length scales involved in fracture processes. Specific aspects of the present simulations which are relevant for the interpretation of the simulation results are addressed here.

Potential A general feature of the simulations was the tendency towards twin formation by emission of partial dislocations on adjacent planes, and the frequent observation of single partial dislocations. As mentioned in sec. 10.4 and chap. 11 this is related to the characteristics of the potential [31, 297]. I.e. the same simulations with different potentials can lead to the formation of full dislocations and no twinning. Similarly the characteristics of dislocation emission and the tendency towards cross-slip should depend on the potential.

Simulated time Only relatively short time periods were simulated (the longest simulation was 80 ps). Therefore slower processes could not be observed. Furthermore, processes

like the emission of trailing partials, which require that a dislocation has moved a certain distance from the crack tip may have been missed.

Temperature All simulations were performed without temperature control at an initial temperature of 0 K. Therefore processes requiring thermal activation could not be recorded. Simulation of fracture at elevated temperatures is possible [223], but outside the scope of this thesis.

Size limitations The most severe limitations are due to the restrictions on the number of atoms that can reasonably be simulated^a, leading to limited system sizes. As already mentioned, the size limitation has several consequences. The large strains required by the Griffith criterion can lead to artefacts. The pinning of the dislocation at the box boundaries has a significant influence on the possible dislocation processes. The reflection of sound waves and the image forces caused by the boundary conditions furthermore influence the dislocation behavior. Some aspects of the influence of the boundary conditions on the dislocation - crack interaction are discussed in appendix C.

An other aspect is that in relation to the small system size even displacements by only $1b$ are relatively large. A blunting by one atomic layer is extremely small on the experimental scale, it is however still noticeable if the entire system has a height of 100 layers (small system). The emission of a single dislocation does not significantly reduce the load on a crack tip under experimental conditions. Incontrast, the expansion of a full dislocation loop in the entire small system decreases the strain by about 1%.

All these limitations have to be considered when discussing the simulation results. The independence of the processes from system size and boundary conditions as well as physical reasoning based on the crystallography or stress field can however allow to draw generalizable conclusions.

12.2 Interaction mechanisms between dislocations and cracks

The interplay between cracks and dislocations was studied in the following settings:

- Nucleation of dislocations from static cracks
- Nucleation of dislocations from fast, propagating cracks
- Generation of dislocations during the interaction of a propagating crack with static obstacles
- Interaction between mobile dislocations with static cracks.

Whereas the first two cases have previously been studied to some extent by atomistic simulations (see sec. 2.2.3), the latter have not yet been addressed by simulations. Although similar processes might be active in these cases, the emission of dislocations from a propagating crack is conceptually different from the nucleation of dislocations from static cracks.

^aGiven the computational resources, larger simulation runs are possible. However, the amount of data which has to be analyzed becomes a critical parameter. A typical simulation run with about 38 million atoms generates about 150 GB of data.

The nucleation and propagation of dislocations at static cracks determines the initial fracture toughness K_{Ic} , possibly as a function of loading rate \dot{K} and temperature T . This case is addressed by most BDT models. The emission of dislocations from propagating cracks, either by dynamic instability or by the interaction with obstacles, in contrast, is related to the crack arrest toughness K_{Ia} . Although of greatest technical relevance, the atomistic and mesoscopic processes leading to the arrest of propagating cracks by the evolution of a plastic zone are not fully understood. In the following the processes in the simulations of the above cases are summarized and discussed.

12.2.1 Dislocation emission from static cracks

Static cracks blunted by removal of one atomic layer are relatively stable against the emission of dislocations. At loads larger than the Griffith load, brittle cleavage rather than dislocation emission takes place. A step created by the relative displacement of atomic planes at the crack tip by \mathbf{b} does not lead to the emission of dislocations at $0.95\epsilon_G$. Similarly the strain field of a dislocation placed at the blunted crack tip does not lead to dislocation emission. Larger displacements of the crack fronts leads to dislocation emission on the inclined (*c*) and (*d*) planes. Relative displacements produced by cuts along the (*a*) plane produced less stable crack configurations compared to cracks along the (*d*) plane, see sec. 10.3.

The step height of $2-3b$ at which a dislocation nucleated can be compared with the nudged elastic band calculation of dislocation loop emission on an inclined plane (configuration (a) in Fig. 2.11) by Zhu *et al.* [188]. At the saddle point configuration their partial dislocation in copper had a forward and lateral extension of 10 and $30b$, respectively. The corresponding activation barrier is $\Delta E_{\text{act}} = 1.1$ eV, such homogeneous dislocation nucleation is therefore unlikely to take place in experiments [188]. The presence of heterogeneities along the crack front should significantly reduce the activation energy for (inhomogeneous) dislocation nucleation, but small disturbances ($1-2b$) are not necessarily sufficient.

12.2.2 Dislocation emission from propagating cracks

Perfect atomically sharp cracks propagated by brittle cleavage upto loads of $1.1\epsilon_G$. Homogeneous nucleation of dislocations on all glide planes occurred along the crack front at $1.2\epsilon_G$. This process is different from the emission of partial dislocation loops from static cracks. Almost all dislocations on the (*c*) and (*d*) planes were connected by stair-rod dislocations with blunting dislocations on the (*a*) and (*b*) planes. Such dislocation emission has not been reported in the previous studies on γ -oriented cracks in fcc [184,187]. These simulations, however were performed at very high loads or loading rates. Therefore the dislocation nucleation process might not be comparable to the present simulations. However, it has to be mentioned that large differences in the nature of the emitted dislocations have been observed between Al and Cu [187]. The observed type of coupled dislocation emission can therefore be eventually specific to the potential. The influence of material properties like elastic anisotropy, generalized stacking fault energies and bonding characteristics on dislocation emission from cracks in three dimensions has not been studied in detail.

Two processes can be envisaged that generate joint dislocations like $C\delta + \delta\alpha + \alpha C$: the nucleation of a blunting dislocation αC at local variations of the crack front orientation which subsequently cross-slips onto the (*d*)-plane, or the creation of a nucleus from which dislocations on both planes grow simultaneously. Analysis of the simulations did not allow to

determine which process is active. Defects like steps on the propagating crack front can lead to localized dislocation emission at lower loads and velocities. The process, however, is the same as for homogeneous nucleation. The crack front orientation is clearly changed by this process.

12.2.3 Dislocation generation during crack-obstacle interactions

The interaction of the propagating crack with a void and the dislocation $DB(a)$ in the large sample caused the massive emission of partial dislocations on the blunting planes (a) and (b). These dislocations were coupled to dislocations on the (c) and (d) planes like the dislocations emitted from propagating cracks. The symmetric upwards and downwards emission of dislocations on (a) and (b) leads to an effective blunting of the crack. As a consequence, the propagation of the crack stops and the crack assumes locally an orientation parallel to $B\alpha$ or βA . As the unaffected crack region keeps propagating and the blunting dislocations expand further, the crack front becomes 'V'-shaped.

This was not the case for the crack interacting at low overload with the dislocation $DC(a)$. Here the expansion of a full dislocation loop effectively unloaded the small sample and crack propagation stopped also in the unaffected crack regions.

The emission of blunting dislocations from propagating cracks which due to the interaction with obstacles assume local crack front orientations which are contained in the blunting planes should be a *general* phenomenon for a crack in the γ -orientation. The observed coupling to non-blunting dislocations may be specific to the present simulations and is not required for the emission of blunting dislocations.

12.2.4 Interactions between preexisting dislocations and cracks

Most of the processes involved in the dislocation - crack interaction are qualitatively different from the above described processes. The following mechanisms relevant to crack tip plasticity could be identified from the simulations of dislocation - crack interactions:

Stimulated emission The emission of a dislocation at the intersection of dislocation and crack front was relatively frequently observed (see e.g. Fig. 11.6), however only for incoming dislocations on the (a)-plane^b and under plane stress conditions. From the simulations with $\mathbf{b} = DB(a)$ only the horizontal 30° dislocation did not lead to stimulated emission. Partial as well as full dislocation were emitted on both the (c) and (d) planes. Their nucleation and propagation is not coupled to the existence of blunting dislocations. One incoming dislocation can stimulate the emission of multiple dislocations, and activate both glide planes (c) and (d). The number of dislocations generated by stimulated emission increases with increasing load. The emission of dislocation loops efficiently reduces the strain energy stored in the system, see Fig. 11.18. Whether stimulated emission takes place depends on the impinging velocity of the dislocation. Slow dislocations do not trigger dislocation nucleation, but fast dislocations can generate new ones. This indicates that stimulated dislocation emission still requires the overcoming of a significant activation barrier. In experiments, thermal activation should facilitate stimulated emission.

^bOnly in one case in the small system nucleation on top of the stacking fault produced by an incoming dislocation on the (c)-plane was observed, however, not directly after impact of the dislocation, see Fig. 11.4.

Partial cross-slip The change of glide plane of one partial dislocation according to e.g. $D\alpha \rightarrow D\beta + \beta\alpha$ occurred in nearly all simulations where the dislocation cut the crack front, see e.g. Fig. 11.5, but also Fig. 11.26. This process only takes place on one side of the crack, highlighting the general asymmetry of dislocation-crack interactions with respect to the cleavage plane. The resulting stair-rod dislocation at the crack tip frequently acted as *nucleus* for the nucleation of partial dislocations. They can lead to an "unzipping" of the initial dislocation into two new dislocations according to $DB(a) \rightarrow DB(c) + CB(a)$, see e.g. Fig. 11.5. The generation of new dislocation line length by this process, however, takes place mostly behind the crack tip. It therefore does not efficiently shield the crack from the stressed region in front of the crack tip.

Cross-slip Some dislocations on the (*a*)-plane which reached screw orientation in front of the crack cross-slipped onto the (*c*)-plane, see e.g. Fig. 11.12. Cross-slip always proceeded by the Fleischer mechanism, i.e. without prior constriction of the dislocation. In most cases cross-slip occurred through the acute angle, in some cases the cross-slipped dislocation formed an acute and an obtuse angle with the remaining dislocation on the initial glide plane. Cross-slip took place preferably under plane stress conditions, cross-slip under plane strain conditions was observed only in one simulation. Cross-slip occurred towards and away from the crack, and the cross slipped part of the dislocation could intersect the crack front at a different point than the original dislocation. Cross-slip of a kinked dislocation line by the Fleischer mechanism leads to extended jogs on the cross-slip plane. Upon glide these jogs produced rows of vacancies. Cross-slip by the Fleischer mechanism has already been reported in atomistic simulations at high stresses [34] and in fracture simulations [35]. The Fleischer mechanism seems therefore a viable alternative to the Friedel-Escaig mechanism of cross-slip, at least at high stresses and low temperatures.

Spiral source Under certain circumstances cross-slip lead to the creation of a spiral source, see e.g. Fig. 11.29. This can be the case e.g. for the screw dislocation $DB(a)$ which is attracted towards the crack surface and repelled by the crack tip. It therefore intersects the crack surface behind the crack tip. If a part of the dislocation cross-slips above the crack plane, it will cut the crack front. The non-cross-slipped part which ends on the crack surface can then act as the pole of a spiral source around which the cross-slipped dislocation on the (*c*)-plane is revolving. Such a configuration for a spiral sources can also be seen in Fig. 11.21. However, in this and other configurations the sources did not operate for one full cycle as the spiral was blocked by stacking faults on the (*d*)-plane. Only the spiral source in Fig. 11.29 operated for one entire cycle.

Formation of sharp cracks For blunted cracks close to the Griffith load, the stress field of a dislocation lead to the development of atomically sharp cracks in the anti-shielded region of the crack front, see e.g. Fig. 11.6. Crack closure in the shielded region, however, is not possible for the blunted cracks.

All but the last of the above mechanisms can be active for dislocations interacting with both, blunted or sharp cracks. Dislocations which interacted with atomically sharp cracks – either already existent or formed in the presence of the dislocation – showed two additional mechanisms:

Induced dislocation emission The stress field of a dislocation can induce the emission of a dislocation on the (*c*) or (*d*)-plane from a propagating sharp crack towards the dislocation, see e.g. Fig. 11.34. The dislocation emission process is different from that of a propagating unstable crack insofar that it is localized and not coupled to dislocations on the blunting planes. The same crack at the same load does not emit dislocations without presence of the dislocation stress field.

Crack front reorientation The stress field of the incoming dislocation or of emitted dislocations can lead to a curved crack front. If the crack front direction attains an orientation which lies within the vertical, blunting slip planes (*a*) or (*b*), the same processes like in sec. 12.2.3 can be active.

Depending on the nature of the dislocation and the crack and the initial position of the dislocation, these mechanisms were able to produce pronounced crack tip plasticity, e.g. by creating within 30 ps three full dislocations and two partial dislocations of significant line length (see Fig. 11.29). The overall dislocation activity increases with increasing load and is higher under plane-stress conditions than for plane-strain conditions.

12.3 Dislocations in the stress field of cracks

In sec. 10.2 the stress fields of the cracks under plane strain and plane stress-like loading conditions were determined from the atomistic calculations. As expected, due to the boundary conditions the atomistic stress fields are qualitatively and quantitatively different from the anisotropic solution for a semi-infinite crack in an infinite, linear elastic continuum [295]. The consideration of the Poisson contraction reduces the *z*-components of the stress tensor $\boldsymbol{\sigma}$. The simulations modeling plane stress loading show however still plane strain characteristics. The mathematical idealization of plane stress conditions can not be fully reached in large scale, three dimensional simulations.

The atomistic stress fields as well as the stress field of the continuum theory can be used to calculate the glide component of the Peach-Koehler force [12]

$$F_{PK} = \frac{[(\mathbf{b} \cdot \boldsymbol{\sigma}) \times \boldsymbol{\xi}] \cdot [\boldsymbol{\xi} \times (\mathbf{b} \times \boldsymbol{\xi})]}{|\mathbf{b} \times \boldsymbol{\xi}|} \quad (12.1)$$

that a dislocation segment of unit length would experience at any given point within the sample.^c With the exception of the region close to the boundaries, the stress field of the straight crack front is independent of *z*. It is therefore sufficient to calculate F_{PK} on a plane normal to the *z*-axis.^d The magnitude F_{PK} of the glide component of the Peach-Koehler force caused by the stress field of the simulated cracks was calculated under plane strain and plane stress conditions with the matlab program package DISPROCRAST [299]. The results are shown in Figs. 12.1 - 12.4. These figures show also the glide force calculated with the anisotropic plane strain and plane stress solution for the stress field of a semi-infinite crack

^cThis approach neglects however the image force on the dislocation caused by the free fracture surfaces. An inclusion of these forces for arbitrary oriented dislocations would require a numerical treatment.

^dThis plane does not correspond to a glide plane. However, only the distance of the dislocation segment from the crack front determines the stress at the location of the dislocation, not the projected distance on the glide plane. A projection on the glide plane is therefore not necessary.

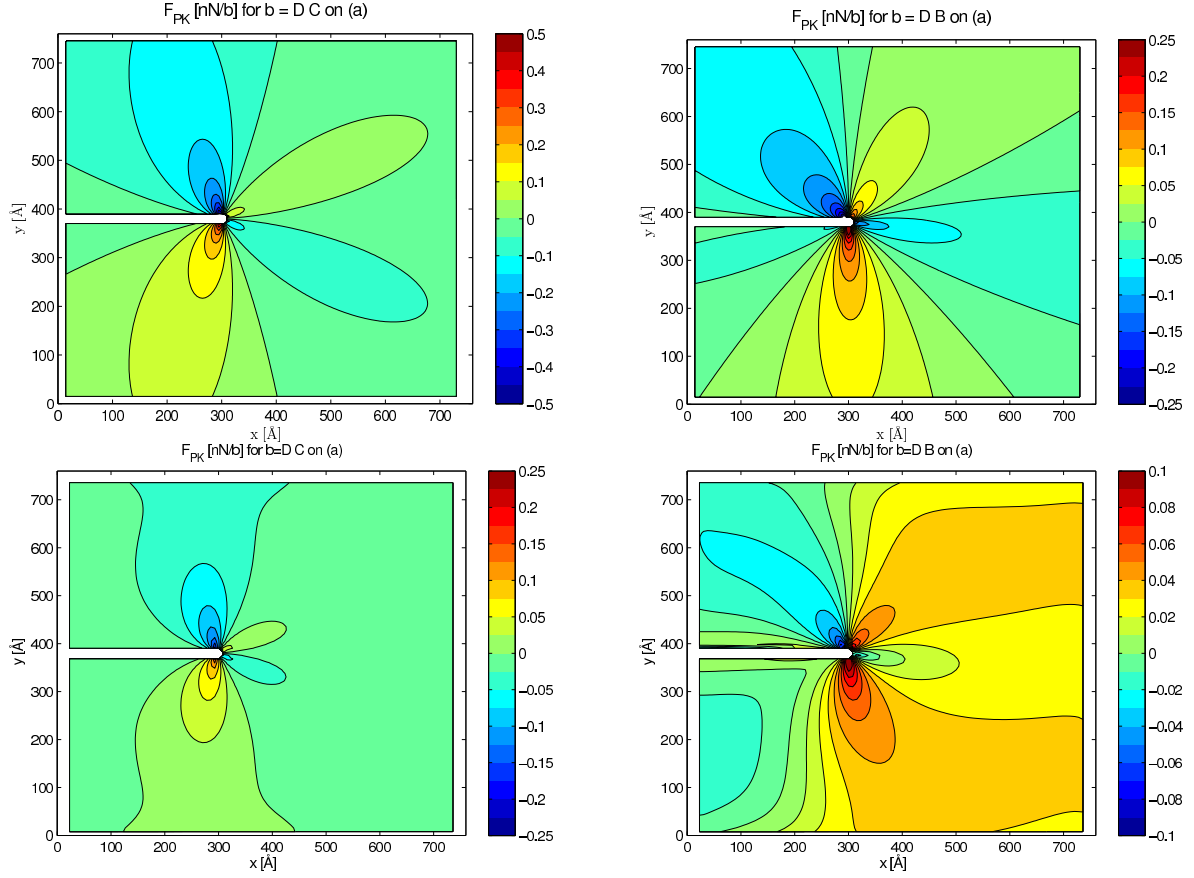


Figure 12.1: Glide component F_{PK} of the Peach-Koehler force on dislocations on the (a) -plane calculated from the crack stress field under *plane strain* conditions. The top row shows the results for the crack stress field calculated with anisotropic elasticity theory (K_I for $\epsilon = 0.018$). The bottom row shows F_{PK} calculated from the stress determined from the relaxed crack in the large sample ($\epsilon = 0.018$, crack blunted by one layer). The dislocation $DC(a)$ (left) belongs to the symmetry class III, $DB(a)$ represents class I. Note the different color scales.

(compare also to Fig. 10.4). The plots include slip systems from each of the classes I-III of Tab. 11.1. Fig. 12.1 and Fig. 12.3 for example show that $DC(a)$ and $AB(c)$ indeed belong to the same symmetry class (III) of slip systems with respect to the driving forces caused by γ -oriented cracks.

The differences between the stress fields derived from the atomistic calculations and from the continuum solution are reflected in the Peach-Koehler force. The main characteristics of the driving force near the crack tip are however present in the atomistic simulations, see Figs. 12.1 - 12.4. Although including the Poisson contraction reduced the σ_{zz} component of the crack tip stress field, Figs. 12.2 and 12.4 show that the characteristics of the glide force is still dominated by the plane strain conditions. The boundary conditions modeling the plane stress conditions however increased the driving force for dislocations like $DB(c)$ compared to the plane strain case. This led to the higher tendency towards cross-slip in the simulations modeling plane stress conditions compared to the simulations under plane strain loading, in agreement with the ideal plane stress case.

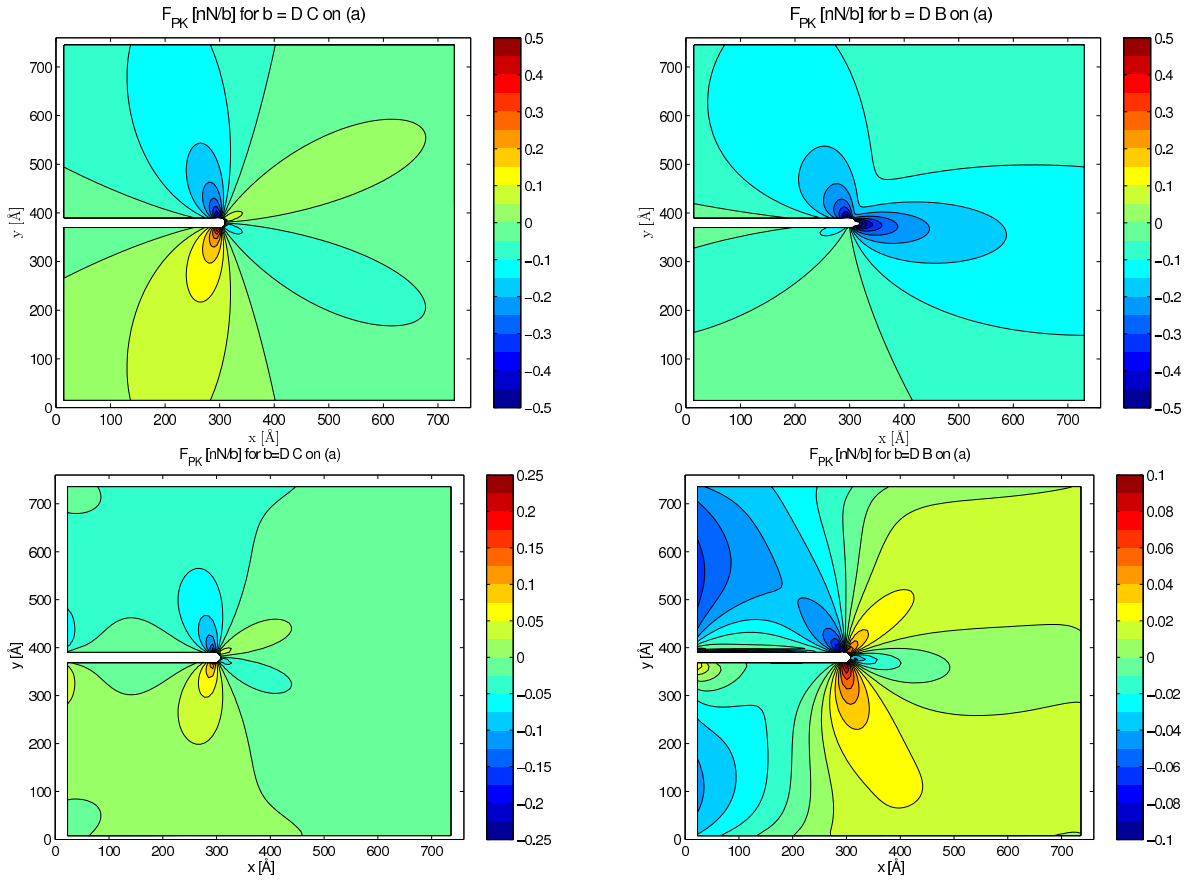


Figure 12.2: Same as Fig. 12.1 but the top row shows the glide force calculated from the anisotropic elastic solution for *plane stress* conditions. The lower row shows the results obtained from the stress field of the simulation using plane stress-like boundary conditions ($\epsilon = 0.024$, large sample, crack blunted by one layer).

The plots of the glide force in Figs. 12.1 - 12.4 can be used to analyze the motion of the incoming dislocations in chapter 11. For this purpose the absolute value of F_{PK} is not important. The existence of regions of different sign of the glide force already provides some qualitative understanding of the behavior of the dislocations in the stress field of the crack. The relative magnitude of F_{PK} on different slip systems can be used to assess the tendency of dislocation segments in screw orientation to cross-slip to another plane. By assuming that a screw dislocation will cross-slip to the plane with the highest resolved shear stress, $|F_{PK}(a)| - |F_{PK}(c)|$ can be used to quantify this tendency. Fig. 12.5 shows the cross-slip tendency for the dislocation BD . For both, plane strain and plane stress conditions, the dislocation experiences nearly everywhere a higher driving force on the (c) plane. The same kind of reasoning can be used to study the tendency towards partial cross-slip according to e.g. $\alpha C \rightarrow \delta C + \alpha\delta$. The difference in glide force between $\alpha C(a)$ and $\delta C(d)$ is shown in Fig. 12.6. From this figure it can be seen that indeed the blunting partial dislocations emitted on the (a) and (b) -planes, e.g. by a propagating crack (see Fig. 10.8), should have a strong tendency to change their glide plane.

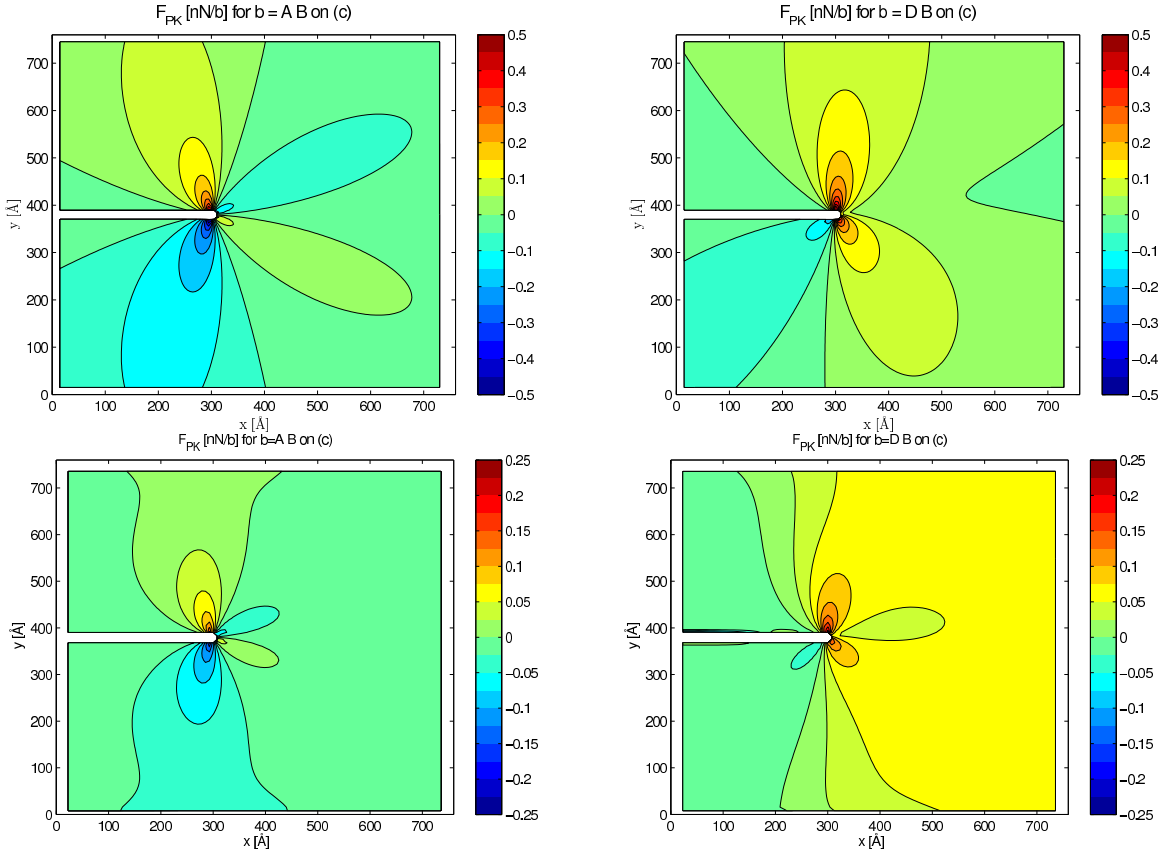


Figure 12.3: Same as Fig. 12.1 for dislocations on the (c) -plane (plane strain). $AB(c)$ (left) belongs to the same class III as $DC(a)$ from Fig. 12.1. $DB(c)$ is part of symmetry class II.

By using the continuum solution to analyze the processes in our simulations rather than the F_{PK} directly derived from the atomistic calculations, the interpretation of the simulations can be *generalized* to γ -cracks in materials with the same slip systems.^e In the following, the above described qualitative analysis is illustrated using some of the simulation results. In all cases the continuum solution for the plane strain case are used, as the simulations using boundary conditions modeling the plane stress case were still dominated by plane strain.

Vertical 60° dislocation $\mathbf{b} = DB(a)$ in front of the crack Fig. 12.1 shows the glide force acting on dislocation segments on the (a) -plane with $\mathbf{b} = DB$. The straight dislocation line in front of the crack is attracted towards the crack above and below the crack plane. The shape of the dislocation, see e.g. Fig. 11.9, is bowed out according to these forces, with a bulge where the dislocation experiences a repulsive force. Upon contact with the crack front, the lower part of the dislocation still experiences a positive glide force while the upper part of the dislocation stopped at the boundary of the region where the glide force changes its sign. At the crack surface, the leading partial dislocation can change its glide plane. This is

^eThe stress field of the crack depends however on the anisotropy of the crystal. This can lead to small differences in the relative magnitude of F_{PK} , however without changing the main characteristics.

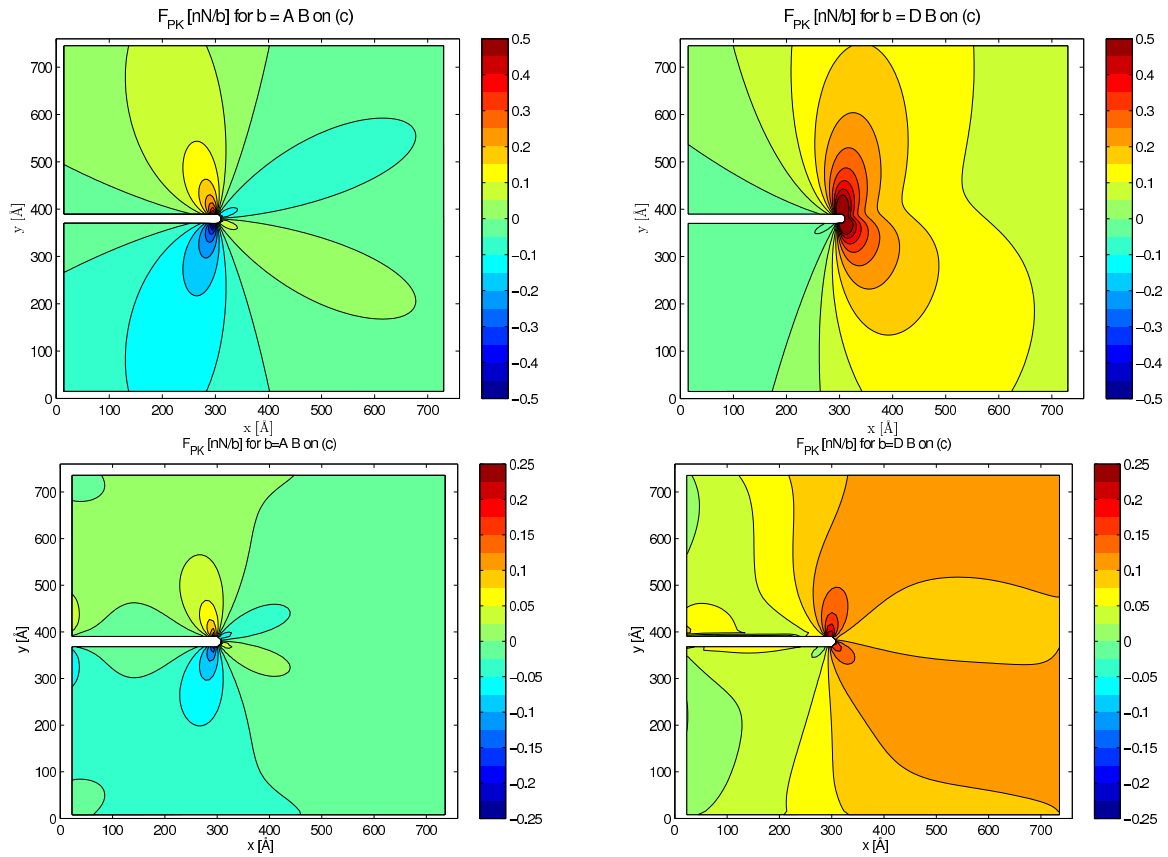


Figure 12.4: Same as Fig. 12.2 for dislocations on the (c) -plane (plane stress).

avored by the higher driving force in this region of the crack on $D\beta(b)$ compared to $D\beta(b)$, see Fig. 12.6.

The continuum analysis can of course not provide any insight on the atomistic processes leading to the stimulated emission of dislocation loops. However, it shows that the emitted loops, e.g. $CB(d)$ in Fig. 11.6, experience a large driving force and can expand over a large portion of the glide plane, see Fig. 12.3 ($CB(d)$ is mirror symmetric to the depicted $DB(c)$, see Tab. 11.1). The emission of dislocations on the (c) and (d) planes is more favorable under plane stress-like loading than under plane strain conditions, compare Figs. 12.3 and 12.4.

Horizontal 30° dislocations $\mathbf{b} = \pm DB(a)$ above and below the crack Fig. 12.1 can also be used to analyze the 30° dislocations. The horizontal dislocation $\mathbf{b} = DB(a)$ above the crack, Fig. 11.14, experiences a downwards acting (negative) glide force towards the crack surface and is repelled by the crack tip. The same dislocation positioned below the crack, Fig. 11.15, experiences an upward (positive) attraction by the crack tip and a repulsion by the crack surface. As can be seen from Fig. 12.1 the acting forces are not mirror symmetric with respect to the cleavage plane. The repulsion directly at the crack tip is different for the two dislocations, their behavior at the crack tip was therefore also different. Whereas the trailing partial of the dislocation above the crack plane changed its glide plane to (b) , the same dislocation below the crack cross-slipped on the (c) -plane. The cross-slip took place

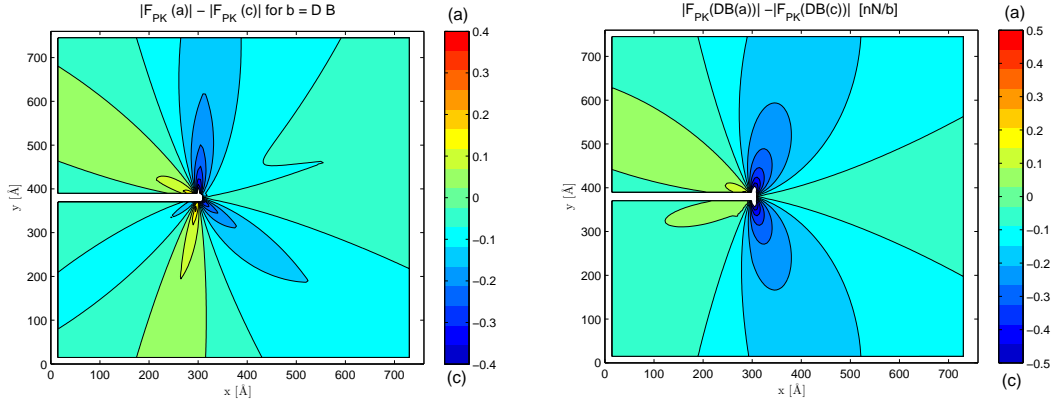


Figure 12.5: Cross-slip tendency for dislocation segments with $\mathbf{b} = DB$ in screw orientation calculated by comparing the magnitude of the driving force on the two planes (a) and (c). Calculated from the continuum solution of a semi-infinite crack under plane strain (left) and plane stress conditions (right).

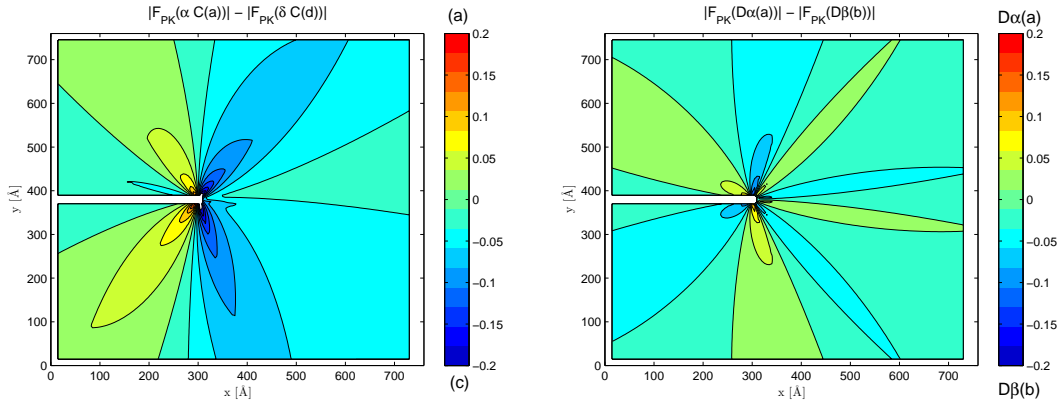


Figure 12.6: Difference in the absolute magnitude of the Peach-Koehler force F_{PK} on partial dislocations on different glide planes calculated from the continuum solution of a semi-infinite crack under plane strain. The plots indicate the tendency that a partial dislocation changes its glide plane according to $\alpha C \rightarrow \delta C + \alpha \delta$ (left) or $D\alpha \rightarrow D\beta + \beta\alpha$ (right).

in the region expected from Fig. 12.5. Cross-slip is also favorable above the crack, however, the initially horizontal dislocation $= DB(a)$ can not reach the screw orientation above the crack. The differences between the simulations under plane strain conditions and under the conditions modeling plane stress-like loading can be rationalized by the different development of the stress field in front of the crack in the atomistic simulations, see Figs. 12.1 and 12.2.

Inclined screw dislocation $\mathbf{b} = \pm DB(a)$ The importance of the position of the inclined screw dislocation with respect to the crack front can be directly seen in Fig. 12.1. Depending on the portion of the dislocation line which resides in an attractive region (corresponding e.g. to a negative force for $\mathbf{b} = DB(a)$ above the crack), the dislocation is either attracted or repelled. The location of the pinning points also determines whether the dislocation within the stress field of the crack can assume screw orientation in the regions favorable for cross-slip, see Fig. 12.5.

Dislocations on the (c) plane The (c) and (d) planes are contained in two of the three symmetry classes of slip systems, see Tab. 11.1. However, only dislocations on (c) and (d) planes belonging to class II have been observed experimentally, see sec. 2.2.2.1. The studied dislocation $DB(c)$ belongs to this class. The driving force on this dislocation is significantly higher on the (c) -plane than on the (a) -plane, especially for the plane stress case, see Figs. 12.3 and 12.4. This led to the high dislocation velocities in sec. 11.2.2. The dislocations with $\mathbf{b} = \pm DB(c)$ experience a glide force of the same sign in most of the glide plane. The dislocations in the simulation showed no cross-slip or other dislocation processes. Cross-slip to (a) is only favorable in very small regions in which the dislocations have to reach screw character, see Fig. 12.5. In the region favorable for cross-slip which is close to the surface, however, additional effects due to image forces have to be expected.

Conditions favorable for multiple operation of dislocation sources The atomistic simulations showed that the creation of an operating spiral source is possible under certain conditions, see Fig. 11.29. In order to operate multiple times, a dislocation source should of course not be blocked by other dislocations or stacking faults. However, the back stress of emitted dislocations is also an important factor for the operation of a source. Dislocations in the stress field of cracks stop in the region where the Peach-Koehler force changes its sign. Dislocations emitted from a source will thus pile up in these regions leading to a back stress on the source and eventually to a "running dry" of the source. Only cross-slip – which can become favorable in the stress field of a dislocation pile-up – can reduce the back stress. Multiply operating sources of any type at or near cracks should therefore be found most probably in slip systems with large regions in which the driving force does not change its sign. For the γ -crack under plane strain conditions this is only the case for slip systems of the type $DB(c)$, see Fig. 12.3, which belong to the symmetry class II (see Tab. 11.1). Under ideal plane stress conditions the system $DB(a)$ (class I) also becomes favorable for multiply operating dislocation sources, see Fig. 12.2.

The above considerations are only a first step towards a qualitative understanding of dislocation processes at or near crack tips. By considering only the forces on dislocation segments caused by the stress field of the crack, several basic aspects are neglected. Besides the lack of image forces and the effect of the line tension of the dislocation, the reaction of the crack is neglected. This can include crack opening or closing, crack front reorientation and the change of the stress field by crack tip blunting. In the above treatment the three dimensional nature of the problem is furthermore only incorporated by accounting for the different glide planes.

A further important aspect that is neglected is the existence of multiple dislocations. The emission of dislocations lead to a shielding of the crack. The stress field of dislocations and dislocation pile-ups can significantly influence the the behavior of dislocations close to cracks. A deeper understanding of the role of dislocation-crack interactions for the crack initiation and crack arrest toughness as well as the brittle-to-ductile transition most probably requires the modeling of dislocation ensembles close to the crack. The explicit (stimulated) nucleation of dislocations at crack fronts can however not be directly included in pure continuum models. Currently, only atomistic calculations can provide dislocation nucleation criteria.

12.4 Atomistic aspects

A detailed investigation of the atomistic mechanisms during the nucleation of dislocations from propagating or static cracks is not intended here. The analysis of the reaction pathway and of the critical configuration for dislocation nucleation at crack tips would require other methods like the nudged elastic band method (NEB) [300], see also [188]. These methods require information on realistic starting and end configurations, which could in principle be determined from the present simulations. It is however unclear how transferable these results would be with respect to other potentials or materials. In addition there is currently no possibility to link such kind of detailed atomistic information (in Ni) to available experimental observations. The study of the atomistic mechanisms of (stimulated) dislocation nucleation is therefore left for future investigations, and only more general atomistic aspects are addressed in this section.

One more general question is in how far the Burgers vector and glide plane of the nucleated dislocation is (energetically) determined by the stress field and to what extent it is (kinetically) determined by the nature of the defect at the crack front [2]. The effect of the nature of the dislocation source on the emitted dislocations is usually discussed in the context of dislocation emission from cleavage ledges [1, 2, 166, 168]. Besides the resolved shear stress the creation of new surfaces and the line energy of the nucleated dislocation is considered as parameter determining the character of the dislocation [1]. In the light of our simulations the last aspect however seems questionable. The nucleation of a full dislocation always proceeds via the nucleation of two separate partial dislocations. The kinetics of the nucleation process should therefore be determined by the nucleation barriers of the partial dislocations and not by the line energy of the full dislocation.

The influence of the nature of the dislocation source on the character of the emitted dislocation can be clearly seen when comparing the dislocation emission from propagating cracks, e.g. Fig. 10.8, with that from static cracks, e.g. Figs. 10.5 (blunted crack) or Fig. 11.28 (sharp crack). Although the characteristics of the crack stress field should be similar, different types of dislocations are nucleated. However, the "co-nucleation" of dislocations on (*a*) and (*d*)-planes from propagating cracks is probably due to local variations of the crack front direction which enable the emission of blunting dislocations on the (*a*) and (*b*)-planes similar to the emission in the case of the interaction of the crack front with an obstacle, Fig. 10.9. The nature of the crack is therefore not directly comparable to a straight, static crack.

A detailed inspection of a stimulated emission process revealed the configuration shown in Fig. 12.7. It shows that upon contact of the 30° dislocation $DB(a)$ with the crack front three partial dislocation nuclei were generated. They all lie on the inclined planes (*c*) and (*d*). The Burgers vectors $C\delta(d)$ and $D\gamma(c)$ experience the same driving force, but not $\delta B(d)$. From these nuclei only the dislocation $D\gamma(c)$ grew during the following picosecond, whereas the others disappeared. This is an indication that at least in this case the nature of the defect created by the incoming dislocation may perhaps determine the type of the glide plane, but not the Burgers vector of the emitted dislocation.

An other question is why not all types of dislocations led to stimulated dislocation emission in the simulations. For all the incoming dislocations DB on the (*a*) plane which cut the crack front, only the 30° dislocation starting from below the crack did not lead to stimulated dislocation emission. This might be related to the fact that the trailing partial dislocation

αB contrary to all the other cases did not cut the crack front. This partial dislocation does not lead to crack opening but only produces a kink in the crack front. This kink might lead to an energetically unfavorable crack tip configuration that is prone to dislocation emission.

A more general and perhaps more important observation is that incoming dislocations on the (*c*) plane did not stimulate dislocation emission. This is the case although they have the same Burgers vector DB which caused stimulated emission when gliding on the (*a*) plane. The dislocations furthermore intersected the crack front with a significant kinetic energy. One possible explanation for this observation is that the expansion of the dislocations on the (*c*)-plane efficiently reduced the strain in the sample. Dislocations $DB(c)$ can in general relieve more strain than on the (*a*)-plane, however, in a large sample this effect should become smaller. An other possible reason lies in the nature of the created defect on the crack front. The static simulations of cracks cut according to the passage of dislocations with $\mathbf{b} = BC(d)$ and $\mathbf{b} = DB(a)$ showed that the cuts made by the dislocation on the (*c*) or (*d*)-plane (according to symmetry class II) were more stable than cuts on the (*a*)-plane (symmetry class I) which make an acute angle with the crack front, see sec. 10.3. In this case, however, the passage of more dislocations, e.g. coming from the same source on (*c*), might trigger dislocation emission. An other aspect is that the dislocation with $\mathbf{b} = BC(d)$ did not have to stop at the crack tip (see the plot of the Peach-Koehler force, Fig. 12.3). The fact that a part of the dislocation $DB(a)$ has to stay at the crack tip might be important for stimulated emission. This might be even more relevant in the experimental situation, where thermal activation processes should facilitate stimulated dislocation emission. The first step to simulate the effect of temperature on a dislocation resting at the crack front, Fig. 10.6 showed however no dislocation emission.

The few experimental results on stimulated emission can not clarify the above questions. In the γ -orientation, only stimulated emission triggered by dislocations on the (*a*) and (*b*) plane were reported [153]. The sole case of stimulated emission in the β -orientation was triggered by $CB(a)$ [2, 153]. According to the Peach-Koehler force due to the stress field of the crack, one part of this dislocation would also have to stop at the crack front. This dislocation, however, does not lead to the creation of a crack front ledge. This is an indication that also kinks in the crack front can lead to dislocation emission.

Further modeling and experimental studies are necessary to identify the exact mechanisms of stimulated dislocation emission and to clarify whether all types of dislocations or only dislocations on certain slip systems can trigger dislocation emission from crack tips.

12.5 Relation to experiments

In the present study, nickel was used as *model material* to elucidate fundamental mechanisms of dislocation-crack interactions. The face-centered cubic metals have the same slip systems as the diamond-cubic structure of silicon. There are of course significant differences between both materials. These are addressed in the following section. A discussion of the simulation results in the context of available experimental results is limited to general aspects like the nature of the generated dislocations and the characteristics of dislocation source configurations. A qualitative discussion of these aspects is given in the sections 12.5.2 and 12.5.3.

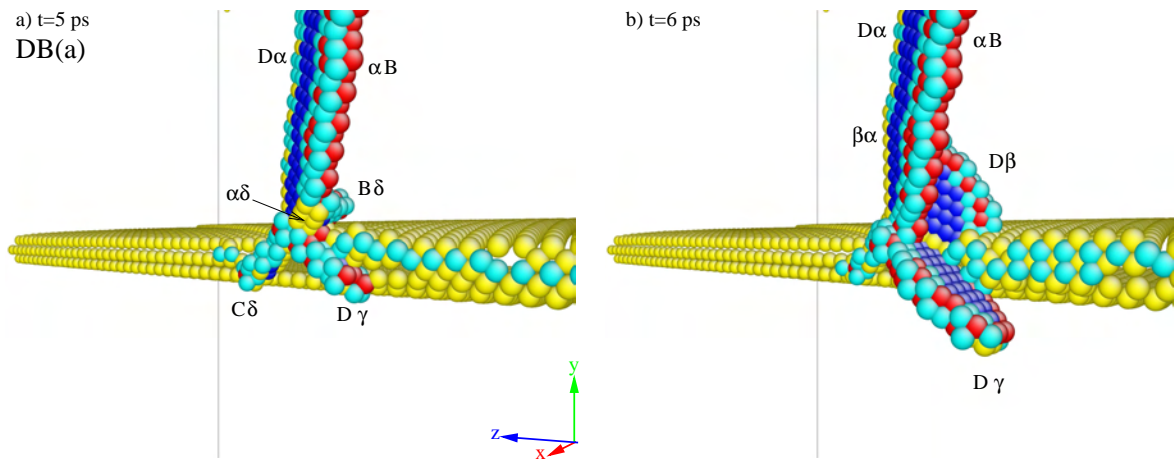


Figure 12.7: Detail of the emission process of the partial dislocation $D\gamma$ from the simulation of the 30° dislocation $DB(a)$ coming from above the crack ($0.88\epsilon_G$, large sample, plane stress, $\Delta y = 50$ nm, crack blunted by one layer), see Fig.11.14. Atoms are colored according to their CNA value. The assumed Burgers vectors of the dislocation nuclei in a) are based on the determination of the slip vector.

12.5.1 Nickel versus silicon

In addition to sharing the same slip systems as Si, brittle cleavage of cracks in the γ -orientation is possible in the Ni-potential. This is not the case for semiempirical potentials for Si [172]. The Nickel potential thus allows to reproduce the basic crystallographic ingredients to model fracture in Si.

However, the strong tetrahedral bonding in Si results in a more complex dislocation core structure and higher Peierls stress compared to fcc metals [13]. This results e.g. in a strongly anisotropic line energy of dislocations which lead to the well-known preferential orientation of the dislocation line along Peierls valleys [12]. The dislocations in Si therefore do not bow out as easily as in Ni, and dislocation loops acquire a hexagonal shape. The atomic bonding in Si furthermore leads to a directional cleavage anisotropy: crack propagation on a $\{110\}$ plane is easy along $\langle 110 \rangle$ directions and difficult in the $\langle 001 \rangle$ directions [173]. Therefore inducing crack front curvature should be more difficult in Si compared to Ni. The bonding also influences the mobility of dislocations in Si. However, at temperatures close to the brittle-to-ductile transition temperature (BDTT) dislocations on the glide set in Si are mobile, and their velocity is fairly isotropic [301]. This aspect is adequately modeled by the simulations in Ni at 0 K.

Further differences between the simulations in Ni and experiments in Si can arise due to the stronger elastic anisotropy of Ni compared to Si. The resulting driving forces on dislocations in the stress field of a crack under plane strain loading calculated with anisotropic elasticity theory are shown in Fig. 12.8. They show the same characteristics than for Ni (Figs. 12.1 and 12.3). The minor differences between Ni and Si are reflected in the plots for the cross-slip tendency, Fig. 12.9.

In conclusion, the simulations using Ni as model material should capture most of the fundamental aspects of dislocation - crack interactions in Si near the BDTT which are related to the stress field of the crack and to crystallography. The specific atomistic mechanisms of dislocation nucleation, however, depend on the nature of the atomic bonding and can not be transferred from Ni to Si.

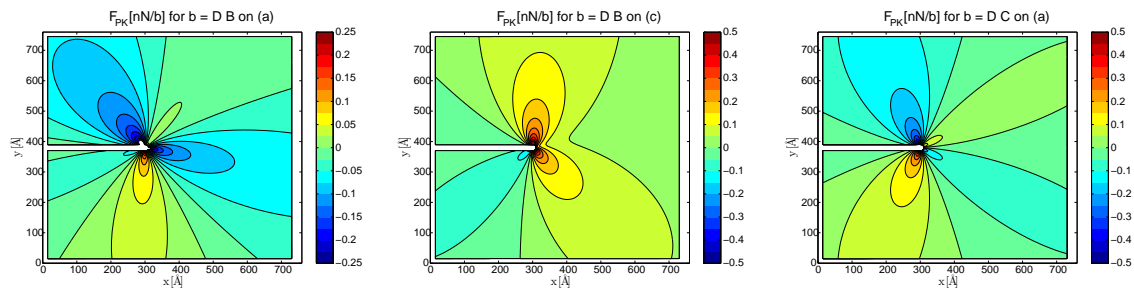


Figure 12.8: Driving forces on the three different classes of slip systems in Si. Compare to Figs. 12.1 and 12.3.

12.5.2 Comparison of observed dislocations

The slip systems which were observed in the simulations presented in the chapters 10 and 11 are summarized in Tab. 12.1. Only slip systems on which new dislocations of significant line length were created are considered. The generally observed predominance of partial

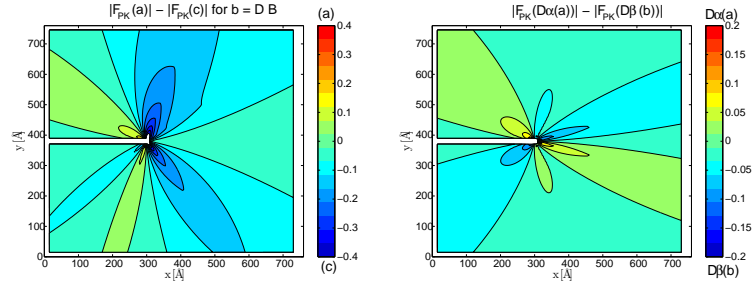


Figure 12.9: Cross-slip tendency in Si for dislocation segments with $\mathbf{b} = DB$ in screw orientation, compare to Fig. 12.5.

dislocations over full dislocations is linked to the already mentioned tendency of the potential towards emission of partial dislocations and the relatively short simulated times. However, the different mechanisms observed in the dislocation generation from propagating cracks and from cracks at rest are reflected in the activated slip systems. Dislocation generation from propagating cracks took place on the (a) and (b) planes, which was connected – probably by cross-slip – with dislocations on the (c) and (d) planes. Dislocation emission on (a) and (b) planes was not observed from static cracks containing defects of the crack front. Only in few cases dislocation activity on these planes was observed during the interaction of incoming dislocations with the crack tip. No stimulated emission on (a) and (b) planes was observed. Dislocations on (a) and (b) were created by ”assisted nucleation” during the ”unzipping” of the initial dislocation, see Fig. 11.5.

The activated slip systems in the simulations can be directly compared with the experimental observations in Tabs. 2.1 and 2.2. Like in the simulations of stimulated emission, the predominant dislocation activity in the experimental study took place on the (d) plane (see Tab. 2.2 and [153]). Some dislocation activity on the (a) and (b) planes was also reported, however, the analysis of the dislocation configuration was performed after a significant plastic zone has developed [153]. The population of these glide planes therefore is not necessarily caused by stimulated emission and can be also linked to cross-slip processes. The comparison with the experimental data is eased by the used of the symmetry classes defined in Tab. 11.1. Like in the corresponding experiments, the simulations of dislocation nucleation from stable cracks and of stimulated emission showed activity of slip systems belonging to class I and II. No dislocations with Burgers vector parallel or vertical to the crack front orientation (class III) were observed.

In their crack arrest experiments Argon and Gally observed *only* dislocations on the (a) and (b) planes [1, 134, 151]. They could not determine the Burgers vector of the emitted dislocations. Based on energetic considerations on the emission of dislocations from cleavage ledges [166, 168] they assumed that the dislocations were emitted as pure screw dislocations with Burgers vector CD [1, 134, 151], see also sec. 2.2.2.1. As only partial dislocations were emitted in the simulations of propagating cracks, no statement concerning the Burgers vector of full dislocations emitted from propagating cracks can be made. Gally and Argon [1] attributed the differences between the activated slip system in their experiments and the slip systems observed by Michot and coworkers to the predominance of the plane stress conditions in the thin samples used by Michot *et al.*

The simulations in the chapters 10 and 11 however showed that significant differences in the characteristics of dislocation emission and available dislocation sources exist between

simulation set-up	Slip plane			
	(a)	(b)	(c)	(d)
propagating crack	$\alpha D, \alpha C$	$D\beta, C\beta$	$D\gamma$	$C\delta$
propagating crack + obstacle	$\alpha D, \alpha C$	$D\beta, C\beta$	$D\gamma$	$C\delta$
crack front defect	-	-	$D\gamma$	$C\delta$
stimulated emission	(CB)	(DC)	$D\gamma, DB$	$CB, (C\delta)$

Tab. 12.1: Activated slip systems in the different simulation set-ups. Burgers vectors in brackets denote slip systems which were only sometimes observed or did not show significant dislocation line lengths. Compare to Tab. 2.1 and 2.2.

propagating cracks and static cracks. These differences could well be the reason for the activation of different slip systems in the groups of Michot and Argon. In the light of the present simulations and the experiments by Michot and Argon, it can be postulated that *different processes can be active in the formation of plastic zones from propagating cracks and from initially static cracks*. Conceptionally, the development of a plastic zone from propagating crack is connected to the crack arrest toughness K_{Ia} , whereas the evolution of local dislocation structures at a crack tip under increasing remote loading determines the fracture initiation toughness K_{Ic} . The current models of the brittle-to-ductile transition do not address crack tip processes involved in the continued propagation of cleavage cracks, or their arrest by the emission of crack tip shielding dislocations.

12.5.3 Sources of dislocations

12.5.3.1 Propagating cracks

The crack arrest experiments by Gally and Argon [1,151] revealed \wedge -shaped etch pit patterns which are identified to emanate from potent dislocation sources at the crack tip which produced sufficient dislocation line length to fully shield the crack front. These \wedge -sources are shown in Fig. 2.8, and the interpretation of the mechanism leading to these configurations was given in sec. 2.2.2.1.

The simulation results of propagating cracks interacting with defects (see Figs. 10.7, 10.9 and 11.33), however, suggest the mechanism described in sec. 12.2.3 leading to a 'V'-shaped configuration of the crack front as alternative source mechanism for the crack arrest experiments of Gally and Argon [1,151]. This mechanism would produce the same configuration of etch pits seen in Fig. 2.8. However, the location of the sources would then *not* be at the indicated 'S' in Fig. 2.8 but at the lower intersection of the etch-pit rows delineating the intersection of the (a) and (b) planes with the cleavage plane. Emission of the blunting half loops on the (a) and (b) planes would then take place with the propagating crack front, rather than backwards as suggested by Gally and Argon [1,151]. The blunting dislocation half loops should shield the crack front more efficiently than the suggested expansion of dislocation loops to the flank regions of the crack where the strain is already partially relieved.

The process of dislocation emission in the crack arrest experiments by Gally and Argon can thus be re-interpreted as follows: In the initial stages of crack front arrest, crack front ledges or other defects lead to retarding forces on the crack front, which assumes a cusped shape. Ideally blunting dislocation half loops can be emitted upwards and downwards on the (a) and (b) planes when the crack front direction locally reaches an orientation parallel to $[1\bar{1}2]$

or $[1\bar{1}\bar{2}]$. This process only takes place when the temperature at the crack tip is sufficiently large to allow for the necessary thermal activation of dislocation nucleation and propagation.^f The expansion of blunting dislocation half loops is connected with the propagating, sharp crack tip, see e.g. Figs. 10.9 and 11.33. This leads to the 'V'-shaped etch pit pattern in Fig. 2.8. Crack propagation should halt when the blunted crack fronts meet (at the points 'S' in Fig. 2.8). Edge dislocations with $\mathbf{b} = \pm DC$ are the most probable candidate for the emitted dislocation half loops, as they experience a large driving force and would lead to maximal blunting of the crack tip (by symmetric upwards and downwards emission by $2b$). However, also dislocations of type $DB(a)$ are possible. The emission of blunting half loops needs not to occur symmetrically on both sides of the crack, which agrees with the etch-pit patterns. The cross-slip process observed in the simulations is probably specific to the potential. However, cross-slip could also explain the region of high dislocation density in front of the arrested crack tip.

It has to be stressed that the above dislocation source mechanism leading to 'V'-shaped crack fronts is *specific to propagating cracks*. It should however be a general feature in different materials and crystal structures, as long as multiple blunting slip systems exist for the given crack orientation, which intersect the crack front direction at an angle attainable by local variations of the crack front orientation (e.g. the (100)[001] system in bcc). One consequence of such a mechanism would be that the crack arrest toughness K_{Ia} could in principle show a different orientation dependence than the fracture initiation toughness K_{Ic} .

12.5.3.2 Static cracks

In their study on the formation of dislocation loops at static crack tips, Michot and coworkers distinguish between primary and secondary dislocation sources, see also sec. 2.2.2.1. The present study focuses on secondary sources, i.e. sources that are not associated with detectable pre-existing defects on the crack front. The general observation of George and Michot [147] of preferred dislocation nucleation at and close to the sample surface agrees well with the increased slip activity on (c) and (d) planes in the simulations modeling plane stress compared to plane strain.

Single Burgers vector source A special case observed by George and Michot [147] was a source configuration producing only one Burgers vector (see also sec. 2.2.2.1). In several cases these dislocations emanated from crack tip ledges. An alternative source configuration for a one-Burgers-vector-source for the observed cases without ledges would be the *spiral-source* observed in the simulations, see sec. 12.2.4. Once such a source is formed, it can operate multiple times – as long as it is not blocked by other dislocations or the back stress of dislocation pile-ups. The nucleation from crack tip ledges on the other hand becomes more difficult for each emitted dislocation, as the height of the ledge is reduced by each emitted dislocation.

Stimulated emission and dislocation multiplication The simulations confirmed the experimental observation, that the intersection of the crack front by an attracted dislo-

^fIn their study of the interaction of a propagating crack in Si with a stationary inclined dislocation Sherman and Be'ery [302] showed that at room temperature the crack is deflected and no dislocation nucleation takes place. This situation is comparable to Fig. 11.34. In the Ni potential, however, dislocation nucleation takes place at 0 K, as would be the case in Si close to the BDTT.

cation can stimulate the emission of dislocations [2, 150, 153]. As discussed above, the type of the generated dislocations in the simulations corresponds to the experimentally observed dislocations. It has to be pointed out, that the simulations showed no stimulated emission for intersecting dislocations on the (d) or (c) planes. Experimental results on stimulated emission from such dislocations have not been reported. The question whether all attracted dislocations can lead to stimulated emission is decisive for models of dislocation source multiplications. Based on atomistic calculations such mesoscopic models of source multiplication could include criteria for stimulated dislocation emission, possibly combined with a nucleation rate.

The exact atomistic mechanisms of the process of stimulated emission are most probably related to the atomic bonding. These mechanisms were not further examined. The simulations have however revealed further mechanisms which can be active in the interaction of dislocations and cracks, e.g. the formation of sharp cracks in the stress field of the dislocation and the reorientation of the crack front.

Cross-slip of dislocations from the (a) plane on the (c) or (d) planes was an important feature in the simulations. Cross-slip of emitted dislocations is required by the dislocation source multiplication models of Michot [148] and Scandian [153], see also sec. 2.2.2.2. With stimulated emission on the (d)-plane, the model of Scandian, Fig. 2.12 b), requires cross-slip on the (b)-plane. Such cross-slip processes were not seen in the simulations and are according to Fig. 12.5 only favorable in very small regions. As already stated by Michot *et al.* [148], the existence of many dislocations is a necessary to create a back stress on the emitted dislocation and thus facilitate its cross-slip. With the size and time limitations of MD the simulation of avalanche multiplication processes involving e.g. external dislocation sources is currently out of reach. Atomistic simulations can however be used to study the fundamental mechanisms like cross-slip and stimulated emission involved in such processes. Based on this information, mesoscopic modeling can then be used to describe the interaction of pre-existing and nucleated dislocations and the crack, thus enabling a deeper understanding of the role of primary and secondary dislocation sources on crack tip plasticity.

Chapter 13

Conclusions II: Dislocation Nucleation and Multiplication at Crack Tips

In part II of this work dislocation generation at crack tips has been investigated with molecular dynamics simulations. The use of an EAM potential for nickel thereby allowed to model generic features related to crystallography and dislocation mobility of fracture in silicon close to the brittle-to-ductile transition temperature. Molecular dynamics simulations have inherent size and time limitations which affect the dislocation processes at the crack tip. General mechanisms can however be derived from the simulations by relating the observed processes to the underlying crystallography and to the linear elastic crack tip stress field. The discussion of the dislocation processes can be furthermore limited to three slip systems which represent different symmetry classes.

Dislocation nucleation at cracks in the γ -orientation was studied for propagating cracks as well as for static crack tips. It was found that in both cases different mechanisms leading to the generation of dislocations can be active, and that therefore dislocations populate different slip systems. This can explain the observation of different active glide planes in the crack arrest experiments by Gally and Argon [1, 151] and the experiments by George and Michot [147] on static cracks subjected to a constant loading rate.

Propagating cracks The local crack front orientation of propagating cracks can differ from the global crack front direction. For fast cracks this can be caused by dynamic instabilities of the crack front. However, also defects on the crack front like ledges, or the interaction of the propagating crack with lattice defects can locally deflect the crack front. When the local crack front orientation lies within a blunting slip plane, blunting dislocation half-loops can be emitted, see e.g. Fig. 10.9. This process offers an alternative explanation for the 'V'-shaped dislocation sources, Fig. 2.8, observed by Gally and Argon [1, 151]. The above mechanism of dislocation emission is specific to propagating cracks. It can be however transferred to other crystal structures and orientations.

Static cracks and stimulated emission Contrary to the propagating cracks, defects on static crack fronts led only to nucleation of dislocations on the oblique glide planes. Dislo-

cation emission from defects at the crack front ("primary sources") alone can not account for the brittle-to-ductile transition in silicon [148, 149]. The creation of "Secondary" dislocation sources by the interaction of dislocations with the crack front was therefore postulated by Michot and coworkers [2, 135, 148, 149]. The simulations confirmed the experimental observation, that the intersection of the crack front by an attracted dislocation can stimulate the emission of dislocations [2, 150, 153]. However, in the simulations only incoming dislocations on slip planes orthogonal to the cleavage plane led to stimulated emission of dislocations. Models of dislocation source multiplication based on stimulated emission and cross-slip as proposed by Michot [148] and Scandian [2] do currently not include criteria for stimulated dislocation emission. In these models the dislocation cross-slip is a result of the interaction of many dislocations with the crack. Therefore such "avalanche multiplication" processes are not suited for MD simulations.

The first simulations of dislocation-crack interaction showed furthermore various other effects. They depend on the nature of the dislocation, and the characteristics of the crack, as well as on the stress state. The relative orientation of the dislocation with respect to the crack and its initial distance have to be taken into account as further parameter determining the possible dislocation processes. The cross-slip of dislocations in the stress field of the crack by the Fleischer mechanism is one central process. At high stresses and low temperatures the Fleischer mechanism seems therefore a viable alternative to the Friedel-Escaig mechanism of cross-slip. Cross-slip above the crack flank led to the creation of a spiral source. Such a source could correspond to the experimentally observed 'one-Burgers-vector-source' [147] which were not linked to crack tip ledges.

Chapter 14

Outlook II

The study of fracture processes by large scale, three dimensional atomistic simulations is still in the early stages. In particular, the interaction between cracks and pre-existing lattice defects has not been simulated before. Therefore this study can only present a first step towards a deeper understanding of the origin and the multiplication of dislocations at crack tips. Further atomistic simulations and modeling efforts on different scales in combination with dedicated model experiments are necessary to shed light on the processes leading to crack tip plasticity and the brittle-to-ductile transition. Some suggestions for future investigations are summarized below.

Dislocation nucleation processes Probably the greatest open issue is the understanding of the dislocation nucleation process and its dependence on the crack front morphology and the atomic bonding. Three dimensional simulations of dynamical fracture showed pronounced differences in the emission of dislocations from cracks in Al and Cu [187]. It is currently not clear how elastic anisotropy and differences in the GSF-curves influence the nucleation of dislocations from cracks. Detailed studies using the same set-up and different atomic potentials should elucidate this question. Especially studies complementary to the present one using potentials with low tendency towards twinning and increased tendency towards emission of full dislocations, e.g. Al_I [31], would be desirable.

Dislocation nucleation from defects at the crack front has only been studied in detail for cleavage ledges in a Peierls-Nabarro framework [167, 168]. Clearly, further studies on the effect of the nature and magnitude of crack front defects on dislocation nucleation are required to get a better understanding of dislocation emission from more realistic crack fronts. Such studies would possibly require new simulation methods or the combination of dynamic and static methods to explore different potential reaction pathways leading to dislocation nucleation. A critical issue in dislocation nucleation processes is thermal activation and thus the possibility of qualitative differences in the dislocation-crack interaction processes at higher temperatures. Future studies should therefore include dynamic simulations of dynamic and static cracks, with and without defects, at elevated temperatures.^a

Additional simulations of dislocations intersecting crack fronts could clarify further the influence of the boundary conditions and of the absolute strain on the stimulated dislocation emission and following processes. Especially simulations using significantly larger samples would be desirable. This would reduce the absolute strain and should also reduce dislocation-

^aMethods for the study of fracture processes at elevated temperatures are described e.g. in [223].

dislocation reaction which may block potential source mechanisms.^b Alternatively one could during the simulation increase the load to account for the strain relief and back stress caused by emitted dislocations. This would help to clarify whether the intersection of a dislocation with the crack front can create a source for many dislocations.

A natural extension of this work would be the simulation of dislocation - crack interactions in other material classes like bcc or intermetallics. However, in these cases the dislocation mobility might however be a critical aspect requiring elevated temperatures. With the advent of reliable tight binding descriptions of silicon [303] and new concepts like fitting on the fly [304], simulations of dislocation - crack interactions should in the future also become possible for silicon.

Dislocations in the stress fields of cracks The pinning of the dislocation at the box boundaries leads to a significant restriction to the configurations attainable by the dislocation in the stress field of the crack. While larger simulation boxes could alleviate these restrictions, the underlying problem would remain. Dislocation dynamics simulations could be used to assess the differences between the pinned dislocation in the simulation box and an unbounded dislocation in the stress field of the crack. By studying the motion of dislocations coming from far sources towards the crack, DD simulations could provide information on realistic initial dislocation positions for the atomistic simulations.

Mesosopic modeling of dislocation - crack interactions A full understanding of crack tip plasticity requires the modeling of dislocation nucleation processes as well as of their motion and interaction with each other and with the crack. Most current dislocation dynamics simulations of crack tip plasticity [139] do not take into account the full three dimensional nature of the problem. To reproduce semi-brittle fracture processes a three dimensional mesoscale model should include primary sources and the possibility of stimulated dislocation nucleation as well as pre-existing bulk dislocations. The information on dislocation nucleation criteria can currently only be provided by atomistic modeling. Similarly, information on the activation energy of dislocation cross-slip by the Fleischer mechanism can be derived from atomistic simulation. However, a particular challenge for mesoscopic modeling of dynamic fracture processes will be the coupling between crack propagation, closing or blunting and dislocation processes. In the long term, information from atomistically informed mesoscale models should lead to an improved continuum theory of basic material fracture phenomena.

^bE.g. in some of the simulations potential spiral sources were blocked by the stacking fault produced by emitted dislocations.

Appendix A

Properties of the atomic interaction potentials

Table A.1 summarizes the properties of the different used potentials relevant for the study of dislocation motion and dislocation interactions with voids and crack tips. The values for all the properties are determined at 0 K. Where available the values are taken from the original publications. Most of these values were confirmed by test calculations. Other properties were calculated within the izbs potential documentation project or extracted from the literature.

a_0 is the lattice parameter; E_0 the cohesive energy of the potential; $\gamma_{sf}, \gamma_{usf}, \gamma_{utf}$ are the stacking fault, unstable stacking fault and unstable twin fault energy, respectively; c_{ij} are the elastic stiffness constants; μ', ν' are the shear modulus and the Poisson's ratio in slip plane and slip direction; A is the anisotropy factor; c_l and $c_{t_{1,2}}$ are the velocities of longitudinal and transversal sound waves, see Eq. 2.41; c_R is the Rayleigh wave speed, Eq. 2.43; ν_t are the frequencies of transverse phonons at the points X and L of the Brillouin zone; T_m is the melting temperature; Θ_D is the Debye temperature according to [16]; α is the linear expansion coefficient; $1/\tau_\eta$ is the coupling parameter for the Nosé-Hoover thermostat in IMD^a.

^aPlease refer to [198] and the actual IMD distribution for the implementation of the parameter `inv_tau_eta`.

		Cu	Ni _I	Ni _{II}	Al _I	Al _{II}
a_0	[Å]	3.615	3.52	3.52	4.032	4.05
E_0	[eV/atom]	-3.54	-4.45	-4.45	-3.36	-3.36
γ_{sf}	[mJ/m ²]	44.4	88.8	134.6	106.0	145.5
γ_{usf}	[mJ/m ²]	162.0	212.1	297.3	128.2	167.4
γ_{utf}	[mJ/m ²]	183.4	254.1	359.8	168.9	219.7
$\gamma_{(111)}$	[mJ/m ²]	1239	1928	1759	870	870
$\gamma_{(110)}$	[mJ/m ²]	1475	2350	2087	1035	1006
c_{11}	[GPa]	169.9	264.4	241.3	118.1	114
c_{12}	[GPa]	122.6	147.3	150.8	62.3	61.6
c_{44}	[GPa]	76.2	124.8	127.3	36.7	31.6
μ'	[GPa]	41.2	74.6	72.6	30.8	28
ν'		0.446	0.363	0.376	0.34	0.348
A		3.22	2.52	2.81	1.32	1.21
c_l	[km/s]	4.99	6.008	6.024	6.856	6.650
c_{t_1}	[km/s]	2.92	3.742	3.779	3.687	3.421
c_{t_2}	[km/s]	1.63	2.358	2.254	3.215	3.115
c_R	[km/s]	1.62	2.347	2.245	3.145	3.032
$\nu_t(X)$	[THz]	5.2	6.44	6.78	5.8	5.98
$\nu_t(L)$	[THz]	3.32		4.29	4.2	4.3
T_m	[K]	1327	1478 ± 25		939 ± 3	
Θ_D	[K]	331	476	476	408	408
α	[10 ⁻⁶ 1/K]	20.3	16.6	8.2	22.5	20.7
$1/\tau_\eta$	[ps ⁻¹]	33	30	30	30	33

Tab. A.1: Properties relevant to the study of dislocations of different potentials: Ni_I by Angelo *et al.* [209], Ni_{II} by Mishin [213], Al_I by Ercolessi and Adams [206], Al_{II} by Mishin and Farkas [207] and Cu by Mishin [214].

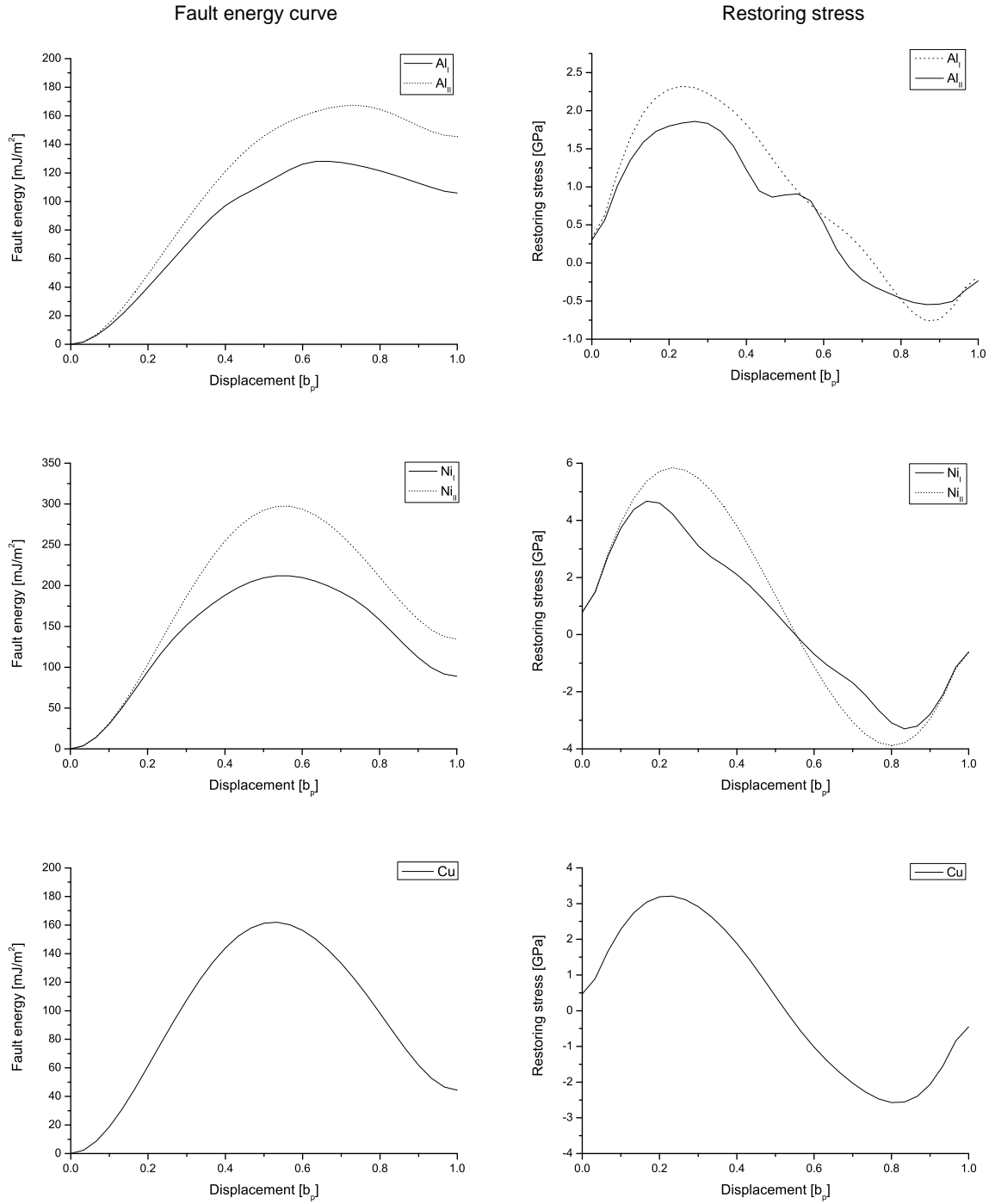


Figure A.1: Left: fault energy curves as a function of rigid displacement in partial Burgers vector direction $\mathbf{b}_p = \frac{a_0}{6} \langle 112 \rangle$ on a glide plane for the the different potentials. Right: restoring stress calculated as gradient from the fault energy curve.

Appendix B

Relaxation methods

Providing mechanical equilibrium structures as initial configurations for dynamic simulations is of fundamental importance for the simulations of dislocations and cracks. This corresponds to finding the (nearest) atomistic configuration of minimal potential energy, starting from a given starting structure. Finding such structures is a general problem in computational materials science, solid state physics and chemistry. A large variety of well established optimization methods can be applied to minimize the energy of a group of atoms, like steepest descent and conjugated gradient methods, or Newton-Raphson methods [190, 199, 260, 305]. In addition to the application of these classical optimization methods to atomistic configurations, there are many variants to use molecular dynamics for minimization purposes by removing kinetic energy from the system (quenching) [300, 306, 307]. A thorough treatment of optimization algorithms is provided in [260, 305], and their applications to atomistic modeling are discussed in [190, 199].

In general, there is no ‘best’ method for finding minimum energy configurations. The choice of the minimization algorithm depends on a number of factors. Different methods can be appropriate, depending on whether only thermal noise should be removed from a system, the optimal structure of an atomic arrangement should be determined, or whether the range of mechanical stability of a system under load should be tested. Relaxation algorithms implemented in the molecular dynamics package IMD are the conjugate gradient (CG) method by Fletcher and Reeves [260], the micro convergence (MIC) scheme by Beeler [306], and the global convergence (GLOC) scheme by Bitzek and Gumbsch [263]. The frequent need for the relaxation of very large systems, e.g. to determine ϵ_G , however, called for more efficient relaxation methods.

The global convergence method is a modification of the micro convergence method [306]. Instead of calculating the scalar product between force \vec{F}_i and velocity \vec{v}_i of each atom and setting $\vec{v}_i = 0$ if $\vec{F}_i \cdot \vec{v}_i \leq 0$, it operates on the $3N$ -dimensional global force and velocity vectors $\mathbf{F} = (F_{1,x}, F_{1,y}, F_{1,z}, \dots, F_{N,x}, F_{N,y}, F_{N,z})$ and $\mathbf{v} = (v_{1,x}, v_{1,y}, v_{1,z}, \dots, v_{N,x}, v_{N,y}, v_{N,z})$. So, whenever the whole system (consisting of N atoms) is passing a minimum of the $3N$ -dimensional energy surface ($\mathbf{F} \cdot \mathbf{v} \leq 0$) the velocities of all atoms are set to zero. This method is extremely simple to implement in the MD integration scheme and is usually somewhat faster than the conjugate gradient method. It circumvents the slow propagation of information over long ranges (e.g. via stress fields) inherent in the local damping of MIC. However, with increasing system sizes plateau-phases corresponding to internal modes of vibration dominate the relaxation process with GLOC (see Fig. B.1).

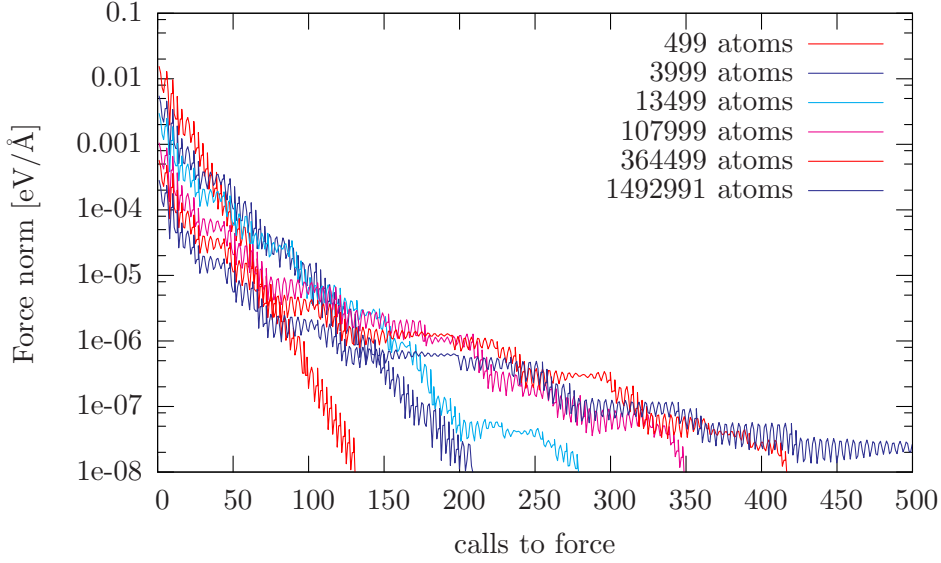


Figure B.1: The relaxation with GLOC of a void in Cu shows with increasing system size (PBC in all directions) the emergence of plateaus in the force norm. These plateaus are related to internal vibration modes and slow down the relaxation process.

The only parameter necessary for GLOC and MIC is the time step Δt for the MD integrator. A straight forward choice would be to take the same time step as for a MD simulation of the system Δt_{MD} . However, as the intention of GLOC and MIC is *not* the accurate reproduction of atomic trajectories but the search for a minimum energy configuration, larger time steps can be used, thus significantly speeding up the relaxation process. In general, each system will have a different maximal time step for which stable relaxation is still possible.

By using a simple adaptive time step algorithm, the system can be rapidly propagated towards a minimum by increasing the time step. Once the system has passed a minimum, the velocities are set to zero, the atomic positions are reset to the positions of the last integration step, and Δt is reduced. When care is taken that Δt is not becoming too large and the time step is not directly increased from the start on or after passing the minimum, the adaptive global convergence algorithm (ADGLOC) is fast (see Fig. B.2) and extremely robust.

The efficiency of the algorithm can further be improved by modifying the global velocity vector to point more in the direction of the forces [308].

The resulting algorithm of the so called FIRE (Fast Inertial Relaxation Engine) method consists of an iteration of the following steps:

1. calculate \mathbf{F} , \mathbf{v}
2. change the velocities to $\mathbf{v} = (1 - \text{mix})\mathbf{v} + \text{mix} \frac{\mathbf{F}}{|\mathbf{F}|} |\mathbf{v}|$
3. if the number of steps since the last minimum is larger than `minsteps`, increase Δt : $\Delta t = \Delta t \cdot \text{incfac}$, but only as long as $\Delta t \leq \Delta t_{max}$, else the time step is Δt_{max} . Decrease `mix`: `mix = mix · mix_dec`
4. if $\mathbf{F} \cdot \mathbf{v} \leq 0$ decrease Δt : $\Delta t = \Delta t \cdot \text{decfac}$, set all velocities to zero: $\mathbf{v} = \mathbf{0}$ and set `mix` back to the starting value `mix_start`.

5. propagate atoms according a molecular dynamics integration scheme.

The parameters `minsteps`, `incfac`, `decfac`, `mix_start`, `mix_dec` are not directly linked to the physics of the system which should be relaxed. Like for the five parameters in the standard conjugated gradient implementation [260], their choice is guided by experience. The following set of parameters yielded a fast and robust behavior for nearly all the systems studied in this thesis: `minsteps=5`, `incfac=1.1`, `decfac=0.5`, `mix_start=0.1`, `mix_dec=0.99`. The maximal time step Δt_{max} is related to the vibrational properties of the system. Taking the typical time step Δt_{MD} used in a MD simulation^a of the same system as reference (e.g. $\Delta t_{MD} = 2$ fs for most of the studied systems), for most configurations the following time steps will produce fast and robust relaxation: MIC: $\Delta t_{MIC} = 10\Delta t_{MD}$, GLOC: $\Delta t_{GLOC} = 3\Delta t_{MD}$, ADGLOC and FIRE: $\Delta t_{max} = 10\Delta t_{MD}$. To relax localized disturbances which can lead to large forces, the relaxation can be preceded by 50-100 MIC steps after which all velocities are set to zero.

FIRE has been extensively tested and reaches in all test cases the minimum energy configuration using significantly less function evaluations ('calls to force') than the conjugated gradient^b, thus leading to a faster relaxation of the system [200].

To measure the degree of relaxation, the smallness of the root-mean-square (RMS) of the global force $F_{RMS} = |\mathbf{F}|/(3N)^{\frac{1}{2}}$, often referred to as the force norm, is taken as a representative measure for the degree of relaxation^c.

Fig. B.2 shows exemplary the behavior of different algorithms, in this case while relaxing a small sample containing a crack. The reduction of the plateau phase by the adaptive time stepping can be clearly seen. The modification of the global velocity vector by the 'mixing' leads to an additional performance increase. By starting the relaxation process with 50 MIC steps, the algorithms benefit from the fast initial relaxation of localized disturbances by MIC. The total time required to relax e.g. a dislocation could thus be reduced by a factor of about 3 compared to the previously used method.

The algorithm and its performance is discussed in more detail in [200]. Its computational efficiency, its robustness and simplicity make FIRE a versatile alternative to standard relaxation methods. The use of FIRE is not restricted to molecular modeling – preliminary studies on other, more general, multidimensional minimization problems show it to be much more efficient than previously used common algorithms [309]. An application for patent for FIRE has been filed.

^aThe MD time step is usually chosen to sample about 30-50 times the maximal vibration frequency of the system.

^bTo increase the stability and performance, the standard implementation of the "Numerical Recipes" [260] has been modified so that the first bracketing step in each CG-step is chosen to be twice as large as the minimizing step from the previous CG-step, and the bracketing routine was modified to ensure that only steps in the positive search direction are performed. All parameters are chosen such as to minimize the required calls to force (especially `linmintol = 0.01`).

^cTo ensure that the minimum has been reached, this measure has to be combined with others, like the maximum force on an atom.

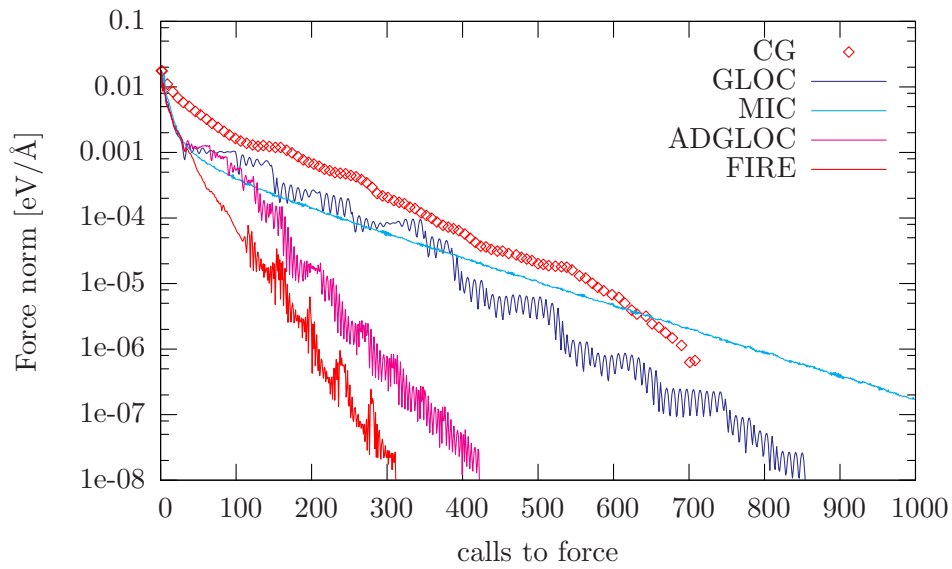


Figure B.2: Relaxation of a crack in a small test system with different algorithms. The newly developed algorithm FIRE reduces the necessary computation time by a factor of about three compared to the formerly used algorithms like conjugated gradient (CG) or GLOC [200].

Appendix C

Influence of boundary conditions on the dislocation - crack interaction

Due to the long range stress fields of cracks and dislocations the choice of boundary conditions is of major importance. In dynamic simulations of finite size the boundaries will always affect the simulation outcome. The reasons for the choice of the simulation set-up were described in sec. 3.2.2. To assess the influence of the boundary conditions on the mechanisms during the dislocation-crack interaction some simulations with alternative boundary conditions in x -direction were performed.

Fig. C.1 shows the differences during the simulation of a sharp crack under plane strain loading in a small sample interacting with the 60° dislocation $DB(a)$ when 2D dynamic boundary conditions were applied instead of the fixed boundaries on the $-x$ -surface. The 2D dynamic boundary conditions clearly favored the closing of the crack. Furthermore, they caused attractive image forces on the dislocations. Therefore the dislocations show significantly stronger bow out.

Although the overall configuration and the dynamics of the dislocation - crack interaction was significantly different for the two boundary conditions, the *mechanisms* were the same: partial dislocation cross slip with nucleation of a new partial dislocation at the stair-rod dislocation, crack front motion and nucleation of partial dislocation half loops at the crack front connected by stair-rod dislocation with partial dislocation on the (d) -plane. These mechanisms therefore seem to be insensitive to the actual boundary conditions.

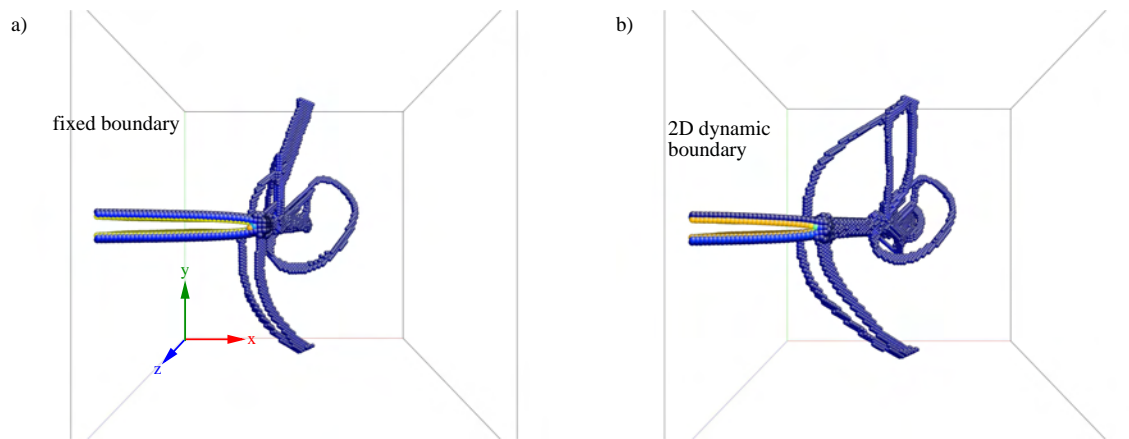


Figure C.1: Comparison between the simulation using fixed boundary conditions (a) and 2D dynamic boundary conditions (b) at the $-x$ surface of the 60° dislocation $DB(a)$ interacting with a sharp crack ($0.96\epsilon_G$, small sample under plane strain, $t = 10$ ps).

Bibliography

- [1] B. J. Gally and A. S. Argon, “Brittle-to-ductile transitions in the fracture of silicon single crystals by dynamic crack arrest,” *Philos. Mag. A* **81**, 699 – 740 (2001).
- [2] C. Scandian, H. Azzouzi, N. Maloufi, G. Michot, and A. George, “Dislocation Nucleation and Multiplication at Crack Tips in Silicon,” *Phys. Status Solidi A* **171**, 67 – 82 (1999).
- [3] M. Eberhart, “Why Things Break,” *Sci. Am.* **281**, 66 (1999).
- [4] B. Devincre and L. P. Kubin, “Mesoscopic simulations of dislocations and plasticity,” *Mater. Sci. Eng. A* **234-236**, 8 – 14 (1997).
- [5] T. D. de la Rubia, H. M. Zbib, T. A. Khraishi, B. D. Wirth, M. Victoria, and M. J. Caturla, “Multiscale modelling of plastic flow localization in irradiated materials,” *Nature* **406**, 871–874 (2000).
- [6] N. M. Ghoniem, E. Busso, N. Kioussis, and H. Huang, “Multiscale modelling of nanomechanics and micromechanics: an overview,” *Philos. Mag.* **83**, 3475 – 3352 (2003).
- [7] L. P. Kubin, G. Canova, M. Condat, B. Devincre, V. Pontikis, and Y. Bréchet, “Dislocation microstructures and plastic flow: A 3D simulation,” *Solid-State Phys.* **23&24**, 455–472 (1992).
- [8] J. Li, A. H. W. Ngan, and P. Gumbsch, “Atomistic modeling of mechanical behavior,” *Acta Mater.* **51**, 5711 – 5742 (2003).
- [9] E. Nembach, *Particle strengthening of metals and alloys* (John Wiley & Sons, Inc., New York, 1997).
- [10] J. Friedel, in *Dislocations, Cambridge solid state science series*, R. W. Cahn, M. Thompson, and I. M. Ward, eds., (Pergamon Press, 1964).
- [11] F. R. N. Nabarro, *Theory of crystal dislocations* (Clarendon Press, 1967).
- [12] J. P. Hirth and J. Lothe, *Theory of Dislocations*, 2. ed. (John Wiley & Sons, New York, 1982).
- [13] D. Hull and D. J. Bacon, *Introduction to Dislocations*, 4. ed. (Butterworth-Heinemann, Oxford, 2001).
- [14] L. J. Teutonico, “Uniformly moving dislocations of arbitrary orientation in anisotropic media,” *Phys. Rev.* **127**, 413 –418 (1962).

- [15] T. R. Duncan and D. Kuhlmann-Wilsdorf, "Shear stresses and strain energies of edge dislocations in anisotropic cubic crystals," *J. Appl. Phys.* **38**, 313–322 (1967).
- [16] E. M. Nadgornyi, "Dislocation Dynamics and Mechanical Properties of Crystals," in *Dislocation Dynamics and Mechanical Properties of Crystals*, Vol. 31 of *Progress in Materials Science*, Christian, Haasen, and Massalski, eds., (Pergamon Press, Oxford, 1988).
- [17] L. M. Brown, "The self stress of dislocations and the shape of extended nodes," *Philos. Mag.* **10**, 441–466 (1964).
- [18] T. H. Courtney, *Mechanical behavior of materials*, 2. ed. (McGraw-Hill, 2000).
- [19] R. Phillips, *Crystals, defects and microstructures* (Cambridge University Press, 2001).
- [20] *Plastic deformation and fracture of materials*, Vol. 6 of *Materials science and technology*, H. Mughrabi, ed., (VCH, 1993).
- [21] R. Peierls, "The Size of a Dislocation," *Proc. Phys. Soc.* **52**, 34–37 (1940).
- [22] F. Nabarro, "Dislocations in a simple cubic lattice," *Proc. Phys. Soc.* **59**, 256–272 (1947).
- [23] G. Lu, in *Handbook of materials modeling*, S. Yip, ed., (Springer, Berlin, 2005), Chap. 2.20, The Peierls-Nabarro model of dislocations: a venerable theory and its current development, pp. 793–811.
- [24] G. Schoeck, "The peierls dislocation: line energy, line tension, dissociation and deviation," *Acta Mater.* **45**, 2597–2605 (1997).
- [25] G. Schoeck, "The dissociation energy of extended dislocations in fcc lattices," *Philos. Mag. A* **79**, 1207–1215 (1999).
- [26] G. Schoeck, "The core structure of dislocations in Al: a critical assessment," *Mater. Sci. Eng., A* **333**, 390–396 (2002).
- [27] G. Schoeck, "The Peierls model: Progress and limitations," *Mater. Sci. Eng., A* **400-401**, 7–17 (2005).
- [28] V. V. Bulatov and E. Kaxiras, "Semidiscrete Variational Peierls Framework for Dislocation Core Properties," *Phys. Rev. Lett.* **78**, 4221–4224 (1997).
- [29] M. S. Duesbery, "Dislocation motion, constriction and cross-slip in fcc metals," *Modelling Simul. Mater. Sci. Eng.* **6**, 35–49 (1998).
- [30] V. Vitek, "Intrinsic stacking faults in body-centred cubic crystals," *Philos. Mag.* **18**, 773 (1968).
- [31] H. Van Swygenhoven, P. M. Derlet, and A. G. Frøseth, "Stacking fault energies and slip in nanocrystalline metals," *Nat. Mater.* **3**, 399–403 (2004).
- [32] J. R. Rice, "Dislocation nucleation from a crack tip: an analysis based on the Peierls concept," *J. Mech. Phys. Solids* **40**, 239–271 (1992).

- [33] R. Fleischer, "Cross slip of extended dislocations," *Acta Mater.* **7**, 134–135 (1959).
- [34] W. Cai, V. Bulatov, J. P. Ghang, J. Li, and S. Yip, "Dislocation core effects on mobility," in *Dislocations in solids* (Elsevier, Amsterdam, 2004), Vol. 12, Chap. 64, pp. 1 – 80.
- [35] M. J. Buehler, A. Hartmaier, M. A. Duchaineau, F. Abraham, and H. Gao, "The dynamical complexity of work-hardening: a large-scale molecular dynamics simulation," *Acta Mech. Sinica* **21**, 103–111 (2005).
- [36] T. L. T. Rasmussen, K. W. Jacobsen and O. Pedersen, "Simulations of the atomic structure , energetics and cross slip of screw dislocations in copper," *Phys. Rev. B* **56**, 2977 (1997).
- [37] V. V. Bulatov, "Dangers of "common knowledge" in materials simulations," in *Handbook of materials modeling*, S. Yip, ed., (Springer, Berlin, 2005), pp. 2695–2700.
- [38] J. S. Koehler, in *Imperfections in nearly perfect crystals*, W. Shockley, ed., (Wiley, New York, 1952), p. 197.
- [39] A. Granato and K. Lücke, "Theory of mechanical damping due to dislocations," *J. Appl. Phys.* **27**, 583 –593 (1956).
- [40] A. Granato, K. Lücke, J. Schlipf, and L. Teutonico, "Entropy factors for thermally activated unpinning of dislocations," *J. Appl. Phys.* **35**, 2732 –2745 (1964).
- [41] G. Leibfried, in *Dislocations and mechanical properties of crystals*, J. C. Fisher, ed., (Wiley, New York, 1957), p. 495.
- [42] A. H. Cottrell, *Theory of Crystal Dislocations, Documents on Modern Physics* (Gordon and Breach, New York, 1964).
- [43] J. P. Hirth, H. M. Zbib, and J. Lothe, "Forces on high velocity dislocations," *Modelling Simul. Mater. Sci. Eng.* **6**, 165–169 (1998).
- [44] J. Weertman and J. R. Weertman, in *Dislocations in Solids*, F. R. N. Nabarro, ed., (North-Holland, Amsterdam, 1980), Vol. 3, pp. 1–60.
- [45] J. Lothe, in *Uniformly moving dislocations; surface waves*, Vol. 31 of *Modern problems in condensed matter sciences*, V. L. Indenboom and J. Lothe, eds., (North-Holland, Amsterdam, 1992), Chap. 7, pp. 447 – 487.
- [46] F. C. Frank, "On the equations of motion of crystal dislocations," *Proc. Phys. Soc. London, Sect. A* **62**, 131 – 134 (1949).
- [47] J. Weertman, "High Velocity Dislocations," In *Response of Metals to High Velocity Deformation*, P. G. Shewmon and V. F. Zackay, eds., Metallurgical Society Conferences pp. 205–247 (Interscience, New York, 1961).
- [48] M. Sakamoto, "High-velocity dislocations: effective mass, effective line tension and multiplication," *Philos. Mag. A* **63**, 1241–1248 (1991).
- [49] V. A. Alshitz and V. L. Indenbom, "Dynamic dragging of dislocations," *Sov. Phys. Usp.* **18**, 1 – 20 (1975).

- [50] J. Weertman, "Fast Moving Edge Dislocations on the (111) Plane in Anisotropic Face-Centered-Cubic Crystals," *J. Appl. Phys.* **33**, 1631–1635 (1962).
- [51] A. Darinskii, "On the theory of leaky waves in crystals," *wave motion* **25**, 35 – 49 (1997).
- [52] J. D. Eshelby, "Supersonic dislocations and dislocations in dispersive media," *Proc. Phys. Soc. B* **69**, 1013 – 1019 (1956).
- [53] D. L. Olmsted, L. G. Hector Jr, W. A. Curtin, and R. J. Clifton, "Atomistic simulations of dislocation mobility in Al, Ni and Al/Mg alloys," *Modelling Simul. Mater. Sci. Eng.* **13**, 371 – 388 (2005).
- [54] V. Celli and N. Flytzanis, "Motion of a screw dislocation in a crystal," *J. Appl. Phys.* **41**, 4443 – 4447 (1970).
- [55] N. Flytzanis and V. Celli, "Motion of a screw dislocation in a crystal at finite temperature," *J. Appl. Phys.* **43**, 3301 – 3306 (1972).
- [56] N. Bhate, Ph.D. thesis, Brown university, 2001.
- [57] P. Gumbsch and H. Gao, "Dislocations Faster than the Speed of Sound," *Science* **283**, 965–968 (1999).
- [58] D. Rodney and G. Martin, "Dislocation pinning by glissile interstitial loops in a nickel crystal: A molecular-dynamics study," *Phys. Rev. B* **61**, 8714 – 8725 (2000).
- [59] C.-H. Woo, "Dynamics of fast dislocations," *Mater. Sci. Eng. A* **350**, 223 – 232 (2003).
- [60] J. Y. Vandersall and B. Wirth, "Supersonic dislocation stability and nano-twin formation at high strain rate," *Philos. Mag.* **84**, 755 – 3769 (2004).
- [61] P. Rosakis, "Supersonic Dislocation Kinetics from an Augmented Peierls Model," *Phys. Rev. Lett.* **86**, 95 – 98 (2001).
- [62] P. Gumbsch and H. Gao, "Driving force and nucleation of supersonic dislocations," *J. Comput.-Aided Mat. Design* **6**, 137–144 (1999).
- [63] V. I. Alshits and V. L. Indenbom, "Mechanisms of dislocation drag," in *Dislocations in Solids*, F.R.N.Nabarro, ed., (Elsevier Science Publishers, Amsterdam, 1986), Vol. 7, Chap. 34, pp. 43 – 111.
- [64] V. I. Alshits, in *Elastic strain fields and dislocation mobility*, V. L. Indenbom and J. Lothe, eds., (Elsevier Science Publishers, Amsterdam, 1992), Chap. 11, pp. 625 – 697.
- [65] G. Leibfried, "Über den Einfluß thermisch angeregter Schallwellen auf die plastische Deformation," *Z. Phys.* **127**, 344–356 (1950).
- [66] J. Lothe, "Theory of Dislocation Mobility in Pure Slip," *J. Appl. Phys.* **33**, 2116–2125 (1962).
- [67] H. Koizumi, H. O. K. Kirchner, and T. Suzuki, "Emission of elastic waves from a dislocation in a 2-D discrete lattice," *Mater. Sci. Eng. A* pp. 117–120 (2001).

- [68] H. Koizumi, H. O. K. Kirchner, and T. Suzuki, "Lattice wave emission from a moving dislocation," *Phys. Rev. B* **65**, 214104 (2002).
- [69] L. Lu, R. Schwaiger, Z. Shan, M. Dao, K. Lu, and S. Suresh, "Nano-sized twins induce high strain rate sensitivity of flow stress in pure copper," *Acta Mater.* **53**, 2169 – 2179 (2005).
- [70] J. G. Sevillano, in *Plastic deformation and fracture of materials*, Vol. 6 of *Materials science and technology*, H. Mughrabi, ed., (VCH, Weinheim, 1993), Chap. 2. Flow stress and work hardening, pp. 19 – 88.
- [71] A. V. Granato, "Dislocation Inertial Effects in the Plasticity of Superconductors," *Phys. Rev. B* **4**, 2196–2201 (1971).
- [72] M. Suenaga and J. M. Galligan, "Dislocation motion in the normal and the superconducting states," *Scr. Metall.* **5**, 829–836 (1971).
- [73] R. B. Schwarz and R. Labusch, "Dynamic simulation of solution hardening," *J. Appl. Phys.* **49**, 5174–5187 (1978).
- [74] R. B. Schwarz, "Dislocation stress-velocity dependence in alloys," *Phys. Rev. B* **21**, 5617 –5627 (1980).
- [75] A. I. Landau, "The Effect of Dislocation Inertia on the Thermally Activated Low-Temperature Plasticity of Materials: I. Theory," *Phys. Status Solidi A* **61**, 555–563 (1980).
- [76] R. D. Isaac and A. V. Granato, "Rate theory of dislocation motion: Thermal activation and inertial effects," *Phys. Rev. B* **37**, 9278–9284 (1988).
- [77] M. Hiratani and E. M. Nadgorny, "Combined Modelling of Dislocation Motion with thermally activated and Drag-Dependent Stages," *Acta Mater.* **49**, 4337–4346 (2001).
- [78] J. M. Schwarz and D. S. Fisher, "Depinning with Dynamic Stress Overshoots: Mean Field Theory," *Phys. Rev. Lett.* **87**, 096107–1 (2001).
- [79] M. Hiratani, H. M. Zbib, and M. A. Khaleel, "Modeling of thermally activated dislocation glide and plastic flow through local obstacles," *Int. J. Plast.* **19**, 1271 – 1296 (2003).
- [80] M. Hiratani and V. Bulatov, "Dynamical effects on dislocation glide through weak Obstacles," In *Linking Length Scales in the Mechanical Behavior of Materials*, R. Rudd, T. Balk, W. Windl, and N. Bernstein, eds., *Mater. Res. Soc. Symp. Proc.* **882E**, EE4.4 (Warrendale, PA, 2005).
- [81] V. L. Indenbom and V. Chernov, "Dynamic Waves along dislocations overcoming local obstacles," *Sov. Phys. Solid State* **21**, 759–764 (1979).
- [82] G. Kostorz, "The Influence of the Superconducting Phase Transition on the Plastic Properties of Metals and Alloys," *Phys. Status Solidi B* **58**, 10 – 42 (1973).
- [83] R. D. Isaac, R. Schwarz, and A. Granato, "Internal-friction measurements of dislocation inertial effects in dilute alloys of lead," *Phys. Rev. B* **18**, 4143–4150 (1978).

- [84] T. A. Parkhomenko and V. V. Pustovalov, “The Low-Temperature Yield Stress Anomaly in Metals and Alloys,” *Phys. Status Solidi A* **74**, 12–42 (1982).
- [85] H. Neuhäuser and C. Schwink, in *Plastic deformation and fracture of materials*, Vol. 6 of *Materials science and technology*, H. Mughrabi, ed., (VCH, Weinheim, 1993), Chap. 5. Solid solution strengthening, pp. 191–250.
- [86] E. Vigueras-Santiago, A. A. Krokhin, T. Mckrell, and J. M. Galligan, “Creep at low temperatures: unzipping of dislocations, inertia and criticality processes,” *Physica A* **258**, 11–16 (1998).
- [87] N. Büttner and E. Nembach, “Low temperature anomalies of precipitation hardening in the system copper-cobalt,” *Z. Metallk.* **76**, 82 – 84 (1985).
- [88] K.-D. Fusenig and E. Nembach, “Dynamic dislocation effects in precipitation hardened materials,” *Acta Metall. Mater.* **41**, 3181–3189 (1993).
- [89] H. B. Huntington, J. E. Dickey, and R. Thomson, “Dislocation Energies in NaCl,” *Phys. Rev.* **100**, 1117–1128 (1955).
- [90] R. M. J. Cotterill and M. Doyama, “Energy and atomic configurations of complete and dissociated dislocations. I. Edge dislocation in an fcc Metal,” *Phys. Rev.* **145**, 465 – 478 (1966).
- [91] M. Doyama and R. M. J. Cotterill, “Energy and atomic configurations of complete and dissociated dislocations. II. Screw dislocation in an fcc Metal,” *Phys. Rev.* **150**, 448 – 455 (1966).
- [92] V. B. Shenoy and R. Phillips, “Finite-sized atomistic simulations of screw dislocations,” *Philos. Mag. A* **76**, 367–385 (1997).
- [93] Q. F. Fang and R. Wang, “Atomistic simulation of the atomic structure and diffusion within the core region of an edge dislocation in aluminum,” *Phys. Rev. B* **62**, 9317–9324 (2000).
- [94] D. L. Olmsted, K. Y. Hardikar, and R. Phillips, “Lattice resistance and Peierls stress in finite size atomistic dislocation simulations,” *Modelling Simul. Mater. Sci. Eng.* **9**, 215–247 (2001).
- [95] P. Szelestey, M. Patriarca, and K. Kaski, “Computational study of core structure and Peierls stress of dissociated dislocations in nickel,” *Modelling Simul. Mater. Sci. Eng.* **11**, 883–895 (2003).
- [96] P. Szelestey, M. Patriarca, and K. Kaski, “Dissociated dislocations in Ni: a computational study,” *Mater. Sci. Eng. A* **390**, 393–399 (2005).
- [97] M. Wen, A. Ngan, S. Fukuyama, and K. Yokogawa, “Full-scale atomistic simulations of dislocations in Ni crystal by embedded-atom method,” *Philos. Mag.* **85**, 1917–1929 (2005).
- [98] J. C. H. Henager and R. G. Hoagland, “Dislocation and stacking fault core fields in fcc metals,” *Philos. Mag.* **85**, 4477 – 4508 (2005).

- [99] S. G. Srinivasan, X. Z. Liao, M. I. Baskes, R. J. McCabe, Y. H. Zhao, and Y. T. Zhu, “Compact and Dissociated Dislocations in Aluminum: Implications for Deformation,” *Phys. Rev. Lett.* **94**, 125502 (2005).
- [100] M. S. Daw, M. I. Baskes, C. L. Bisson, and W. G. Wolfer, “Application of the Embedded Atom Method to Fracture, Dislocation Dynamics, and Hydrogen Embrittlement,” In *Proc. Conf. Modeling Environmental Effects on Crack Growth Processes*, pp. 99–124 (The Metallurgical Society AIME, 1986).
- [101] M. S. Daw, S. M. Foiles, and M. I. Baskes, “The Embedded Atom Method: A Review of Theory and Applications,” *Mat. Sci. Reports* **9**, 251 (1993).
- [102] D. Rodney, Thèse, Institut National Polytechnique de Grenoble, 1999.
- [103] D. Mordehai, Y. Ashkenazy, and I. Kelson, “Dynamic properties of screw dislocations in Cu: A molecular dynamics study,” *Phys. Rev. B* **67**, 024112 (2003).
- [104] S. Zhou, D. L. Preston, P. Lomdahl, and D. Beazley, “Large-Scale Molecular Dynamics Simulation of Dislocation Intersection in Copper,” *Science* **279**, 1525 (1998).
- [105] D. Rodney and R. Phillips, “Structure and Strength of Dislocation Junctions: An Atomic Level Analysis,” *Phys. Rev. Lett.* **82**, 1704–1707 (1999).
- [106] M. De Koning, R. Miller, V. Bulatov, and F. F. Abraham, “Modelling grain-boundary resistance in intergranular dislocation slip transmission,” *Philos. Mag. A* **82**, 2511 – 2527 (2002).
- [107] Z.-H. Jin, P. Gumbsch, E. Ma, K. Albe, K. Lu, H. Hahn, and H. Gleiter, “The interaction mechanism of screw dislocations with coherent twin boundaries in different face-centred cubic metals,” *Scripta Mater.* **54**, 1163 – 1168 (2006).
- [108] L. Proville, D. Rodney, Y. Brechet, and G. Martin, “Atomic-scale study of dislocation glide in a model solid solution,” *Philos. Mag.* **86**, 3839 – 3920 (2006).
- [109] D. L. Olmsted, L. G. Hector Jr., and W. A. Curtin, “Molecular dynamics study of solute strengthening in Al/Mg alloys,” *J. Mech. Phys. Solids* **54**, 1763 – 1788 (2006).
- [110] K. Hardikar, V. Shenoy, and R. Phillips, “Reconciliation of atomic-level and continuum notions concerning the interaction of dislocations and obstacles,” *J. Mech. Phys. Solids* **49**, 1951–1967 (2001).
- [111] Y. N. Osetsky and D. J. Bacon, “Atomic modelling of strengthening mechanisms due to voids and copper precipitates in α -iron,” *Philos. Mag.* **83**, 3623 – 3641 (2003).
- [112] D. Rodney and G. Martin, “Dislocation Pinning by Small Interstitial Loops: A Molecular Dynamics Study,” *Phys. Rev. Lett.* **82**, 3272–3275 (1999).
- [113] Y. N. Osetsky and D. J. Bacon, “Atomic-level interaction of an edge dislocation with localized obstacles in fcc and bcc metals,” In *IUTAM Symposium on Mesoscopic Dynamics of Fracture Process and Material Strength*, H. Kitagawa and Y. Shibutani, eds., pp. 193 –202 (Kluwer Academic Publishers, Dordrecht, 2004).

- [114] Y. N. Osetsky and D. J. Bacon, “Comparison of void strengthening in fcc and bcc metals: Large-scale atomic-level modelling,” *Mater. Sci. Eng. A* **400-401**, 374 – 377 (2005).
- [115] D. J. Bacon and Y. N. Osetsky, “Modelling dislocation - obstacle interactions in metals exposed to an irradiation environment,” *Mater. Sci. Eng. A* **400-401**, 353 – 361 (2005).
- [116] T. Hatano and H. Matsui, “Molecular dynamics investigation of dislocation pinning by a nanovoid in copper,” *Phys. Rev. B* **72**, 094105 (2005).
- [117] Y. Osetsky, D. Rodney, and D. Bacon, “Atomic-scale study of dislocation-stacking fault tetrahedron interactions. Part I: mechanisms,” *Philos. Mag.* **86**, 2295 – 2313 (2006).
- [118] J. S. Robach, I. M. Robertson, H.-J. Lee, and B. D. Wirth, “Dynamic observations and atomistic simulations of dislocation-defect interactions in rapidly quenched copper and gold,” *Acta Mater.* **54**, 1679 – 1690 (2006).
- [119] H. Riedel, in *Plastic deformation and fracture of materials*, Vol. 6 of *Materials science and technology: a comprehensive treatment*, R. W. Cahn, P. Haasen, and E. J. Kramer, eds., (VCH, Weinheim, 1993), Chap. 12 Fracture Mechanisms, pp. 565 – 633.
- [120] D. Gross and T. Seelig, *Bruchmechanik*, 3. ed. (Springer, Berlin, 2001).
- [121] B. Lawn, *Fracture of Brittle Solids - Second Edition* (University Press, Cambridge, 1993).
- [122] R. Thomson, “Physics of Fracture,” In *Solid State Physics*, H. Ehrenreich and D. Turnbull, eds., **39**, 1–129 (Academic Press, New York, 1986).
- [123] D. Broek, *Elementary engineering fracture mechanics*, 4. rev. ed., repr. ed. (Kluwer, 2002).
- [124] G. R. Irwin, “Analysis of Stresses and Strains Near the End of a Crack Traversing a Plate,” *J. Appl. Mech.* pp. 361 – 364 (1957).
- [125] A. Kelly, W. R. Tyson, and A. H. Cottrell, “Ductile and Brittle Crystals,” *Philos. Mag. A* pp. 567 – 568 (1967).
- [126] C. St. John, “The brittle-to-ductile transition in pre-cleaved silicon single crystals,” *Philos. Mag. A* pp. 1193 – 1212 (1975).
- [127] M. Brede and P. Hasen, “The brittle-to-ductile transition in doped silicon as a model substance,” *Acta Mater.* **36**, 2003 – 2018 (1988).
- [128] S. Roberts, A. Booth, and P. Hirsch, “Dislocation activity and brittle-ductile transitions in single crystals,” *Mater. Sci. Eng. A* **176**, 91 – 98 (1994).
- [129] H.-S. Kim and S. Roberts, “Brittle-Ductile Transition and Dislocation Mobility in Sapphire,” *J. Am. Ceram. Soc.* **77**, 3099 (1994).
- [130] G. Bergmann and H. Vehoff, “Effect of environment on the brittle-to-ductile transition of pre-cracked NiAl single and polycrystals,” *Mater. Sci. Eng. A* **192-193**, 309–315 (1995).

- [131] M. F. P. Schall and K. Urban, “Plastic deformation behaviour of decagonal $Al_{70}Ni_{15}Co_{15}$ single quasicrystals,” *Philos. Mag. Lett.* **81**, 339 – 349 (2001).
- [132] J. R. Rice and R. Thomson, “Ductile versus brittle behaviour of crystals,” *Phil. Mag.* **29**, 73–97 (1974).
- [133] P. Gumbsch, “Brittle fracture and the brittle-to-ductile transition of tungsten,” *J. Nucl. Mater.* **323**, 304–312 (2003).
- [134] A. Argon, “Mechanics and Physics of Brittle to Ductile Transitions in Fracture,” *J. Eng. Mat. Tech.* **123**, 1 – 11 (2001).
- [135] G. Michot, H. Azzouzi, N. Maloufi, M. Loyola de Oliveira, C. Scandian, and A. George, “Possible Mechanisms for Dislocations Multiplication at, or close to, a Crack Tip,” in *Multiscale Phenomena in Plasticity*, J. L. et al., ed., (Kluwer Academic Press, 2000), pp. 117 – 125.
- [136] J. Riedle, Ph.D. thesis, Universität Stuttgart, 1995.
- [137] J. Riedle, P. Gumbsch, and H. F. Fischmeister, “Cleavage Anisotropy in Tungsten Single Crystals,” *Phys. Rev. Lett.* **76**, 3594–3597 (1996).
- [138] P. Gumbsch, J. Riedle, A. Hartmaier, and H. F. Fischmeister, “Controlling Factors for the Brittle-to-Ductile Transition in Tungsten Single Crystals,” *Science* **282**, 1293–1295 (1998).
- [139] A. Hartmaier and P. Gumbsch, in *Continuum scale simulation of engineering materials*, D. Raabe, ed., (Wiley-VCH, Weinheim, Germany, 2004), Chap. Discrete dislocation dynamics simulation of crack-tip plasticity, pp. 413 – 427.
- [140] A. Hartmaier and P. Gumbsch, “Thermal activation of crack-tip plasticity: The brittle or ductile response of a stationary crack loaded to failure,” *Phys. Rev. B* **71**, 024108 (2005).
- [141] G. Michot and A. George, “Dislocation Emission from Cracks – Observations by X-Ray Topography in Silicon,” *Scripta Metall.* **20**, 1495–1500 (1986).
- [142] P. Warren, “The Brittle-Ductile Transition in Silicon: The Influence of Pre-Existing Dislocation Arrangements,” *Scripta Metall.* **23**, 637–642 (1989).
- [143] P. B. Hirsch and S. G. Roberts, “Comment on the Britte-to-Ductile Transition: a cooperative Dislocation Generation Instability; Dislocation Dynamics and the Strain-Rate Dependence of the Transition Temperature,” *Acta Mater.* **44**, 2361 – 2371 (1996).
- [144] J. Samuels and S. Roberts, “The Brittle-Ductile transition in Silicon. I. Experiments,” *Proc. R. Soc. London, Ser. A* **421**, 1 – 23 (1989).
- [145] P. B. Hirsch, S. G. Roberts, and J. Samuels, “The Brittle-Ductile Transition in Silicon. II. Interpretation,” *Proc. R. Soc. London, Ser. A* **421**, 25 – 53 (1989).
- [146] P. B. Hirsch and S. G. Roberts, “The brittle-ductile transition in silicon,” *Physica A* **64**, 55 – 80 (1991).

- [147] A. George and G. Michot, "Dislocation loops at crack tips: nucleation and growth - and experimental study in silicon," *Mater. Sci. Eng. A* **164**, 118 – 134 (1993).
- [148] G. Michot, M. A. Loyola de Oliveira, and G. Champier, "A model of dislocation multiplication at a crack tip: influence on the brittle to ductile transition," *Mater. Sci. Eng. A* **272**, 83–89 (1999).
- [149] G. Michot and M. A. Loyola de Oliveira, "Plastic Relaxation at Crack Tip: from Brittle to Ductile Behaviour," *Mat. Trans.* **42**, 14 – 19 (2001).
- [150] G. Michot, M. A. Loyola de Oliveira, and H. Koizumi, "Size scale effects on brittle to ductile transition," *J. Phys. IV France* **8**, Pr4–145 – Pr4–153 (1989).
- [151] A. S. Argon and B. J. Gally, "Selection of crack-tip slip systems in the thermal arrest of cleavage cracks in dislocation-free silicon single crystals," *Scr. Mat.* **45**, 1287 – 1294 (2001).
- [152] M. A. Loyola de Oliveira, A. George, and G. Michot, "Dislocation emission at crack tips in silicon under mixed mode loading," *J. Phys. D* **28**, A38 – A41 (1995).
- [153] C. Scandian, Ph.D. thesis, Institut National Polytechnique de Lorraine, 2000.
- [154] M. Tanaka and K. Higashida, "High-voltage electron-microscopical observation of crack-tip dislocations in silicon crystals," *Mater. Sci. Eng. A* **400-401**, 426 – 430 (2005).
- [155] A. S. Argon, "Brittle to ductile transition in cleavage fracture," *Acta Mater.* **35**, 185 – 197 (1987).
- [156] G. Schoeck and W. Püschl, "The formation of dislocation loops at the crack tips in three dimensions," *Phil. Mag. A* **64**, 931–949 (1991).
- [157] G. Schoeck, "Dislocation emission from crack tips," *Phil. Mag. A* **63**, 111–120 (1991).
- [158] Y. Sun, G. Beltz, and J. Rice, "Estimates from Atomic Models of Tension-Shear Coupling in Dislocation Nucleation from a Crack Tip," *Mater. Sci. Eng. A* **170**, 67–85 (1993).
- [159] G. Schoeck, "Dislocation emission from crack tips as a variational problem of the crack energy," *J. Mech. Phys. Solids* **44**, 413 – 437 (1996).
- [160] G. Schoeck, "The emission of dislocations from crack tips: A critical assessment," *Mater. Sci. Eng. A* **356**, 93 – 101 (2003).
- [161] G. E. Beltz and J. R. Rice, "Dislocation Nucleation at Metal-Ceramic Interfaces," *Acta Metall. Mater.* **40**, 321 – 331 (1992).
- [162] E. Kaxiras and M. Duesbery, "Free Energies of Generalized Stacking Faults in Si and Implications for the Brittle-Ductile Transition," *Phys. Rev. Lett.* **70**, 3752–3755 (1993).
- [163] J. Knap and K. Sieradzki, "Crack Tip Dislocation Nucleation in FCC Solids," *Phys. Rev. Lett.* **82**, 1700–1703 (1999).

- [164] G. Xu, in *Dislocations in Solids*, F. R. N. Nabarro and J. P. Hirth, eds., (Elsevier, Amsterdam, 2004), Vol. 12, Chap. Dislocation Nucleation from Crack Tips and Brittle to Ductile Transitions in Cleavage Fracture, pp. 81–145.
- [165] Q. Lu and B. Bhattacharya, “The role of atomistic simulations in probing the small-scale aspects of fracture - a case study on a single-walled carbon nanotube,” *Eng. Fract. Mech.* **72**, 2037 – 2071 (2005).
- [166] S. J. Zhou and R. Thomson, “Dislocation emission at ledges on cracks,” *J. Mater. Res.* **6**, 639 – 653 (1991).
- [167] G. Xu, A. S. Argon, and M. Ortiz, “Nucleation of dislocations from crack tips under mixed modes of loading: implications for brittle against ductile behaviour of crystals,” *Philos. Mag. A* **72**, 415 – 451 (1995).
- [168] G. Xu, A. S. Argon, and M. Ortiz, “Critical configurations for dislocation nucleation from crack tips,” *Philos. Mag. A* **75**, 341 – 367 (1997).
- [169] M. Loyola de Oliveira and G. Michot, “Three dimensional analysis of the interaction between a crack and a dislocation loop,” *Acta Mater.* **46**, 1371–1383 (1998).
- [170] R. Thomson, C. Hsieh, and V. Rana, “Lattice Trapping of Fracture Cracks,” *J. Appl. Phys.* **42**, 3154–3160 (1971).
- [171] P. Gumbsch and R. M. Cannon, “Atomistic Aspects of Brittle Fracture,” *MRS Bull.* **25**, 15–20 (2000).
- [172] P. Gumbsch, “Brittle Fracture and the Breaking of Atomic Bond,” in *Materials Science for the 21st Century* (JSMS, The Society of Materials Science, Japan, 2001), Vol. A, pp. 50–58.
- [173] R. Pérez and P. Gumbsch, “Directional Anisotropy in the Cleavage Fracture of Silicon,” *Phys. Rev. Lett.* **84**, 5347–5350 (2000).
- [174] M. Marder and S. Gross, “Origin of crack tip instabilities,” *J. Mech. Phys. Solids* **43**, 1–48 (1995).
- [175] P. Gumbsch, S. Zhou, and L. Holian, “Molecular dynamics investigation of dynamic crack stability,” *Phys. Rev. B* **55**, 3445–3455 (1997).
- [176] J. A. Hauch, D. Holland, M. P. Marder, and H. L. Swinney, “Dynamic Fracture in Single Crystal Silicon,” *Phys. Rev. Lett.* **82**, 3823 – 3826 (1999).
- [177] M. J. Buehler, F. F. Abraham, and H. Gao, “Hyperelasticity governs dynamic fracture at a critical length scale,” *Nature* **426**, 141 – 146 (2003).
- [178] M. J. Buehler and H. Gao, “Dynamical fracture instabilities due to local hyperelasticity at crack tips,” *Nature* **439**, 307 – 310 (2006).
- [179] “Atomistic Theory and Simulation of Fracture,” *MRS Bull.* 25 (2000).
- [180] J. Li, T. Zhu, S. Yip, K. J. Van Vliet, and S. Suresh, “Elastic criterion for dislocation nucleation,” *Mater. Sci. Eng. A* **365**, 25–30 (2003).

- [181] D. Farkas and R. L. B. Selinger, in *Handbook of materials modeling*, S. Yip, ed., (Springer, Berlin, 2005), Chap. 2.23, Atomistics of Fracture, pp. 839 – 853.
- [182] F. F. Abraham, D. Schneider, B. Land, D. Lifka, J. Skovira, J. Gerner, and M. Rosenkrantz, “Instability dynamics in three-dimensional fracture: an atomistic simulation,” *J. Mech. Phys. Solids* **45**, 1461 –1471 (1997).
- [183] F. F. Abraham, R. Walkup, H. Gao, M. Duchaineau, T. D. D. L. Rubia, and M. Seager, “Simulating materials failure by using up one billion atoms and the world’s fastest computer: Work-hardening,” *Proc. Nat. Acad. Sci. U.S.A.* **99**, 5783–5787 (2002).
- [184] M. J. Buehler, A. Hartmaier, H. G. M. Duchaineau, and F. F. Abraham, “Atomic plasticity: description and analysis of a one-billion atom simulation of ductile materials failure,” *Comput. Methods Appl. Mech. Engrg.* **193**, 5257 – 5282 (2004).
- [185] S. J. Zhou, D. M. Beazley, P. S. Lomdahl, and B. L. Holian, “Large-Scale Molecular Dynamics Simulations of Three-Dimensional Ductile Failure,” *Phys. Rev. Lett.* **78**, 479–482 (1997).
- [186] S. Zhou, P. Lomdahl, A. Voter, and B. Holian, “Three-dimensional fracture via large-scale molecular dynamics,” *Eng. Fract. Mech.* **61**, 173–187 (1998).
- [187] H. Kimizuka, H. Karubaki, F. Shimizu, and J. Li, “Crack-tip dislocation nanostructures in dynamical fracture of fcc metals: A molecular dynamics study,” *J. Comput. Aided Mater. Des.* **10**, 143 – 154 (2003).
- [188] T. Zhu, J. Li, and S. Yip, “Atomistic Study of Dislocation Loop Emission from a Crack Tip,” *Phys. Rev. Lett.* **93**, 025503 (2004).
- [189] M. P. Allen and D. J. Tildesley, *Computer simulation of liquids* (Clarendon Press, Oxford , UK, 1996).
- [190] A. R. Leach, *Molecular Modelling: principles and applications*, 2nd ed. (Prentice Hall, Harlow , UK, 2001).
- [191] D. Raabe, *Computational materials science* (Wiley-VCH, 1998).
- [192] D. Frenkel and B. Smit, *Understanding molecular simulation*, 2. ed. (Academic Press, 2002).
- [193] D. C. Rapaport, *The art of molecular dynamics simulation*, 2. ed. (Cambridge Univ. Press, 2004).
- [194] S. Yip, *Handbook of materials modeling* (Springer, Berlin, 2005).
- [195] J. Stadler, R. Mikulla, and H.-R. Trebin, “ IMD : A Software package for molecular dynamics studies on parallel computers,” *Int. J. Mod. Phys. C* **8**, 1131–1140 (1997).
- [196] J. Roth *et al.*, “ IMD – A Massively Parallel MD Package for Classical Simulations in Condensed Matter,” In *High Performance Comput. in Sci. and Eng. '99*, E. Krause and W. Jäger, eds., pp. 72–81 (Springer, Berlin, 2000).

- [197] E. Bitzek, F. Gähler, J. Hahn, C. Kohler, G. Krdzalic, J. Roth, C. Rudhart, G. Schaaf, J. Stadler, and H.-R. Trebin, “Recent developments in IMD : Interactions for covalent and metallic systems,” In *High Performance Computing in Science and Engineering 2000*, E. Krause and W. Jäger, eds., pp. 37 – 47 (Springer , Heidelberg, 2001).
- [198] IMD, “the ITAP Molecular Dynamics Program,” <http://www.itap.physik.uni-stuttgart.de/~imd>.
- [199] T. Schlick, *Molecular modeling and simulation: an interdisciplinary guide*, Vol. 21 of *Interdisciplinary Applied Mathematics* (Springer-Verlag, New York, 2002).
- [200] E. Bitzek, P. Koskinen, F. Gähler, M. Moseler, and P. Gumbsch, “Structural Relaxation Made Simple,” *Phys. Rev. Lett.* **97**, 170201 (2006).
- [201] M. S. Daw and M. I. Baskes, “Embedded- Atom Method: Derivation and application to impurities, surfaces, and other defects in metals,” *Phys. Rev. B* **29**, 6443–6453 (1984).
- [202] S. M. Foiles, M. I. Baskes, and M. S. Daw, “Embedded-atom-method functions for the fcc metals Cu, Ag, Au, Ni, Pd, Pt and their alloys,” *Phys. Rev. B* **33**, 7983–7991 (1986).
- [203] M. S. Daw, “Model of Metallic Cohesion: The Embedded-Atom Method ,” *Phys. Rev. B* **39**, 7441–7452 (1989).
- [204] M. S. Daw, S. M. Foiles, and M. I. Baskes, “The Embedded Atom Method: A Review of Theory and Applications,” *Mat. Sci. Reports* **9**, 251 (1993).
- [205] Y. Mishin, in *Handbook of materials modeling*, S. Yip, ed., (Springer, Berlin, 2005), Chap. 2.2, Interatomic potentials for metals, pp. 459 – 478.
- [206] F. Ercolessi and J. B. Adams, “Interatomic Potentials from First-Principles Calculations: the Force-Matching Method,” *Europhys. Lett.* **26**, 583–588 (1994).
- [207] Y. Mishin, D. Farkas, M. J. Mehl, and D. A. Papaconstantopoulos, “Interatomic potentials for monoatomic metals from experimental data and *ab initio* calculations,” *Phys. Rev. B* **59**, 3393–3407 (1999).
- [208] J. A. Zimmerman, H. Gao, and F. F. Abraham, “Generalized stacking fault energies for embedded atom fcc metals,” *Modelling Simul. Mater. Sci. Eng.* **8**, 103–115 (2000).
- [209] J. E. Angelo, N. R. Moody, and M. I. Baskes, “Trapping of hydrogen to lattice defects in nickel,” *Modelling Simul. Mater. Sci. Eng.* **3**, 289 – 307 (1995).
- [210] M. I. Baskes *et al.*, “Comment: Trapping of hydrogen to lattice defects in nickel,” *Modelling Simul. Mater. Sci. Eng.* **5**, 651 (1997).
- [211] M. Baskes, private communication (unpublished).
- [212] L. Dupuy, private communication (unpublished).
- [213] Y. Mishin, “Atomistic modeling of the γ and γ' -phases of the Ni-Al system,” *Acta Mater.* **52**, 1451–1467 (2004).

- [214] Y. Mishin, M. J. Mehl, D. A. Papaconstantopoulos, A. F. Voter, and J. D. Kress, “Structural stability and lattice defects in copper: *ab initio*, tight binding and embedded-atom calculations,” *Phys. Rev. B* **63**, 224106 (2001).
- [215] S. Nosé, “A unified formulation of the constant temperature molecular dynamics methods,” *J. Chem. Phys.* **81**, 511–519 (1984).
- [216] W. G. Hoover, “Canonical dynamics: Equilibrium phase-space distributions,” *Phys. Rev. A* **31**, 1695–1697 (1985).
- [217] B. L. Holian, A. F. Voter, and R. Ravelo, “Thermostatted Molecular dynamics: how to avoid the Toda demon hidden in Nosé-Hoover dynamics,” *Phys. Rev. E* **52**, 2338–2347 (1995).
- [218] M. W. Finnis, P. Agnew, and A. J. E. Foreman, “Thermal excitation of electrons in energetic displacement cascades,” *Phys. Rev. B* **44**, 567–574 (1991).
- [219] A. Aslanides and V. Pontikis, “Atomistic calculation of the interaction between an edge dislocation and a free surface,” *Philos. Mag. Lett.* **78**, 377–383 (1998).
- [220] B. Pestman *et al.* (unpublished).
- [221] E. Bitzek, Master’s thesis, Universität Stuttgart, 2000.
- [222] E. Bitzek and P. Gumbsch, “Atomistic Simulations of Dislocation - Crack interaction,” In *High Performance Computing in Science and Engineering*, (Springer, Heidelberg, 2006), accepted for publication.
- [223] C. Rudhart, Ph.D. thesis, Universität Stuttgart, 2004.
- [224] C. L. Kelchner, S. J. Plimpton, and J. C. Hamilton, “Dislocation nucleation and defect structure during surface indentation,” *Phys. Rev. B* **58**, 11085–11088 (1998).
- [225] J. Honeycutt and H. Andersen, “Molecular-dynamics study of melting and freezing of small lennard-jones clusters,” *J. Phys. Chem.* **91**, 4950–4963 (1987).
- [226] A. Clarke and H. Jónsson, “Structural-changes accompanying densification of random hard-sphere packings,” *Phys. Rev. E* **47**, 3975–3984 (1993).
- [227] J. A. Zimmerman, C. L. Kelchner, P. A. Klein, J. C. Hamilton, and S. M. Foiles, “Surface Step Effects on Nanoindentation,” *Phys. Rev. Lett.* **87**, (165507–1)–(165507–4) (2001).
- [228] C. S. Hartley and Y. Mishin, “Characterization and visualization of the lattice misfit associated with dislocation cores,” *Acta Mater.* **53**, 1313–1321 (2005).
- [229] J. Li, “AtomEye: an efficient atomistic configuration viewer,” *Modelling Simul. Mater. Sci. Eng.* **11**, 173 – 177 (2003).
- [230] “<http://www.cognigraph.com/LibGen/index.html>,”.
- [231] E. Bitzek and E. Bringa, unpublished (unpublished).
- [232] A. Roos, J. T. M. De Hosson, and E. Van der Giessen, “High-speed dislocations in high strain-rate deformations,” *Comp. Mat. Sci.* **20**, 19–27 (2001).

- [233] H. Stöcker, *Taschenbuch der Physik*, 3. ed. (Deutsch, Frankfurt am Main, 1998).
- [234] R. O. Scattergood and D. J. Bacon, “The strengthening effect of voids,” *Acta Mater.* **30**, 1665 – 1677 (1982).
- [235] S. Zinkle and K. Farwell, “Void swelling and defect cluster formation in reactor-irradiated copper,” *J. Nucl. Mater.* **168**, 262 – 267 (1989).
- [236] Y. N. Osetsky and D. J. Bacon, “An atomic-level model for studying the dynamics of edge dislocations in metals,” *Modelling Simul. Mater. Sci. Eng.* **11**, 427 – 446 (2003).
- [237] W. Cai, V. V. Bulatov, J. Chang, J. Li, and S. Yip, “Dislocation core effects on mobility,” in *Dislocations in Solids*, F. R. N. Nabarro and J. P. Hirth, eds., (North-Holland, Amsterdam, 2004), Vol. 12, pp. 1 – 80.
- [238] M. S. Duesbery, “The dislocation core and plasticity,” in *Dislocations in Solids*, F. R. N. Nabarro, ed., (North-Holland, Amsterdam, 1989), Vol. 8, pp. 67 – 174.
- [239] A. Stroh, “Dislocations and cracks in anisotropic elasticity,” *Philos. Mag.* **3**, 625– 646 (1958).
- [240] J. Douin, *Documentation succincte du programme DISDI*, 2004.
- [241] A. K. Head, P. Humble, L. M. Clareborough, A. I. Morton, and C. T. Forwood, *Computed electron micrographs and defect identification*, Vol. 7 of *Defects in crystalline solids* (North-Holland, Amsterdam, 1973).
- [242] C. B. Carter and S. M. Holmes, “The stacking fault of nickel,” *Philos. Mag.* **35**, 1161 – 1172 (1977).
- [243] C. B. Carter, “What’s new in dislocation dissociation,” In *Dislocations 1984 : Comptes rendus du Colloque International du CNRS Dislocations : structure de coeur et propriétés physiques*, P. Veyssi re, ed., pp. 227 – 252 (Centre National de la Recherche Scientifique, Paris, 1984).
- [244] B. von Sydow, J. Hartford, and G. Wahnstr m, “Atomistic simulation and Peierls-Nabarro analysis of the Schockley partial dislocations in palladium,” *Comp. Mat. Sci.* **15**, 367–379 (1999).
- [245] G. Schoeck, “The core structure of dislocations: Peierls model vs. atomic simulation,” *Acta Mater.* **54**, 4865 – 4870 (2006).
- [246] J. Hartford, B. von Sydow, G. Wahnstr m, and B. Lundqvist, “Peierls barriers and stresses for edge dislocations in Pd and Al calculated from first principles,” *Phys. Rev. B* **58**, 2487–2496 (1998).
- [247] Y. Mishin, private communication.
- [248] B. Jo s and M. S. Duesbery, “The Peierls Stress of Dislocations: An Analytic Formula,” *Phys. Rev. Lett.* **78**, 266 – 270 (1997).
- [249] F. R. N. Nabarro, “Fifty-year study of the Peierls-Nabarro stress,” *Mater. Sci. Eng. A* **234-236**, 67–76 (1997).

- [250] F. R. N. Nabarro, “Theoretical and experimental estimates of the Peierls stress,” *Philos. Mag. A* **75**, 703–711 (1997).
- [251] V. V. Bulatov, O. Richmond, and M. V. Glazov, “An atomistic dislocation mechanism of pressure-dependent plastic flow in aluminum,” *Acta Metall.* **47**, 3507 – 3514 (1999).
- [252] R. C. Pasianot and A. Moreno-Gobbi, “On the Peierls stress in Al and Cu: An atomistic simulation and comparison with experiment,” *Phys. Status Solidi B* **241**, 1261–1268 (2004).
- [253] G. Lu, N. Kioussis, V. V. Bulatov, and E. Kaxiras, “Generalized-stacking-fault energy surface and dislocation properties of aluminum,” *Phys. Rev. B* **62**, 3099–3108 (2000).
- [254] G. Lu and N. Kioussis, “The Peierls-Nabarro model revisited,” *Philos. Mag. Lett.* **80**, 675–682 (2000).
- [255] A. Gitt-Gehrke, Ph.D. thesis, Universität Braunschweig, 2002.
- [256] G. Lu, N. Kioussis, V. V. Bulatov, and E. Kaxiras, “Generalized-stacking-fault energy surface and dislocation properties of aluminum,” *Phys. Rev. B* **62**, 3099–3108 (2000).
- [257] W. Benoit, M. Bujard, and G. Gremaud, “Kink Dynamics in F.C.C. Metals,” *Phys. Status Solidi A* **104**, 427–441 (1987).
- [258] G. Schoeck, “The Peierls stress and the flow stress in fcc metals,” *Scripta Metall. Mater.* **30**, 611–613 (1994).
- [259] S. Wolfram, *The mathematica book*, 4. ed. (Wolfram Media, 1999).
- [260] W. H. Press, B. P. Flannery, S. A. Teukolsky, and W. T. Vetterling, *Numerical Recipes in C* (Cambridge University Press, Cambridge, 1997).
- [261] J. Li, C.-Z. Wang, J.-P. Chang, W. Cai, V. V. Bulatov, K.-M. Ho, and S. Yip, “Core energy and Peierls stress of a screw dislocation in bcc molybdenum: A periodic-cell tight-binding study,” *Phys. Rev. B* **70**, 104113 (2004).
- [262] J. A. Gorman, D. Wood, and T. Vreeland Jr., “Mobilities of dislocations in Aluminum at 74 and 83 K,” *J. Appl. Phys.* **40**, 903 – 904 (1969).
- [263] E. Bitzek, D. Weygand, and P. Gumbsch, “Atomistic study of edge dislocations in fcc metals: drag and inertial effects,” In *IUTAM Symposium on Mesoscopic Dynamics of Fracture Process and Material Strength*, H. Kitagawa and Y. Shibutani, eds., pp. 45 – 57 (Kluwer Academic Publishers , Dordrecht, 2004).
- [264] D. Weygand, “A discrete dislocation dynamics investigation of formation and stability of Lomer locks,” In *IUTAM Symposium on Mesoscopic Dynamics of Fracture Process and Material Strength*, H. Kitagawa and Y. Shibutani, eds., pp. 23 – 33 (Kluwer Academic Publishers , Dordrecht, 2004).
- [265] A. Walcker, D. Weygand, and O. Kraft, “Inertial effects on dislocation damping under cyclic loading with ultra-high frequencies,” *Mater. Sci. Eng. A* **400-401**, 397 –400 (2005).

- [266] A. Hikata, R. Johnson, and C. Elbaum, "Interaction of dislocations with electrons and phonons," *Phys. Rev. B* **2**, 4856 – 4863 (1970).
- [267] K. M. Jassby and J. T. Vreeland, "An Experimental Study of the Mobility of Edge Dislocations in Pure Copper Single Crystals," *Philos. Mag.* **21**, 1147–1168 (1970).
- [268] N. P. Kobelev, Y. M. Soifer, and V. Al'shits, "Relationship between viscous and relaxation components of the dislocation attenuation of high-frequency ultrasound in copper," *Soviet Phys. Solid St.* **21**, 680 – 684 (1979).
- [269] B. D. Wirth, M. J. Caturla, T. D. de la Rubia, T. Khraishi, and H. Zbib, "Mechanical property degradation in irradiated materials: A multiscale modeling approach," *Nucl. Instrum. Meth. B* **180**, 23 – 31 (2001).
- [270] R. O. Scattergood and D. J. Bacon, "The Orowan mechanism in anisotropic crystals," *Philos. Mag.* **31**, 179 – 198 (1975).
- [271] J. S. Robach, I. M. Robertson, and A. Arsenlis, "In-situ transmission electron microscopy observations and molecular dynamics simulations of dislocation-defect interactions in ion-irradiated copper," *Philos. Mag.* **83**, 955 – 967 (2003).
- [272] E. Bitzek and P. Gumbsch, "Atomistic study of drag, surface and inertial effects on edge dislocations in face-centered cubic metals," *Mater. Sci. Eng. A* **387-389**, 11–15 (2004).
- [273] E. Bitzek and P. Gumbsch, "Dynamics aspects of dislocation motion: atomistic simulations," *Mater. Sci. Eng. A* **400-401**, 40–44 (2005).
- [274] M. Fivel, M. Verdier, and G. Canova, "3D simulation of a nanoindentation test at a Mesoscopic scale," *Mater. Sci. Eng. A* **234-236**, 923–926 (1997).
- [275] V. Bulatov, F. F. Abraham, L. Kubin, B. Devincere, and S. Yip, "Connecting atomistic and mesoscale simulations of crystal plasticity," *Nature* **391**, 669–672 (1998).
- [276] D. Weygand, L. Friedman, E. Van der Giessen, and A. Needleman, "Aspects of boundary-value problem solutions with three-dimensional dislocation dynamics," *Modelling Simul. Mater. Sci. Eng.* **10**, 437–468 (2002).
- [277] L. Pillon, C. Denoual, R. Madec, and Y. Pellegrini, "Influence of inertia on the formation of dislocation dipoles," *J. Phys. IV France* **134**, 49–54 (2006).
- [278] H. M. Zbib and T. D. de la Rubia, "A multiscale model of plasticity," *Int. J. Plasticity* **18**, 1133 – 1163 (2002).
- [279] J.-H. Shim, H.-J. Lee, and B. D. Wirth, "Temperature dependent dislocation bypass mechanism for coherent precipitates in Cu-Co alloys," submitted to *Nature Materials*.
- [280] E. Arzt, "Size effects in materials due to microstructural and dimensional constraints: a comparative review," *Acta Mater.* **46**, 5611 – 5626 (1998).
- [281] M. D. Uchic, D. M. Dimiduk, R. Wheeler, P. A. Shade, and H. L. Fraser, "Application of micro-sample testing to study fundamental aspects of plastic flow," *Scr. Mat.* **54**, 759 – 764 (2006).

- [282] J. R. Greer and W. D. Nix, “Nanoscale gold pillars strengthened through dislocation starvation,” *Phys. Rev. B* **73**, 245410,1–6 (2006).
- [283] D. Dimiduk, M. Uchic, and T. Parthasarathy, “Size-affected single-slip behavior of pure nickel microcrystals,” *Acta Mater.* **53**, 4065 – 4077 (2005).
- [284] F. Csikor, private communication (unpublished).
- [285] V. D. Natsik and E. Minenko, “Effect of hte dislocation structure of a crystal on dynamic braking of mobile dislocations,” *Sov. Phys. Solid State* **12**, 1668 – 1672 (1971).
- [286] I. Groma, “Statistical physical approach to describe the collective properties of dislocations,” unpublished (2005), statistical Physics of Dislocations: Multi Scale Modelling of Plasticity, Advanced School, CISM, Udine.
- [287] A. Maurel, V. Pagneux, F. Barra, and F. Lund, “Interaction between an elastic wave and a single pinned dislocation,” *Phys. Rev. B* **72**, 174110 (2005).
- [288] A. Maurel, V. Pagneux, F. Barra, and F. Lund, “Wave propagation through a random array of pinned dislocations: Velocity change and attenuation in a generalized Granato and Lücke theory,” *Phys. Rev. B* **72**, 174111 (2005).
- [289] D. Shilo and E. Zolotoyabko, “Stroboscopic X-Ray Imaging of Vibrating Dislocations Excited by 0.58 GHz Phonons,” *Phys. Rev. Lett.* **91**, 115506 (2003).
- [290] C. Eberl, R. Spolenak, E. Arzt, F. Kubat, A. Leidl, W. Ruile, and O. Kraft, “Ultra high-cycle fatigue in pure Al thin Films and line structures,” *Mater. Sci. Eng., A* **421**, 68 – 76 (2006).
- [291] J. Weiss and D. Marsan, “Three-Dimensional Mapping of Dislocation Avalanches: Clustering and Space/Time Coupling,” *science* **299**, 89–91 (2003).
- [292] J. Weiss and F. Louchet, “Seismology of plastic deformation,” *Scripta Mater.* **54**, 747 – 751 (2006).
- [293] D. Rouby, P. Fleischman, and C. Duvergier, “Un modèle de source d’émission acoustique pour l’analyse de l’émission continue et de l’émission par salves: I. Analyse théorique,” *Philos. Mag. A* **47**, 671–687 (1983).
- [294] P. Gumbsch, “An Atomistic Study of Brittle Fracture: Towards Explicit Failure Criteria from Atomistic Modelling,” *J. Mater. Res.* **10**, 2897–2907 (1995).
- [295] G. C. Sih and H. Liebowitz, in *Fracture , An Advanced Treatise*, H. Liebowitz, ed., (Academic Press , New York, 1968), Chap. 2, pp. 67–190.
- [296] F. Rösch, C. Rudhart, J. Roth, H.-R. Trebin, and P. Gumbsch, “Dynamic fracture of icosahedral model quasicrystals: A molecular dynamics study,” *Phys. Rev. B* **72**, 014128 (2005).
- [297] E. B. Tadmor and S. Hai, “A Peierls criterion for the onset of deformation twinning at a crack tip,” *J. Mech. Phys. Solids* **51**, 765 – 793 (2003).

- [298] S. Ogata, J. Li, and S. Yip, “Energy landscape of deformation twinning in bcc and fcc metals,” *Phys. Rev. B* **71**, 224102 (2005).
- [299] C. Brandl and E. Bitzek, “DISPROCRAST, a program package for the analysis of Dislocation PROCesses in CRAck STress fields,” 2006.
- [300] H. Jónsson, G. Mills, and W. Jacobsen, in *Classical and Quantum Dynamics in Condensed Phase Simulations* (World Scientific, Singapur, 1998), p. 385.
- [301] A. George and G. Champier, “Velocities of Screw and 60 deg Dislocations in n- and p-Type Silicon,” *Phys. Status Solidi A* **53**, 529–540 (1979).
- [302] D. Sherman and I. Be’ery, “Dislocations Deflect and Perturb Dynamically Propagating Cracks,” *Phys. Rev. Lett.* **93**, 265501 (2004).
- [303] C. Z. Wang, B. C. Pan, and K. M. Ho, “An environment-dependent tight-binding potential for Si,” *J. Phys. Cond. Mat.* **11**, 2043 – 2049 (1999).
- [304] G. Trimarchi, T. Albaret, P. Gumbsch, S. Meriani, J. V. Barth, and A. de Vita, “Tuning force fields for the simulation of large systems,” In *Proc. Int. CIMTEC*, pp. 35–42 (Florence, 2002).
- [305] P. E. Gill, W. Murray, and M. H. Wright, *Practical Optimization* (Academic Press, New York, 1981).
- [306] J. R. Beeler, in *Radiation Effects Computer Experiments* (North-Holland, Amsterdam, 1983), p. 27.
- [307] S. A. Trygubenko and D. Wales, “A doubly nudged elastic band method for finding transition states,” *J. Comput. Phys.* **120**, 2082 (2004).
- [308] P. Koskinen, private communication.
- [309] T. Schenk, “Global optimization of Chaboche’s model, including the ADAPTGLOC method and Lennard-Jones clusters,” Technical report, Fraunhofer Institut Werkstoffmechanik (2005) .

Acknowledgments

This thesis would not have been possible without the help of a great number of people, to whom I want to express my gratefulness.

In particular, I am deeply indebted to my advisor Prof. Peter Gumbsch for the guidance, support, freedom and encouragement that he provided during my time in Stuttgart and Karlsruhe, as well as for the unique opportunity to participate in the foundation of the izbs.

I thank my thesis committee members, Prof. Alexander Wanner for agreeing on assuming the “Mitbericht” for this dissertation, as well as for interesting discussions, and Prof. Thomas Böhlke for agreeing on assuming the “Prüfungsvorsitz”.

I am especially thankful to the system administrators of the izbs: Werner Augustin, Ingo Haag and Dr. Daniel Weygand for their invaluable support, particularly after I lost my data on the cluster. I also want to thank our Secretary Andrea Doer for always being very helpful.

I would like to thank all co-developers of IMD, in particular Dr. Franz Gähler, for constantly improving the code, as well as the other developers of “FIRE”, Dr. Pekka Koskinen, Dr. Michael Moseler and Prof. Peter Gumbsch for this fruitful collaboration.

I thank Prof. Joël Douin for providing me with his program DISDI, Dr. Matous Mrovec for providing me the source code of Disloelast, and Prof. Ju Li for making AtomEye Public Domain.

I also thank Christian Brandl for helping with the analysis of some of the crack simulations and for introducing me to Matlab.

I have benefited a lot from the numerous discussions with colleagues and friends. I would like to thank all the participants of the “Mikroplastizitätsrunde” which provided a valuable link to the experiments. I am also very thankful for the interesting and encouraging discussions with Dr. Daniel Weygand as well as with Dr. Ruth Schwaiger, Prof. Oliver Kraft, Prof. Ottmar Vöhringer, Prof. Alexander Hartmaier, Prof. Zhaohui Jin, Dr. Rebecca Janisch, Prof. Gunther Schöck, Prof. Ladislav Kubin, Dr. David Rodney, Prof. Gerard Michot, Prof. Yuri Mishin, Prof. Brian Wirth, Prof. Huajian Gao and Prof. Ali Argon. And of course I want to thank all my colleagues at the izbs for the great time there, especially my office-mates Prof. Yoshitaka Umeno, Dr. Ferenc Csikor and Dr. Burghard von Blanckenhagen, as well as the colleagues at the IWM and my former colleagues at the Max-Planck Institut für Metallforschung.

I thank Senta Kuhnert and Gunter Blache for the proof-reading of the manuscript, Elisabeth Charbonnier for her help with the French language, and Prof. Alexander Hartmaier for valuable comments on the manuscript.

“Life is tough and then you graduate” – I am grateful for the moral support offered by my “Leidensgenossen” Tanja Nitschke, Andreas Eichinger and in particular Christof Horn, the Café Palaver and the comics by Dr. Jorge Cham (www.phdcomics.com).

Finally, I want to acknowledge the help and support of my family and all my friends.